

Bangor University

DOCTOR OF PHILOSOPHY

Low temperature routes to heterogeneous catalysts

Cavanagh, Edward Antony

Award date:
2002

Awarding institution:
University of Wales, Bangor

[Link to publication](#)

General rights

Copyright and moral rights for the publications made accessible in the public portal are retained by the authors and/or other copyright owners and it is a condition of accessing publications that users recognise and abide by the legal requirements associated with these rights.

- Users may download and print one copy of any publication from the public portal for the purpose of private study or research.
- You may not further distribute the material or use it for any profit-making activity or commercial gain
- You may freely distribute the URL identifying the publication in the public portal ?

Take down policy

If you believe that this document breaches copyright please contact us providing details, and we will remove access to the work immediately and investigate your claim.

Download date: 10. Apr. 2024

Low Temperature Routes to Heterogeneous Catalysts

A thesis submitted to the

University of Wales, Bangor

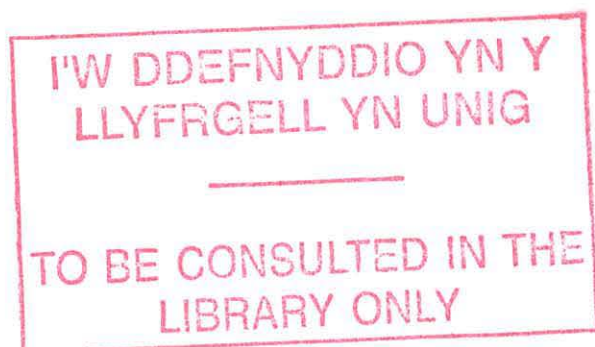
In candidature for the degree of

Doctor of Philosophy

by

Edward Antony Cavanagh

2002



For H'

Acknowledgements

My initial thanks go to my supervisor, Dr. Peter Holliman. I hope that I have repaid the help and support he has given me over the past three years with the work I have returned. He has been relaxed throughout, allowing me to take the initiative and listening to any ideas, good or bad, I have had.

I would also like to thank each of the technical staff for their time and effort. The extensive list includes Glyn Connelly, Denis Williams, Gwynfor Davies, Mike Lewis and Gwerydd Griffiths for providing me with (sometimes) fully functional equipment and instrumentation. John Charles has been a constant source of advice and has made, or repaired, the vast majority of the glassware and miscellaneous pieces of equipment I've used. The expertise of Andrew Davies of the biology department has been essential to the quality of the electron microscopy, the information he has provided concerning the foibles of the instrumentation can only be described as invaluable. Thanks must also go to Dr. Dave Jenkins of the soil science department for providing me with both information on mineralogy and access to the DTA and X-ray diffractometer used in the early stages of my research.

A huge cheer of thanks goes to Manchester United who have kept me going in times of stress with their unparalleled level of skill and tenacity. They have also been the source of a fair amount of stress although I was never in any doubt of them completing *the* historic Treble of the Carling Premiership, FA Cup and European Cup, obviously. Are you watching Liverpool?

Erika, maybe we can get 'back to normal' now and enjoy ourselves a bit more again. It's been hard work but we've coped, just, and you've had your own career to manage aswell - something you've done very successfully. I'm very proud of you, well done. I think you're the bestest. That is, along with my boy, Becks. He's had to listen to my ramblings every day but has never once complained which isn't really surprising given the number of distractions he has to contend with such as where his next meal is coming from or where that last rabbit went.

Ultimately, my biggest thanks must go to my Mum and Dad who set me on the right path from the start. They struggled to provide me with a level of education they never had. Their effort hasn't been wasted.

Abstract

A series of synthetic minerals based on hydrotalcite, $\text{Mg}_6\text{Al}_2(\text{OH})_{16}\text{CO}_3 \cdot 4\text{H}_2\text{O}$, has been prepared using coprecipitation techniques in order to yield materials with similar morphologies and yet greater potential for forming heterogeneous catalysts after a relatively low temperature activation step. The idealised formulae of these hydrotalcite-type compounds (HTc's) covered a range of increasing Fe^{II} -for- Mg^{II} substitution from $\text{Mg}_6\text{Al}_2(\text{OH})_{16}\text{CO}_3 \cdot 4\text{H}_2\text{O}$ through to $\text{Fe}_6\text{Al}_2(\text{OH})_{16}\text{CO}_3 \cdot 4\text{H}_2\text{O}$. These catalyst precursor materials have been characterised using a range of techniques which include infrared spectroscopy, X-ray powder diffraction, scanning electron microscopy and differential thermal analysis. A number of aluminium-substituted iron oxides have also been prepared both directly and *via* the iron oxide intermediate known as 'green rust', which is isostructural with hydrotalcite. These materials were prepared and characterised for comparison with the HTc's due to their chemical and structural similarities and their potential for use as heterogeneous catalysts.

A study of the calcination of the HTc's has been undertaken, with the aim of producing high porosity/surface area materials whilst retaining the platelet morphology displayed by the HTc's and attaining as low a maximum calcination temperature as possible. The effects of various temperature regimes were explored and the calcined materials characterised.

The use of the prepared HTc's as base catalysts was investigated using the cyanoethylation of a range of alcohols as a test reaction. The study included a study of the activation of the HTc's prior to the reaction and their subsequent activity and selectivity for the reaction.

The activity and selectivity of the calcined HTc's for the oxidation of sulfur dioxide to sulfur trioxide and the dehydrogenation of cyclohexane was also investigated. A purpose-built test rig utilising in-line gas chromatography was constructed in order to do this.

Abbreviations

AAS	Atomic absorption spectroscopy
CEC	Cation exchange capacity
DTA	Differential thermal analysis
EDAX	Energy-dispersive analysis of X-rays
FID	Flame ionisation detector
GC	Gas chromatography/Gas chromatograph
GHSV	Gas hourly space velocity
H	Hexagonal
HTc	Hydrotalcite-type compound – also used to represent ‘ $(\text{OH})_{16}\text{CO}_3 \cdot 4\text{H}_2\text{O}$ ’
ICP	Inductively-coupled plasma
IR	Infrared
JCPDS	Joint Committee on Powder Diffraction Standards
MS	Mass spectrometry
MFC	Mass flow controller
PID	Proportional-integral-derivative
PILAC	Pillared layered anionic clay
R	Rhombohedral
SEM	Scanning electron microscopy
TCD	Thermal conductivity detector
TGA	Thermo-gravimetric analysis
TPD	Temperature programmed desorption
XRD	X-ray diffraction
XRPD	X-ray powder diffraction

Contents

1. Introduction.....	1
1.1 Area of Study.....	1
1.1.1 Overview of Catalysis.....	1
1.1.2 Outline of Research Area.....	3
1.2 Base Catalysis.....	6
1.3 Oxidation Catalysis.....	8
1.4 Clays and Clay Minerals in Catalysis.....	14
1.4.1 Cationic Clays.....	14
1.4.2 Anionic Clays.....	18
1.4.3 Iron Oxides.....	23
1.5 Hydrotalcite-type Compounds.....	30
1.5.1 Structure.....	30
1.5.2 Preparation.....	32
1.5.3 Calcination.....	34
1.5.4 Catalysis.....	36
1.6 Green Rusts and their Oxidation Products.....	38
1.7 References.....	40
 2. Preparation and Characterisation of Precursor Materials.....	 47
2.1 Hydrotalcite-type Compounds.....	47
2.1.1 Preparative Methodology.....	47
2.1.2 Infrared Spectroscopy.....	49
2.1.3 X-ray Powder Diffraction.....	57
2.1.4 Scanning Electron Microscopy and Energy Dispersive Analysis of X-rays.....	64
2.1.5 Differential Thermal Analysis.....	74
2.1.6 Conclusions.....	79
2.2 Green Rusts and Iron Oxides.....	81
2.2.1 Preparative Methodology.....	81
2.2.2 Infrared Spectroscopy.....	83
2.2.3 X-ray Powder Diffraction.....	89
2.2.4 Scanning Electron Microscopy and Energy Dispersive Analysis of X-rays.....	94
2.2.5 Conclusions.....	102
2.3 References.....	104

3. Precursor Activation.....	110
3.1 Calcination Studies.....	110
3.1.1 Methodology.....	110
3.1.2 Infrared Spectroscopy.....	111
3.1.3 X-ray Powder Diffraction.....	116
3.1.4 Scanning Electron Microscopy.....	121
3.1.5 Conclusions.....	125
3.2 Cyanoethylation Catalyst Activation.....	126
3.2.1 Methodology.....	126
3.2.2 Infrared Spectroscopy.....	127
3.2.3 X-ray Powder Diffraction.....	130
3.2.4 Scanning Electron Microscopy.....	133
3.2.5 Conclusions.....	140
3.3 References.....	140
4. Base Catalysis.....	145
4.1 Cyanoethylation of Alcohols.....	145
4.1.1 Methodology.....	145
4.1.2 Cyanoethylation Reactions.....	147
4.1.3 Conclusions.....	154
4.2 References.....	155
5. Oxidation Catalysis.....	157
5.1 Sulfur Dioxide Oxidation.....	157
5.1.1 Methodology.....	157
5.1.2 Gas Chromatography.....	158
5.1.3 Infrared Spectroscopy.....	164
5.1.4 X-ray Powder Diffraction.....	167
5.1.5 Scanning Electron Microscopy and Energy Dispersive Analysis of X-rays.....	169
5.1.6 Conclusions.....	176
5.2 Cyclohexane Dehydrogenation.....	177
5.2.1 Methodology.....	177
5.2.2 Gas Chromatography.....	178
5.2.3 Conclusions.....	179
5.3 References.....	180

6. Summary of Conclusions and Further Work.....	181
6.1 Precursor Materials.....	181
6.2 Catalyst Activation.....	182
6.3 Base Catalysis.....	184
6.4 Oxidation Catalysis.....	185
6.5 References.....	187
7. Experimental.....	188
7.1 Preparation of Hydrotalcite-type Compounds.....	188
7.1.1 Preparation of Hydrotalcite, $\text{Mg}_6\text{Al}_2(\text{OH})_{16}\text{CO}_3 \cdot 4\text{H}_2\text{O}$	188
7.1.2 Air-sensitive Preparation of Iron-containing Hydrotalcite-type Compounds.....	190
7.2 Calcination of Hydrotalcite-type Compounds.....	193
7.3 Preparation of Green Rusts.....	195
7.4 Preparation of Iron Oxides.....	196
7.5 Cyanoethylation of Alcohols.....	197
7.5.1 Activation of Hydrotalcite-type Compounds.....	197
7.5.2 Cyanoethylation Experiments.....	198
7.6 Sulfur Dioxide Oxidation.....	198
7.6.1 Activation of Hydrotalcite-type Compounds.....	198
7.6.2 Sulfur Dioxide Oxidation Experiments.....	199
7.7 Cyclohexane Dehydrogenation.....	203
7.7.1 Activation of Hydrotalcite-type Compounds.....	203
7.7.2 Cyclohexane Dehydrogenation Experiments.....	203
7.8 Analytical Techniques.....	205
7.8.1 Infrared Spectroscopy.....	205
7.8.2 X-ray Powder Diffraction.....	205
7.8.3 Scanning Electron Microscopy.....	206
7.8.4 Differential Thermal Analysis.....	207
7.8.5 Gas Chromatography and Gas Chromatography-Mass Spectrometry.....	207
7.9 Sources of Chemicals and Methods of Purification.....	209
7.10 References.....	211

Chapter 1

Introduction

1.1 Area of Study

1.1.1 Overview of Catalysis

Some of the greatest challenges that face the modern-day chemist, whether academic or industrial, arise whilst attempting to make chemical processes more efficient. In order to meet increasingly demanding environmental and monetary constraints, overarching aims include making desired reactions faster, more selective and more cost effective (with respect to both feedstocks and plant design/construction). Catalysts are often used to meet these objectives by enabling reactions to proceed *via* a lower energy pathway, increasing the rate at which the reaction of interest approaches equilibrium.¹ In fact, catalysts can facilitate the formation of desired products from reactions which would otherwise be inhibitive slow. This may occur to such a degree that production on a commercial scale may become viable. To illustrate their importance, it is estimated that over 90 % of chemical manufacturing processes in the world employ catalysts of some description.²

There are two well-defined divisions of catalysis, homogeneous and heterogeneous. Homogeneous catalysts exist in the same phase as the reactants, the most common scenario being the liquid phase. In this case, the reactions are often highly selective but liquid phase reactions do place restrictions on temperature and pressure which, combined with an inherent need for post-reaction product separation steps, can complicate plant equipment which increases the overall cost.³ Therefore, the use of homogeneous catalysts is generally restricted to the manufacture of foodstuffs, medicinal drugs and speciality chemicals. Some notable exceptions are the Monsanto process for acetic acid production, hydroformylation of alkenes using the Oxo process and benzene alkylation to

form ethylbenzene.⁴ Heterogeneous catalysis is defined by the presence of a phase boundary separating the catalyst from the reactants.¹ This offers a number of permutations, the most common industrially being a solid catalyst combined with liquid or gaseous reactants.³ Although this phase separation makes the study of catalytic reactions and their rates more difficult as factors such as diffusion and adsorption become important, there are marked advantages for industrial use. For instance, plant design can be relatively straightforward since the catalyst is often pelletised and the reactants flow through or over them, which normally allows the use of a simple column arrangement or a stirred or fluidised bed. This results in dependable operation, good reaction control over a range of operating conditions and facilitated separation from reaction products.³

Enzymes constitute what is generally regarded as a third division of catalysts, forming lyophilic colloids acting in solution, which does not offer such a clear distinction of phase boundaries.³ They offer remarkably high selectivity for a given product, often at very high rates of conversion but their industrial use is very limited due to their high level of selectivity (which restricts their application severely) and their inability to withstand conditions which deviate from those generally found in biological systems.

The research described in this thesis is focussed upon the production and testing of new heterogeneous catalysts, one objective being to carry out an academic study whilst being aware of factors which are important industrially. A study of this type requires a multi-disciplinary approach, requiring some knowledge of a number of subject areas or, failing this, at least an awareness of issues important in other areas which may need to be taken into account.² The formulation of a catalytically active material, arguably the most critical stage of process design, requires a thorough grounding in inorganic chemistry. The next stage, the formation of the actual particles to be used in the reaction, whether they are pellets, rings or powder, requires a knowledge of materials science and engineering; the size and shape of the manufactured catalyst being influenced by such factors as heat and mass transfer and the pressure drop across the reactor. The reactor itself may be any one of a number of types, each necessitating an understanding of basic chemical engineering to aid in the correct choice of reactor for a particular conversion; an assessment of the scale-up procedures, phase mixing and heating and cooling

requirements being fundamental to this choice. Of course, the reaction to be catalysed must be understood to permit the development of a catalyst which will have the desired effect upon the conversion and selectivity. Some knowledge of the reaction thermodynamics and kinetics is also necessary, requiring an understanding of the fundamentals of physical chemistry.

The chief concerns of the research detailed in this thesis are the production and characterisation of a range of synthetic minerals for use as, or as precursors to, heterogeneous catalysts. A study of the catalytic behaviour of these materials is, therefore, also necessary in order to assess their suitability as catalysts. Inorganic chemistry will dominate the study, though the factors originating from the other disciplines outlined above have also been borne in mind.

1.1.2 Outline of Research Area

The main aims are to produce catalytically efficient materials for heterogeneous base and oxidation catalysis; the criteria used to assess this efficiency being catalytic activity, selectivity and, to a lesser extent, lifetime. To define each of these parameters; the activity refers to the rate at which the desired reaction proceeds, the selectivity is the yield of the desired product from the range of possible products and the lifetime is the period for which the catalyst maintains the required level of activity and/or selectivity.⁵

There are a range of variables such as temperature, pressure and concentration of reactants which influence the activity of a catalyst but, if high yields can be obtained at low temperatures and pressures, there is an obvious financial benefit and thus an incentive to produce catalysts capable of operating under such conditions.¹ High activity and selectivity may be achieved by using the optimum chemical formulation and producing the desired surface characteristics for the catalyst. The latter is done by using the appropriate preparative method for the precursor and, where necessary, using a further activation step to form the active catalyst. If the ideal choices are made, the reactant molecules may then gain the desired access to the active sites of the catalyst.³

Not only do these desired qualities need to be achieved but also maintained - although the widely recognised definition of a catalyst specifies that it should remain unchanged at the end of a catalytic reaction, the properties of real catalysts do change with time.³ This change is almost always to the detriment of the catalytic material and is known as deactivation. There are a range of mechanical, thermal and chemical causes of deactivation,³ probably the three most important being sintering, coking and poisoning. Sintering is a thermal effect which, in the case of metal oxides, causes a loss of available surface for reaction as pore collapse occurs, smaller pores gradually merging to form larger pores with reduced surface area. Particle failure in a catalyst bed may cause sintering *via* plugging, channelling and subsequent pressure drop increase which lead to the formation of 'hot-spots' in the catalyst bed. These, in turn, result in rapid deterioration of the catalyst from exacerbated thermal effects such as sintering and coking. Coking is a term used to describe the deposition/build-up of carbonaceous deposits on a catalyst surface which results in a reduction in the number of active sites available for interaction with reactant molecules. Since these deposits are found in significant amounts whenever carbon-containing feeds are used they affect most catalysts to some extent. This deposition from hydrocarbons occurs in two distinct ways; on acid sites (*e.g.* cracking catalysts) and on dehydrogenation sites (*e.g.* during catalytic reforming), although the latter can be less of a problem due to the presence of hydrogen.³ Coking can be reversible, most commonly utilising oxidative treatment, but this may be detrimental to the catalyst surface if it causes sintering.³ Poisoning is a chemical phenomenon, usually a result of the presence of chemical species in the feedstock which bind very strongly to the active sites on the catalyst surface, making them either temporarily or permanently unavailable for interaction with the reactants, thus decreasing activity. This is, therefore, mainly a concern of feedstock purification rather than catalyst design. However, if specific poisons are normally found in a particular reactant and are not easily removed, catalytic components which do not interact strongly with these species should be selected, where possible.³

An important aim of this work is to develop catalytic materials which are capable of high activities at low temperatures since deactivation is often increased at elevated temperatures. A further aim is to increase resistance to structural degradation at higher temperatures if they are to be attained for any period of time. Relatively low

temperatures will be maintained at all stages in the synthesis, activation and testing of the materials, in order to achieve maximum benefit. The reactions highlighted for study are base-catalysed reactions and oxidation reactions for reasons outlined in later sections. The catalytic materials selected for investigation are iron-substituted hydrotalcites and aluminium-substituted iron oxides. The structures of hydrotalcites and the precursors to the iron oxides are similar, allowing the formation of high surface area materials at low temperatures which should achieve the aim of high activities at low temperatures.² Inclusion of iron in the hydrotalcite structure will form a mixed valence system with enhanced redox possibilities whilst the aluminium present in each system should reduce sintering.

Therefore, the structure of the results section of this thesis is based around the three main stages in the formulation of a heterogeneous catalyst. These are;

- i) the preparation of a suitable precursor material
- ii) the subsequent activation of the precursor to form a compound which may exhibit catalytic activity and
- iii) testing of the material as a catalyst for predetermined reactions.

Detailed characterisation of the inorganic materials has been carried out after each of these stages. A reactor system has also been designed and constructed in order to study the oxidation reactions. Details concerning this section of the practical work will be provided in the Experimental section, Chapter 7.

The remainder of the introduction will commence with an overview of heterogeneous base and oxidation catalysis, the two areas of activity testing, highlighting previous research in these areas and opportunities for potential improvement of current catalytic materials *i.e.* the problem. The subsequent section will provide an insight to the use of clays and clay minerals in catalysis, past and present. Following this will be a review of a potential solution; the use hydrotalcite-type materials and the structurally similar iron oxides. Information will also be provided on the precursor materials of the latter, which are based on the mineral green rust and are structurally similar to hydrotalcites.

1.2 Base Catalysis

Solid base catalysts have a number of advantages over liquid base reagents.⁶ For instance; their physical state renders them essentially non-corrosive and environmentally benign which results in fewer disposal problems. This is particularly observable in the elimination of wastewater streams otherwise produced from the aqueous bases which are typically used in large volumes. Aside from the environmental advantages, there is also a financial incentive similar to that for the heterogeneous catalysts used in a conventional sense *i.e.* improved separation and recovery of reaction products, and solvents, from the catalyst. In addition, for some reactions, high activities and selectivities are only attainable by using solid base catalysts. The challenge is to maintain this level of activity and selectivity on an industrially practical scale without significant deactivation.

By comparison with base catalysis, significantly more research has been carried out in the area of acid catalysis, reflecting their industrial importance, which will be discussed in more detail in section 1.4.1. A recent survey by Tanabe and Hölderich⁷ revealed that, whilst there were over one hundred industrial processes which utilise solid acid catalysts, there were only ten utilising solid base catalysts. However it is expected that, as more novel base materials are found and new base catalysed reactions become of greater industrial importance, additional studies of solid bases will be necessary for them to achieve similar levels of industrial use.⁶ The first study of heterogeneous base catalysts was reported by Pines *et al.* in 1955.⁸ This concerned the use of sodium metal dispersed on alumina to catalyse the double bond migration of alkenes. In this case, the mechanism of catalysis was thought to involve the donation of electrons from sodium. Subsequent work has illustrated the activity of single component metal oxides not involving alkali metals as the basic catalysts and an array of types of heterogeneous base catalysts have been discovered since, some of which are outlined in Table 1.1.

Table 1.1 Common Types of Heterogeneous Base Catalysts^{6, 9}

Type of Base Catalyst	Examples
Supported Alkali Metals	Na/Al ₂ O ₃ , Na/MgO, KNO ₃ /Al ₂ O ₃ , KOH/Al ₂ O ₃ , Na/NaOH/Al ₂ O ₃ , Cs/NPC [†]
Single Component Metal Oxides	MgO, CaO, SrO, BaO, Al ₂ O ₃ , Sm ₂ O ₃ , Eu ₂ O ₃ , Yb ₂ O ₃
Mixed Metal Oxides*	[4CaO,Al ₂ O ₃], [4MgO, Al ₂ O ₃]
Clay Minerals	hydrotalcite, zeolites (alkali-ion exchanged and added), chrysotile, sepiolite
Non-Oxides	KF on Al ₂ O ₃ , lanthanide imides and nitrides on zeolites
Basic Phosphate Oxynitrides	AlPON, ZrPON, VAlPON, AlGaPON

[†] nanoporous carbon

* prepared from hydrotalcite-type structure

The range of materials given in Table 1.1 are capable of catalysing a number of reactions, details of which are reviewed in recent publications.^{6, 9} Some of the more important reactions are the isomerisation of alkenes, alcohol dehydrogenations, olefin hydrogenations and aldol condensations.

One of the greatest problems with the use of many of the solid base catalysts is their rapid deactivation when exposed to air for any period of time. This is due to the rapid poisoning of the sites by acidic molecules such as carbon dioxide and water. Therefore, the generation of basic sites often requires pre-treatment at elevated temperatures (typically over 800 K for metal oxides) in order to remove surface carbon dioxide and water followed by handling in an inert atmosphere prior to use. Indeed, before the nature of this poisoning was recognised, the use of some materials as catalysts was overlooked due to their apparent inactivity.⁹

Hydrotalcite-type materials feature in Table 1.1 but will not be discussed in any great detail in this section. More detail is provided on these materials in sections 1.4 and 1.5. They have been shown to be active base catalysts but still suffer from deactivation upon prolonged exposure to the atmosphere, after activation. The activity of the range of

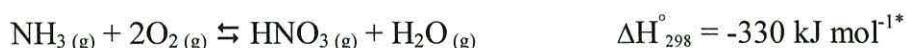
materials prepared in this research towards a base catalysed reaction will be investigated since there is a need for more stable catalysts. However, the development of a highly basic catalyst is not the main objective of the work.

1.3 Oxidation Catalysis

A large number of oxidation reactions may be considered to be of great importance, both industrially and academically. This diversity is reflected in the literature which is wide-ranging, in relation to reactions studied and in the development and subsequent study of heterogeneous catalysts for these reactions. With so much detail available, it can be difficult to see why particular catalysts are important. This is often because, especially in the earlier days of catalyst development, an empirical approach was taken with regards to the selection of materials as possible catalysts. Further optimisation of the initial selections was made afterwards. An element of serendipity has also been known to aid formulation. For instance, during the development of the ammonia synthesis catalyst, the Swedish magnetite selected for some of the testing contained minor impurities of alumina and potassium oxide which were later shown to be crucial to the improved yields experienced with this material.^{1, 2, 5} This prompted testing of a range of other iron composites which not only led to the development of the ammonia synthesis catalyst but also other catalytically active materials.² Empirical methods worked effectively for a number of years but the initial design stages of catalyst development are now receiving more attention *e.g.* synthetic zeolite design. This section of the review seeks to rationalise the choices of catalyst for a small number of reactions which are of importance historically and industrially. The detail provided is limited to addressing the important general principles of oxidation catalysis. Two processes from the inorganic chemicals sector, nitric acid formation and sulfur dioxide oxidation are particularly important and have been selected for further discussion. In addition, methanol oxidation has been discussed to introduce some of the finer details of selective oxidations. Other relevant examples of oxidation reactions and the catalysts utilised for these have also been included and the relevance of the research detailed in this thesis outlined.

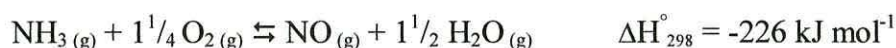
The majority of nitric acid produced in the world today, if not used directly as a chemical in its own right, is used to produce ammonium nitrate for use in the fertiliser industry *via* the direct reaction of ammonia and nitric acid.² Although the direct oxidation of ammonia to nitric acid is theoretically possible (Equation 1.1), no suitable catalyst has been found to be capable of operating at sufficiently low temperatures to avoid nitric acid decomposition.⁵ This would require a catalyst exhibiting a much higher activity for this reaction than is currently available. Instead, nitric oxide is produced catalytically, as an intermediate, by the controlled oxidation of ammonia (Equation 1.2).^{1, 5}

Equation 1.1 Direct oxidation of ammonia⁵



* All enthalpies of formation throughout this thesis are calculated at 1 bar pressure, 298 K from literature values¹⁰ and are based on the formation of 1 mole of product, for comparative purposes.

Equation 1.2 Catalytically controlled oxidation of ammonia⁵



Two, uncatalysed, reactions are then used to produce nitric acid; the oxidation of nitric oxide to form nitrogen peroxide and subsequent absorption of nitrogen peroxide in water to form nitric acid. The catalyst selected for Equation 1.2, nitric oxide formation, has been chosen for its selectivity for this reaction rather than the formation of the more thermodynamically stable products, nitrogen and water (Equation 1.3).⁵

Equation 1.3 Uncontrolled oxidation of ammonia⁵



Kuhlmann made the discovery that platinum is selective for nitric oxide formation from the reaction of ammonia with oxygen and obtained the first patent in 1838.¹ Prior to this, other metals and oxides had only been used on a laboratory scale.⁵ However, because

platinum was rapidly poisoned by the sulfur and arsenic compounds present in the gas-works liquors from which the ammonia was obtained, the industrial application of the process had to wait until high-purity ammonia was available.¹ Since then the increased demand for nitric acid has seen a large expansion of the nitric acid industry.⁵ Platinum is still the catalyst of choice, in the form of a fine mesh gauze through which the reactant gases flow, although rhodium is now incorporated (*ca.* 10 %) to mechanically strengthen the gauze which otherwise deteriorates quite rapidly.⁵ Other catalysts have been produced, including the promoted iron and cobalt oxides formulated in the 1970's^{11, 12, 13} but the increased efficiency and lifetime available by using platinum outweighs the cost advantages of cheaper materials. The physical advantages of platinum allow it to be drawn and formed into a gauze which reduces the pressure drop that would occur if the platinum was dispersed over a porous inert support or if an oxide catalyst were to be used instead. The physical state of the gauze also reduces the mass-transfer limitations that would occur for such a fast reaction since the active sites of such a material are found on the external, rather than the internal, structure.^{2, 5}

By comparison with nitric acid, sulfuric acid ranks as the number one chemical produced industrially, based on mass produced, and the key step in its production is the oxidation of sulfur dioxide to sulfur trioxide.⁵ The reaction is exothermic and is thermodynamically controlled so the catalyst required to increase the rate of reaction does not need to be selective but rather needs to have a high activity at low temperatures.⁵ The original catalyst for this reaction, which was used in the 'Chamber process', was homogeneous - in the form of nitrous oxides. This was soon replaced by the 'Contact process', the original patent issued to Peregrine Phillips in 1831 for the use of a platinum catalyst. Almost forty years later, the demand for sulfuric acid from the synthetic dye industry caused a dramatic increase in production. The platinum catalyst developed by Phillips was used to meet this demand, until a less active, but cheaper, catalyst was formulated in the early 1900's. This catalyst was based on vanadium, the forerunner of the catalysts still used today. Two important vanadium-based catalysts during the early stages of development were the 'Seldon mass' and the 'Monsanto catalyst'. The latter became the most widely used and was prepared from the precipitation of potassium silicate with hydrochloric acid in the presence of ammonium metavanadate and potassium hydroxide to form a silica gel. The product of this reaction was then dried, extruded and calcined.

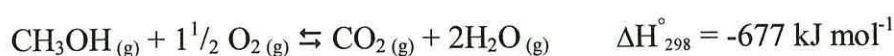
Following this, catalysts exhibiting higher activities at lower temperatures were developed. These contained both sodium and potassium, a typical composition being; SiO_2 , 57.2 %; SO_3 , 19.2 %; K_2O , 6.8 %; V_2O_5 , 5.4 %; Na_2O , 1.6 %; Al_2O_3 , 1.0 %.⁵ However, catalytic activity was relatively short-lived, falling back to the level of the conventional catalyst after approximately one year on-line. Current catalysts may be expected to have a lifetime of up to twenty years. The vanadium content is generally between 5 % and 9 % by weight (as V_2O_5) and the $\text{V}_2\text{O}_5:\text{K}_2\text{O}$ ratio *ca.* 2.5:4.5. The support is normally either a diatomaceous earth or precipitated silica gel. The vanadium catalyst has been described as a 'hybrid-type' catalyst to reflect the physical state of the catalytically active species which is in the molten phase under normal operating conditions.⁵ It has been suggested that this, combined with its oxidising power, is responsible for its high activity - the mobility of the molten vanadium pentoxide phase ensuring constant renewal of the catalytic surface.¹

One of the main areas of investigation for further improvement of the sulfur dioxide oxidation catalyst continues to be the development of materials which exhibit greater activity at low temperatures since one of the main reasons for loss of activity of vanadium catalysts is the loss of structural integrity.⁵ This produces dust which blinds the beds which can only be remedied with regular screening of the catalyst. This may only be carried out on an annual basis but down-time on the plant is a major contribution to loss in productivity. In addition, running the reaction process at increased temperatures for sustained periods of time has also been attributed to crystallisation of the silica support material. A relatively minor problem, considering the catalyst lifetime achievable, is the disposal of the catalysts after use. Vanadium compounds are known irritants to the conjunctive and respiratory tracts. Consequently, any catalyst which poses less of an environmental hazard, whilst achieving increased activities at lower temperatures, would be desirable. Iron oxides have been shown to be capable of the oxidation of sulfur dioxide¹⁴ but may not possess the physical integrity necessary to withstand the required process conditions. A possible solution to this problem will be investigated in Chapter 5.

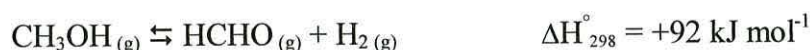
The oxidation of methanol, to form formaldehyde, is one of the more commercially significant organic reactions which utilise heterogeneous catalysts. Formaldehyde has been of great commercial importance since the beginning of the last century, its main use

being in the production of resins for chipboard and plywood manufacture.^{1, 5} Whilst the combustion of methanol yields carbon dioxide and water *via* total oxidation (Equation 1.4), formaldehyde is formed selectively *via* either one of two dehydrogenation mechanisms (Equations 1.5 and 1.6), using either a silver or a mixed metal oxide catalyst.

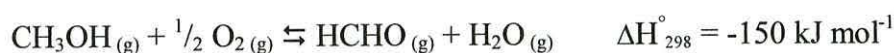
Equation 1.4 Uncatalysed oxidation (combustion) of methanol⁵



Equation 1.5 Dehydrogenation of methanol⁵



Equation 1.6 Oxidative dehydrogenation of methanol⁵



Whilst the silver catalyst is capable of catalyzing the reactions shown in both Equations 1.5 and 1.6, the mixed metal oxide catalyst favours only the oxidative dehydrogenation illustrated by Equation 1.6. The most commonly used metal oxide catalyst is a mixed iron molybdate, $\text{Fe}_2(\text{MoO}_4)_3$, material.⁵ This is produced by the formation of a precipitate, from solutions of iron and molybdenum salts, which is then calcined and pelletised for use. This catalyst gives higher conversions than the silver catalyst which proceeds predominantly *via* the direct dehydrogenation reaction (Equation 1.5).⁵ Although less active, the silver catalyst (which is used as high purity silver metal in a crystalline form or gauze) is still of great importance industrially due, in part, to its ease of recycling and regeneration.

All three reactions, Equations 1.4, 1.5 and 1.6, are examples of oxidation reactions and are useful to clarify terminology. The first, Equation 1.4, is an example of ‘deep’ oxidation which is the total oxidation to form carbon dioxide and water.¹ By comparison; Equations 1.5 and 1.6 are examples of selective oxidation since a product other than the

most thermodynamically stable is preferred. The second reaction (Equation 1.5) is a dehydrogenation reaction which is generally regarded as an oxidation reaction due to the loss of hydrogen from the organic molecule and its subsequent transformation from an alcohol to an aldehyde.¹⁵ The third reaction (Equation 1.6) is an example of oxidative dehydrogenation which implies that the substrate is dehydrogenated by the catalyst, as in Equation 1.5, but this is then followed by oxidation of the adsorbed hydrogen atoms.¹⁶ This results in the oxidation of the organic molecule due to its dehydrogenation, as previously, but also in the production of water. Consequently, due to the enthalpy change during the formation of water, the overall reaction is exothermic in comparison with Equation 1.5 which is endothermic.¹

Selective oxidation plays an important role in many areas of chemistry but there appear to be few generalisations that can be made regarding the essential ingredients for a successful catalyst. Many of the better catalysts do, however, combine elements from different groups of the Periodic Table, which often results in the formation of a mixed valence material. For example, a bismuth molybdate mixed metal oxide catalyst is utilised for propene oxidation to acrolein (propenal) and the ammoxidation of propene to acrylonitrile, both of which are important industrial reactions. Tin-antimony and uranium-antimony mixed metal oxide catalysts are also both utilised for acrolein synthesis and a number of mixed-metal catalysts may be used for methanol oxidation. These include vanadium-molybdenum, vanadium-titanium and iron-antimony oxides, in addition to the ferric molybdate system discussed previously.¹

The research detailed in this thesis includes the investigation of two oxidation reactions in particular; the total oxidation of sulfur dioxide to sulfur trioxide (for the reasons outlined earlier in this section) and the dehydrogenation of cyclohexane to form benzene. The latter is normally catalysed by metals such as nickel, platinum and palladium but both platinum and palladium are expensive and nickel is easily poisoned by sulfur. Magnetite has been reported to catalyse the dehydrogenation of cyclohexanes³ but does not compete with the use of the aforementioned metal catalysts industrially. These two reactions have been selected due to the catalytic potential offered by the materials developed in this research and the need for an improved catalyst for each. In addition, the two reactions have different requirements regarding the qualities offered by the

catalyst for each which make their study interesting viz. total oxidation for the exothermic oxidation of sulfur dioxide and selective oxidation in the endothermic dehydrogenation of cyclohexane. A mixed metal oxide catalyst derived from hydrotalcite-type materials will be investigated for each reaction in Chapter 5.

1.4 Clays and Clay Minerals in Catalysis

1.4.1 Cationic Clays

Although this research is focussed upon the applications of synthetic clays in catalysis, there have been suggestions in the literature that natural clays also exhibit catalytic behaviour in the environment. Due to the nature of the microenvironments formed in the interlamellar spaces of clays, a feature so critical in their use as industrial catalysts, Paecht-Horowitz suggested they may have been heavily involved in the origin of life,¹⁷ playing a pivotal role in a chemical evolution which preceded biological evolution. The basis for this discussion is that the relatively high surface areas of most clays, combined with a structure capable of favourable interactions with organic molecules may well have provided the ideal location for the prebiotic synthesis of complex organic molecules. It was shown in simple experiments developed by Miller that the simpler organic molecules necessary for the formation of more complex molecules could have been formed from the gaseous constituents of the primordial atmosphere.^{18, 19} He simulated the effects of lightning on these gases by passing electrical discharges through a mixture of methane, hydrogen, ammonia and water vapour and produced a number of water-soluble organic molecules, including several amino acids. Paecht-Horowitz *et al.* have since shown that certain clays, particularly swelling phyllosilicates such as illite and montmorillonite, could then act as heterogeneous catalysts for the polycondensation of active forms of amino acids to form polypeptides, the biopolymers necessary for protein formation.²⁰ Further speculation regarding the roles of clays in replication and evolution can be found in articles by Cairns-Smith^{21, 22} and Weiss.²³

Cationic, montmorillonite-based, clays have also been of historical importance industrially, since they were amongst the first cracking catalysts used in the early days of petroleum refining.¹ Montmorillonite clays were later replaced as cracking catalysts by synthetic silica-alumina gels after the Second World War and subsequently even these gels have been replaced by the zeolites used today which exhibit superior activity and selectivity.² The montmorillonites are selected here for further discussion for three main reasons *viz.*; i) their geological abundance, ii) their industrial significance and iii) the parallels that may be drawn between the structures of montmorillonite and hydrotalcite.

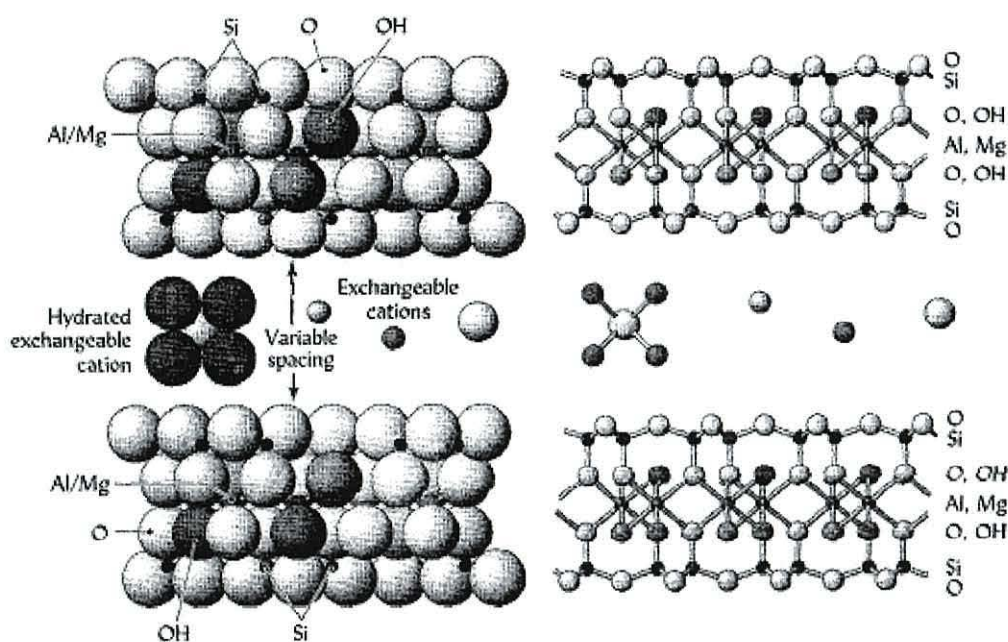


Figure 1.1 Structure of montmorillonite showing two 2:1 layers and the resulting interlayer spacing occupied by the exchangeable cations (space-filling to left and ‘ball and stick’ schematic arrangement to right)²⁴

The montmorillonites form part of a catalytically important group of swelling clays known as smectites which are of the 2:1 type and are typical of naturally occurring clays in that they have a grain size generally less than 2 μm in diameter and have a layered structure as illustrated in Figure 1.1. They are described as 2:1 type minerals due to the relationship between the single octahedral sheet formed between the two tetrahedral sheets within each layer, each of these layers carrying a net negative charge due to the partial substitution of Mg^{2+} for Al^{3+} in the octahedral sheet. Every one of these substitutions requires a positive charge to maintain electrical neutrality within the

structure as a whole and this charge is provided by the interlamellar hydrated cations (commonly Ca^{2+} and Na^+ in montmorillonites) residing between each 2:1 layer.^{25, 26} This occurrence of interlayer cations has resulted in the term ‘cationic clays’ being used to describe this family of structures and allows direct comparison with the anionic clays (including hydrotalcite) described in the next section.

It is the presence of the negatively charged layers (and, therefore, the inclusion of the charge-neutralising interlayer cations) combined with their small particle size that makes the swelling cationic clays so important for a range of applications,^{27, 28} including catalysis.^{2, 27, 29} However, although the inherent cation exchange capacity (CEC) of these materials may be utilised when incorporating positively charged organic molecules into the interlayer region (*via* simple ion-exchange processes), the mechanism of intercalation of neutral organic molecules is less obvious. Pinnavaia²⁹ stated that a number of binding mechanisms may operate, but that complex formation between the exchange cation and the intercalant was particularly important. The importance of the strength of the interaction of the organic molecules with a solid surface, in catalysis, was summarised by Vaccari²⁷ who highlighted the fact that a weak interaction would preclude any catalytic step but too strong an interaction and the desorption of any reaction product would be too slow. Boyd *et al.*,³⁰ believed that an important factor influencing this interaction is that the mineral surface is normally hydrophilic, due to the presence of the hydrated inorganic interlayer cations. These are expected to reduce, but not prevent, catalysis by reducing the sorptive capacity of the clays for neutral organic compounds; this is believed to be especially true in aqueous solutions. If particularly strong interactions between the clay and the organic species are desired, in the remediation of contaminated land for example, then the inorganic cations generally residing in the interlayers may be exchanged for quaternary ammonium cations and the like which create an organophilic environment within the clays.³⁰ By comparison, in catalysis, weaker interactions are generally sufficient.²⁷ For some reactions, one problem with the use of cationic clays is their thermal instability. This is due to the dehydration and subsequent collapse of the layered structure of these materials above *ca.* 500 K which makes the entry of reactant molecules into the structure increasingly difficult.^{2, 29} In order to form thermally stable materials with a three-dimensional network structure, not dissimilar to that of zeolites, the CEC of the clays may be utilised to introduce molecular props or ‘pillars’ into the

layers. These are often in the form of cationic Keggin ions such as $[\text{Al}_{13}\text{O}_4(\text{OH})_{24}(\text{H}_2\text{O})_{12}]^{7+}$ which can be used to prop the layers open to a pre-determined spacing.^{2, 27, 29, 31, 32} A great deal of research has been carried out into the use of these materials as catalysts for a range of reactions, many for utilisation in the oil refining industry.² The particularly large pore sizes attainable with these pillared clays allow catalysis of reactions involving bulky organic molecules such as those found in residual crude oils and in the synthesis of durene (1,2,4,5-tetramethylbenzene).^{27, 29} A great deal of this effort has gone into investigating the use of pillared clays at high temperature to exploit their thermal stability but they are often less active than the unmodified clays at lower temperatures.²⁷ In contrast, the work in this thesis seeks to produce materials which are not only catalytically active at low temperatures but also thermally stable over a reasonable working range.

A key feature of the cationic clays discussed thus far (pillared and unpillared) is their strong acidity which has led to their use in the catalysis of a range of organic reactions² including the cracking of hydrocarbons, as noted earlier. The nature of this acidity has been widely recognised as being of the Brönsted type,^{2, 27, 29, 33} either because of the internal electrostatic fields exerted on the interlayer water, which generates protons by dissociation and/or because of the presence of hydrated interlayer cations, particularly Al^{3+} . Pinnavaia²⁹ suggested that the hydrated cations functioning in such a manner and the intercalant acting as a base may provide an important intercalation mechanism. In addition, there are also Lewis acid sites^{2, 27} created whenever Al^{3+} substitutes for Si^{4+} in tetrahedral sites or Mg^{2+} for Al^{3+} in octahedral sites. Although these sites are found within the sheets, the Lewis acid sites are also found within the interlamellar region.²

There have been numerous attempts at synthesis of smectite-type clays, summarised by Klopogge *et al.*,³⁴ but synthesis of the majority of these minerals have proved to be of limited success at ambient pressures and low temperatures (<373 K). Therefore, the relative decline in interest of cationic clays in catalysis, in comparison to the more readily synthesised anionic clays discussed in the next section, may be attributed to two main reasons. Firstly, natural clays are not often single phase materials, their physical properties being quite variable between and within batches which introduces an element of unpredictability not favoured in industrial processes.²⁹ Secondly, natural clays are

generally more stable in conditions most similar to that of their origin *i.e.* moderate pH and low temperatures.²⁵ Consequently, they are less suitable than synthetic clays for use in modern day chemical reactors which may operate at much higher temperatures and pressures.

1.4.2 Anionic Clays

There is still a degree of argument regarding the correct terminology for this group of materials, for which hydrotalcite $[\text{Mg}_6\text{Al}_2(\text{OH})_{16}\text{CO}_3 \cdot 4\text{H}_2\text{O}]$ is the most widely known example. There are three common terms used to describe them; anionic clays, layered double hydroxides and hydrotalcite-type compounds. Each of these terms has its associated problems which will be outlined and reasons given as to which term will be used predominantly in this review. The first, anionic clays, is descriptive of the main structural feature of the materials, reflecting the differences between these and the cationic clays described earlier *i.e.* the charge on the exchangeable ion. In fact, anionic clays are often described as anti-types of 2:1 cationic clays. The structure of hydrotalcite is illustrated in Figure 1.2 and will be described in more detail in a later section dedicated to its structure.

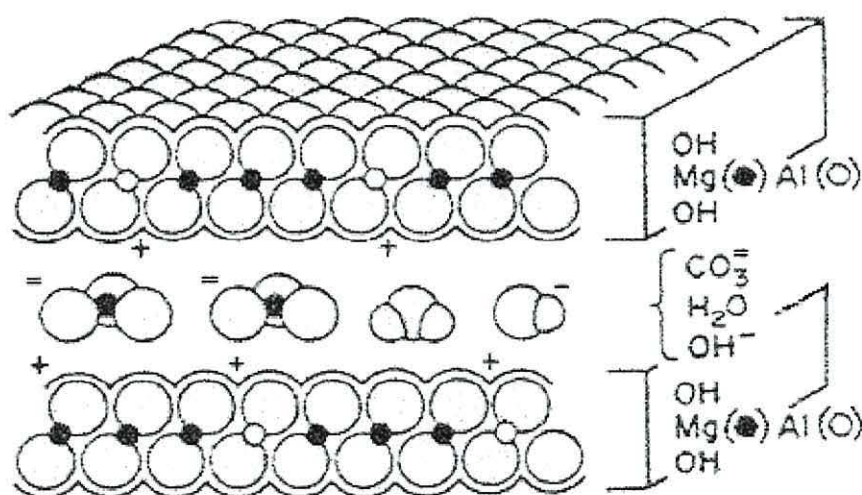


Figure 1.2 Hydrotalcite structure³⁵

It will suffice, at this stage, to say that the structure consists of positively charged metal hydroxide layers which contain anions in the interlayer region in order to maintain electrical neutrality within the structure as a whole. However, because these materials do not possess some of the requirements generally deemed necessary, in geological terms, to be called a ‘clay’ *e.g.* their increased particle size, the term anionic clays is not regarded as the correct terminology in certain circles. The term layered double hydroxide (LDH) is, however, widely accepted despite the fact that the originally hypothesised structure that this was used to describe was dismissed over thirty years ago. This description arose from a report in 1942 where Feitknecht³⁶ synthesised compounds having a double hydroxide sheet structure, assuming that there were two discreet metal hydroxide sheets intercalated with one another. Allman³⁷ and Taylor³⁸ later refuted this structural hypothesis, using X-ray crystallographic studies, correctly concluding that the two cationic species are localised within the same layer whilst the carbonate ions and water molecules are found within the interlayer regions. For the purposes of this thesis, the term hydrotalcite-type compounds (HTc’s) will be used since any materials based on this structure are isomorphous to the Mg/Al hydrotalcite which has been the subject of much physico-chemical characterisation. This is probably because it was one of the first naturally occurring examples of anionic clays and is relatively cheap and easy to synthesise.^{39, 40} A general formula for HTc’s commonly used in the literature is provided (Formula 1.1).^{27, 39, 41}



where M = metal and A = interlayer anion.

This formula is representative of many anionic clays *i.e.* there are two metals present, one bivalent and one trivalent, and one type of interlayer anion. For naturally occurring HTc’s, $x = ca. 0.25$ and the carbonate anion occurs most frequently.³⁹ There are other naturally occurring minerals with a similar structure but which deviate from the stoichiometry of hydrotalcite and these are shown in Table 1.2.

Table 1.2 Minerals with a hydrotalcite structure but with differing stoichiometries⁴²

Mineral Name	Formula
Motukoreaite	$\text{Mg}_{1.82}\text{Mn}_{0.03}\text{Zn}_{0.02}\text{Al}_{1.12}(\text{OH})_{5.15}(\text{Na}_{0.07}\text{K}_{0.01})(\text{CO}_3)_{0.63}(\text{SO}_4)_{0.40} \cdot 2.74\text{H}_2\text{O}$
Wermalandite	$\text{Mg}_7(\text{Al}_{0.57}\text{Fe}^{\text{III}}_{0.43})_2(\text{OH})_{18}(\text{Ca}_{0.6}\text{Mg}_{0.4})(\text{SO}_4)_2 \cdot 12\text{H}_2\text{O}$
Meixnerite	$\text{Mg}_6\text{Al}_2(\text{OH})_{18} \cdot 4\text{H}_2\text{O}$
Coalingite	$\text{Mg}_{10}\text{Fe}^{\text{III}}_2(\text{OH})_{24} \text{CO}_3 \cdot 2\text{H}_2\text{O}$
Chlormagaluminitite	$\text{Mg}_{3.55}\text{Fe}^{\text{II}}_{0.27}\text{Na}_{0.05}\text{Al}_{1.93}\text{Fe}^{\text{III}}_{0.07}\text{Ti}_{0.01}(\text{OH})_{12}\text{Cl}_{1.48}(0.5\text{CO}_3)_{0.24} \cdot 2\text{H}_2\text{O}$
Carrboydite	$(\text{Ni,Cu})_{6.90}\text{Al}_{4.48}(\text{OH})_{21.69}(\text{SO}_4,\text{CO}_3)_{2.78} \cdot 3.67\text{H}_2\text{O}$
Honessite	$\text{Ni}_{5.55}\text{Mg}_{0.10}\text{Fe}^{\text{III}}_{2.35}(\text{OH})_{16}(\text{SO}_4)_{1.18} \cdot 4\text{H}_2\text{O}$
Woodwardite	$\text{Cu}_4\text{Al}_2(\text{OH})_{12}\text{SO}_4 \cdot 4\text{H}_2\text{O}$
Iowaite	$\text{Mg}_{4.63}\text{Fe}^{\text{III}}_{1.32}(\text{OH})_{12}\text{Cl}_{1.22} \cdot 1.95\text{H}_2\text{O}$

Many of these have more than two metal cations present and/or more than one species of anion.⁴² Both magnesium and aluminium occur frequently in these minerals, whilst iron, nickel and copper are also common. The sulfate anion is present in many of these species, as is carbonate, hydroxide and, to a lesser extent, chloride but the nitrate anion is not observed. This may be used as an indication of the stability of materials with these components and the capacity for exchange of the nitrate anion within these structures. These minerals are not discussed in any further detail here since they are not commonly reproduced synthetically whereas the simpler, two cation plus one anion, materials are. The restrictions on the cations which may be accommodated within the hydrotalcite structure will be elaborated upon in a later section. Some examples of naturally occurring HTc's approximating to the formula given previously are shown in Table 1.3.

Table 1.3 HTc's with formulae approximating to $[\text{M}^{\text{II}}_{1-x}\text{M}^{\text{III}}_x(\text{OH})_2]^{x+}(\text{A}^{n-}_{x/n}) \cdot m\text{H}_2\text{O}$ ³⁹

Common Mineralogical Name	Formula
Hydrotalcite	$\text{Mg}_6\text{Al}_2(\text{OH})_{16}\text{CO}_3 \cdot 4\text{H}_2\text{O}$
Pyroaurite	$\text{Mg}_6\text{Fe}_2(\text{OH})_{16}\text{CO}_3 \cdot 4.5\text{H}_2\text{O}$
Stichtite	$\text{Mg}_6\text{Cr}_2(\text{OH})_{16}\text{CO}_3 \cdot 4\text{H}_2\text{O}$
Takovite	$\text{Ni}_6\text{Al}_2(\text{OH})_{16}\text{CO}_3 \cdot \text{OH} \cdot 4\text{H}_2\text{O}$
Reevesite	$\text{Ni}_6\text{Fe}_2(\text{OH})_{16}\text{CO}_3 \cdot 4\text{H}_2\text{O}$
Desautelsite	$\text{Mg}_6\text{Mn}_2(\text{OH})_{16}\text{CO}_3 \cdot 4\text{H}_2\text{O}$

All the compounds in the table are of rhombohedral symmetry. Hexagonal symmetry is also known – both polymorphs will be discussed later in the section dedicated to HTc structure.

It is obvious that there is considerable potential for a range of synthetic materials to be produced, based on the hydrotalcite structure, which allows them to be tailored to a variety of situations. In contrast to the cationic clays discussed earlier, HTc's are generally synthesised rather than the naturally occurring materials modified⁴³ which offers greater control of the characteristics of the material.²⁷ So, whilst HTc's are found to occur naturally,^{39, 44} their synthesis is generally cheap and easily controlled on a laboratory or industrial scale.

It has been reported that there is practically no limitation to the nature of the HTc interlayer anions (A^{n-}).^{39, 27} Whilst this may be true, there is undoubtedly a strong preference for the incorporation of the carbonate ion. This makes the preparation of HTc's with other charge-compensating anions more difficult since carbonate is so difficult to totally eliminate from the reaction atmosphere or from aqueous solutions used in the preparation of HTc's.^{39, 40} Nevertheless, much research has been dedicated to studying the range of ions which may be incorporated into the structure and hence a wealth of information generated. A preferential sequence of inclusion for the most common anions incorporated into this interlayer region has also been recorded.^{40, 41} As a result, HTc's have found application as ion-exchangers under conditions which would be unsuitable for conventional anion-exchange resins, for example, in the treatment of the cooling water of nuclear reactors.^{39, 40} Although the total ion exchange capacity is reported as being greater than that of cationic clays, anion exchange in the HTc's is more difficult due to the higher charge density of the metal hydroxide layers which results in an increased electrostatic attraction between the cationic and anionic layers of the structure.²⁷ In order to overcome these difficulties, a number of strategies have been developed. One of these is simply to incorporate the anion of choice during the synthesis stage by excluding carbonate ions from the environment as much as is practically possible. This method has been shown to be successful to a degree.⁴⁵ An ingenious method developed by Bish⁴⁶ involved the use of dilute acids (0.01 M solutions of HCl, H₂SO₄ and HNO₃) to dissolve the carbonate ion and substitute it for the conjugate base

of the acid. This method was shown to work for any acid stronger than carbonic acid. Alternatively, the nitrate ion (NO_3^-) can be incorporated into the structure during synthesis and later exchanged for the desired anion since nitrate is more readily displaced from the structure than carbonate.^{47, 48, 49} Another alternative is to exploit the so-called ‘memory effect’ of HTc’s. This allows the reconstruction of the structure after calcination, and the subsequent loss of the interlayer carbonate, by contacting the thermally treated materials with solutions containing the anions to be introduced.^{27, 39, 40} Such a method is utilised in the production of organohydrotalcites which can then be used for subsequent sorption of organic contaminants from soil and water. Here, a more organophilic environment is created within the interlamellar space of the HTc by introducing organic anions.⁵⁰ Although this technique has been reported to offer enhanced adsorption of neutral organic compounds (*e.g.* the fungicide triadimefon)⁵⁰ HTc’s have been reported to be efficient in the removal of surfactants from aqueous solutions in their own right.⁵¹ Here, Pavan *et al.* stated that the sorption mechanism was dependent on whether or not the HTc had been modified by thermal treatment. Thus, if the HTc was used in the unmodified carbonate form, there was simply surface adsorption of the surfactant molecules whereas if the HTc had been previously calcined there was intercalation and adsorption. HTc’s have also been used as sorbents for the small, but nevertheless harmful, quantities of HCl evolved when polyvinylchloride (found in modern uPVC window frames *etc.*) degrades due to the effects of ultraviolet and infrared radiation. The HTc’s here prevent not only unsightly yellowing but also the consequent loss in strength which would otherwise occur.^{39, 40} They have also been used as halogen scavengers in the catalytic production of polyolefins^{41, 47} but it is in the area of catalysis that synthetic HTc’s are having increasing impact.

The number of papers published in the scientific literature regarding HTc’s has seen a dramatic increase over the last thirty years and the percentage of these papers referring to catalytic applications has also been steadily increasing.⁵² Their specific uses as catalysts will be discussed in more detail in a later section and, for the moment, just their general characteristics will be discussed. HTc’s are potential catalysts for a vast range of reactions because of the number of compositional variables, coupled with the general properties of the structure. For instance, a wide range of cations can be used to form the metal hydroxide sheets, along with a range of $\text{M}^{\text{II}}:\text{M}^{\text{III}}$ ratios. Therefore, metals known to

catalyse certain reactions may be incorporated into the platelet morphology of HTc's, allowing control over their concentration within the final structure. Normally, these materials are then calcined to produce a mixed metal oxide material with a greater surface area and morphology whilst maintaining a homogeneous interdispersion of the elements. Calcination is an important activation procedure in this context because one of the most important applications of HTc's to date remains to be their use as basic catalysts (in contrast with the acidic cationic clays), these basic characteristics being enhanced by thermal activation. An aim of the work reported in this thesis is to substitute varying amounts of magnesium ions in the hydrotalcite structure with iron (II) ions and to exploit the characteristics of the hydrotalcite structure for the catalysis of oxidation reactions as discussed in the section appertaining to oxidation catalysis. The basic characteristics of the HTc's produced will also be investigated, before and after thermal activation.

1.4.3 Iron Oxides

Iron oxides have been important catalytic materials historically, as discussed previously. The iron oxides, hydroxides and oxyhydroxides (commonly all classed as oxides) are widespread in nature,^{26, 53} most frequently occurring in soils. They are formed due to the weathering of iron-containing primary silicate minerals²⁶ and are present in most soils, over a range of climates.²⁶ Due to their intense colour they often dominate the colouration of the soils in which they occur and are commonly used in the pigmentation industry.⁵³ Sixteen iron oxides were recognised in 1996 by Cornell and Schwertmann⁵⁴ and are listed in Table 1.4, the two most commonly found in soils being goethite and haematite. Goethite is more dominant in more humid, temperate climates where it colours the soils with a yellow hue whereas haematite tinges the soils of warmer arid climates red.²⁵

Table 1.4 The Sixteen Recognised Iron Oxides⁵⁴

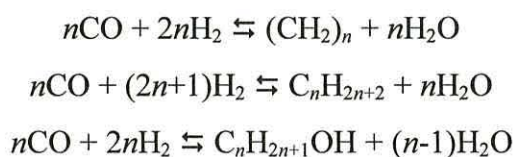
Oxides		Oxyhydroxides & Hydroxides	
Haematite $\alpha\text{-Fe}_2\text{O}_3$	Common in soils Important in catalysis	Goethite $\alpha\text{-FeOOH}$	Common in soils Important pigment
Magnetite Fe_3O_4	Common iron ore Important in catalysis	Lepidocrocite $\gamma\text{-FeOOH}$	Common in soils Goethite polymorph
Maghemite $\gamma\text{-Fe}_2\text{O}_3$	Weathering product of magnetite (isostructural) Magnetic pigment	Akaganeite $\beta\text{-FeOOH}$	Rare in nature Often contains Cl^-
$\beta\text{-Fe}_2\text{O}_3$	Rare Only lab. synthesised	Schwertmannite $\text{Fe}_{16}\text{O}_{16}(\text{OH})_y(\text{SO}_4)_z.n\text{H}_2\text{O}$	Rare, found in acid mine water, <i>cf.</i> akaganeite except SO_4^{2-} replaces Cl^-
$\epsilon\text{-Fe}_2\text{O}_3$	Rare Only lab. synthesised	Feroxyhyte $\delta'\text{-FeOOH}$	Rare in nature, found in surface environments
Wüstite FeO	Stable only $> ca. 850\text{ K}$	$\delta\text{-FeOOH}$	Synthetic, cations more ordered than feroxyhyte
		High pressure FeOOH	Formed synthetically from hydrothermal conversion of haematite
		Ferrihydrite $\text{Fe}_5\text{HO}_8.4\text{H}_2\text{O}^*$	Widespread in surface environments, poorly crystalline
		Bernalite $\text{Fe}(\text{OH})_3$	Very rare, museum specimen only known example
		$\text{Fe}(\text{OH})_2$	Does not exist as mineral, is readily oxidised

* most commonly accepted formula

As shown in Table 1.4, to date only haematite and magnetite have been important catalysts on an industrial scale. Three reactions involving these materials are discussed here in particular detail. These are Fischer-Tropsch synthesis, ammonia synthesis and the high-temperature water-gas shift reaction (often a pre-step to ammonia synthesis itself). Other reactions of interest are also mentioned.

The Fischer-Tropsch synthesis of hydrocarbons and oxygenated hydrocarbons is, arguably, the most important reaction catalysed by iron oxides.⁵⁵ A range of products may be obtained in the combination of carbon monoxide and hydrogen (syn-gas) since a broad spectrum are thermodynamically favourable.¹ Examples of some typical reactions during Fischer-Tropsch synthesis are outlined below (Equations 1.7 a, b and c). The selectivity for particular products may be enhanced by the choice of catalyst. For instance, whilst cobalt catalysts yield mainly hydrocarbons and ruthenium catalysts aid the formation of high molecular weight compounds such as greases and waxes, the production of oxygenated hydrocarbons is favoured by a rhodium catalyst with a basic support or promoter.^{1, 2, 54} The products formed by the rhodium catalyst tend to be C₂ oxygenates such as ethanol, ethanal and ethane-1-2-diol but, in order to yield a range of higher molecular weight oxygenated (and unoxxygenated) hydrocarbons, a promoted iron oxide catalyst is used.^{1, 54}

Equations 1.7 a, b and c Fischer-Tropsch synthesis



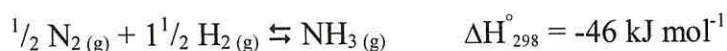
Fischer-Tropsch synthesis of liquid fuels and other chemicals is currently carried out on an industrial scale in South Africa by South African Synthetic Oil Limited (SASOL), using an iron oxide catalyst.^{1, 2, 5} The first commercial plant, SASOL I, was commissioned in 1955 due to the unavailability of either cheap or plentiful supplies of oil and there have been several plants commissioned for this purpose since. Coal, which is readily available, is utilised to produce synthesis gas *via* an unrelated process (see steam reforming, Equation 1.9) which is then used to produce liquid fuels using Fischer-Tropsch synthesis.^{1, 2} The initial stages of preparation of the catalyst used in the fixed-bed SASOL reactors are similar to the co-precipitation techniques used in the preparation of the hydrotalcite-type catalysts prepared in this work. For Fischer-Tropsch synthesis, however, the catalyst is a high surface area (200-300 m²g⁻¹), poorly ordered, promoted haematite.⁵⁴ This is prepared by combining a hot solution of iron and copper

nitrate (Fe:Cu ratio of 20:1) with a hot solution of sodium carbonate at pH 7-8.² The precipitate formed is washed with water to eliminate the sodium nitrate formed from the counter ions and the remaining slurry is mixed with potassium silicate solution. Excess potassium is then removed using nitric acid and the slurry is filtered, partially dried, extruded and further dried to achieve a water content of less than 10 % by weight. The silica formed in the material is thought to stabilise the high surface area of the iron oxide, the pore structure being determined during the initial precipitation step and subsequent drying procedure.² A similar approach was taken in the course of this research, one aim being that the aluminium and magnesium in the hydrotalcite structure would stabilise the substituted iron. Copper has been reported to facilitate reduction at lower temperatures, in the Fischer-Tropsch catalyst, thus suppressing crystal growth and maintaining maximum area of the catalytic material.² Potassium probably plays a similar role to that in ammonia synthesis which will be discussed later in this section. In this case, it is thought to facilitate the dissociation of CO (as opposed to dissociation of dinitrogen in ammonia synthesis), allowing the progressive hydrogenation of the resultant elemental surface carbon and the subsequent production of higher molecular weight products.² The various postulated mechanisms of reaction in Fischer-Tropsch synthesis are outside the scope of this review and will not be discussed in any detail here but are outlined in a number of texts.^{1, 2}

Two types of reactor are employed in the SASOL plants to vary the range of reaction products still further. These are the multitubular shell assembly reactor and the entrained fluidised bed reactor. The former operates at *ca.* 500-625 K and 3.0 MPa pressure, yielding a range of products from C₁ to C₃₅ and above. This mixture typically comprises *ca.* 32 % gasoline and diesel fuels at the lower end of the scale and *ca.* 42 % medium/hard waxes at the upper. An entrained fluidised bed reactor, however, provides mainly gasoline (C₅-C₁₁ paraffins) and some lower weight material but much smaller quantities of waxes. The temperature (595-635 K) and pressure (2.0-2.5 MPa) are not dissimilar to the conditions used in the multitubular shell reactor but here the iron oxide catalyst is finely divided and flows into the feed where the catalyst and reactants pass, as a mixture, through the reactor zone.²

Another important industrial reaction involving iron oxides is ammonia synthesis. Over one hundred million tonnes of ammonia are produced worldwide per annum from nitrogen and hydrogen, placing it amongst the top five synthetic chemicals based on mass produced.⁴ The majority of this is used in the formation of two products, approximately seventy per cent being used for agricultural fertilisers such as ammonium nitrate and ammonium sulfate and approximately twenty five per cent for nitric acid production.¹ The catalyst used in ammonia production is critical given that the rate of the uncatalysed reaction proceeds *ca.* 5×10^{49} times more slowly than the catalysed reaction. To put this in perspective, a typical (100 m^3) reactor may produce 1500 tonnes of ammonia per day. By comparison, under typical ammonia synthesis conditions (775 K, 20 MPa) the uncatalysed reaction would only produce *ca.* 0.1 g of ammonia per day in a reactor as big as our solar system.⁵ What is, perhaps, just as remarkable is that the catalyst used in modern day reactors is much the same as that developed in the early 1900's, following the work of Fritz Haber, by Bosch and co-workers in the laboratories of Badische Anilin und Soda Fabrik (BASF).² They recognised the positive effects of impurities present in the magnetite they were using to produce iron catalysts for the reaction for which Haber had recognised the commercial potential. Most of the catalysts used today are still multicomponent materials based on magnetite with the addition of promoters.^{2, 54} These promoters tend to be either structural, such as alumina (Al_2O_3), or chemical/electronic, such as potassium oxide (K_2O). The alumina in the ammonia synthesis catalyst aids in the maintenance of the high area active iron catalyst, formed from the reduction of magnetite, rather than being involved directly in the catalytic reaction (a similarity with the use of silica in the Fischer-Tropsch catalyst discussed previously). Conversely, the main function of potassium appears to be concerned with the chemisorption and subsequent dissociation of nitrogen which is commonly viewed as the rate-limiting step.^{2, 4, 5, 54} Metallic iron is, predominantly, the active component of the catalyst and this is produced by reducing magnetite with either hydrogen alone or synthesis gas ($\text{CO} + \text{H}_2$) to produce the active $\alpha\text{-Fe}$ catalyst.^{5, 54} Magnetite is used because it has an inverse spinel structure based on cubic close packed oxide ions in the interstices of which lie the Fe^{2+} and Fe^{3+} ions. There is no relaxation of this lattice upon reduction of the iron which leaves a porous metallic iron matrix with a surface area which is in the range of $10\text{-}25 \text{ m}^2\text{g}^{-1}$.^{1, 54}

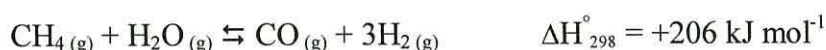
Equation 1.8 Ammonia Synthesis²



The reaction (Equation 1.8) is exothermic and, therefore, applying Le Chatelier's Principle, thermodynamically favoured by lower temperatures. In addition, it is also favoured by elevated pressures since four moles of reactant form two moles of product. However, in practice, the temperature is optimised in the range of 670-720 K to balance thermodynamic and the kinetic effects and, therefore, ensure more rapid conversions. The realistic operational pressure is also limited to 15-35 MPa since higher pressures would entail excessive investment in plant design and construction.^{1,2}

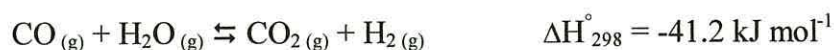
The third reaction of interest utilising iron oxides, the high-temperature water gas shift reaction, was once of significant importance in the production of hydrogen for petroleum reforming, fat hardening, ammonia synthesis and numerous other processes.¹ It has, however, since been replaced to some extent by the steam-reforming of hydrocarbons (Equation 1.9) as a source of hydrogen since methane is relatively cheap and readily available and is more hydrogen-rich than water (the previous source of hydrogen using the water-gas reaction).¹

Equation 1.9 Steam-reforming of hydrocarbons



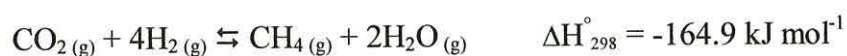
However, water-gas shift reactions still play an important role in hydrogen production since steam reforming produces a mixture of carbon monoxide and hydrogen (syn-gas). Therefore, water-gas shift reactions are employed to reduce concentrations of undesired carbon monoxide in the product from steam reformers and, therefore, increase the proportion of hydrogen (Equation 1.10).²

Equation 1.10 Water-Gas Shift



Usually, a high-temperature (600-800 K) shift process precedes a low-temperature (500 K) process; the first catalyst is based on magnetite and performs much (85-90 %) of the conversion with moderate activity, whilst the second catalyst must be more active to function at the lower partial pressure of CO and lower temperature dictated by thermodynamic considerations.^{2, 5} Therefore, a catalyst of copper on a zinc oxide/alumina support is used as this second catalyst to convert much of the remaining CO.^{1, 5} Magnetite is used for the high-temperature shift because of its high activity for the conversion whilst possessing sufficient selectivity to avoid methanation by-products (Equation 1.11).⁵

Equation 1.11 Methanation



By comparison, pure haematite is not used for this reaction due to the high temperature regime it would require. This would result in sintering of the crystallites of the active Fe_3O_4 phase and a subsequent loss in surface area.⁵ Indeed, chromium oxide is combined with the magnetite to inhibit crystal growth by sintering since it is suitably refractory and compatible.^{5, 54} In practice, ICI catalyst 15-4 (conventional activity/low pressure drop) and 15-5 (high activity/conventional pressure drop) are commonly used for high-temperature water gas shift reactions⁵ but the iron oxide is supplied in the haematite form which must be reduced to magnetite before use. This reduction is carefully controlled to prevent total reduction to metallic iron which would promote methanation and CO disproportionation.⁵⁶

One final example of the use of iron oxides in catalysis involves the use of a hydrous iron oxide, similar to ferrihydrite, which is used either pure or admixed with haematite. It is a high surface area material (*ca.* 200 m^2g^{-1}) and is manufactured by Mach I, Inc. under the trade name Nanocat[®] using a patented process (U.S. patents 4854981, 4881994 and 5,047,382). It is used as a burning rate catalyst for solid rocket fuels (NH_4ClO_4) and also shows activity for direct coal liquifaction.^{54, 57}

1.5 Hydrotalcite-type Compounds

1.5.1 Structure

The anionic clays, hydrotalcite $[\text{Mg}_6\text{Al}_2(\text{OH})_{16}\text{CO}_3 \cdot 4\text{H}_2\text{O}]$ and pyroaurite $[\text{Mg}_6\text{Fe}_2(\text{OH})_{16}\text{CO}_3 \cdot 4\text{H}_2\text{O}]$ were first described and analysed in the mid 1800's by Hostetter⁵⁸ and Igelström,⁵⁹ respectively.⁶⁰ They, and other isostructural compounds, have been the subject of a great deal of interest. This was initially focussed on the characterisation of the natural minerals and is now mainly concerned with the use of their synthetic analogues as catalysts and their precursors. Despite this interest, it wasn't until 1915 that the first exact formula was assigned to hydrotalcite by Manasse.^{39, 61} Soon after, Aminoff and Broomé recognized the existence of two polytypes of hydrotalcite.^{39, 62} To understand the nature of these polytypes, the information given in the section regarding anionic clays and their structures must be elaborated upon. The basic structure of HTc's is generally described as consisting of brucite-like $[\text{Mg}(\text{OH})_2]$ layers in which some of the divalent metal cations have been substituted by trivalent cations to form positively charged sheets. The metal cations occupy the centers of the octahedra whose vertices are hydroxide ions. These octahedra are connected to one another by edge-sharing to form an infinite sheet.⁶³ The overall positive charge generated in the cationic layers is compensated for with the addition of interlayer anions, as described previously. Schematic arrangements of the octahedra in brucite and hydrotalcite are shown in Figures 1.3 and 1.4 to highlight the similarities in their structures.

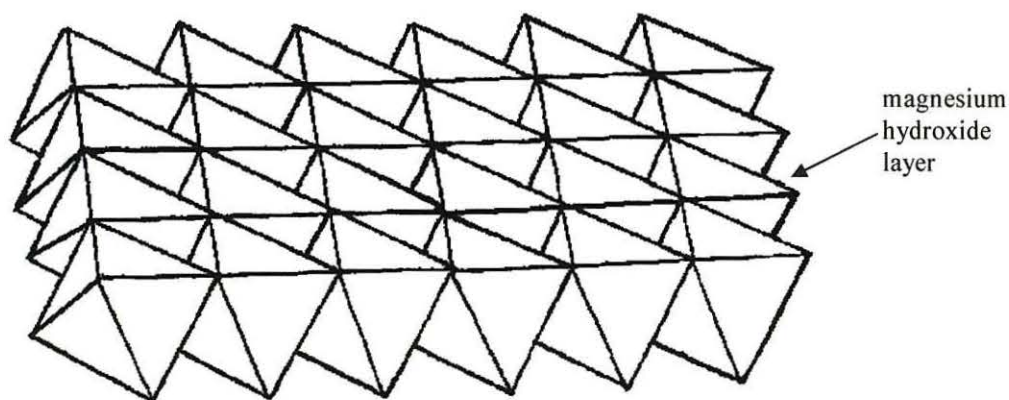


Figure 1.3 The edge-sharing $[\text{Mg}(\text{OH})_2]$ octahedra of brucite³⁹

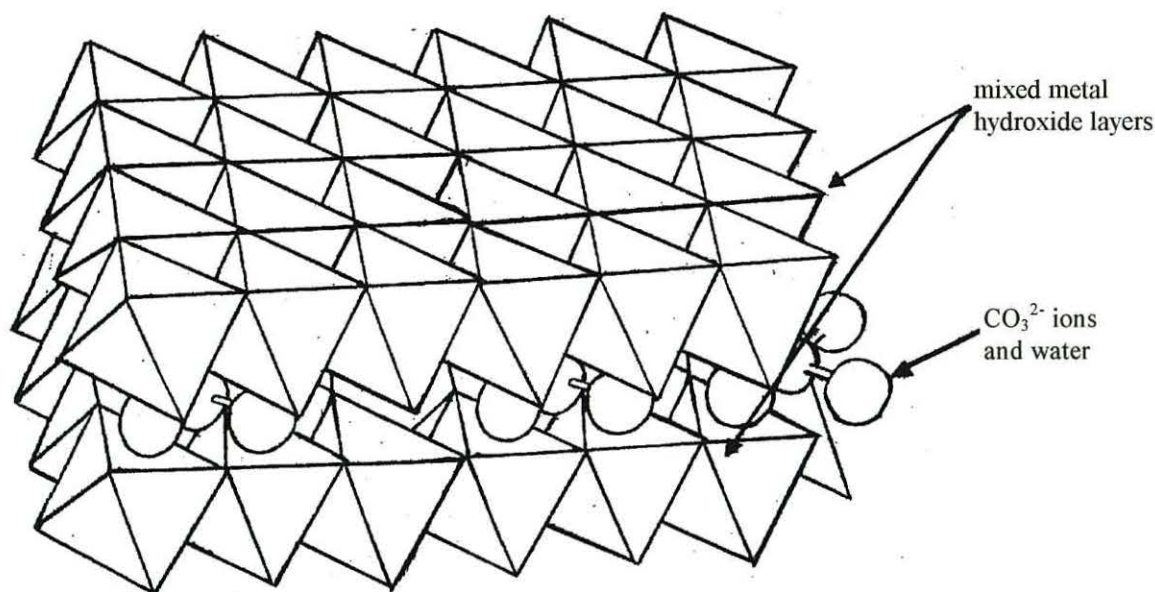


Figure 1.4 The arrangement of octahedra and interlayer species in HTc's³⁹

By comparison with the brucite-like description of the metal hydroxide layers, it was suggested by Taylor that the metal hydroxide sheets do not stack in a manner analogous to brucite but rather like gibbsite [γ -Al(OH)₃], with the hydroxyl groups on the lower surface of the cation layer directly above those on the upper surface of the one below.⁶⁴ However, the brucite layer description has been, and still is, widely used. In compliance with this arrangement there are also two different symmetries with which the brucite-like sheets can stack; rhombohedral (R) or hexagonal (H). It is thought that the hexagonal polytype may be the high-temperature form of the rhombohedral³⁹ and the two have been shown to exist together.⁶⁵ The HTc's with rhombohedral symmetry are those commonly found in nature and are also easier to form in the laboratory.⁴⁰ The hexagonal polymorph of hydrotalcite, was named manasseite, after Manasse. Frondel⁶⁰ published work in 1941 entitled 'Constitution and Polymorphism of the Pyroaurite and Sjögrenite Groups' which was dedicated to the investigation of the dimorphism of hydrotalcite (R)/manasseite (H), pyroaurite (R)/sjögrenite (H) and stichtite (R)/barbertanite (H) HTc's. Indeed the pyroaurite/sjögrenite system was the subject of much of the earlier work dedicated to structure elucidation and it was the work of Taylor³⁸ and Allman³⁷ on this system which finally established the structure recognized today. The work of Taylor was also concerned with the segregation and cation ordering within the structure. He suggested that the names pyroaurite and sjögrenite be used for each polytype, irrespective of the

Mg:Fe ratio, segregation or cation ordering in the respective materials. Further work by Vucelic *et al.*⁶⁶ on the pyroaurite system suggested that, although there is no correlation between the trivalent cation positions in the metal hydroxide sheets over distances of a few nanometres, there is a very high level of local ordering which prevents the occurrence of neighbouring trivalent cations. This is, however, dependent upon the fraction of $M^{III}/(M^{III}+M^{II})$ - *i.e.* x in the often quoted general HTc representative formula $[M^{II}_{1-x}M^{III}_x(OH)_2]^{x+}(A^{n-}_{x/n}).mH_2O$ - which must, it is generally agreed, remain within the range of 0.20 to 0.33 to form pure HTc's. If excess Al is present during synthesis then amorphous $Al(OH)_3$ may form and adjacent $Al(OH)_6$ octahedra would be present within the structure.^{39, 65}

The nature of the cations which may occur within the brucite-like layers are suggested to only be limited by their size *i.e.* their ionic radii must not differ too greatly from that of Mg^{2+} , the cation upon which the layered structure is based.³⁹ Consequently, a vast range of variations are possible, which have been well documented and reviewed.³⁹ However, although the Mg_6Fe_2HTc is well documented as the pyroaurite/sjögrenite system and the Fe_6Al_2HTc system has also been investigated,^{67, 68, 69} detailed characterization has not been published over the range Mg_6Al_2HTc to Fe_6Al_2HTc with increasing Fe for Mg substitution. This research seeks to investigate this transition thoroughly and test the catalytic activity of the materials and their thermally activated derivatives for a number of reactions.

1.5.2 Preparation

As mentioned in section 1.4.2, hydrotalcite is relatively cheap and reliable to synthesise, as are the majority of HTc's, and precipitation is the most widely used method for their synthesis.²⁷ There are other methods but these are often less suitable for the preparation of this type of material for catalytic applications since they do not offer sufficient product control and, therefore, reproducibility. In addition, alternative methods are generally less efficient. For example, the hydrothermal synthesis of $MgAlHTc$ from mixtures of MgO and Al_2O_3 requires higher temperatures, pressures and a longer ageing period. There are

two main methods of precipitation used when synthesising HTc's; sequential precipitation (precipitation at variable pH) or coprecipitation (precipitation at constant pH). Both methods have been reported in the literature but it would appear that coprecipitation is better suited to the preparation of materials to be utilised as catalysts, for reasons given later in this section. Indeed, coprecipitation is more widely used and is recognised as one of the most reliable and reproducible techniques for the preparation of non-noble metal-based catalysts.³⁹ Sequential precipitation at variable pH involves the titration of an aqueous alkaline solution with a metal salt solution which results in a sequential precipitation of the metal ions, forming a range of products as a consequence. Although pure hydrotalcite is formed at some stage of the precipitation, other products are also formed during the reaction *e.g.* $\text{Al}(\text{OH})_3$ at *ca.* pH 4.0-4.5 and $\text{Mg}(\text{OH})_2$ at *ca.* pH 9.5 for a mixture of magnesium and aluminium salts.⁷⁰ Ageing of the final product mixture can result in dissolution, followed by coprecipitation, which can give rise to a more homogeneous product but the final material would not be expected to be as pure as one precipitated under coprecipitation conditions. Whilst it is true that the presence of minor phases may have a beneficial effect on the final product (*cf.* ammonia synthesis catalyst), initial studies of catalyst preparation are simplified by the investigation of single-phase materials.

In a recent review of precipitation methods by Crepaldi and co-workers,⁷¹ coprecipitation was said to yield materials with a higher degree of crystallinity, smaller particle size and higher specific surface area than those obtained at variable pH. It should be noted that this study was restricted to MgAlHTc and ZnCrHTc on the basis that the authors regarded them as being amongst the most frequently used combinations. The interlayer anions incorporated into these structures were terephthalate and dodecylsulfate, since these were described as being expected to provide 'representative materials'. The review of hydrotalcite-type anionic clays by Cavani *et al.* provides details regarding the fundamentals of hydrotalcite synthesis.³⁹ It states that particular attention must be paid to the relative proportions of starting materials used in a combination reaction such as this if a pure material is to be formed. In general, the ratios of cations should be combined in the desired final ratio whilst an excess of the anion for incorporation into the interlayer region is used to preclude the incorporation of undesired anions. Nitrate salts of the metal cations are normally used since these anions will only be

incorporated preferentially over carbonate if the pH is lower than *ca.* 6 or if the carbonate anion is present in extremely low concentrations. Nitrates are also commonly chosen as counterions due to their ease of elimination from the final product, by washing. As discussed previously, if carbonate is not desired in the final structure, it must be eliminated from the solutions and carbon dioxide eliminated from the atmosphere. The metal salt solutions and the alkali solutions are combined at a pH which is greater than, or equal to, the pH at which the more soluble hydroxide precipitates. Thus, the common range is *ca.* pH 8-10 since most of the hydroxides of the metals which form HTc's precipitate within this range and yet it is sufficiently low to avoid aluminium dissolution which occurs at *ca.* pH > 10. There are also a number of other variables to be taken into consideration *viz.* precipitation temperature, reagent concentration, ageing time and temperature, anion for incorporation and washing and drying techniques. Probably the most frequently used method is to combine solutions with relatively low concentrations (0.5-2.0 mol l⁻¹) quite slowly. This results in a material comprised of less, larger, more crystalline crystallites than that precipitated from the rapid combination of more concentrated solutions. This is because, for the latter, the rate of nucleation exceeds the rate of crystal growth. Increased reaction and ageing temperatures/times allow dissolution and subsequent recrystallisation of the precipitate to a more ordered structure.⁷² Finally, a washing stage eliminates the soluble reaction by-products and excess reagents and the product is dried at a sufficiently low temperature (typically *ca.* 383 K) to remove adsorbed water without initiating calcination.

1.5.3 Calcination

Calcination is a term used to describe the controlled heating of a material, generally with the aim of forming a new structure possessing enhanced qualities for a particular purpose; for instance increased catalytic activity or, as previously mentioned, to utilise the 'memory effect' to reconstitute the materials with exchanged interlayer anions.³⁹ Basic catalysts can be prepared from HTc's by calcining the material at *ca.* 723 K – these materials will be discussed in more detail in section 1.5.4 and Chapters 3 and 4. The discussion in this section will focus upon the changes which take place in HTc's during

the heating process, focussing particularly on the mineral hydrotalcite $[\text{Mg}_6\text{Al}_2(\text{OH})_{16}\text{CO}_3 \cdot 4\text{H}_2\text{O}]$. The main methods reported in the literature for the characterisation of HTc's during calcination have been differential thermal analysis (DTA), thermo-gravimetric analysis (TGA), X-ray diffraction (XRD), infrared (IR) spectroscopy and scanning electron microscopy (SEM). Using a combination of these techniques, information has been pieced together regarding the changes which occur in HTc's during calcination. However, there are still minor inconsistencies in the literature regarding exact transition temperatures *etc.*, even for the common HTc mineral phases and there is little information available regarding HTc's which occur less frequently or those which are purely synthetic. The changes, which occur in hydrotalcite $[\text{Mg}_6\text{Al}_2(\text{OH})_{16}\text{CO}_3 \cdot 4\text{H}_2\text{O}]$ during calcination, have been reported as follows.

After an initial loss of adsorbed water, the interlayer water is lost, as steam, at *ca.* 473-523 K. Dehydroxylation of the metal hydroxide layers begins at *ca.* 573 K,⁷³ and MgO begins to form and is present as the only phase identifiable by XRD at this stage, as the structure continues to dehydroxylate.^{39, 73, 74, 75} The majority of decarbonation occurs shortly after dehydroxylation, generally between 673-773 K.⁷⁶ However, a high-Al HTc has been shown to retain as much as *ca.* 20 % of the interlayer carbonate at 773 K, due to the increased layer charge.^{73, 74} The thermal stability of the layered structure of the HTc's at elevated temperatures is an area under debate. Some sources claim that it is maintained and that the parent structure may be recovered, at least partially, when rehydrolysed as long as the calcination temperature does not exceed 773 K.^{39, 74, 77, 78} Others claim that the layered structure is destroyed at 723 K but may still be regained, at least in part, following rehydration⁴³ and it has also been shown that structural regeneration is dependent upon the cations present and their relative ratios.⁷⁹ Nonetheless, a more widely agreed fact is that a material with a surface area *ca.* 2-3 times that of the uncalcined material is formed after calcination at these temperatures.^{27, 39, 75} This increase in surface area has been described as being due to the release of steam (from the interlayer water and hydroxyl groups) and carbon dioxide (from the interlayer carbonate) which burst through the layers, forming pores.⁸⁰ The heating rate is believed to be vital, however, since too low a rate would cause the gases to simply 'seep' from the edges of the layers, without forming pores.⁸¹ Conversely, an excessively high ramp-rate would cause the gases to burst through the layers in an

uncontrolled manner, forming excessively large pores.⁴⁰ This pore formation mechanism is illustrated diagrammatically in Figure 1.5; the gas evolution both *via* the edges and through the layers is shown.

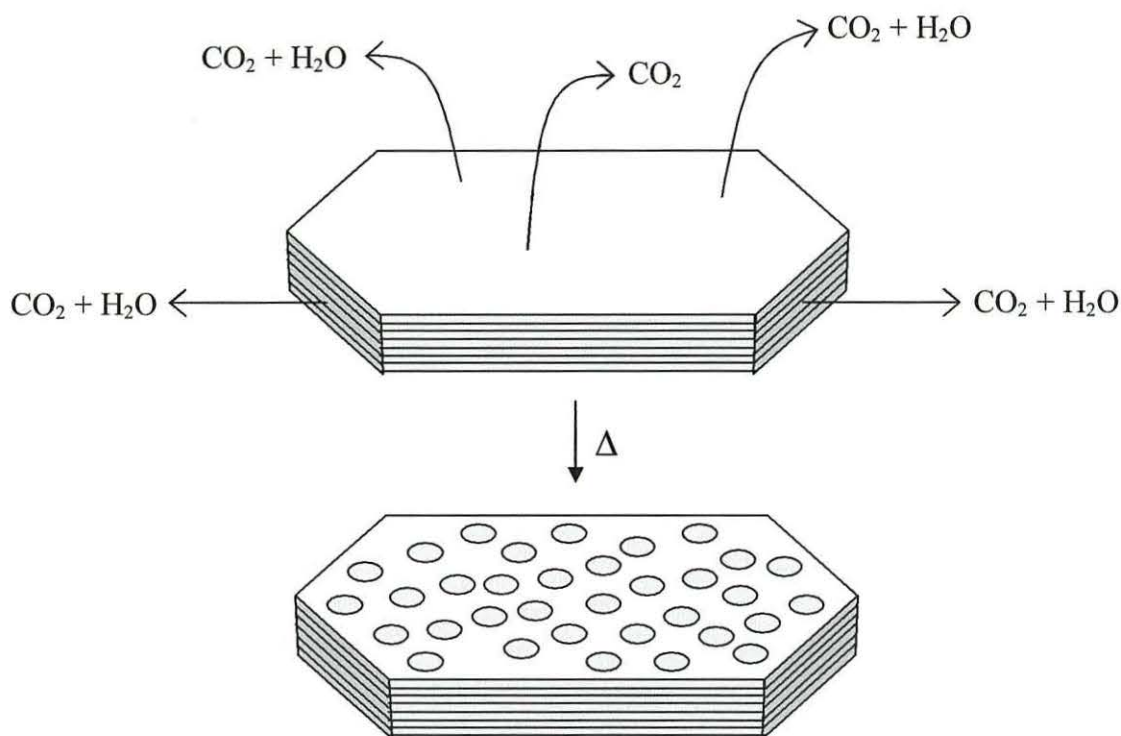


Figure 1.5 Exaggerated effects of heating on pore formation in HTc's

If however, the temperature is increased further, the surface area begins to decrease steadily due to sintering and, eventually, above *ca.* 1273 K a magnesium aluminium spinel (MgAl_2O_4) forms and remains upon cooling.^{27, 39, 75}

In summary, for $\text{Mg}_6\text{Al}_2\text{HTc}$, at *ca.* 673-773 K using an optimised heating rate, a material can be produced with a high surface area/porosity and a homogeneous interdispersion of elements.

1.5.4 Catalysis

As a consequence of the diversity of HTc's which may be synthesised there is a vast range of reactions for which their catalytic potential may be investigated. Many of these

reactions fall beyond the scope of this review which instead focuses on some of the fundamentals of HTc's in catalysis. However, reviews by Cavani *et al.* and Vaccari do summarise some of the more significant developments in the general use of HTc's in catalysis.^{27, 39} The literature concerning base catalysis using HTc's is reasonably mature and will be discussed in more detail. However, the literature concerning the use of HTc's as oxidation catalysts is still quite diverse since this is a less well-researched area although a recent paper by Kaneda *et al.*⁸² specifically investigated the design of HTc's for use as oxidation catalysts.

The first reported use of HTc's in catalysis has been documented as being the patent which appeared in 1970 appertaining to the use of precipitated HTc's as hydrogenation catalysts.⁸³ Although similarly produced materials route may have been utilised as catalysts prior to this, there does not appear to be any literature which suggests they had a HTc structure. Since 1970 the number of scientific papers reporting the use of synthetic HTc's as, or as precursors to, catalysts has seen an exponential increase.⁵² Much of the literature to date focuses upon their use once calcined since this activation stage has been shown to enhance the characteristics often desired in a catalytically active material, as discussed in section 1.5.3. This is especially true in the application of HTc's as base catalysts, an area which has seen, and continues to see, much dedicated investigation in the literature. In a general review of hydrotalcite-type anionic clays by Cavani *et al.* in 1991, the section on basic catalysis focussed on just two reactions. These were the polymerisation of alkene oxides and the aldol condensations of aldehydes and ketones, since these reactions had been the subject of much of the investigation into the use of HTc's as basic catalysts until then.³⁹ Since then, however, the use of HTc's in a range of base catalysed reactions has been investigated. For instance, in 1995 Tichit *et al.* reported an investigation of the influence of the carbonate content, Mg:Al ratio and subsequent activation temperature of synthetic MgAlHTc's on a reaction sensitive to catalyst basicity *viz.* the condensation of benzaldehyde and acetone.⁷⁷ They concluded that all three of these factors could be used to modify the basicity of the HTc and also drew some interesting conclusions regarding the nature of the basic sites. They suggested the presence of moderately basic OH sites in addition to more strongly basic O²⁻ sites after calcination. More recently, Tichit *et al.* have investigated the acid-base properties of calcined MgAl and NiAl HTc's obtained by either sol-gel or coprecipitation methods.⁸⁴

In order to do this they used CO₂ and NH₃ temperature programmed desorption (TPD) for characterisation of the acid/base sites and acetone condensation was the catalytic reaction studied. Their major conclusions (in addition to those from their earlier work) were that the magnesium-containing HTc's were more basic than the nickel-containing HTc's and that the preparative method did have an influence on the basicity due to the difference in the textural and morphological features obtained. Kagunya *et al.* used the ethanolysis of propylene oxide, a reaction which may be either acid or base catalysed, to investigate the nature of the active sites of both calcined and uncalcined HTc's.⁸⁵ This work is especially interesting since it contrasts the acid/base activity of a range of HTc's. These include HTc's with a number of cation combinations, anions other than carbonate and polyoxometalate pillared derivatives. They showed that there are basic sites of different origins present in the calcined derivatives of the HTc's and that there are also acidic sites present for some of the materials, especially the pillared derivatives. In 1999, Kirisci and co-workers furthered the investigation of pillared HTc's as base catalysts, this time using both organic and inorganic pillared HTc derivatives.⁴³ They suggested that, in this case, calcination destroys the layered structure of HTc's which is only partially restored by rehydration. They found that the disadvantage of the pillared materials was their decreased thermal stability, noting that this would need to be improved for their effective catalytic use. The development of pillared layered anionic clays (PILAC's) has been the subject of an increasing amount of research. This has been focussed upon the development of shape-selective adsorbents and catalysts and was recently reviewed by Vaccari.²⁷ One key factor reiterated in this review regards the low thermal stability of PILAC's which was, again, not regarded to be conducive to their general use as catalysts. Consequently, these materials have not been studied and are beyond the scope of this review.

1.6 Green Rusts and their Oxidation Products

The iron-hydroxy compounds known as 'green rusts' are isostructural with HTc's and occur naturally as intermediate phases in the formation of iron oxides, hydroxides and oxyhydroxides.⁵³ Because the first occurrence of these blue green compounds was

associated with the corrosion of steel (in oxygen-deficient conditions) they were called green rusts.⁵⁴

The structure of green rusts is known to be of a hydrotalcite-type, the Fe^{III} ions imparting a net positive charge on the metal hydroxide layers which is balanced by the intercalated anions.²⁶ Although sulfate and chloride are commonly found as interlayer anions, it is thought that the carbonate forms are more likely to exist in nature.⁸⁶ This is expected due to the preference of the HTc's for intercalation of carbonate, as discussed in Section 1.4.2, and because of the high concentrations of this anion in waterlogged soils.⁸⁷ The $\text{Fe}^{\text{II}}:\text{Fe}^{\text{III}}$ ratio is often 3:1,⁸⁸ resulting in a formula $[\text{Fe}^{\text{II}}_6\text{Fe}^{\text{III}}_2(\text{OH})_{16}\text{CO}_3 \cdot 4\text{H}_2\text{O}]$ analogous to that of hydrotalcite $[\text{Mg}_6\text{Al}_2(\text{OH})_{16}\text{CO}_3 \cdot 4\text{H}_2\text{O}]$ but may vary, and has been reported as low as 2:1.⁸⁹

The general preparative procedure for green rusts involves the neutralisation of an Fe^{II} solution in an inert atmosphere.⁵³ Taylor and Schwertmann⁹⁰ showed that a range of iron oxides could be formed from this precursor material, depending on the rate of oxidation and the Fe^{II} concentration in solution. Following this work, Taylor and McKenzie⁶⁷ produced an $\text{Fe}^{\text{II}}\text{Al}^{\text{III}}$ hydroxy-carbonate (HTc) which was also isostructural with hydrotalcite but was, in common with the green rusts, very unstable in air, rapidly oxidising to form an Al-substituted goethite.

The high sensitivity of green rusts towards oxidation makes their isolation and characterisation difficult⁸⁹ but they are worthy of investigation as intermediates in the formation of iron oxides with physical characteristics similar to that of calcined hydrotalcite *i.e.* high surface area/porosity. In addition, this work investigates the isomorphous substitution of Al^{III} into the iron oxides formed, upon oxidation, with the aim of increasing the mechanical strength to reduce sintering of these materials if they are to be used as catalysts. The materials formed using this method should yield aluminium-substituted iron oxides, the properties of which will be contrasted with those of the iron-substituted hydrotalcites already discussed.

1.7 References

- 1 G.C. Bond, Heterogeneous Catalysis – Principles and Applications (2nd Edition), Oxford University Press, Oxford, 1990.
- 2 J.M. Thomas and W.J. Thomas, Principles and Practice of Heterogeneous Catalysis, VCH, Weinheim, 1997.
- 3 J.T. Richardson, Principles of Catalyst Development, Plenum Press, New York, 1989.
- 4 D.F. Shriver, P.W. Atkins and C.H. Langford, Inorganic Chemistry, Oxford University Press, Oxford, 1990.
- 5 M.V. Twigg (Ed.), Catalyst Handbook (2nd Edition), Manson Publishing Limited, London, 1996.
- 6 Y. Ono, T. Baba, E.J. Duskocil, S. Bordawekar and R.J. Davis, in Catalysis – Royal Society of Chemistry Specialist Periodical Report Volume 15, J.J. Spivey (Senior Reporter), The Royal Society of Chemistry, Cambridge, 2000.
- 7 K. Tanabe and W.F. Hölderich, *Appl. Catal. A: Gen.*, 1999, **181**, 399.
- 8 H. Pines, J.A. Vesely and V.N. Ipatieff, *J. Am. Chem. Soc.*, 1955, **77**, 347.
- 9 H. Hattori, *Chem. Rev.*, 1995, **95**, 537.
- 10 P.W. Atkins, Physical Chemistry (4th Edition), Oxford University Press, Oxford, 1990.
- 11 G.C. Chinchin, 1971, UK Patent 1,342,577.

- 12 D.O. Hughes, 1971, UK Patent 1,350,242.
- 13 I.R. Shannon, 1976, UK Patent 1,542,634.
- 14 J.P. Dunn, H.G. Stenger Jr. and I.E. Wachs, *J. Catal.*, 1999, **181**, 233.
- 15 J. March, *Advanced Organic Chemistry – Reactions, Mechanisms and Structure*, (4th Edition), John Wiley & Sons, New York, 1992.
- 16 P. Vinke, D. de Wit, A.T.J.W. de Goede and H. van Bakkum, *in Studies in Surface Science and Catalysis Vol. 72 – New Developments in Selective Oxidation by Heterogeneous Catalysis*, P. Ruiz and B. Delmon (Eds.), Elsevier, London, 1992.
- 17 M. Paecht-Horowitz, *Angew. Chem. Int. Ed. Engl.*, 1973, **12**, 349.
- 18 S.L. Miller, *Science*, 1953, **117**, 528.
- 19 S.L. Miller, *J. Am. Chem. Soc.*, 1955, **77**, 2351.
- 20 M. Paecht-Horowitz, J. Berger and A. Katchalsky, *Nature*, 1970, **228**, 636.
- 21 A.G. Cairns-Smith, *Scientific American*, 1985, **252**, 74.
- 22 A.G. Cairns-Smith, *New Scientist*, 2nd Jan. 1986, 34.
- 23 A. Weiss, *Angew. Chem. Int. Ed. Engl.*, 1981, **20**, 850.
- 24 N.C. Brady and R.R. Weil, *The Nature and Properties of Soils* (12th Edition), Prentice-Hall Inc., New Jersey, 1999.
- 25 B. Velde, *Introduction to Clay Minerals - Chemistry, Origins, Uses and Environmental Significance*, Chapman & Hall, London, 1992.

- 26 J.B. Dixon and S.B. Weed (Eds.), SSA Book Series: 1 – Minerals in Soil Environments (2nd Edition), Soil Science Society of America, Madison, 1989.
- 27 A. Vaccari, *Appl. Clay Sci.*, 1999, **14**, 161.
- 28 N.N. Greenwood and A. Earnshaw, Chemistry of the Elements, Pergamon Press, Oxford, 1993.
- 29 T.J. Pinnavaia, *Science*, 1983, **220**, 365.
- 30 S.A. Boyd, M.M. Mortland and C.T. Chiou, *Soil Sci. Soc. Am. J.*, 1988, **52**, 652.
- 31 M.L. Occelli and R.M. Tindwa, *Clays and Clay Minerals*, 1983, **31**(1), 22.
- 32 R.A. Schoonheydt, H. Leeman, A. Scorpion, I. Lenotte and P. Grobet, *Clays and Clay Minerals*, 1994, **42**(5), 518.
- 33 M.R. Sun Kou, S. Mendioroz and V. Muñoz, *Clays and Clay Minerals*, 2000, **48**(5), 528.
- 34 J.T. Klopogge, S. Komarneni and J.E. Amonette, *Clays and Clay Minerals*, 1999, **47**(5), 529.
- 35 C.J. Serna, J.L. White and S.L. Hem, *J. Pharm. Sci.*, 1978, **67**, 324.
- 36 W. Feitknecht, *Helv. Chim. Acta*, 1942, **25**, 131.
- 37 R. Allman, *Acta Cryst.*, 1968, **B24**, 972.
- 38 H.F.W. Taylor, *Min. Mag.*, 1969, **37**, 338.

- 39 F. Cavani, F. Trifirò and A. Vaccari, *Catal. Today*, 1991, **11**, 173.
- 40 S. Carlino, *Chem. Brit.*, 1997, September, 59.
- 41 S. Miyata, *Clays and Clay Minerals*, 1983, **31**(4), 305.
- 42 V.A. Drits, T.N. Sokolova, G.V. Sokolova and V.I. Cherkashin, *Clays and Clay Minerals*, 1987, **35**(6), 401.
- 43 A. Béres, I. Pálanko, I. Kiricsi, J.B. Nagy, Y. Kiyozumi and F. Mizukami, *App. Catal. A: General*, 1999, **182**, 237.
- 44 A. Hall and M.G. Stamatakis, *Journal of Sedimentary Research*, 2000, **70**, 549.
- 45 S. Miyata, *Clays and Clay Minerals*, 1975, **23**, 369.
- 46 D.L. Bish, *Bull. Mineral.*, 1980, **103**, 170.
- 47 M. Meyn, K. Beneke and G. Lagaly, *Inorg. Chem.*, 1990, **29**, 5201.
- 48 H. Zhao and G.F. Vance, *J. Chem. Soc., Dalton Trans.*, 1997, 1961.
- 49 H. Kopka, K. Beneke and G. Lagaly, *J. Colloid Interface Sci.*, 1988, **123**, 427.
- 50 R. Celis, W.C. Koskinen, M.C. Hermosín, M.A. Ulibarri and J. Cornejo, *Soil Sci. Soc. Am. J.*, 2000, **64**, 36.
- 51 P.C. Pavan, E.L. Crepaldi and J.B. Valim, *J. Colloid Interface Sci.*, 2000, **229**, 346.
- 52 D. Tichit and A. Vaccari, *Appl. Clay Sci.*, 1998, **13**, 311.

- 53 U. Schwertmann and R.M. Cornell, *Iron Oxides in the Laboratory*, VCH, Weinheim, 1991.
- 54 R.M. Cornell and U. Schwertmann, *The Iron Oxides – Structure, Properties, Reactions, Occurrence and Uses*, VCH, Weinheim, 1996.
- 55 A. Glisenti, G. Favero and G. Granozzi, *J. Chem. Soc., Faraday Trans.*, 1998, **94**(1), 173.
- 56 Anon., ICI Internal Document.
- 57 J. Zhao, F.E. Huggins, Z. Feng, F. Lu, N. Shah and G.P. Huffman, *J. Catal.*, 1993, **143**, 499.
- 58 C. Hostetter, *Jour. Prakt. Chem.*, 1842, **27**, 376.
- 59 L.J. Igelström, *Öfv. Vetensk. Akad. Forh., Stokholm*, 1865, no. 9.
- 60 C. Frondel, *Am. Mineral.*, 1941, **26**, 295.
- 61 E. Manasse, *Atti Soc. Toscana Sc. Nat., Proc. Verb.*, 1915, **24**, 92.
- 62 G. Aminoff and B. Broomé, *Kungl. Sven. Vetensk. Handl.* 9, 1930, **3**, 23.
- 63 F. Millange, R.I. Walton and D. O'Hare, *J. Mater. Chem.*, 2000, **10**, 1713.
- 64 H.F.W. Taylor, *Min. Mag.*, 1973, **39**, 377.
- 65 I. Pausch, H-H. Lohse, K. Schürmann and R. Allman, *Clays and Clay Minerals*, 1986, **34**(5), 507.

- 66 M. Vucelic, W.Jones and G.D. Moggridge, *Clays and Clay Minerals*, 1997, **45**(6), 803.
- 67 R.M. Taylor and R.M. McKenzie, *Clays and Clay Minerals*, 1980, **28**(3), 179.
- 68 R.M. Taylor, *Clay Minerals*, 1982, **17**, 369.
- 69 S.M. Auer, J-D. Grunwaldt, R.A. Köppel and A. Baiker, *J. Mol Cat. A: Chemical*, 1999, **139**, 305.
- 70 G.J. Ross and H. Kodama, *Amer. Min.*, 1967, **52**, 1037.
- 71 E.L. Crepaldi, P.C. Pavan and J.B. Valim, *J. Braz. Chem. Soc.*, 2000, **11**, 64.
- 72 W.T. Reichle, *Solid State Ionics*, 1986, **22**, 135.
- 73 T. Hibino, Y. Yamashita, K. Kosuge and A. Tsunashima, *Clays and Clay Minerals*, 1995, **43**(4), 427.
- 74 E. Kanezaki, *Inorg. Chem.*, 1998, **37**, 2588.
- 75 S. Narayanan and K. Krishna, *Chem. Commun.*, 1997, 1991.
- 76 C.W. Beck, *Am. Mineral.*, 1950, **35**, 985.
- 77 D. Tichit, M.H. Lhouty, A. Guida, B.H. Chiche, F. Figueras, A. Auroux, D. Bartalini and E. Garrone, *J. Catal.*, 1995, **151**, 50.
- 78 K. Chibwe and W. Jones, *J. Chem. Soc., Chem. Commun.*, 1989, 926.
- 79 M. Sychev, R. Prihod'ko, K. Erdmann, A. Mangel and R.A. van Santen, *Applied Clay Science*, 2001, **18**, 103.

- 80 W.T. Reichle, S.Y. Kang and D.S. Everhardt, *J. Catal.*, 1986, **101**, 352.
- 81 S. Carlino and M.J. Hudson, *J. Mater. Chem.*, 1995, **5**, 1433.
- 82 K. Kaneda, K. Yamaguchi, K. Mori, T. Mizugaki and K. Ebitani, *Catalysis Surveys from Japan*, 2000, **4**, 31.
- 83 F.J. Bröcker and L. Kainer, German Patent 2,024,282 (1970) and corresponding UK Patent 1,342,020 (1971).
- 84 F. Prinetto, G. Ghiotti, R. Durand and D. Tichit, *J. Phys. Chem. B*, 2000, **104**, 11117.
- 85 W. Kagunya, Z. Hassan and W. Jones, *Inorg. Chem.*, 1996, **35**, 5970.
- 86 R.M. Taylor, U. Schwertmann and H. Fechter, *Clay Minerals*, 1985, **20**, 147.
- 87 U. Schwertmann and H. Fechter, *Clay Minerals*, 1994, **29**, 87.
- 88 E. Murad and R.M. Taylor, *Clay Minerals*, 1984, **19**, 77.
- 89 H.C.B. Hansen, *Clay Minerals*, 1989, **24**, 663.
- 90 R.M. Taylor and U. Schwertmann, *Clay Minerals*, 1974, **10**, 299.

Chapter 2

Preparation and Characterisation of Precursor Materials

2.1 Hydrotalcite-type compounds

2.1.1 Preparative Methodology

Many of the reasons for the choice of materials with the hydrotalcite structure as the basis for the research described in this thesis have been discussed in Chapter 1, particularly in section 1.5. To recap, hydrotalcite-type compounds (HTc's) possess a desirable morphology, particularly following thermal activation, for use as catalysts and sorbent materials. The metal cations are highly dispersed within the layers which results in the formation of a homogeneous dispersion following calcination. The hydrotalcite structure has been shown to allow isomorphous substitution for a range of divalent and trivalent cations which allows the chemical properties of the derived HTc's to be optimised with respect to a particular aim. The objectives of the research detailed here include the substitution of Fe^{II} for Mg^{II} in the parent hydrotalcite structure in order to investigate the activity of the resulting materials for both base and oxidation reactions, following calcination.

The $\text{Mg}_6\text{Al}_2\text{HTc}$ system was used as a basis for the research here because this area has been researched in the past and, as a consequence, offered a good starting point from which to progress into the investigation of the isomorphous substitution of Fe^{II} for Mg^{II} in this structure. Aside from the advantage of having a range of previous studies with which to compare information and results, $\text{Mg}_6\text{Al}_2\text{HTc}$ was a comparable material since the carbonate ion is the interlayer charge neutralising anion. As previously discussed, the carbonate ion is relatively easily incorporated into the structure which would allow the synthesis of this material to be more commercially viable. This anion may also be

thermally released from the structure with a calcination stage which requires heating to a relatively low temperature. This has been shown to yield a material with an even greater surface area/porosity than the precursor HTc *via* the formation of pores in the already relatively high surface area platelet morphology of the HTc.^{1,2}

Two subtly different preparative methods were selected for comparison in the preparation of the $\text{Mg}_6\text{Al}_2\text{HTc}$'s. The first, summarised in Reaction Scheme 7.1 in the Experimental section, was similar to that used by Baird and co-workers in the preparation of CoZnAlHTc 's.³ Essentially, NaHCO_3 was present in a *ca.* 10 % excess with respect to neutralisation of metal (Mg^{II} and Al^{III}) salt counterions (NO_3^-) whilst the NaOH was present in order to increase the pH to the desired value (*ca.* pH 9). This relative ratio of reactants was selected in the preparation of the Fe-containing HTc's reported here, with appropriate adjustments to the proportions of Mg^{II} and Fe^{II} to provide the desired final product stoichiometry. The second preparative method, summarised by Reaction Scheme 7.2 in the Experimental section, was similar to that adopted by Rao and co-workers in the preparation of $\text{Mg}_6\text{Al}_2\text{HTc}$'s for subsequent use as base catalysts for aldol condensations.⁴ The relative proportions of reactants in this procedure were similar to those suggested by Reichle in an earlier well-cited article.⁵ Here, the NaOH was used as the main neutralising agent whilst the Na_2CO_3 was present in a ratio closer to the stoichiometry of CO_3^{2-} in the final product.

The Fe^{III} -containing mineral known as pyroaurite, $\text{Mg}_6\text{Fe}_2\text{HTc}$, was discovered at a similar time as hydrotalcite and has since been found to be isostructural. Consequently, this system is also well represented in the literature.⁶⁻¹⁰ The Fe_6Fe_2 hydroxy-carbonate mixed $\text{Fe}^{\text{II}}/\text{Fe}^{\text{III}}$ valency compound known as green rust has also been observed in nature and has already been described in Chapter 1 since it is subject to further investigation in this thesis; in section 2.2 in particular. Therefore, it is not discussed in any further detail in this section. There has been a very limited amount of investigation into the $\text{Fe}_6\text{Al}_2\text{HTc}$ system previously but this work has not fully explored the range of isomorphous Fe^{II} for Mg^{II} substitution thought to be possible within the structure.^{5, 11, 12, 13} The work detailed in this thesis seeks to address this area with the formation and subsequent characterisation of the materials having idealised formulae of $\text{Mg}_6\text{Al}_2\text{HTc}$, $\text{Mg}_5\text{FeAl}_2\text{HTc}$, $\text{Mg}_4\text{Fe}_2\text{Al}_2\text{HTc}$, $\text{Mg}_3\text{Fe}_3\text{Al}_2\text{HTc}$, $\text{Mg}_2\text{Fe}_4\text{Al}_2\text{HTc}$, $\text{MgFe}_5\text{Al}_2\text{HTc}$ and $\text{Fe}_6\text{Al}_2\text{HTc}$.

N.B.

It should be noted that the Fe^{II} present in the synthesised HTc's rapidly oxidised to Fe^{III} prior to characterisation. This oxidation was evident as a change in colouration from green/blue to orange/brown and occurred as soon as the products were removed from solution. The colour change was initially apparent as an orange coloured surface film on the wet material but became obvious throughout the sample as air penetrated the bulk material upon drying.

2.1.2 Infrared (IR) Spectroscopy

IR spectroscopy was selected here as one of the characterisation techniques for a number of reasons. Perhaps most importantly, it is complementary to the more traditional techniques of mineral characterisation such as X-ray powder diffraction (XRPD) since it can detect the presence of non-crystalline material. Because the technique is reliant upon the absorption of IR radiation by the chemical bonds within the structure, at a characteristic frequency, it has been used here to provide chemical information to complement the structural data produced by XRPD. In the past, for mineralogical samples, IR spectroscopy has been used for specific tasks such as to distinguish between structural hydroxyl groups and water of crystallisation.¹⁴ In HTc's specifically, IR spectroscopy has also been used to provide information regarding the identity of interlayer anion species, such as carbonate, nitrate or sulfate.¹⁵ During the experimental stages of the work described in this thesis, IR spectroscopy was utilised as a means of assessing whether the product washing stage was sufficiently thorough since the presence of nitrate ions (the counterions in preparative stage) would result in a readily identifiable sharp absorption maximum at *ca.* 1384 cm^{-1} due to the characteristically intense NO_3^- asymmetric stretching vibration (ν_3).¹⁶ In addition, because the positions of the absorption bands are sensitive to mass, charge and bonding characteristics of constituent ions, IR can offer information regarding cationic composition. For example, White¹⁷ has discussed the effects of cation substitution on the IR spectra of an isostructural series of carbonates. In general, the substitution of

larger and heavier cations lowers absorption frequencies,¹⁶ as explained by the well established fundamentals of vibrational spectroscopy.¹⁸

The characteristic IR spectrum of hydrotalcite [$\text{Mg}_6\text{Al}_2(\text{OH})_{16}\text{CO}_3 \cdot 4\text{H}_2\text{O}$], both natural and synthetic, has been thoroughly investigated and described in the literature and is discussed here. There appears to be general agreement regarding the origin of the majority of absorption bands, with the exception of some minor differences in opinion regarding the interpretation of some finer points. For this reason, the spectra recorded for the $\text{Mg}_6\text{Al}_2\text{HTc}$ products using the two subtly different preparations (Reaction Schemes 7.1 and 7.2 in the Experimental section, Chapter 7; labelled methods 1 & 2, respectively, in the tables *etc.*) are described in detail. Some of the conflicting views expressed in the literature are summarised and conclusions are drawn. This is followed by an explanation of the differences in spectra through the range of increasing Fe^{2+} for Mg^{2+} substitution, to the product with the idealised formula of $\text{Fe}_6\text{Al}_2\text{HTc}$. The IR absorption bands recorded for each product are summarised in Table 2.1 and some representative spectra are illustrated in Figure 2.1 (a-c).

The strong, fairly broad, band in the region of $3400\text{--}3600\text{ cm}^{-1}$ has been attributed to the stretching vibrations of the structural hydroxyl groups in the brucite-like mixed metal hydroxide layers¹⁰ and those of adsorbed water.¹⁹ The broad shoulder associated with this band, clearly visible at $3000\text{--}3100\text{ cm}^{-1}$, has generally been assigned as a result of hydrogen bonding between water molecules and the incorporated anion within the interlayer.²⁰ Klopogge and Frost have carried out a more detailed band component analysis in which they propose the presence of four bands in this region of the spectrum.²¹ They assign the highest frequency band (at 3597 cm^{-1} in their data) to a hydroxyl group coordinated to a combination of both bivalent and trivalent metals, not clearly assigning it to either metal, there being a shared coordination expected within the structure. At slightly lower frequency (3467 cm^{-1} in their data) there appears to be some confusion since they give reasoning to assign this band to the divalent metal on grounds of relative abundance within the structure, its absorption at this frequency being the most intense, and yet actually assign the major contribution to this band to the Al-OH bond. Logically, it would be expected that the more intense absorption at lower frequency should be attributed to the Mg-OH due to its greater relative abundance, as mentioned by Klopogge and Frost, and that the less intense absorption band at slightly

Table 2.1 HTc infrared absorption bands (cm^{-1}) recorded between 4000 and 400 cm^{-1}

Mg₆Al₂HTc Exptl. method 1	Mg₆Al₂HTc Exptl. method 2	Mg₅FeAl₂HTc	Mg₄Fe₂Al₂HTc	Mg₃Fe₃Al₂HTc	Mg₂Fe₄Al₂HTc	MgFe₅Al₂HTc	Fe₆Al₂HTc
3455 s	3495 s	3452 s	3440 s	3440 s	3430 s	3430 s	3422 s
							3200 m, br
3100 br, shldr	3100 br, shldr	3100 br, shldr	3050 br, shldr	3000 br, shldr	3000 br, shldr	3000 br, shldr	2900 w
1636 m, br	1636 m, br	1636 m, br	1630 m, br	1630 m, br	1630 m/w, br	1630 m/w, br	1630 m/w, br
1525 s, shp							
	1500 w, br	1500 w, br	1500 w, br	1500 w, br	1500 w, br	1500 w, shldr	
1488 s, shp							1438 m, br
1425 s, shp							
1369 s, shp	1375 s, shp	1364 s, shp	1363 m, shp	1364 m	1370 m	1400 w, br	
		900 vw	950 w, br	950 w, br	950 w, br	950 vw, br	904 m
853 m	850 w	850 w, br	850 w	850 w	850 w	866 m	860 m
800 m	750 w	770 m	782 m	778 m	700 m	670 m	796 m
669 m	650 s	662 m	665 m	669 m	600 vw		690 m
		560 vw	568 w	565 w		560 m	560 s
						472 s	492 s

N.B. Formulae are idealised – based on preparative stoichiometry, where HTc = $[(\text{OH})_{16}\text{CO}_3 \cdot 4\text{H}_2\text{O}]$

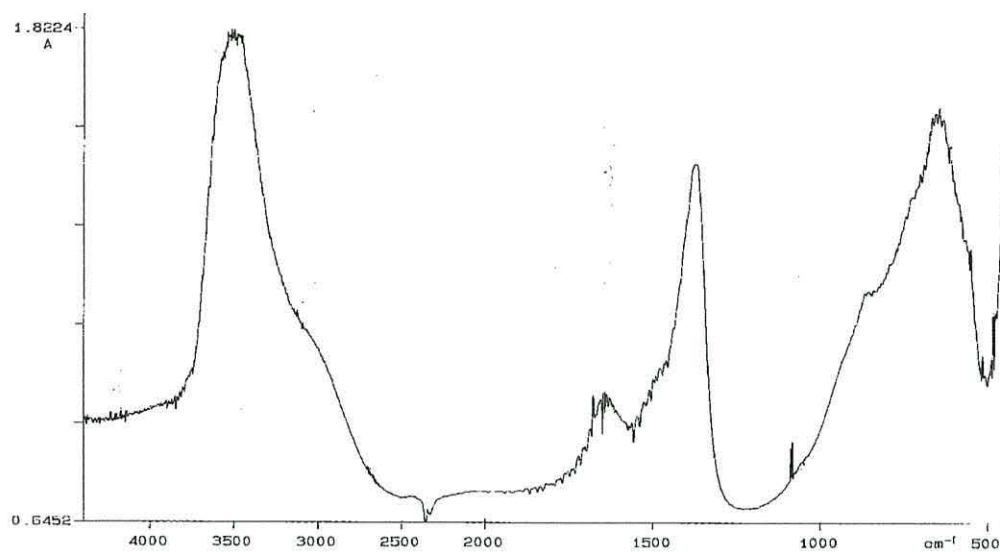


Figure 2.1 (a) IR spectrum of $\text{Mg}_6\text{Al}_2\text{HTc}$ product (Exptl. Method 2)

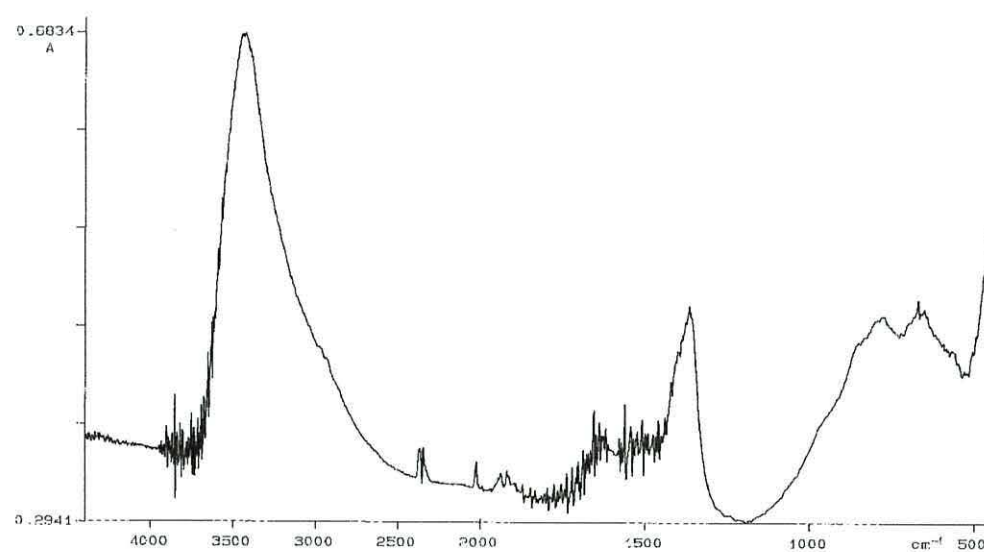


Figure 2.1 (b) IR spectrum of $\text{Mg}_3\text{Fe}_3\text{Al}_2\text{HTc}$ product

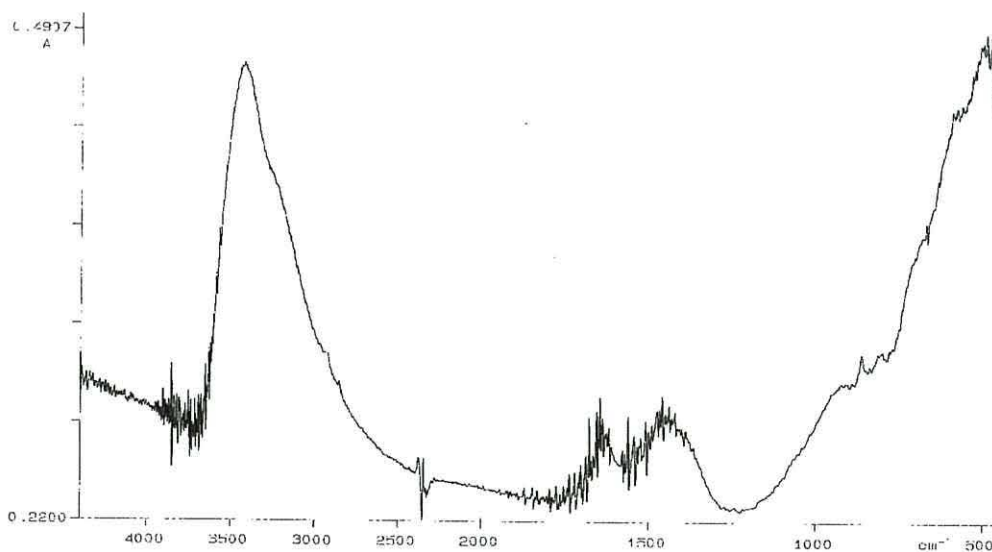


Figure 2.1 (c) IR spectrum of $\text{Fe}_6\text{Al}_2\text{HTc}$ product

higher frequency could be due to the presence of Al-OH within the structure. The greater charge density on the Al^{3+} ions may cause a shift to higher frequency absorption despite its marginally greater mass in comparison with Mg^{2+} .¹⁴ In contrast, IR spectra recorded by Hernandez-Moreno *et al.*²² for MgAlHTc's of $\text{Mg}^{2+}:\text{Al}^{3+}$ ratios of 2:1 and 3:1 showed a shift to lower frequency of the broad M-OH stretching band at *ca.* 3400-3600 cm^{-1} with increased Al substitution *i.e.* $\text{Mg}^{2+}:\text{Al}^{3+}$ of 2:1. This was explained as being a result of a decrease in layer spacing. There was also a smaller half-width for the 2:1 absorption band which was viewed as reflecting a more ordered cation distribution in the structure. As previously discussed, the main constituent of the shoulder at lower frequency (*ca.* 3000-3100 cm^{-1}) has been widely assigned to the CO_3^{2-} - H_2O bridging mode and this view is upheld by Klopogge and Frost but they also assigned a band at a slightly higher frequency, only evident using band component analysis peak fitting software, solely to hydrogen bonded interlayer water which results in an amalgamation of the peaks. The hydrogen bonding expected within the structure is depicted in Figure 2.2.

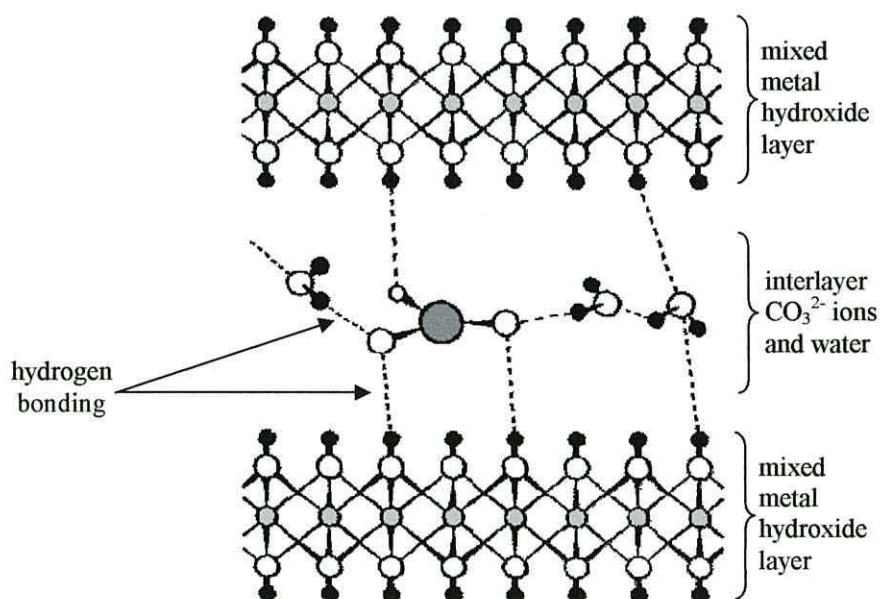


Figure 2.2 Hydrogen bonding in the interlayer region, adapted from Carlino¹

The relatively weak, broad band which was consistently centred around 1636 cm^{-1} has generally been attributed to the deformation band of adsorbed¹⁹ and interlayer¹⁰ water; the intensity varying according to the type of anion and amount of interlayer water.

The interlayer carbonate ions in the HTc structure would be expected to have six (3N-6) fundamental vibrations.²³ These are illustrated in Figure 2.3. The unperturbed carbonate ion has D_{3h} symmetry,¹⁷ which, in theory, has three IR active bands *viz.* ν_2 , ν_3 and ν_4 , since ν_3 and ν_4 are degenerate and ν_1 is IR inactive as there is no change in dipole moment during that particular molecular vibration. The absorption bands correlating to these vibrations have previously been found to occur at 1350-1380 cm^{-1} (ν_3), 850-880 cm^{-1} (ν_2) and 670-690 cm^{-1} (ν_4) in HTc's.^{10, 22, 24} These absorption maxima were observed in the spectra recorded for both $\text{Mg}_6\text{Al}_2\text{HTc}$ products (Table 2.1) obtained using the two subtly different preparative procedures (see Reaction Schemes 7.1 and 7.2). However, the IR spectrum recorded for the $\text{Mg}_6\text{Al}_2\text{HTc}$ using preparative method 1 (Reaction Scheme 7.1) also had three additional bands in the 1425-1525 cm^{-1} region. Bish and Brindley²⁵ observed splitting of the degenerate ν_3 vibrations to give two bands at 1350 and 1390 cm^{-1} for takovites (nickel aluminium hydroxy-carbonates) which they proposed was due to a lowering of symmetry of the carbonate ion. Serna *et al.* also observed an apparent splitting of the carbonate ν_3 vibration to produce two bands at 1360 and 1400 cm^{-1} when their natural hydrotalcite sample was evacuated and they attributed this to an interaction of interlayer carbonate with the Mg-Al sheets.²⁶ It appears that what both Bish and Brindley and Serna *et al.* proposed is that the carbonate adopts C_{2v} symmetry, presumably due to bidentate coordination to the mixed metal hydroxide layers, which would result in splitting of the degenerate ν_3 vibration.²³ It would also result in the splitting of the degenerate ν_4 vibration and the appearance of the previously inactive ν_1 vibration but the presence of these bands was not highlighted, presumably because they were not observed. Although the ν_1 vibration would be expected at *ca.* 1050 cm^{-1} ,^{10, 22} the absorption band may be weak, as may some of the other vibrations which would become active in the transition from D_{3h} to C_{2v} carbonate symmetry *e.g.* only minimal splitting (up to *ca.* 50 cm^{-1}) of the ν_3 carbonate vibration has been observed.²² However, since there were three additional bands observed for the $\text{Mg}_6\text{Al}_2\text{HTc}$ prepared using preparative method 1, quite separate from the band at 1369 cm^{-1} , it is suspected that they are indicative of carbonate in a quite different environment rather than just exhibiting a change in coordination. Coupled with the data from the XRPD patterns discussed in the next section, the IR spectrum of this product suggests the presence of hydromagnesite (as a minor phase in addition to hydrotalcite as the major component) which is reported as having three IR active bands in this region

due to carbonate.¹⁷ This is due to its quite different structural arrangement in hydromagnesite in which the carbonate is reported to have D_2 symmetry.¹⁷ The weak, broad absorption band at *ca.* 1500 cm^{-1} in the spectrum of $\text{Mg}_6\text{Al}_2\text{HTc}$ produced using preparative method 2 has previously been interpreted to indicate the presence of amorphous aluminium hydroxycarbonate.¹⁹ This was borne in mind during characterisation and Energy-Dispersive Analysis of X-rays (EDAX) was used to investigate this possibility during the Scanning Electron Microscopy (SEM) analysis (Section 2.1.4).

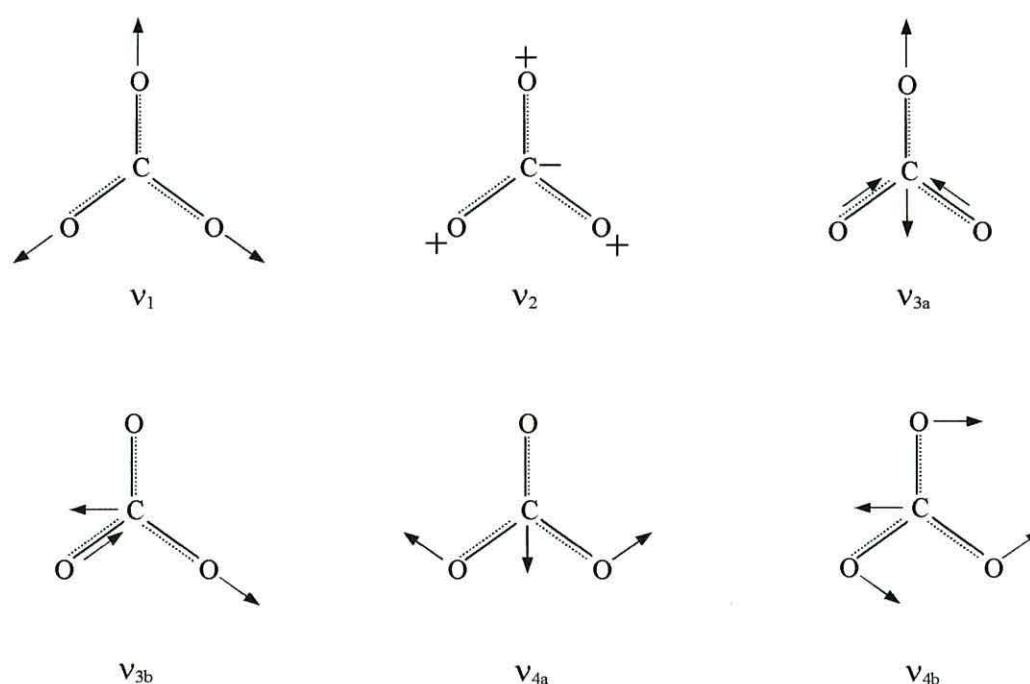


Figure 2.3 Fundamental vibrations of the carbonate ion, after Farmer and Lazarev²⁷

Due to the poor resolution observed in the $1000\text{--}400\text{ cm}^{-1}$ region, it is difficult to draw any definite conclusions regarding the exact nature of the bands for the spectra obtained. However, other than the v_2 ($850\text{--}880\text{ cm}^{-1}$) and v_4 ($670\text{--}690\text{ cm}^{-1}$) carbonate vibrations, the absorption bands within this region have previously been attributed to skeletal metal cation-oxygen vibrations.^{10, 24}

The spectra recorded for the products $\text{Mg}_5\text{FeAl}_2\text{HTc}$ to $\text{Mg}_2\text{Fe}_4\text{Al}_2\text{HTc}$ showed absorption bands of similar intensities and frequency positions to those recorded for the

Mg₆Al₂HTc's, especially when compared with the product prepared using preparative method 2 (Reaction Scheme 7.2). However, a gradual trend was observed in the spectra for a reduction in intensity of the ν_3 carbonate vibration at *ca.* 1360-1375 cm⁻¹ and a (less obvious) decrease in intensity of the bands below 1000 cm⁻¹, with increasing Fe for Mg substitution. Possible reasons for a decrease in intensity of carbonate absorption bands in the spectra may be due to a decrease in charge density on the metal hydroxide layers resulting in a decrease in carbonate required to compensate for charge imbalance or there may have been a reduced amount of HTc's or other carbonates in the reaction product. The first option appears unlikely since the synthesised Fe²⁺-containing materials should require similar levels of carbonate ions for charge compensation as Mg²⁺-containing products and, even once oxidised, the Fe³⁺ would then require an increased level of carbonate ions in order to neutralise the charge on the overall structure. The second option, therefore, appears to be more likely – other non-carbonate materials formed in addition to some HTc's as reaction products – but the additional phases were not obviously present in these IR spectra. A second, more subtle change in the spectra, was the gradual decrease in frequency at which the M-OH stretching vibration occurred in the 3400-3500 cm⁻¹ region, also through the sequence of increasing Fe for Mg substitution. As previously discussed, Hernandez-Moreno *et al.*²² noted a similar change when spectra of HTc's with various compositions were recorded. They observed that compounds with an octahedral M^{II}/M^{III} relationship of 2/1 could be differentiated from those with M^{II}/M^{III} of 3/1 by the higher vibrational frequencies for the M-OH stretching motion in the latter. They explained this change as being due to the change in interlayer spacing brought about by the change in charge on the metal hydroxide layers. In the same way, the gradual decrease in frequency of this band recorded for the MgFeAlHTc samples could be due to the increase in layer charge due to the presence of Fe³⁺ (oxidised Fe²⁺) in addition to Al³⁺, resulting in a decrease in the basal spacing of the layers. If this were the case, however, an increase in the quantity of interlayer carbonate necessary to neutralise the overall charge in the structure would be expected, accompanied by an increase in intensity of the carbonate absorption bands. Since a decrease in intensity of the carbonate bands was observed, this observation reinforces the theory that there was less HTc product formed. There may still have been an increase in quantity of interlayer carbonate per mole of HTc product but less of the desired HTc product formed overall.

The spectra recorded for the $\text{MgFe}_5\text{Al}_2\text{HTc}$ and $\text{Fe}_6\text{Al}_2\text{HTc}$ products were more indicative of the formation of iron oxides. The band at *ca.* 3400 cm^{-1} (in both) was ascribed to the presence of hydroxyl groups, as for the HTc's described previously. However, evidence of an additional band at *ca.* 3200 cm^{-1} was observed only in the $\text{Fe}_6\text{Al}_2\text{HTc}$ spectrum which was similar in position to that recorded by Schwertmann and Cornell for goethite ($\alpha\text{-FeOOH}$) and lepidocrocite ($\gamma\text{-FeOOH}$) which they attributed to the bulk hydroxyl groups in these materials.²⁸ There was a weak H_2O deformation band evident at *ca.* 1630 cm^{-1} and an absorption band at 1438 cm^{-1} in $\text{Fe}_6\text{Al}_2\text{HTc}$ which was indicative of the presence of carbonate ions. The latter absorption band was, however, weaker and much broader than that observed for the HTc's with lower Fe contents and also occurred at a higher frequency. This broadening and shift to a higher frequency resulted in a band indicative of the presence of a carbonate such as siderite (FeCO_3).¹⁷ The other bands commonly associated with this material, at *ca.* 661 and 734 cm^{-1} were not observed but the presence of a carbonate with this structural arrangement could not be discounted as the region below 1000 cm^{-1} was poorly resolved. However, the bands at *ca.* 796 and 904 cm^{-1} have been attributed to the M-OH bends in goethite by Schwertmann.²⁹ Overall, the greatest similarity with the literature spectra, especially for the $\text{Fe}_6\text{Al}_2\text{HTc}$ product, was with that of aluminium-substituted goethite synthesised by Schwertmann and Cornell at room temperature from an FeCl_2 solution.²⁹

2.1.3 X-ray Powder Diffraction

X-ray powder diffraction (XRPD) has been widely used since the early 1920's as a tool for the identification and analysis of clay minerals.³⁰ In contrast to IR spectroscopy which is sensitive to short-range atomic arrangements, XRPD is sensitive to long-range periodic arrangements of atoms in a crystal lattice.¹⁶ Due to the nature of the structural information obtained from this technique it has been recognised as the primary method for characterisation of clay minerals and is applied here in the characterisation of HTc's and iron oxides.

The XRPD patterns of HTc's have been reported as being difficult to analyse, often due to their low crystallinity which can result in diffraction lines which are broad and asymmetric.¹⁰ In addition, the disorder which can be present in the stacking of the layers can lower the symmetry and, therefore, result in variations in the relative intensities of the lines. Despite these problems, XRPD is still a powerful tool in the physical characterisation of HTc's and an arguable advantage of these factors is the production of highly characteristic XRPD patterns. The data from the patterns recorded for all the HTc's synthesised are reported in Table 2.2a, together with the Joint Committee on Powder Diffraction Standards (JCPDS) reference pattern of hydrotalcite.³¹ Some additional relevant reference patterns are also displayed in Table 2.2b for comparison. The actual patterns recorded for the synthesised HTc's are shown one above the other in Figure 2.4 as a visual aid; the $\text{Mg}_6\text{Al}_2\text{HTc}$'s in the lower region (the product formed using preparative method 1 at the bottom, followed by the product of preparative method 2 slightly above), moving through the series of increasing Fe^{2+} for Mg^{2+} substitution to the product with the idealised formula $\text{Fe}_6\text{Al}_2\text{HTc}$ at the top of the illustration. The [003] and [110] reflections have been labelled for the lower $\text{Mg}_6\text{Al}_2\text{HTc}$ pattern (the significance of these peaks is explained later).

The patterns recorded for the $\text{Mg}_6\text{Al}_2\text{HTc}$'s produced by both preparative methods 1 & 2 displayed the main diffraction lines of the JCPDS standard reference pattern for hydrotalcite. The peak at *ca.* 7.69 Å is known as the basal reflection since it is equivalent to c' , the basal spacing, which is the sum of the thickness of one mixed metal hydroxide layer (brucite-like sheet) plus the interlayer or 'gallery' height,¹⁰ as shown in Figure 2.5. The actual HTc unit cell parameters are given by a and c . The unit cell parameter c is dependent upon the layer stacking sequence and is a three-fold multiple of c' for hydrotalcite since it has rhombohedral symmetry (discussed in Section 1.5.1) whereas c would be a two-fold multiple of c' for manasseite, the hexagonal analogue of hydrotalcite, and other HTc's with hexagonal symmetry. The parameter c' (and therefore c) is mainly dependent upon the size of the interlayer anion and the charge upon the brucite-like layers.¹⁰ The thickness of these sheets is generally reported to be *ca.* 4.8 Å^{32, 33, 34} and the thickness of the planar carbonate ion is regarded to be *ca.* 2.8 Å³⁵ (the approximate diameter of the O^{2-} ion). The resulting distance of *ca.* 7.6 Å equates to a basal spacing of the order of those recorded for the $\text{Mg}_6\text{Al}_2\text{HTc}$'s in Table 2.2a. This correlates with the incorporation of carbonate ions within the structure

Table 2.2a X-ray powder diffraction d-spacing results (Å) for HTc's (relative intensities in parentheses)

Hydrotalcite ³¹ Mg ₆ Al ₂ HTc	Mg ₆ Al ₂ HTc (method 1)	Mg ₆ Al ₂ HTc (method 2)	Mg ₅ FeAl ₂ HTc	Mg ₄ Fe ₂ Al ₂ HTc	Mg ₃ Fe ₃ Al ₂ HTc	Mg ₂ Fe ₄ Al ₂ HTc	MgFe ₅ Al ₂ HTc	Fe ₆ Al ₂ HTc
7.69 (100)	7.71 (100)	7.76 (100)	7.63 (100)	7.60 (100)	7.53 (100)	7.40 (100)	7.29 (100)	7.25 (15)
	5.81 (9)							
							4.85 (5)	4.87 (10)
	4.46 (3)							
	4.19 (6)							4.19 (100)
3.88 (70)	3.86 (45)	3.89 (47)	3.79 (43)	3.79 (39)	3.76 (35)	3.73 (24)	3.67 (20)	
							3.60 (23)	3.60 (15)
								3.37 (13)
	3.28 (2)						3.27 (8)	
	3.14 (3)						3.12 (8)	
	2.90 (6)					2.97 (10)	2.97 (25)	2.97 (24)
			2.76 (2)	2.78 (3)		2.80 (16)	2.79 (86)	2.80 (68)
								2.68 (44)
2.58 (20)	2.58 (35)	2.60 (36)	2.57 (44)	2.58 (38)	2.56 (43)	2.59 (29)		
						2.53 (69)	2.53 (100)	2.53 (93)
							2.49 (60)	2.43 (78)
							2.35 (25)	2.35 (19)
2.30 (20)	2.30 (18)	2.33 (14)	2.29 (23)	2.29 (18)	2.28 (19)	2.24 (26)	2.23 (36)	2.23 (51)
								2.17 (31)
	2.16 (6)		2.11 (2)	2.13 (2)		2.13 (6)	2.13 (22)	2.14 (19)
						2.09 (4)	2.10 (15)	2.10 (14)
	2.03 (9)		2.03 (4)	2.03 (2)	2.03 (3)	2.03 (3)	2.03 (11)	2.03 (7)
1.96 (20)	1.95 (13)	1.98 (9)	1.94 (18)	1.94 (14)	1.93 (13)	1.92 (10)	1.97 (13)	1.97 (12)
								1.80 (7)
1.75 (10)	1.73 (2)		1.72 (3)	1.72 (3)	1.71 (3)	1.72 (4)	1.73 (19)	1.73 (17)
								1.71 (39)
								1.68 (12)
1.65 (10)	1.64 (1)		1.63 (1)	1.63 (1)	1.61 (1)	1.61 (5)	1.61 (11)	1.61 (14)
								1.55 (15)
1.53 (20)	1.53 (18)	1.53 (21)	1.52 (16)	1.53 (16)	1.52 (16)	1.50 (18)	1.50 (16)	1.50 (13)
1.50 (20)	1.50 (15)	1.50 (18)	1.49 (14)	1.49 (14)	1.49 (13)	1.49 (15)		1.48 (30)

Table 2.2b Literature values of X-ray powder diffraction d-spacings (Å) (relative intensities in parentheses) for reference materials

Hydrotalcite ³¹ $\text{Mg}_6\text{Al}_2(\text{OH})_{16}\text{CO}_3 \cdot 4\text{H}_2\text{O}$	Hydromagnesite ³⁶ $\text{Mg}_5(\text{CO}_3)_4(\text{OH})_2 \cdot 4\text{H}_2\text{O}$	Siderite ^{37, 38} FeCO_3	Magnesioferrite ³⁹ MgFe_2O_4	Magnetite ⁴⁰ Fe_3O_4	Goethite ⁴¹ FeOOH	Feroxyhyte ⁴² FeOOH
7.69 (100)						
	5.79 (100)					
			4.83 (5)	4.85 (40)	4.97 (60)	4.95 (100)
	4.46 (17)					
	4.18 (30)				4.18 (100)	
3.88 (70)						
		3.59 (25, 60)				
					3.36 (60)	
	3.32 (30) / 3.21 (16)					3.21 (60)
	3.14 (20)					
	2.90 (80)		2.97 (50)	2.97 (70)		2.94 (80)
		2.79 (100, 100)				2.82 (50) / 2.76 (50)
	2.69 (25)				2.69 (70)	2.67 (50)
2.58 (20)					2.58 (55)	2.55 (40)
			2.53 (100)	2.53 (100)		
	2.50 (20)				2.48 (40)	2.47 (40)
	2.35 (14)	2.35 (20, 50)		2.42 (10)	2.44 (80)	2.41 (40)
2.30 (20)	2.30 (35)				2.30 (10) / 2.25 (60)	2.37 (50) / 2.26 (50)
	2.16 (20) / 2.15 (25)				2.18 (30)	2.24 (50) / 2.18 (30)
	2.15 (19) / 2.14 (12)	2.13 (25, 60)			2.14 (10)	2.12 (30)
			2.09 (50)	2.10 (70)	2.09 (15)	2.06 (10)
					2.01 (20)	2.01 (10) / 1.99 (20)
1.96 (20)	1.99 (25) / 1.99 (19)	1.96 (30, 60)			1.92 (40)	1.93 (30) / 1.90 (30)
		1.80 (16, 50)			1.80 (50)	1.84 (30)
1.75 (10)		1.74 (45, 80)	1.71 (30)	1.71 (60)	1.77 (30) / 1.72 (70)	
					1.69 (50)	1.70 (20)
					1.66 (40)	1.66 (20)
1.65 (10)			1.61 (70)	1.61 (85)	1.60 (50)	1.62 (20) / 1.61 (10)
					1.56 (65)	1.55 (10)
1.53 (20)		1.53 (0, 20)				1.52 (10)
1.50 (20)		1.51 (20, 60)	1.48 (90)	1.48 (85)	1.51 (60)	1.47 (40)

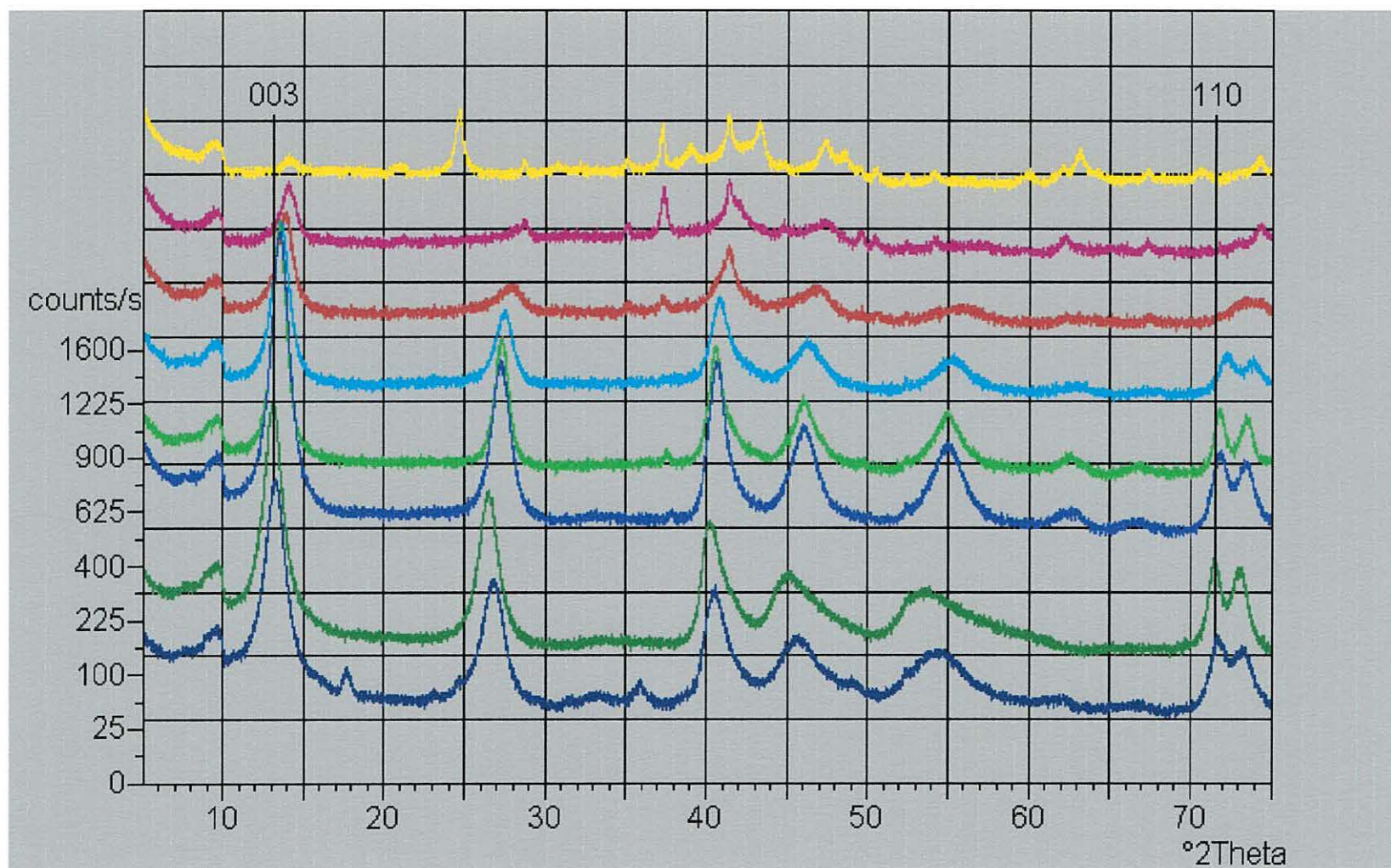


Figure 2.4 A comparison of the recorded HTc XRPD patterns across the range of $\text{Mg}_6\text{Al}_2\text{HTc}$ to $\text{Fe}_6\text{Al}_2\text{HTc}$

as opposed to the possible alternatives with this preparative method, hydroxide or nitrate ions, which would result in slightly lower or higher basal spacings, respectively.⁴³ Looking at the higher 2θ value end of the diffraction patterns, the unit cell parameter a has previously been calculated from the [110] reflection of HTc's as being twice this value.²⁰ The calculated figure for the $\text{Mg}_6\text{Al}_2\text{HTc}$'s in Table 2.2a is, therefore, 3.06 Å which correlates with literature values.^{10, 20} This value of a represents the separation of metal hydroxide centres in the plane of the brucite-like sheets and is dependent upon the nature of the cations.¹⁰ This will be discussed in further detail for the Fe-substituted HTc's. Overall, the patterns recorded for the $\text{Mg}_6\text{Al}_2\text{HTc}$'s were concordant with the literature patterns for hydrotalcite with exception of the presence of a minor hydromagnesite phase in the material formed using method 1. The hydromagnesite material did not appear to be present as a crystalline phase to any significant degree, as illustrated by the strongest peak at *ca.* 5.8 Å which is only approximately one-tenth of the height of the strongest hydrotalcite peak at *ca.* 7.7 Å.

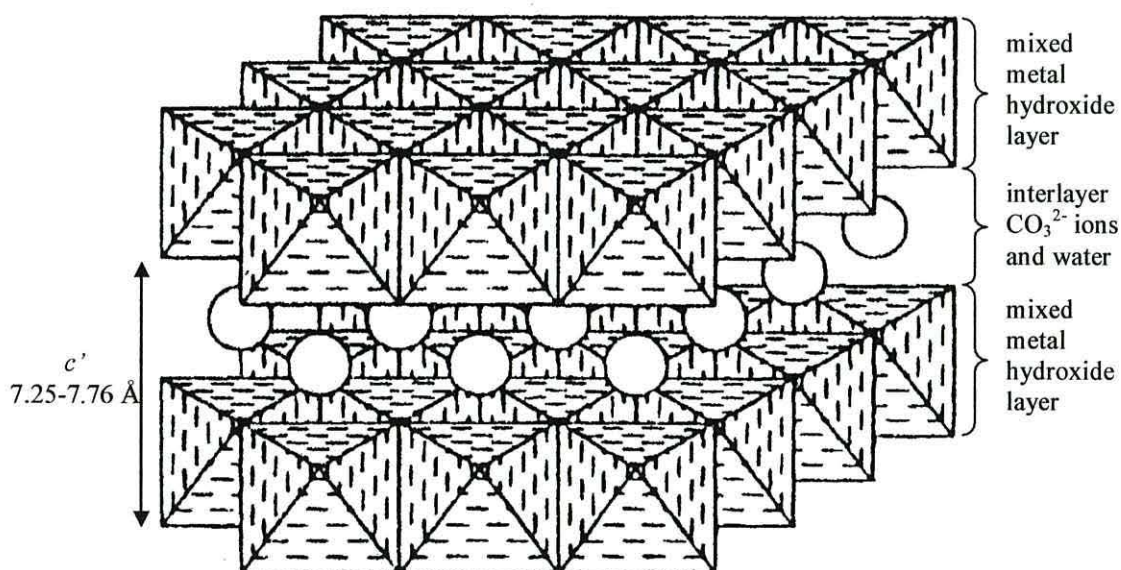


Figure 2.5 Origin of the basal spacing, c' , in HTc's, adapted from Köckerling *et al.*⁴⁴ to show the range of basal spacings recorded for the synthesised HTc products shown in Table 2.2a.

The first detailed discussion of XRPD patterns of HTc's was published by Gastuche *et al.*⁴⁵ This paper, which contrasts the patterns recorded for natural and synthetic HTc's, details the commonly reported Miller indices for the main reflections. It is quite clear from these results and later reports^{20, 24} that the identities of the major

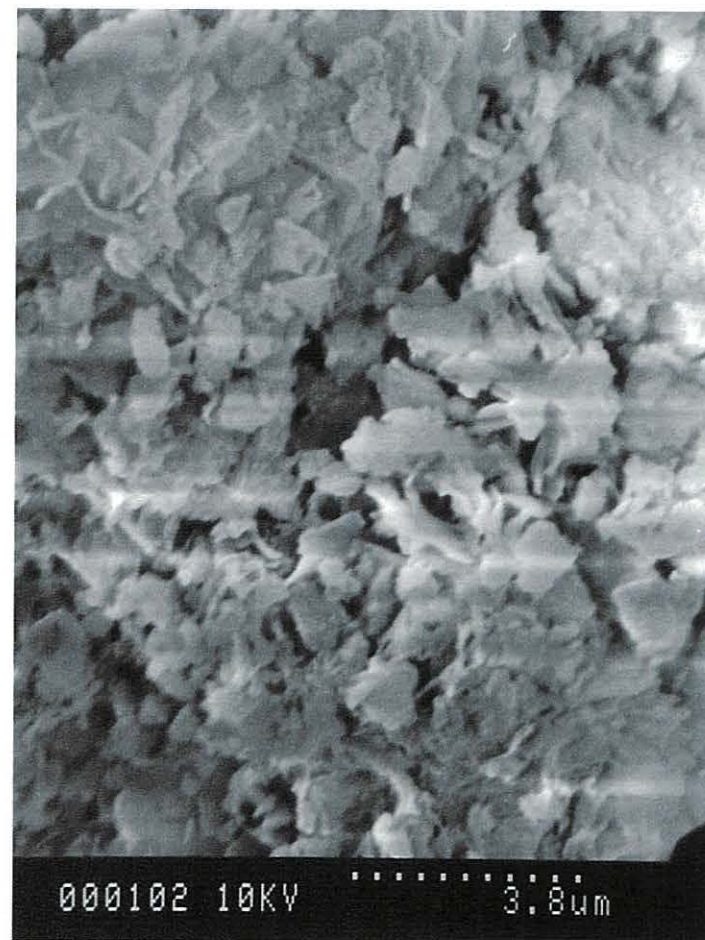
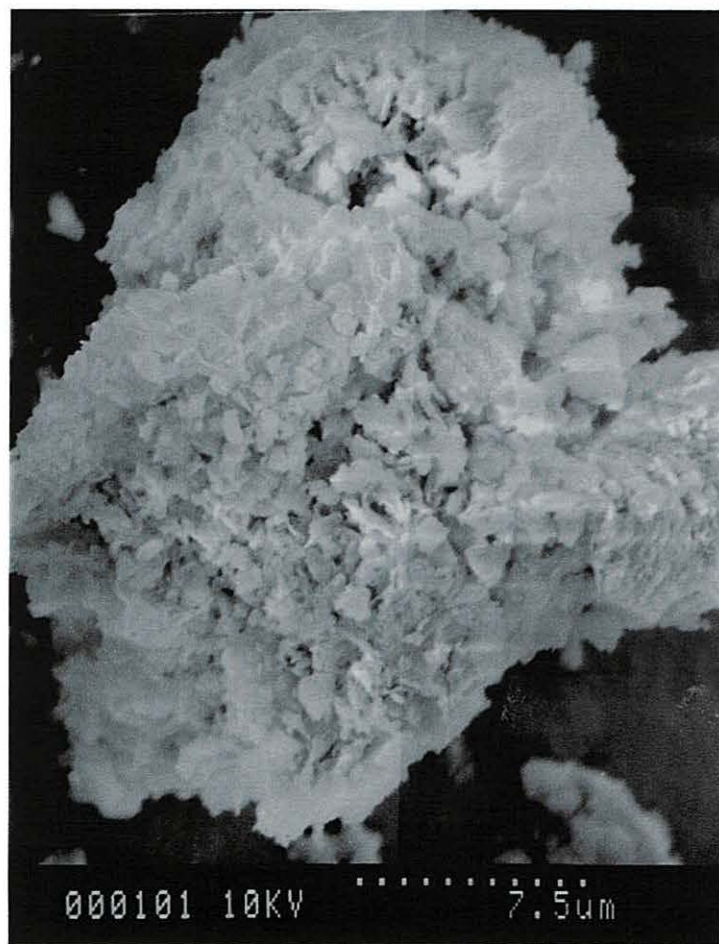
peaks are as follows (d-spacings taken from JCPDS reference pattern 14-0191 for hydrotalcite); 7.69 Å [003], 3.88 Å [006], 2.58 Å [009] and [012], 2.30 Å [015], 1.96 Å [018], 1.53 Å [110] and 1.50 Å [113]. Of these, the [012], [015] and [018] reflections were reported to show the greatest asymmetry²⁰ but the asymmetric appearance of the peak at 2.58 Å has also been attributed to overlap of the [009] and [018] reflections.²⁴

The characteristic hydrotalcite XRPD pattern is clearly identifiable in all Fe-containing HTc's recorded in Table 2.2a, except perhaps for the Fe₆Al₂HTc product, the recorded pattern of which indicates the presence of a number of additional peaks. One key trend shows a very gradual decrease in intensity of the peaks which correlate to the hydrotalcite pattern. However, any additional phases present are minor with the exception of the MgFe₅Al₂HTc and Fe₆Al₂HTc products. They exhibit a wider range of peaks due to the presence of siderite (FeCO₃), magnetite (Fe₃O₄) or an isostructural compound such as magnesioferrite (MgFe₂O₄) and goethite (α-FeOOH) or the isostructural Al-substituted goethite. Two further trends exhibited across the series of products, with increasing Fe for Mg substitution, are the gradual decrease in basal spacing from 7.76 Å to 7.25 Å and a less obvious decrease in the unit cell parameter *a* (calculated from the [110] reflection at *ca.* 1.53 Å). The decrease in basal spacing is consistent with an increase in layer charge due to Fe³⁺ for Mg²⁺ substitution (Fe³⁺ resulting from oxidation of Fe²⁺ prior to analysis). This decrease was previously reported by Brown and Gastuche for HTc's synthesised with high Al:Mg ratios since it results in increased electrostatic attraction between the layers.⁴⁶ In the same paper, a decrease in the metal-metal distance within the sheets, given by unit cell parameter *a*, was also observed as the proportion of Al³⁺ increased which has been attributed to the reduced size of the Al³⁺ ionic radius (0.54 Å) over that of Mg²⁺ (0.72 Å). A similar effect would therefore be expected in these Fe-substituted HTc's since the ionic radius of Fe³⁺ (0.65 Å) is also smaller than that of Mg²⁺.⁴⁷ However, the extent of the decrease for the Fe-containing HTc's was greater than that observed by Brown and Gastuche which can be explained by the greater final ratio of M³⁺ to M²⁺ in the HTc's containing Fe³⁺ (oxidised from Fe²⁺) rather than Mg²⁺, in addition to the Al³⁺.

2.1.4 Scanning Electron Microscopy and Energy-Dispersive Analysis of X-rays

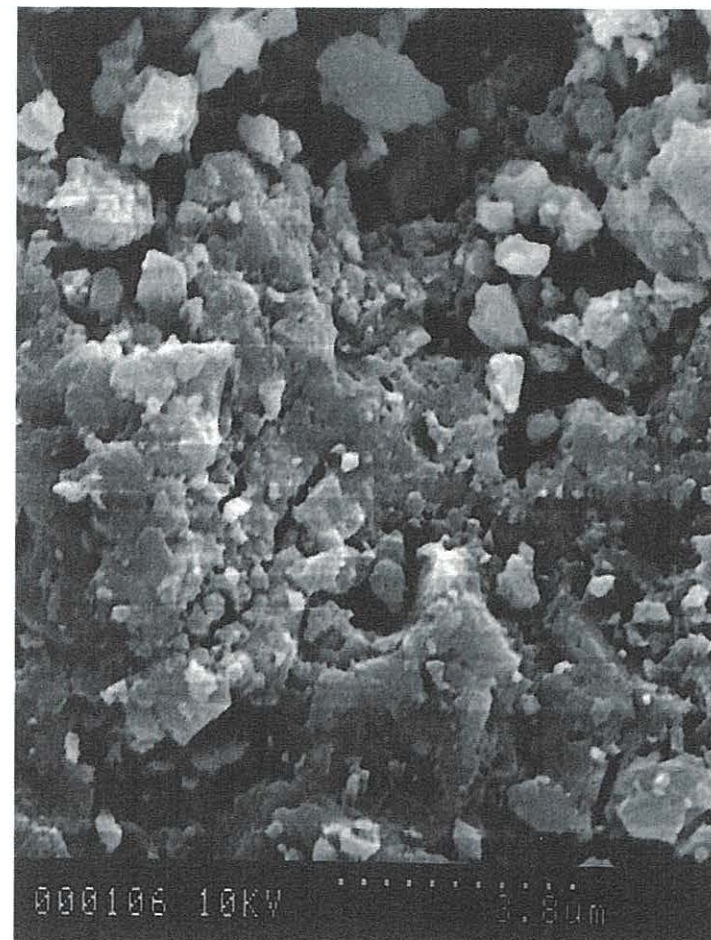
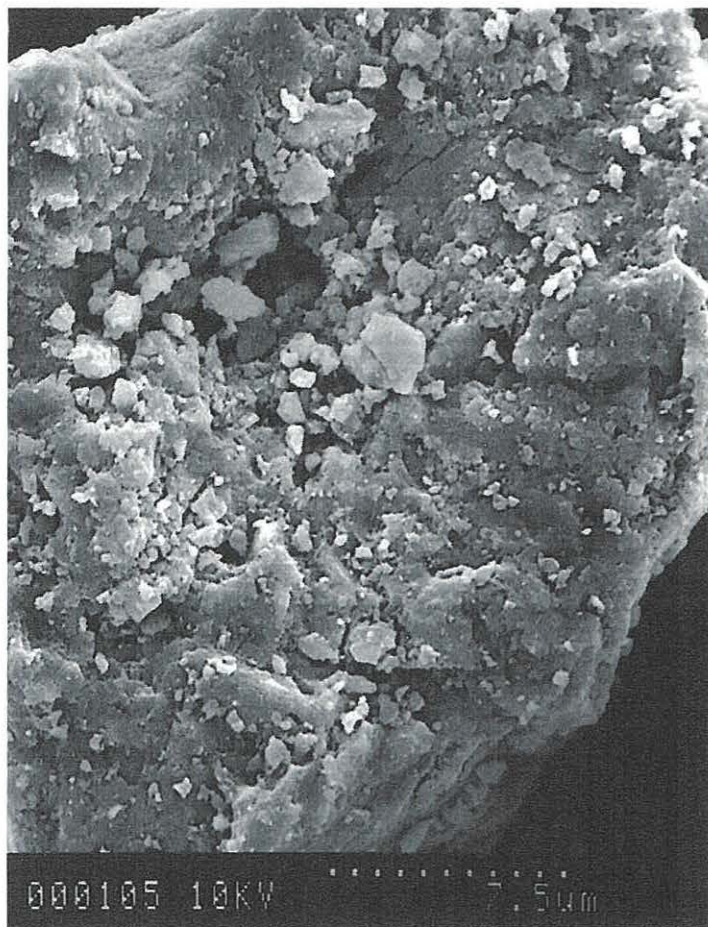
Scanning electron microscopy (SEM) provides information about the surface microtopography and general morphology of materials, which is critical in the study of catalysts. Direct observation of the sample morphology was combined with elemental analysis using energy-dispersive analysis of X-rays (EDAX) in order to analyse the homogeneity, or otherwise, of the samples. The advantage of EDAX over bulk elemental analysis techniques is the ability to focus on small, targeted areas of the material when viewed in the electron microscope. This results in spectra specific to the selected structural features observed.

Example micrographs of each of the HTc products are illustrated in Figures 2.6-2.13. The micrographs were chosen to reflect the typical sample morphology of the reaction product and are shown at comparable scale for each sample. The general morphology observed was plate-like, as expected for HTc's, reflecting the layered structure.^{48, 49} The platelets were up to *ca.* 2 μm across for the $\text{Mg}_6\text{Al}_2\text{HTc}$'s and gradually reduced in size, also becoming thinner, as the amount of Fe for Mg substitution increased. At the far end of the substitution spectrum, the small, fine crystals observed for the $\text{Fe}_6\text{Al}_2\text{HTc}$ were more typical of the morphology of an Al-substituted goethite formed under the synthesis conditions employed *i.e.* they were much smaller and less well developed than for unsubstituted goethites formed from alkaline Fe^{III} solutions.²⁸ Consequently, there appeared to be little or no evidence of material with markedly different morphologies within any of the individual compounds, such as the more elongated blade-like structure which would be expected of siderite.⁵⁰ However, the morphology of hydromagnesite, for example, has been reported to be similar to that of hydrotalcite and could have been present.¹⁹ EDAX analysis was, therefore, employed both over selected areas of the sample and at random points across the sample in order to attempt to identify the presence of mineral phases other than those of the HTc's. The results of this analysis are summarised in Table 2.3 (though it should be noted that this technique, as employed in this thesis, is indicative of the relative ratios of elements rather than being fully quantitative).



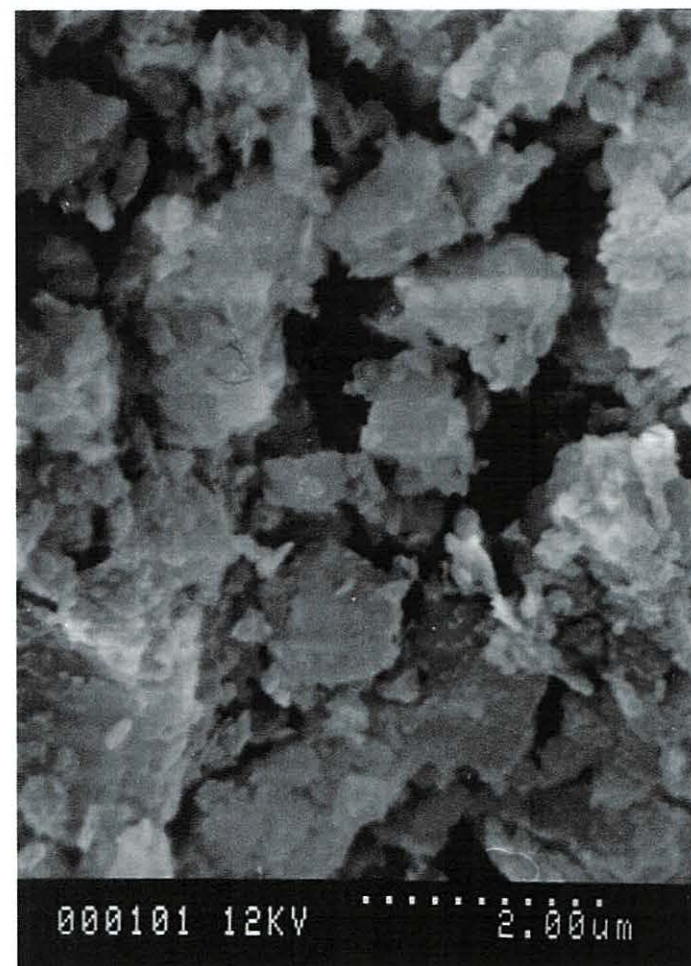
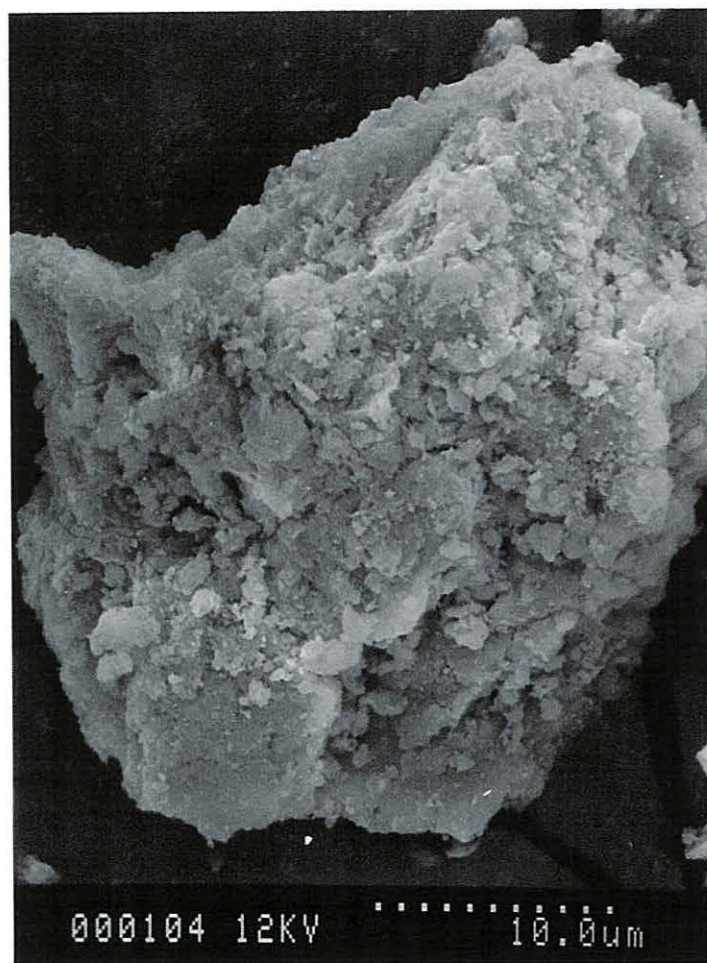
Figures 2.6 (a) & (b): SEM's of $\text{Mg}_6\text{Al}_2\text{HTc}$ product formed using preparative method 1

N.B. Scale bar is represented at the bottom of each micrograph as a series of dots (approximate length $\blacklozenge \text{-----} \blacklozenge$) with the scale below



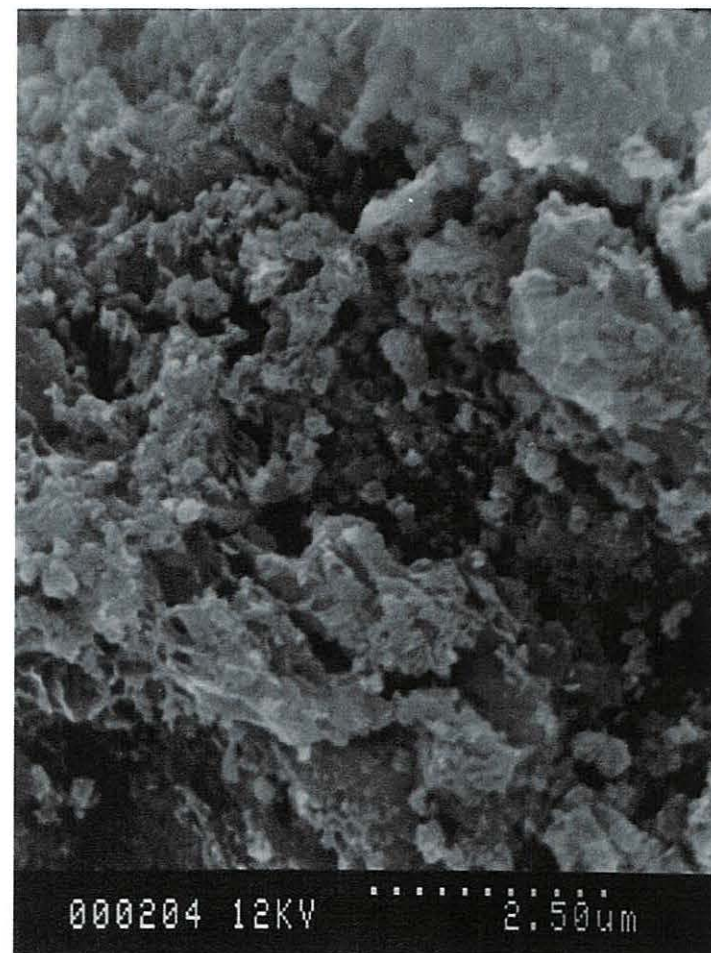
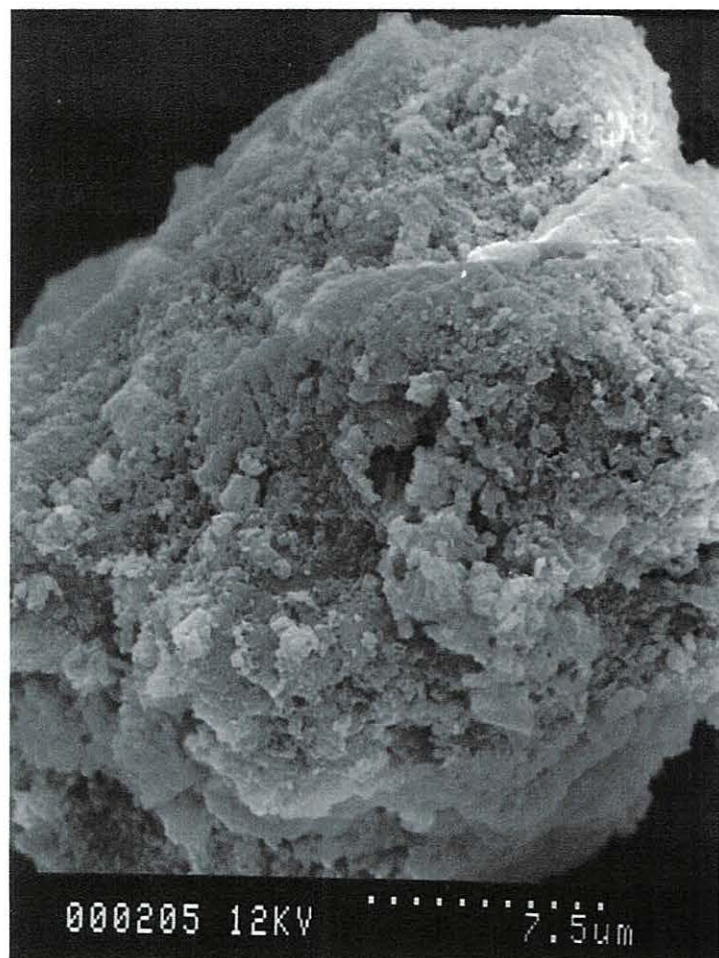
Figures 2.7 (a) & (b): SEM's of $\text{Mg}_6\text{Al}_2\text{HTc}$ product formed using preparative method 2

N.B. Scale bar is represented at the bottom of each micrograph as a series of dots (approximate length $\blacklozenge \longrightarrow \blacklozenge$) with the scale below



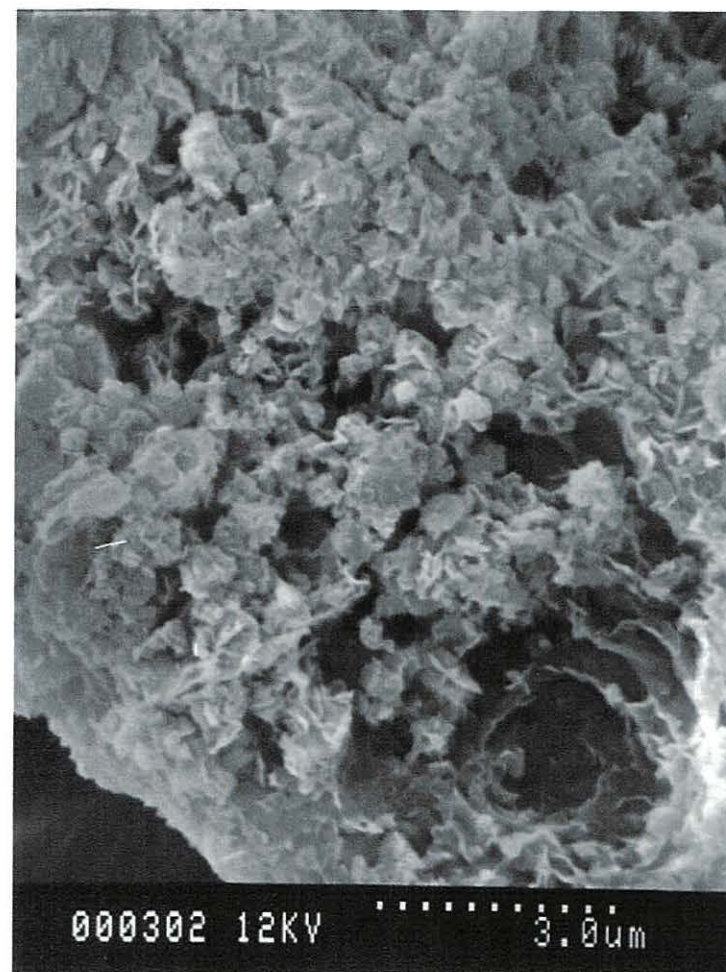
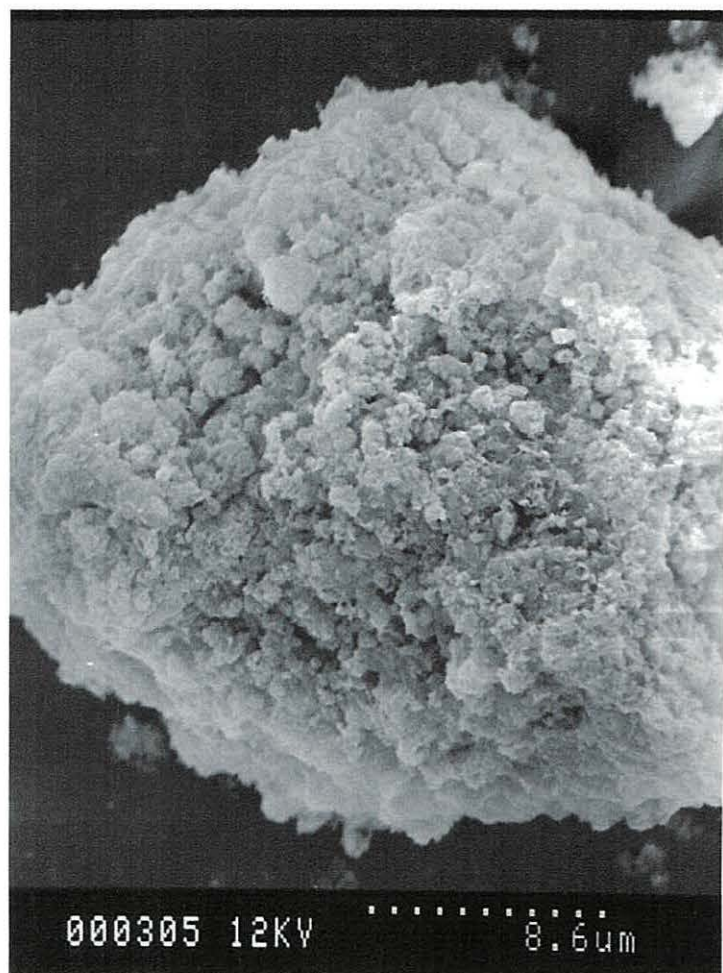
Figures 2.8 (a) & (b): SEM's of $\text{Mg}_5\text{FeAl}_2\text{HTc}$ product

N.B. Scale bar is represented at the bottom of each micrograph as a series of dots (approximate length $\blacklozenge \text{-----} \blacklozenge$) with the scale below



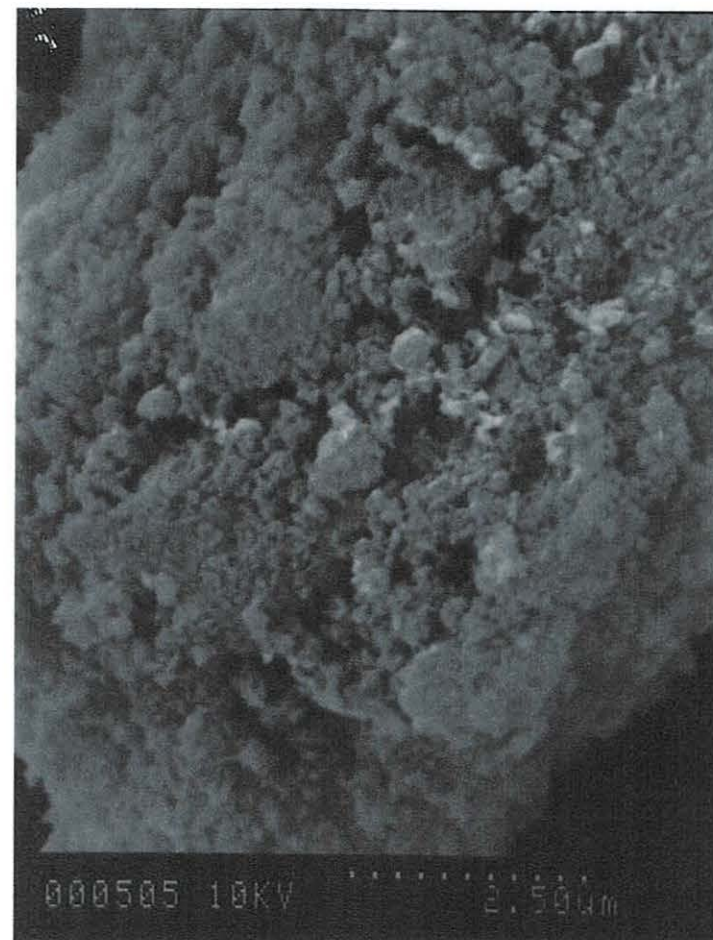
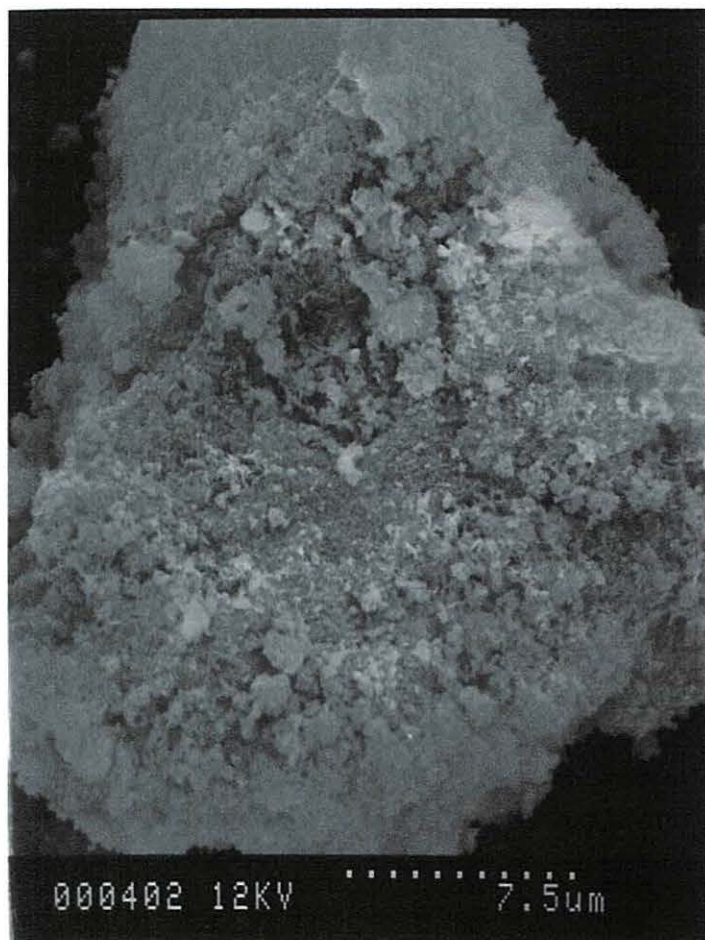
Figures 2.9 (a) & (b): SEM's of $\text{Mg}_4\text{Fe}_2\text{Al}_2\text{HTc}$ product

N.B. Scale bar is represented at the bottom of each micrograph as a series of dots (approximate length $\blacklozenge \longrightarrow \blacklozenge$) with the scale below



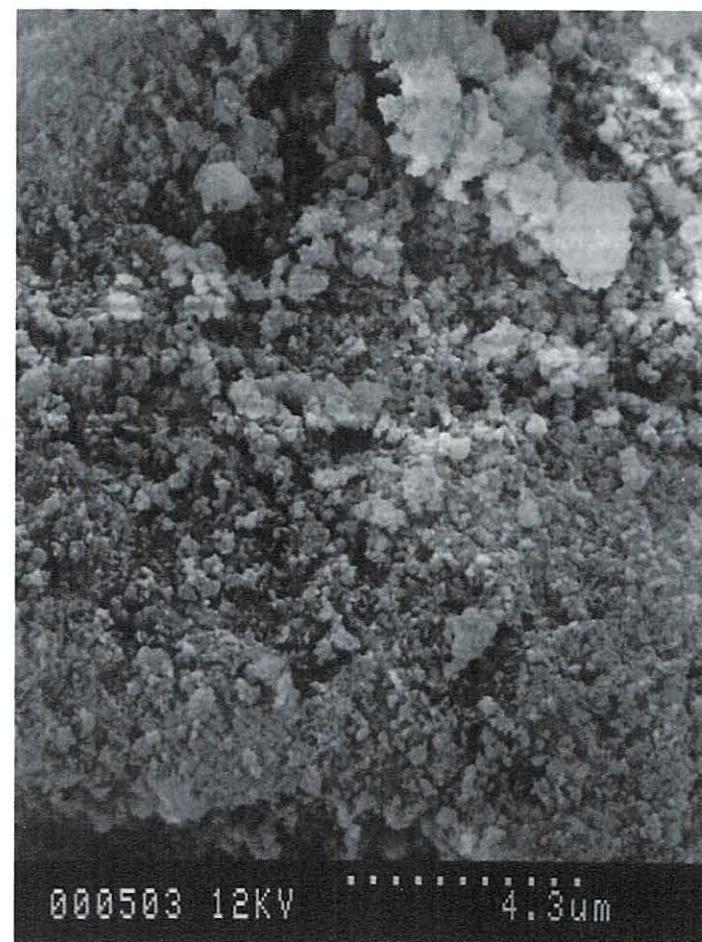
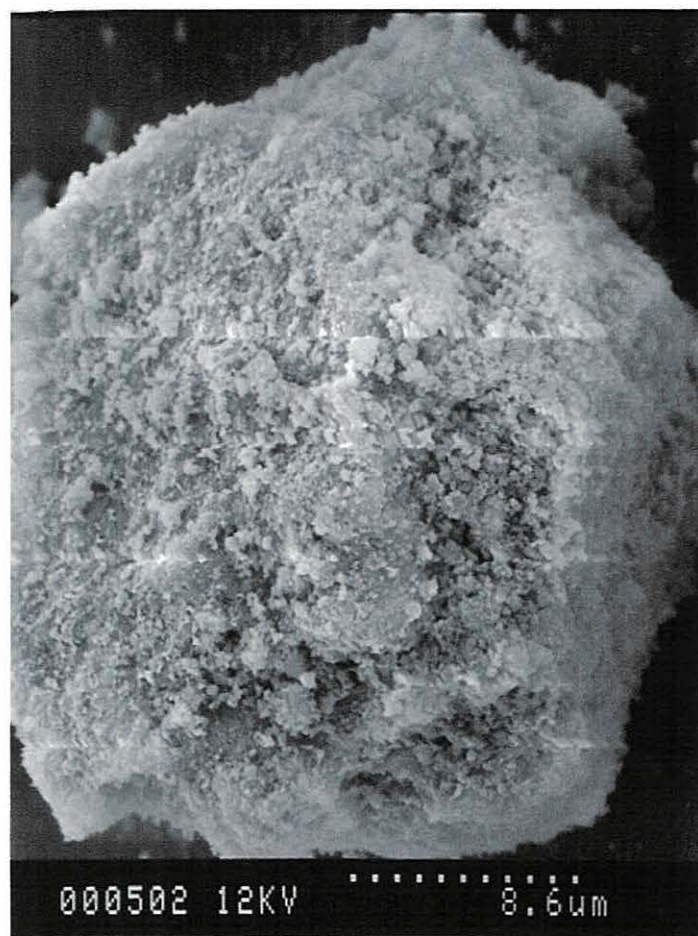
Figures 2.10 (a) & (b): SEM's of $\text{Mg}_3\text{Fe}_3\text{Al}_2\text{HTc}$ product

N.B. Scale bar is represented at the bottom of each micrograph as a series of dots (approximate length $\blacklozenge \longrightarrow \blacklozenge$) with the scale below



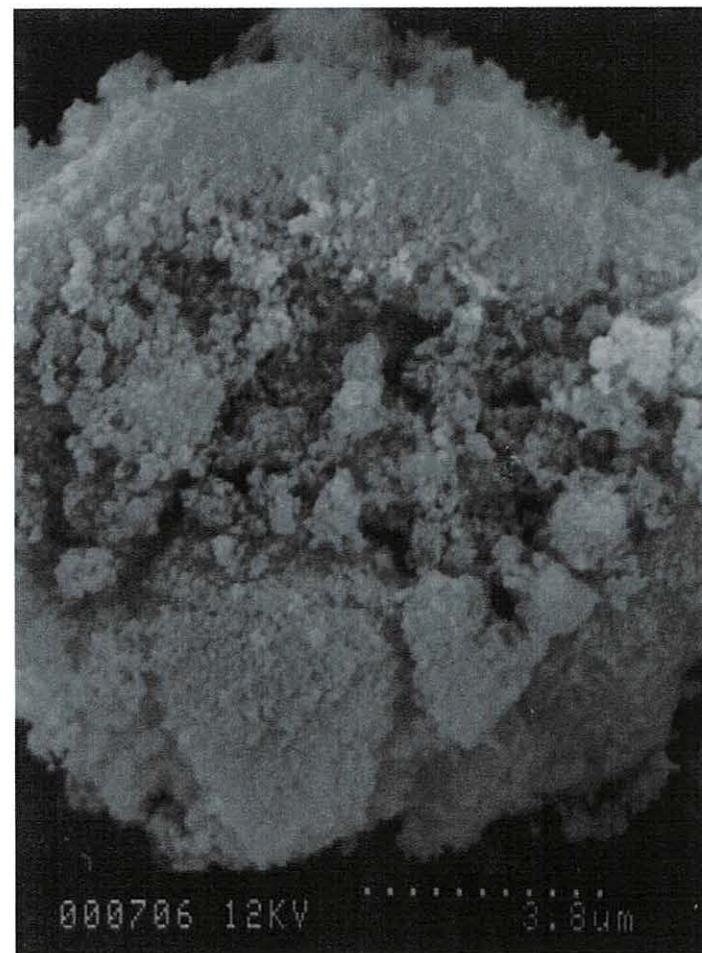
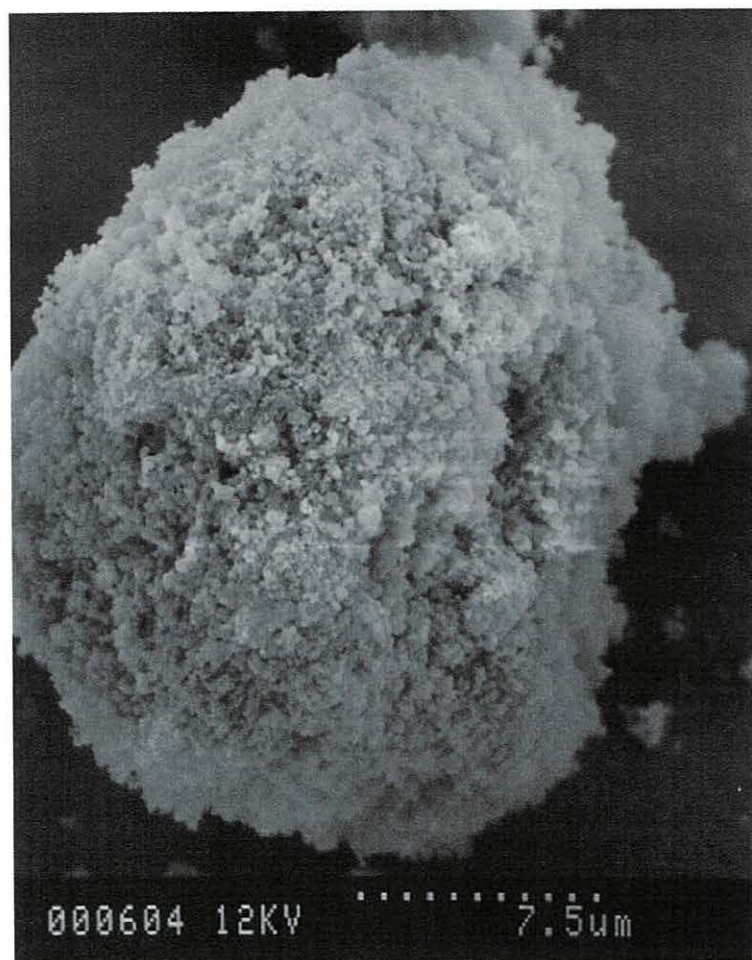
Figures 2.11 (a) & (b): SEM's of $\text{Mg}_2\text{Fe}_4\text{Al}_2\text{HTc}$ product

N.B. Scale bar is represented at the bottom of each micrograph as a series of dots (approximate length $\blacklozenge \text{-----} \blacklozenge$) with the scale below



Figures 2.12 (a) & (b): SEM's of MgFe₅Al₂HTc product

N.B. Scale bar is represented at the bottom of each micrograph as a series of dots (approximate length $\blacklozenge \text{-----} \blacklozenge$) with the scale below



Figures 2.13 (a) & (b): SEM's of $\text{Fe}_6\text{Al}_2\text{HTc}$ product

N.B. Scale bar is represented at the bottom of each micrograph as a series of dots (approximate length $\blacklozenge \longrightarrow \blacklozenge$) with the scale below

Sample	Mg	Fe	Al
Mg ₆ Al ₂ HTc (Exptl. Method 1)	~6.0	-	~2.0
Mg ₆ Al ₂ HTc (Exptl. Method 2)	~6.0	-	~2.0
Mg ₅ FeAl ₂ HTc	5.0-5.2	0.8-1.0	~2.0
Mg ₄ Fe ₂ Al ₂ HTc	3.8-4.2	1.8-2.2	~2.0
Mg ₃ Fe ₃ Al ₂ HTc	~3.0	~3.0	~2.0
Mg ₂ Fe ₄ Al ₂ HTc	~2.0	~4.0	~2.0
MgFe ₅ Al ₂ HTc	0.2-0.8	5.2-5.8	1.8-2.2
Fe ₆ Al ₂ HTc	-	5.8-6.6	1.4-2.2

Table 2.3 Summarised EDAX analysis results for prepared HTc's (expressed as relative ratios of K α peak intensities)

The EDAX spectra recorded for each of the HTc samples illustrated the expected relative ratios of metals based on relative peak heights for the majority of areas analysed across each sample. There was no obvious presence of hydromagnesite phases in the Mg₆Al₂HTc product prepared using preparative method 1, which had been inferred from the XRPD pattern (refer to previous section). A decrease in the relative ratio of aluminium would have been expected if hydromagnesite were present but, since only a finite number of areas may be examined, a small minority of hydromagnesite may have been present but was not identified. In addition, there was no deviation from the expected Mg:Al (3:1) ratio in the Mg₆Al₂HTc product prepared using preparative method 2, which may have been observed if aluminium hydroxycarbonate had been present to a significant degree (this may have been a slight possibility due to an absorption band observed at *ca.* 1500 cm⁻¹ in the IR spectrum, as described in section 2.1.2, but this band was of a weak intensity). The EDAX spectra recorded for the products with idealised formulae of Mg₅FeAl₂HTc, Mg₄Fe₂Al₂HTc, Mg₃Fe₃Al₂HTc and Mg₂Fe₄Al₂HTc exhibited the expected metal ratios with very little deviation from those expected. There was, however, a consistent deviation observed from the ideal metal ratios in the products with the idealised formulae of MgFe₅Al₂HTc and Fe₆Al₂HTc. Approximately twenty per cent of the EDAX spectra for the former exhibited an increase in the quantity of Fe present at the areas analysed whilst the Mg K α peak was barely distinguishable from background noise in those areas. This was consistent with the presence of siderite (FeCO₃) which was observed in the XRPD pattern for this product. However, the elongated blade structure of the siderite crystallites should have been distinguishable from that of the plate-like crystallites which were actually observed, although these plates were very small and may have been indistinguishable

from siderite at the resolution available. Similarly, the EDAX spectra recorded for the $\text{Fe}_6\text{Al}_2\text{HTc}$ product also exhibited an increase in the Fe ratio (over Al) in some areas of the sample. Again, little change in morphology was observed across the sample but the crystallites were so small that the positive identification of other phases would have been extremely difficult. The appearance of the expected additional phases (from the recorded XRPD patterns discussed in section 2.1.3) in comparison with the fine platelets expected of Al-substituted goethite would have been blade-like for siderite or cubic crystals (possibly rounded) for magnetite.^{28, 50}

2.1.5 Differential Thermal Analysis

Differential thermal analysis (DTA) was selected as an analytical technique to aid in the preparation of HTc-derived catalysts since it provides information relating to thermally induced transitions within the sample. Typically, these may be due to dehydration, oxidation, decomposition or polymorphic transformations within the sample as it is heated. The observation of the temperatures at which these transitions occurred allowed the selection of appropriate calcination temperatures when preparing materials to be used as catalysts. The figures quoted which relate to endothermic or exothermic transitions are those relating to the peak maxima, by convention, since these values can be relatively accurately determined. However, since DTA is a dynamic technique, the true characteristic reaction temperature is that corresponding with the initial deviation from the thermodynamic equilibrium temperature. Therefore, in order to keep catalyst preparation temperatures low, the initial deviation temperature was also seen to be important and was borne in mind when selecting calcination temperatures. Much of the early research into the DTA of carbonate minerals, and particularly HTc's, was carried out by Beck, over fifty years ago.⁵¹ Since then, there have not been any significant changes in the interpretations of the DTA curves of HTc's reported. The relatively recent review by Cavani *et al.* covers the major developments.¹⁰ The major endothermic and exothermic transitions for the prepared HTc's during the DTA are reported in Table 2.4.

Table 2.4 Selected differential thermal analysis data for HTc's recorded between 273 and 973 K

Mg₆Al₂HTc (method 1)	Mg₅FeAl₂HTc	Mg₄Fe₂Al₂HTc	Mg₃Fe₃Al₂HTc	Mg₂Fe₄Al₂HTc	MgFe₅Al₂HTc	Fe₆Al₂HTc
444 K (endo)*	416 K (endo)*	430 K (endo)*	412 K (endo)*	409 K (endo)*	411 K (endo)*	418 K (endo)*
500 K (endo)	495 K (endo)	485 K (endo) †	455 K (endo) †	454 K (endo) †	446 K (endo) †	
					515 K (exo)	500 K (exo)
551 K (endo)	546 K (endo)	538 K (endo)	555 K (endo)	551 K (endo)		581 K (endo)
					563 K (exo)	
					619 K (exo)	
633 K (endo) †	628 K (endo)	621 K (endo)	623 K (endo)	619 K (endo)		
701 K (endo)	665 K (endo)	667 K (endo)	649 K (endo)	650 K (endo)		658 K (endo)
773 K (endo)	747 K (endo)	790 K (endo)	739 K (endo)	762 K (endo)		

* gradual increase from room temperature in endothermic deviation

† approximate value due to peak overlap

endo endotherm

exo exotherm

Overall, the DTA traces recorded were similar to those expected for HTc's across the range $\text{Mg}_6\text{Al}_2\text{HTc}$ to $\text{Mg}_2\text{Fe}_4\text{Al}_2\text{HTc}$. The DTA traces for $\text{MgFe}_5\text{Al}_2\text{HTc}$ and $\text{Fe}_6\text{Al}_2\text{HTc}$ were more complex but this would be expected if there were a number of phases present, as suggested by the XRPD studies. However, as a general rule, the temperature at which the trace deviated from the thermal equilibrium position prior to the final peak was judged to occur at less than *ca.* 723 K. This information, combined with literature reports, was used in the selection of calcination temperatures for the HTc's synthesised.

The DTA trace recorded for $\text{Mg}_6\text{Al}_2\text{HTc}$ synthesised using preparative method 1 has been redrawn for illustration purposes in Figure 2.14. The DTA trace of the $\text{Mg}_6\text{Al}_2\text{HTc}$ product synthesised using preparative method 2 could not be recorded due to equipment failure. This was not, however, seen as crucial since the other characterisation methods employed did not reveal a marked difference between the $\text{Mg}_6\text{Al}_2\text{HTc}$ products produced from the two different preparative procedures described in the Experimental section, Chapter 7.

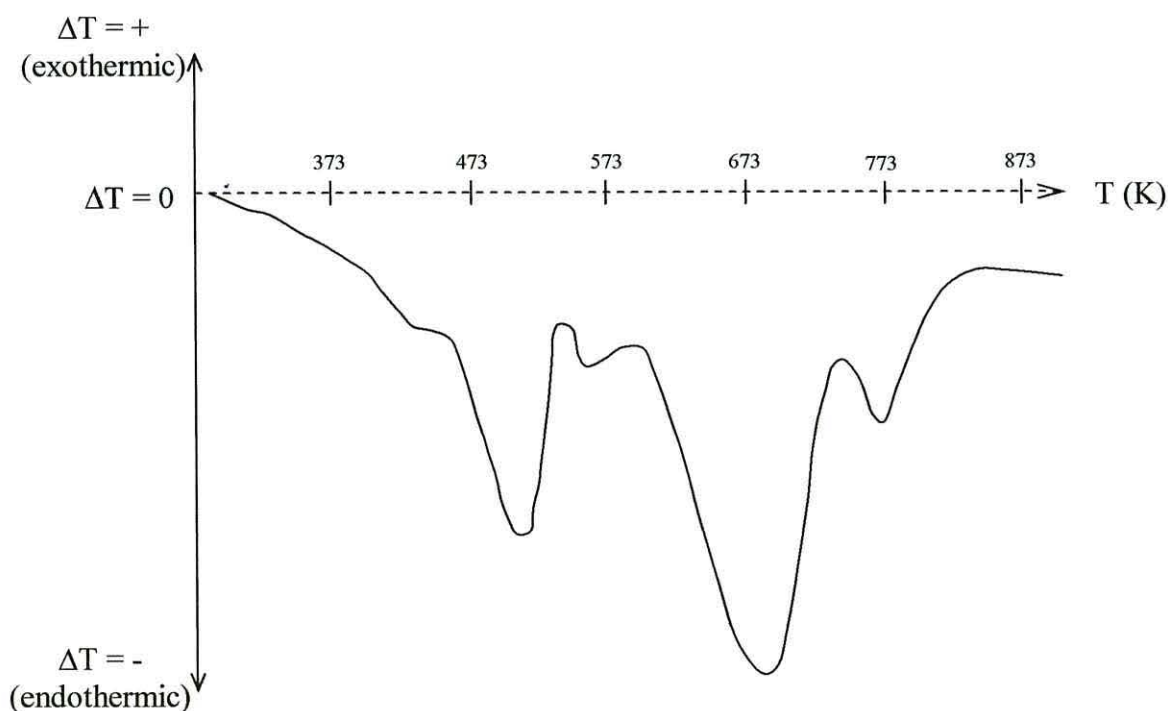


Figure 2.14 Illustration of DTA trace recorded for $\text{Mg}_6\text{Al}_2\text{HTc}$

The gradual endothermic progression to *ca.* 440 K for each of the synthetic HTc's in Table 2.4 resulted from the loss of adsorbed water. The first sharp endothermic peak at *ca.* 500 K was of similar intensity to that reported in the literature as being due to the loss of interlayer water.^{51, 52} However, in the same literature, the maximum of this peak was reported as occurring at *ca.* 545-560 K. The subsequent endothermic peak recorded for many of the HTc's in Table 2.4 fell within this range but was much reduced in comparative intensity. It has been reported¹⁰ that the peak commonly occurring at *ca.* 545-560 K could be split due to the loss of two distinct types of interlayer water. It is suggested that this may be the case here, the water associating with the divalent and trivalent metal cations in a manner distinguishable using this technique. The next peak in Table 2.4 (at 619-633 K) was less distinct than the others reported since there was some peak overlap in this area. Consequently, in the $\text{Mg}_6\text{Al}_2\text{HTc}$ DTA trace this endothermic transition is evident only in the asymmetric nature of the peak whose maximum occurs at 701 K, as noted in Table 2.4. Nonetheless, a peak was reported in this region by Miyata as being due to the dehydration of part of the metal hydroxide layers.⁵³ He showed this to increase in intensity with an increase of aluminium content of a $\text{Mg}_6\text{Al}_2\text{HTc}$ which led him to conclude that it was due to the partial dehydration of the mixed metal hydroxide layers, specifically the structural water bound with aluminium. This conclusion was in agreement with the earlier studies of Beck.⁵¹ The large peak at *ca.* 650-700 K was similar in relative intensity to that widely reported in the literature as being due to a combination of two effects *viz.* the loss of water as a result of the decomposition of the remaining structural hydroxide and the loss of interlayer carbonate as CO_2 .^{51, 52, 53} However, since for the majority of the HTc's in Table 2.4 there is another subsequent smaller peak at *ca.* 740-790 K, it is suggested that the endothermic peaks resulting from the two processes have been resolved. The endotherm at lower temperature was of a greater relative intensity for the $\text{Mg}_6\text{Al}_2\text{HTc}$ product, in comparison with the other Fe-containing HTc products displaying a similar DTA trace. This suggested that the peak was a result of $\text{M}^{2+}\text{-OH}$ decomposition since the $\text{Mg}_6\text{Al}_2\text{HTc}$ product contained the greater relative proportion of M^{2+} (since the Fe^{2+} in the Fe-containing HTc's had oxidised to Fe^{3+} at this stage). Consequently, it is proposed that the decomposition of the interlayer carbonate occurred at *ca.* 740-790 K to result in the endothermic peak in this region of the trace for the products exhibiting a predominantly HTc structure *i.e.* those in the range $\text{Mg}_6\text{Al}_2\text{HTc}$ to $\text{Mg}_2\text{Fe}_4\text{Al}_2\text{HTc}$.

The DTA traces recorded for the $\text{MgFe}_5\text{Al}_2\text{HTc}$ and $\text{Fe}_6\text{Al}_2\text{HTc}$ were more complex, displaying exothermic, in addition to endothermic, peaks and were not recognisable as being representative of HTc's. The initial endothermic peaks displayed by both samples at *ca.* 400-450 K are commonplace amongst a wide range of materials since this region is commonly associated with initial dehydration of the samples. From this point onward, the traces recorded were unrecognisable in comparison with those recorded for the products with lower Fe contents, discussed above. Since the formation of goethite was suspected in the preparation of $\text{Fe}_6\text{Al}_2\text{HTc}$ from previous IR and XRPD results (see earlier sections), the literature was consulted regarding the DTA characteristics of goethite and other similar iron oxides.^{28, 54} These previous studies emphasised the significance of an endothermic peak at *ca.* 580-650 K as the most obvious feature of the goethite DTA trace. This peak corresponded to the dehydroxylation of goethite and the concurrent formation of haematite.⁵⁵ During work dedicated to the investigation of the influence of aluminium-substitution on iron oxides (goethites specifically), Schulze and Schwertmann observed the tendency of this peak to shift to higher temperatures with increasing Al-substitution.⁵⁴ The possible range of temperatures at which the peak maximum was observed to occur was observed to widen (occurring between 493-633 K) and the peak even split, depending on aluminium substitution within the structure. Perhaps surprisingly, Schulze and Schwertmann observed the greatest splitting for their samples when there was no Al-substitution *i.e.* a pure goethite. Earlier work by Schwertmann had attributed this splitting to the formation of an intermediate goethite phase which formed when the domains of the goethite crystals were above a particular size.⁵⁴ The peak at 581 K in the $\text{Fe}_6\text{Al}_2\text{HTc}$ product did occur within this range but comparison with the data reported by Schulze and Schwertmann in order to gauge the degree of aluminium substitution is difficult since they did not observe a single peak maximum at temperatures this low. Rather, this peak had split and correlated to an aluminium substitution of *ca.* 3 mole per cent.⁵⁴ Otherwise, however, the exact nature of the additional peaks in samples $\text{MgFe}_5\text{Al}_2\text{HTc}$ and $\text{Fe}_6\text{Al}_2\text{HTc}$ was not clear, the origins of the exothermic peaks was especially intriguing. The DTA trace of siderite (FeCO_3) had been shown to produce exothermic peaks but always above 800 K. However, the traces of a range of ferric oxide gels reported in the literature do show similarities to those recorded for the $\text{MgFe}_5\text{Al}_2\text{HTc}$ and $\text{Fe}_6\text{Al}_2\text{HTc}$ products.⁵⁵ In particular, the occurrence of a low temperature endothermic peak at *ca.* 420 K followed by a strong, sharp exothermic peak at *ca.* 540-620 K (at a slightly higher range than that

seen for the first exotherms in the HTc products but similar otherwise). The ferric oxide gels have been reported to form under similar conditions to those used in the preparative stage of the HTc's, although from a ferric (rather than ferrous) chloride solution. This preparative method is similar to that used for the synthesis of ferrihydrite²⁹ and it is suggested here that the materials reported as ferric oxide gels in the early literature were variants of ferrihydrite which displays a similar DTA trace.²⁸ The initial endothermic peak also correlates to adsorbed water loss for these materials but the exact nature of the exothermic peak does not appear to be clear in the literature. Much of the evidence did, however, indicate the transformation of the gel/ferrihydrite to form more ordered haematite (α -Fe₂O₃) at this temperature; the same product as is formed from goethite, as previously noted. The other higher temperature peaks observed in the traces of MgFe₅Al₂HTc and Fe₆Al₂HTc were of much lower intensity than the exotherms at 500 K and their origin was unclear. However, the presence of a mixture of phases, as suggested by the XRPD results, would be difficult to resolve which provides a good example of one of the limitations of this technique in sample identification. The main aim of the analysis – to ascertain the temperature at which the main transitions are complete in the formation of a mixed metal oxide – was inferred by the peaks whose maxima occurred at *ca.* 619 K and 658 K. Therefore, the formation of the oxide was adjudged to have occurred by 723 K, the calcination temperature selected as a result of the analysis of the DTA traces recorded for the other HTc products.

2.1.6 Conclusions

Overall, the characterisation techniques utilised illustrated that the hydrotalcite structure was adopted, on the whole, by the products having idealised formulae of Mg₆Al₂HTc (both methods of preparation), Mg₅FeAl₂HTc, Mg₄Fe₂Al₂HTc, Mg₃Fe₃Al₂HTc and Mg₂Fe₄Al₂HTc. The product MgFe₅Al₂HTc actually appeared to contain a range of products including some hydrotalcite-type material, together with some siderite (FeCO₃) and some iron oxide(s). The product Fe₆Al₂HTc appeared to consist predominantly of iron oxides with less evidence of the presence of a hydrotalcite phase. Instead, this product appeared to have formed an aluminium-substituted iron oxide (probably goethite-based) rather than the intended iron-substituted hydrotalcite.

However, the general morphology of these samples did not, as expected, appear to be particularly different which was encouraging from the perspective of their intended eventual uses as catalysts since the plate-like structure was desired in the formation of high porosity/surface area materials. Since the trends observed during each method of analysis have already been described in detail in the respective section dedicated to each specific technique, a general overview follows.

In addition to the general conclusion drawn above, IR spectroscopy provided additional information regarding the presence of some additional phases. For example, the additional carbonate absorption bands seen in the $\text{Mg}_6\text{Al}_2\text{HTc}$ (method 1) product which were ascribed to hydromagnesite and the gradual transition to the spectrum representative of iron oxides and some siderite (FeCO_3). One disadvantage was that many of the iron oxides do exhibit absorption bands at similar frequencies which meant that some minor phases may have been undetected in the high-Fe substituted HTc's.

XRPD verified the adoption of a hydrotalcite structure for the majority of samples, basal spacings being generally consistent with the inclusion of carbonate as the charge-neutralising counter-ions. Additional minor phases were observed in the products $\text{Mg}_6\text{Al}_2\text{HTc}$ (method 1) and $\text{Mg}_2\text{Fe}_4\text{Al}_2\text{HTc}$, being hydromagnesite [$\text{Mg}_5(\text{CO}_3)_4(\text{OH})_2 \cdot 4\text{H}_2\text{O}$] and siderite (FeCO_3) plus magnetite (Fe_3O_4) or magnesioferrite (MgFe_2O_4) respectively. The products $\text{MgFe}_5\text{Al}_2\text{HTc}$ and $\text{Fe}_6\text{Al}_2\text{HTc}$ were more complex and deviated towards the formation of iron oxides with other minor phases as previously described. There was a tendency for the basal [003] spacing to decrease with increasing Fe-substitution which was attributed to increased layer charge (from Fe^{3+}). The unit cell parameter a was also shown to decrease, as indicated by the [110] spacing, which was attributed to the decreased ionic radius of Fe^{3+} over Mg^{2+} .

SEM analysis revealed a general platelet morphology for all of the samples, the trend here being for a decrease in average particle size (both diameter and thickness of plates) with increasing Fe-substitution. The EDAX analysis did infer the presence of some minor phases such as siderite (FeCO_3) since the iron ratio relative to aluminium was greatly increased in some areas of the sample but no change in morphology was observed.

The DTA traces of the products $\text{Mg}_6\text{Al}_2\text{HTc}$ to $\text{Mg}_2\text{Fe}_4\text{Al}_2\text{HTc}$ showed similar traces to those previously recorded in the literature although some splitting of the peaks appeared evident. It is proposed that this was a consequence of the range of cations in the product and some enhanced resolution of peaks during analysis. The traces recorded for the $\text{MgFe}_5\text{Al}_2\text{HTc}$ and $\text{Fe}_6\text{Al}_2\text{HTc}$ products were more complex and appeared to exhibit similarities to those recorded in the literature for ferric oxides. The most important point to be derived from this analysis was the temperature at which the products were expected to form mixed metal oxides. This temperature was below 723 K for all of the samples analysed. This information allowed the maximum temperature for the calcination stage to be selected; the study of which is discussed in the next chapter.

2.2 Green Rusts and Iron Oxides

2.2.1 Preparative Methodology

The term ‘green rusts’ is used to describe a range of blue/green mixed $\text{Fe}^{2+}/\text{Fe}^{3+}$ valency hydroxides which have been shown to be members of the pyroaurite group of compounds.⁸ The divalent and trivalent Fe cations reside in the interstices of hexagonally close-packed O atoms to form $\text{Fe}(\text{OH})_2$ -type layers carrying a net positive charge.²⁹ The charge imbalance on the layers is neutralised by the incorporation of anions between the layers in a manner analogous to that of hydrotalcite (hence the previously mentioned pyroaurite classification). Green rusts are unstable in an oxidising environment but are known to form as intermediates during the oxidation of Fe^{2+} solutions to form a number of the iron oxyhydroxides. The actual product formed as a result of oxidation is dependent upon the synthesis conditions but the most commonly observed products are goethite (α - FeOOH), lepidocrocite (γ - FeOOH) and feroxyhyte (δ' - FeOOH).^{29, 56, 57} Until quite recently, feroxyhyte was probably the least studied of the iron oxyhydroxides.⁵⁸ The naturally occurring mineral feroxyhyte (δ' - FeOOH) is a poorly ordered form of the synthetic material δ - FeOOH (which is also generally named feroxyhyte)⁵⁹ and its structure is relatively similar to that of green rust, from which it is derived, following rapid oxidation. The feroxyhyte structure consists of hexagonally close-packed planes of oxygen atoms with the Fe^{3+} ions in the octahedral interstices. A

layered structural arrangement results but, since the layers carry no net electrostatic charge, there are no ions present between the layers. A low crystallinity has been associated with feroxyhyte which has been linked to the presence of vacant Fe sites (only half of the octahedral sites are alternately packed by cations) and the replacement of oxygen by OH and/or H₂O.²⁹ Feroxyhyte has not been commonly identified in nature, possibly due to the need for a rapid oxidation step in its formation and has not been studied in as much detail as many of the other iron oxides.⁵⁹ There has been some focussed research on the use of feroxyhyte as a hydrogen sulfide sorbent in gas streams⁶⁰ but there is little additional information available in the literature regarding potential uses of feroxyhyte. However, for similar reasons for the selection of feroxyhyte as a gas sorbent by Baird and co-workers, *viz.* the high surface area of the structure and the known affinity of Fe for certain other elements such as sulfur, it is suggested here that feroxyhyte may also be suitable for use as a catalyst for selected reactions. The modification of the chemical composition and structure is investigated here by the incorporation of Al³⁺ into some of the octahedral cation sites otherwise occupied by Fe³⁺. It is suggested that this substitution may result in a material with increased mechanical strength, with improved resistance to sintering at higher temperatures which may make this material suitable for use as a catalyst.

Goethite (α -FeOOH) and lepidocrocite (γ -FeOOH), two of the more common iron oxyhydroxides previously mentioned, have well-known isostructural analogues *viz.* diaspore (α -AlOOH) and boehmite (γ -AlOOH) respectively.²⁸ Consequently, there has been a substantial amount of research dedicated to the investigation of isomorphous substitution in the iron oxides. Goethite is the most studied of the iron oxides with respect to isomorphous substitution and, in turn, Al³⁺ is the most frequently observed example of a cation used to replace Fe³⁺ in the structure.²⁸ This area has been extensively researched^{54, 61, 62, 63} but the isomorphous substitution of cations in the feroxyhyte structure is an area which has seen little recent activity.²⁸ This has possibly been due to a lack of applications for such materials.

One of the aims of this work is to produce catalytically active materials for the oxidation of sulfur dioxide. It is proposed that aluminium-substituted feroxyhytes may be suitable for this reaction, for some of the reasons already discussed, which will be elaborated upon in Chapter 5. Here, in this Chapter, the characterisation of the

materials formed following the attempted isomorphous substitution of Al^{3+} into the feroxyhyte structure will be investigated and the collated data will be discussed. The Al^{3+} substitution of Fe^{3+} in the green rust structure will also be detailed since this is known to be an intermediate in the formation of feroxyhyte. This data should offer an interesting comparison with that presented in section 2.1 of this chapter since here the Al-substitution of iron oxides and their pyroaurite-type intermediates may be contrasted with the Fe-substitution of hydrotalcite-type compounds. Additionally, the synthesis of the unsubstituted green rusts and feroxyhytes in methanol as the reaction solvent (rather than water) is also investigated in order to compare the products formed. Little work has previously been carried out in this area and it is seen as a potentially valuable addition to novel research in the area of iron oxides.

2.2.2 Infrared Spectroscopy

It should be noted that the IR spectra recorded and described for each of the green rust products in this section were actually indicative of their iron oxide products following oxidation since the Fe^{II} -containing green rusts are so unstable in air. There have been some previous studies which have attempted to stabilise green rusts for analysis *viz.* the use of a carbon dioxide atmosphere by Taylor¹² and the wetting of the green rust with glycerol or a similar organic liquid by Hansen.⁶⁴ However, despite the use of these methods, there are still very few IR spectra of green rusts available in the literature for comparison with the green rusts produced here. By comparison, the IR spectra of the iron oxides have been quite thoroughly investigated, particularly for the iron oxides observed most frequently in nature. Cornell and Schwertmann have summarised many of the fundamental studies,²⁸ a significant amount of which research has been authored by Schwertmann himself. The IR absorption bands recorded for each of the green rust and iron oxide products have been tabulated (Table 2.5) to allow direct comparison between products and some representative spectra are illustrated in Figure 2.15 (a-f). The spectrum for each product is also briefly described hereafter, beginning with the green rusts.

Table 2.5 Green rust and iron oxide infrared absorption bands (cm^{-1}) recorded between 4000 and 400 cm^{-1}

Green rust H ₂ O solvent	Green rust CH ₃ OH solvent (not dried)	Green rust CH ₃ OH solvent (MgSO ₄ dried)	Green rust Excess CO ₃ ²⁻	Al-Green rust Excess CO ₃ ²⁻	Feroxyhyte H ₂ O solvent	Feroxyhyte CH ₃ OH solvent (MgSO ₄ dried)	Al-feroxyhyte H ₂ O solvent
3415 s, br	3422 s, br	3410 m, br	3422 s, br	3460 s, br	3423 s, br	3408 s, br	3400 m, br
3193 s, br	3200 m, shldr	3200 w, shldr				3225 s, shldr	
	2950 w, shp	2950 w, shp					
2900 m, shldr	2924 w, shp	2925 w, shp			2900 w, shldr		
	2825 w, shp	2825 w, shp					
	1735 w, br						
1637 w, br	1636 w, br	1636 w, br	1636 w, br	1634 m	1636 w, br	1636 w, br	
			1500 w, br	1520 w			
1400 w, br	1380 w, br		1415 w, br	1375 s		1400 w, br	1404 s, br
	1250 vw						
1150 vw	1150 vw	1168 s, shp				1146 s, shp	
		1137 s, shp			1120 w, shp	1114 s, shp	
1021 m, shp	1050 w	1102 s, shp				1088 s, shp	1075 w
	1008 w	1010 w	1010 w			1000 w, shp	
		1004 w				984 w, shp	
890 w							862 m
792 w, shp			817 w	800 w			
746 w, shp						700 w, br	738 w
	670 m, br	637 w, shp	668 m		685 m, br		
		625 m, shp				622 m	
581 m, br		600 w, shp	582 m	570 m			
504 m, br					516 m, br		
	490 m, br		490 m		470 s, br		

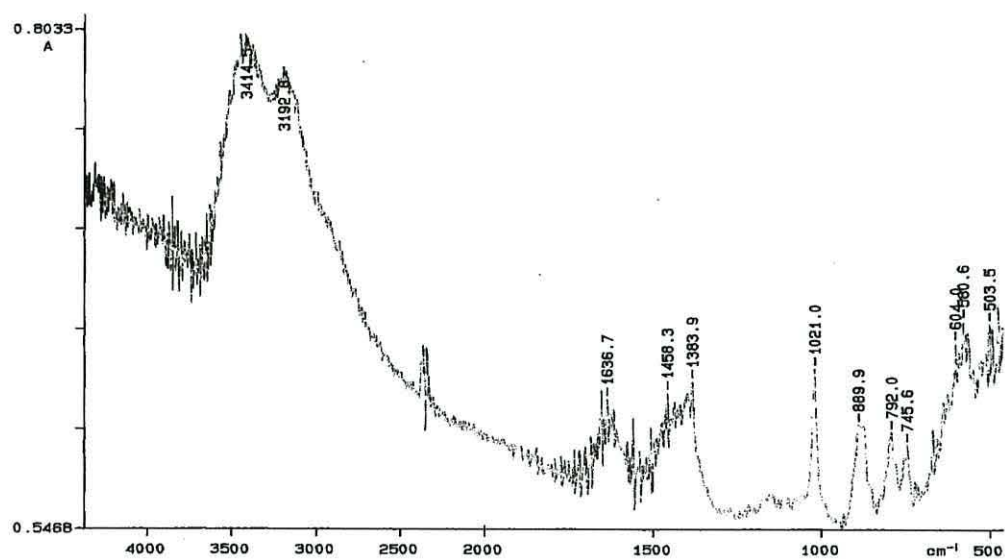


Figure 2.15 (a) Green rust (H_2O solvent) product

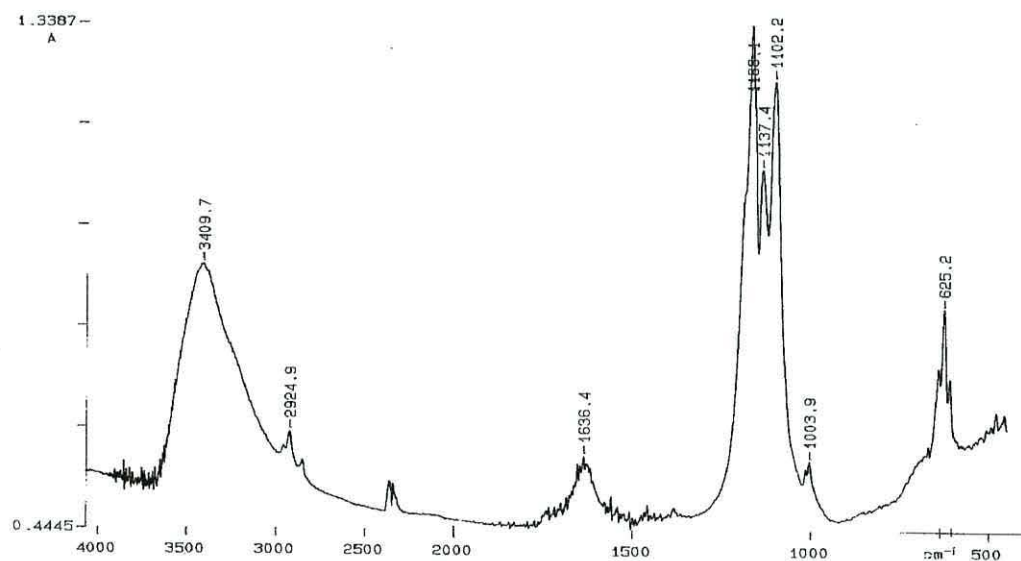


Figure 2.15 (b) Green rust (CH_3OH solvent – MgSO_4 dried) product

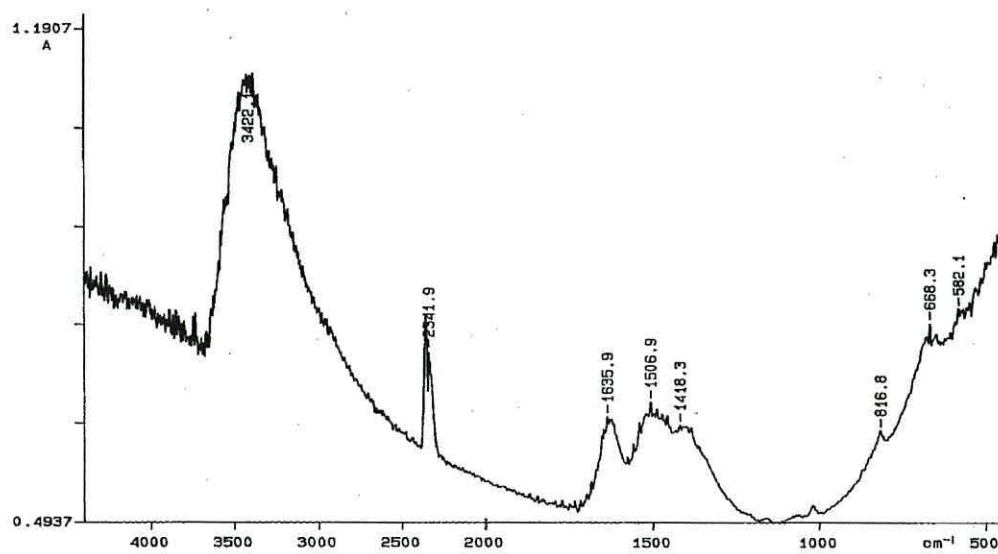


Figure 2.15 (c) Green rust (excess CO_3^{2-}) product

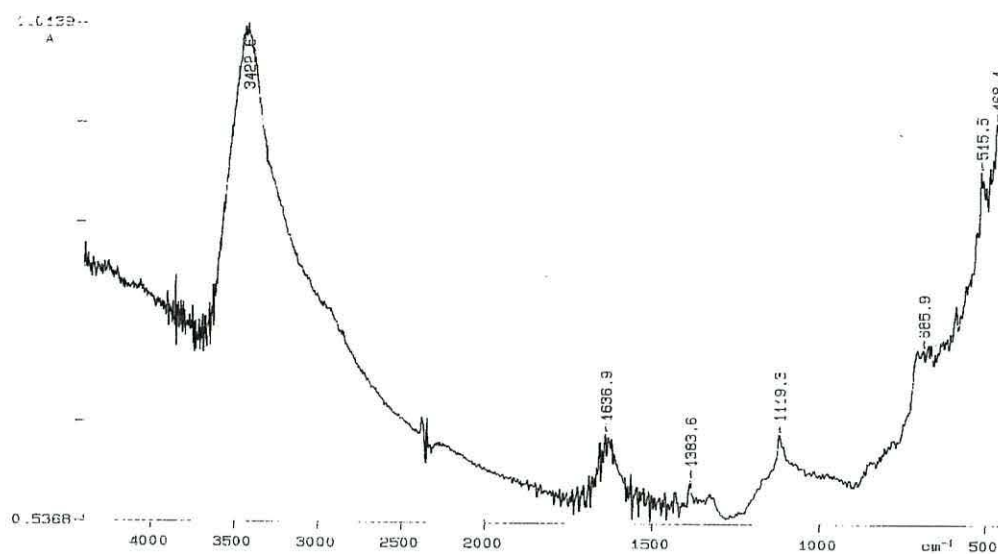


Figure 2.15 (d) Feroxyhyte (H₂O solvent) product

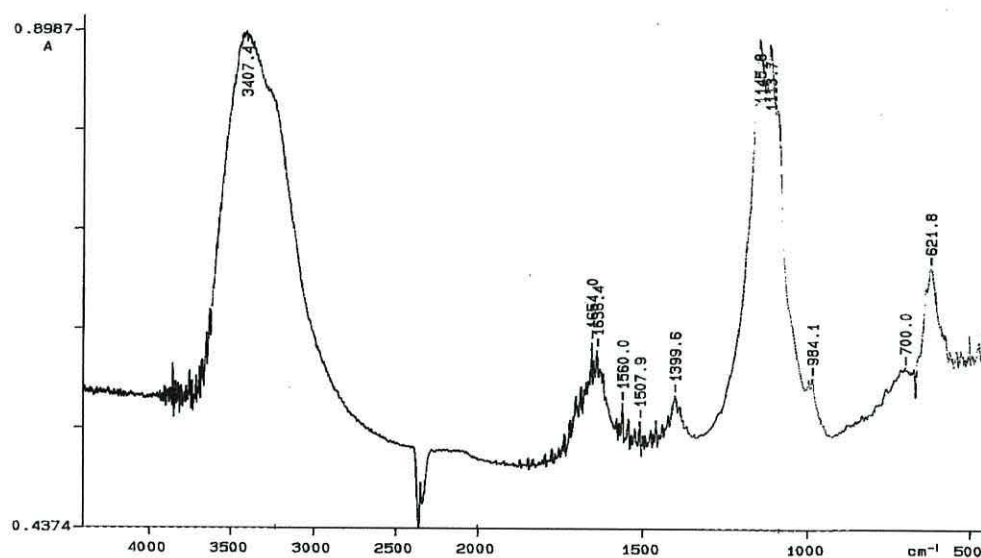


Figure 2.15 (e) Feroxyhyte (CH₃OH solvent – MgSO₄ dried) product

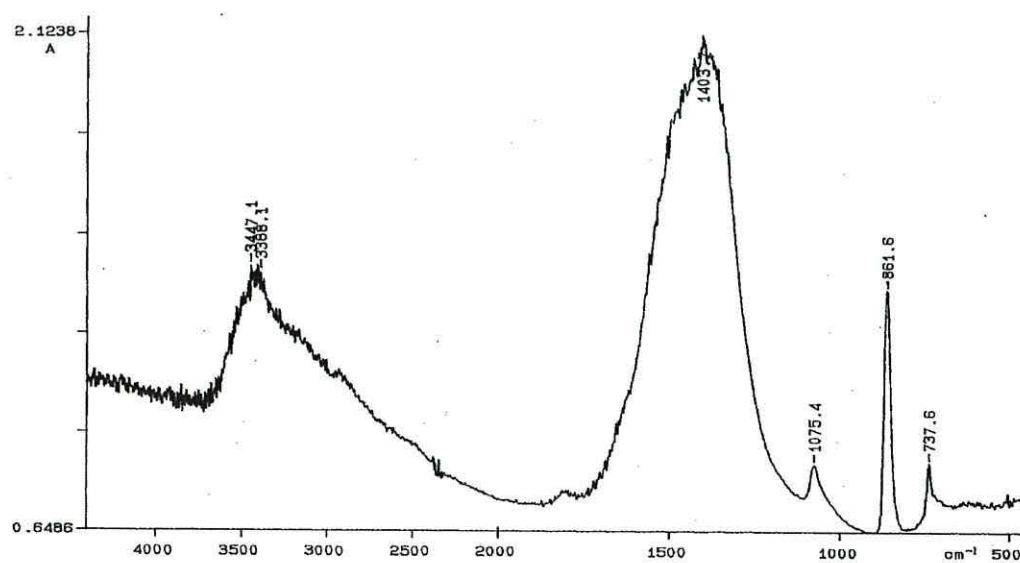


Figure 2.15 (f) Al-Feroxyhyte (H₂O solvent) product

The spectrum recorded for the green rust product synthesised in water was most similar to that which would be expected for lepidocrocite (γ -FeOOH). This was due, in particular, to the absorption band present at 1021 cm^{-1} which is characteristic of this particular iron oxide.²⁸ This has previously been assigned to an in-(100)-plane OH bend, the corresponding out of plane bend occurring at *ca.* 750 cm^{-1} .²⁸ The band at 3193 cm^{-1} and the shoulder at 2900 cm^{-1} arise from the stretching of hydroxyl groups in lepidocrocite having a more plate-like morphology (as opposed to a rod-like morphology which would result a single corresponding band at *ca.* 3060 cm^{-1}).²⁸ The other band characteristic of lepidocrocite which was observed was an additional (to the one previously described at 1021 cm^{-1}), though less intense in-plane OH bend at *ca.* 1150 cm^{-1} . There was also an H-O-H bend at 1637 cm^{-1} which is commonly seen in mineral IR spectra and assigned to adsorbed water molecules, a weak CO_3^{2-} stretch at 1400 cm^{-1} and a number of bands below 600 cm^{-1} probably due to Fe-O stretches. The remaining bands indicated the presence of a second iron oxide phase. These bands were indicative of goethite; a surface hydroxyl stretch at 3415 cm^{-1} , an in-plane OH bend at 890 cm^{-1} and an out of plane OH bend at 792 cm^{-1} . A bulk OH stretch would have overlapped the corresponding lepidocrocite band at *ca.* 3150 cm^{-1} and was, therefore, not observed. Overall, the lepidocrocite absorption bands appeared to be of greater intensity, indicating that this was present as the major phase. This would have been expected since lepidocrocite does tend to form under the synthesis conditions employed.²⁹ If an excess of carbonate ions had been present in solution, goethite would have been expected to form preferentially instead.²⁹

The IR spectrum recorded for the green rust product synthesised using undried methanol as the reaction solvent did not exhibit the characteristic bands described above for lepidocrocite, nor for any of the iron oxides in particular. The bands at 3422 and 3200 cm^{-1} were indicative of OH stretches, the broad band at 1636 cm^{-1} was assigned to the H-O-H bend of adsorbed water and the bands below 700 cm^{-1} were assigned to M-O stretches. The remaining bands of interest, though relatively weak in intensity were those occurring at 2950 , 2924 , 2825 , 1250 and *ca.* 1000 cm^{-1} since some of these occurred at frequencies not commonly assigned to molecular vibrations within iron oxides. However, the methanol C-H stretches would be expected in the region of 2800 - 3000 cm^{-1} and the C-O stretch at *ca.* 1000 cm^{-1} . The band at 1250 cm^{-1} did occur in an area of the spectrum where the O-H bends associated with many alcohols may be

expected; but this is an area in which methanol does not exhibit an absorption band.⁶⁵ However, it should be noted that this band was very weak in intensity.

In direct comparison with the aforementioned spectrum, the spectrum recorded for the green rust product synthesised in methanol reaction solvent which had been dried over MgSO_4 exhibited strong absorption bands in the $1100\text{--}1200\text{ cm}^{-1}$ region which would be expected for the C-O stretch of a primary alcohol.⁶⁵ There were also three sharp, lower intensity, peaks in the $600\text{--}650\text{ cm}^{-1}$ region but the origin of these is less clear since they were not expected for methanol nor similar to those recorded for any of the iron oxides. Otherwise the spectra recorded for the products synthesised in undried and dried methanol were comparable.

The spectra recorded for the two green rust products synthesised in a solution containing an excess of carbonate ions were very similar and will, therefore, be discussed together. The spectra were similar to those recorded for the HTc's discussed in section 2.1.2, particularly that of the Al-containing green rust since the CO_3^{2-} stretch at *ca.* 1400 cm^{-1} was much stronger in this product than for that which did not contain Al. The peak assignments are, therefore, similar to the HTc's and are not discussed in further detail here (refer back to section 2.1.2). It is interesting to note at this point that the green rust containing Al ions did appear to be less susceptible to oxidation in air and may have retained the HTc structure for an extended period of time during characterisation. This may explain the greater similarity to the HTc spectra since a greater proportion of interlayer carbonate would have been retained prior to oxidation to the iron oxide and the subsequent loss of the charge neutralising carbonate ions. In comparison with one of the few green rust IR spectra recorded in the literature,⁵⁶ which itself compares the spectra of hydrotalcite and green rust, the spectra were also very similar. This was expected given the chemical and structural similarities mentioned earlier.

The spectrum recorded for feroxyhyte synthesised in water was in accordance with those recorded in the literature for this material.^{28, 29, 60} The main bands were observed at 3423 and 1636 cm^{-1} due to O-H stretching and bending modes, respectively, and a number of bands below 1000 cm^{-1} which were not easily resolved and were generally assigned to Fe-O and Fe-O-H stretches.

For the iron oxide synthesised in methanol, the IR spectrum differed most obviously from that synthesised in water by the addition of a number of bands in the 1000-1150 cm^{-1} region. These were assigned to C-O stretches of methanol, as previously for the green rust product also synthesised in methanol. In addition, there was a peak evident at 3225 cm^{-1} which was, again, assigned to O-H stretches, due to the presence of methanol since this peak was not observed in the ferroxhyte product synthesised in water. Otherwise, the spectrum was similar to that generally expected for the iron oxides since the IR spectra exhibit few particularly characteristic bands.^{28, 29}

There were few strong bands recorded in the IR spectrum of the Al-ferroxhyte product. The most obvious band occurred at *ca.* 1404 cm^{-1} which was indicative of the presence of carbonate in the sample, upon comparison with the IR spectra of other carbonate-containing products recorded in this thesis. Other than this, there was a peak at *ca.* 3400 cm^{-1} assigned to O-H stretches, a weak band at 1075 cm^{-1} which was possibly another CO_3^{2-} stretch and two bands below 1000 cm^{-1} which were, as for many bands in this region, not obviously assignable but could have been further CO_3^{2-} bands and/or Fe-O/Fe-OH stretches.

2.2.3 X-ray Powder Diffraction

X-ray powder diffraction is a technique widely employed for the identification of clay minerals, as previously discussed in section 2.1.3. It is particularly useful, however, in the identification of iron oxides since IR spectroscopy, the other commonly used technique, is less well suited to distinguish between some of the iron oxides. This is because similar chemical groups and, therefore, bonds are present throughout the range of iron oxides but there is a variation in the structural arrangement of these groups. The XRPD data for the range of materials produced here is presented in Tables 2.6 and 2.7 together with JCPDS data for relevant materials to allow comparisons to be made. The data for each of the products is described hereafter.

Table 2.6 X-ray powder diffraction d-spacing results (Å) for green rusts (relative intensities in parentheses)

Green rust ⁵⁶	Green rust H ₂ O solvent	Green rust CH ₃ OH solvent (not dried)	Green rust CH ₃ OH solvent (MgSO ₄ dried)	Green rust Excess CO ₃ ²⁻	Al-Green rust Excess CO ₃ ²⁻	Lepidocrocite ⁶⁷ γ-FeOOH	Goethite ⁴¹ α-FeOOH
		10.69 (41) broad					
7.50 (100)			7.78 (43) broad				
	6.26 (100)					6.26 (100)	
			5.81 (27)				
	4.99 (9)						4.97 (60)
			4.66 (75)				
	4.20 (29)		4.24 (25)				4.18 (100)
			4.03 (84)				
			3.92 (43)				
			3.84 (21)				
3.76 (25)			3.76 (19)				
	3.36 (8) shldr		3.43 (90)				3.36 (60)
	3.29 (56)	3.26 (19)	3.19 (52)/3.12 (75)			3.29 (90)	
			3.07 (60)				
	2.96 (10)		2.99 (40)/2.92 (54)	2.92 (64)	2.90 (78)	2.97 (10)	
	2.82 (16)	2.82 (100)	2.84 (51)/2.83 (55)				
2.72 (3)			2.79 (100)				
2.67 (20)	2.70 (14)		2.69 (16)				2.69 (70)
	2.59 (12)		2.65 (54)/2.58 (46)				2.58 (55)
	2.53 (31)	2.54 (28)	2.55 (21)				
2.46 (10)	2.48 (57)		2.46 (30)			2.47 (80)	2.48 (40)/2.44 (80)
	2.36 (10)					2.36 (20)	
2.34 (15)	2.34 (6)		2.33 (30)	2.34 (27)	2.32 (35)		2.30 (10)
	2.26 (7)		2.25 (15)				2.25 (60)
	2.19 (6)		2.17 (16)				2.18 (30)/2.14 (10)
2.08 (2)	2.09 (8)					2.09 (20)	2.09 (15)
	2.03 (3)			2.02 (41)	2.04 (62)		
	2.00 (5)	1.99 (36)	2.00 (16)	2.00 (17)			2.01 (20)
	1.94 (25)					1.94 (70)	1.92 (40)
				1.67 (33)	1.65 (35)		
				1.57 (68)	1.58 (100)		

Table 2.7 X-ray powder diffraction d-spacing results (Å) for feroxyhytes (relative intensities in parentheses)

Feroxyhyte ⁴²	Feroxyhyte H ₂ O solvent	Feroxyhyte CH ₃ OH solvent (dried over MgSO ₄)	Al-feroxyhyte H ₂ O solvent
		14.80 (15)	
4.95 (100)			
		3.91 (43)	
		3.76 (38)	3.72 (25)
		3.46 (24)	
3.21 (60)			
2.94 (80)			
2.82 (50)			2.87 (100)
2.76 (50)		2.80 (100)	
2.67 (50)		2.64 (53)	
2.55 (40)	2.55 (100)		
2.47 (40)			
2.41 (40)		2.38 (20)	2.40 (23)
2.37 (50)	2.34 (28)		
2.26 (50) / 2.24 (50)	2.23 (44)		
2.18 (30)			2.17 (20)
2.12 (30)			
2.06 (10)	2.03 (18)	2.03 (14)	
2.01 (10) / 1.99 (20)			2.00 (20)
1.93 (30) / 1.90 (30)		1.96 (16)	
1.84 (30) / 1.70 (20)			1.82 (9) / 1.76 (49)

The product formed from the synthesis of green rust in water exhibited a mixture of at least two distinct phases. The data suggests that the main two are lepidocrocite (γ -FeOOH) and goethite (α -FeOOH), with only one or two remaining peaks unassigned. This can be seen by direct comparison of patterns in Table 2.6. By comparing the approximate peak areas of the lepidocrocite [020] peak at 6.26 Å and the goethite [110] peak at *ca.* 4.18 Å, it could be estimated that the proportion of crystalline material in the product was *ca.* 70 % lepidocrocite, the majority of the remaining 30 % mainly comprising goethite. In order to do this, the formula % Lp = (Lp/Lp + Gt) x 100 % where Lp = lepidocrocite and Gt = goethite was employed, as used by Carlson and Schwertmann.⁶⁶

The XRPD pattern of the green rust synthesised in undried methanol exhibited very few peaks and those that were present displayed considerable variability in peak width as well as height. The peaks whose maxima occurred at *ca.* 10.69 and 2.54 Å were very broad in comparison with the much sharper peaks at 3.26, 2.82 and 1.99 Å, giving the impression of the presence of two separate phases. Neither of these two phases were, however, readily identifiable upon comparison with known JCPDS patterns or those recorded in the literature for green rusts or iron oxides. However, since data relating to products obtained using similar preparative procedures could not be found in the literature, a similar XRPD pattern was not necessarily to be expected.

Again, the XRPD pattern recorded for the green rust synthesised in dried methanol was not fully identifiable but a much greater number of peaks were recorded for this product than for the previous one. However, since there was such a large number and many were of similar intensities, comparison with existing patterns was extremely difficult. The only obvious correlation with previously recorded green rust patterns^{11, 56, 68, 69} was the presence of the peak at 7.78 Å and possibly at 3.76, 2.69, 2.46 and 2.33 Å but the presence of peaks at spacings similar to the latter is fairly common for a number of materials. In addition, there are still a number of peaks left unidentified even if the presence of a green rust pattern similar to that described is removed. The JCPDS siderite patterns^{37, 38} do also exhibit a maximum intensity peak at 2.79 Å but is not particularly comparable otherwise. Following extensive searching, the presence of any completely similar patterns does not appear to exist in the literature other than the possible similarity to the green rust pattern discussed.

Both of the patterns recorded for the green rusts synthesised in an excess of carbonate ions were very similar in peak positions and the intensities of the peaks. None of the peaks recorded for these products were of a significant intensity upon comparison with the baseline and did not form a pattern comparable with any expected within the literature.

The XRPD pattern recorded for the feroxyhyte preparation in water was more similar to those reported in the literature^{28, 60} than the JCPDS pattern for synthetic feroxyhyte.⁴² The absence of the strongest line in the product XRPD, expected at 4.95 Å when compared with the JCPDS pattern, has previously been attributed to greater crystal growth in the *a* direction rather than the *c* direction.^{29, 60} This was assumed to cause such a broadening effect that the peak at 4.95 Å was no longer identifiable.

By comparison with the aforementioned product, the product formed in methanol as the reaction solvent showed no obvious correlation with any of the patterns expected in the literature. The peaks were all of a reasonable intensity when compared with the baseline noise and were all of a similar peak shape, neither particularly broad nor sharp.

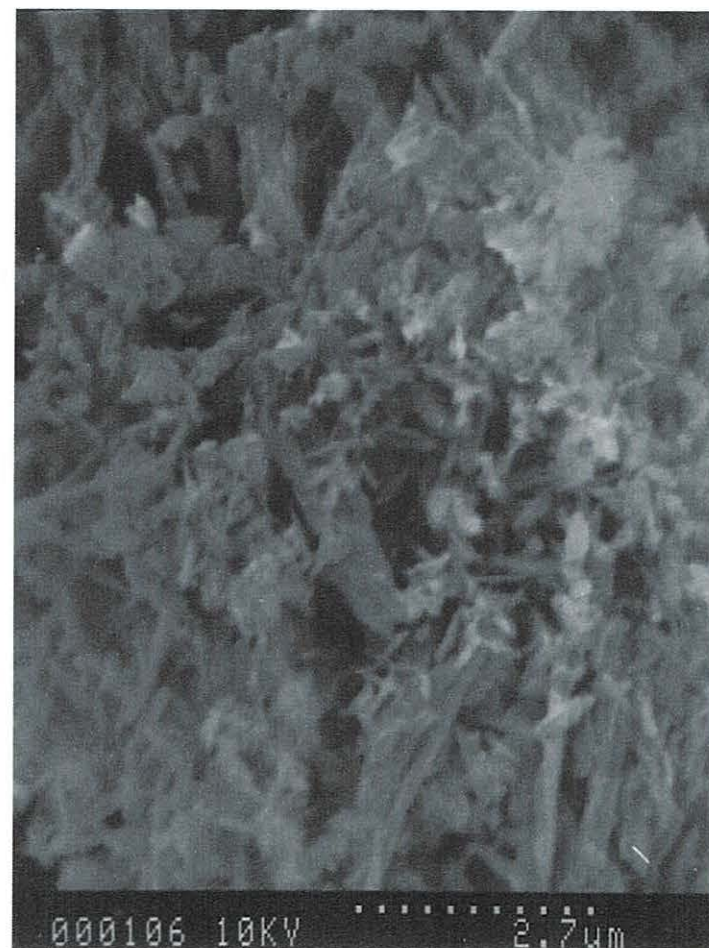
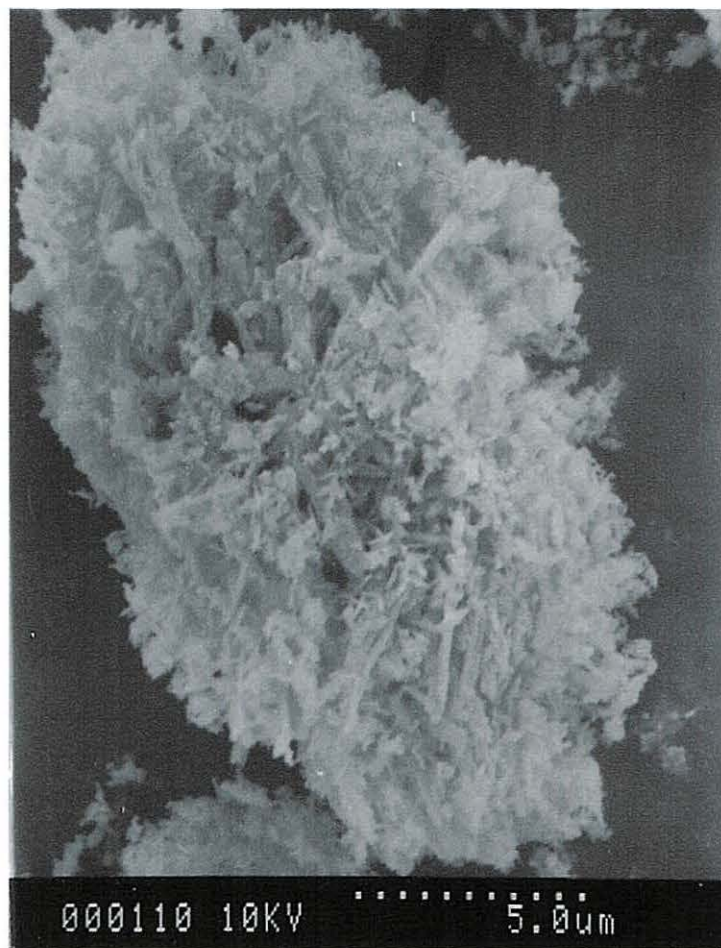
The XRPD pattern recorded for the product which was expected to be an Al-substituted feroxyhyte again showed no similarity to any of the expected products in the literature. However, there do not appear to be any patterns recorded for similar materials in the literature for comparison at this present time. From previous work carried out on the aluminium-substitution of goethites,^{54, 62, 70} it may be expected that the pattern for the Al-substituted product would be comparable with that of the unsubstituted feroxyhyte. The general trends observed in the literature following Al-substitution have been for a gradual shift in the peak positions and a broadening or shape change of the peaks with increased Al-substitution. This was not the case here, as can be seen from Table 2.7. Therefore, from this data it can be concluded that this product does not appear to have undergone isomorphous substitution of aluminium for iron to maintain the feroxyhyte structure.

2.2.4 Scanning Electron Microscopy and Energy-Dispersive Analysis of X-rays

SEM has been utilised here as an additional characterisation method but, since there are only a small number of green rust SEM's available for comparison in the literature, coupled with the fact that some of the synthesis methods used here were novel, much of this work should be viewed as an addition to existing knowledge. SEM's selected as representative of particular products are shown in Figures 2.16-2.21. The SEM's taken for each of these products are described below.

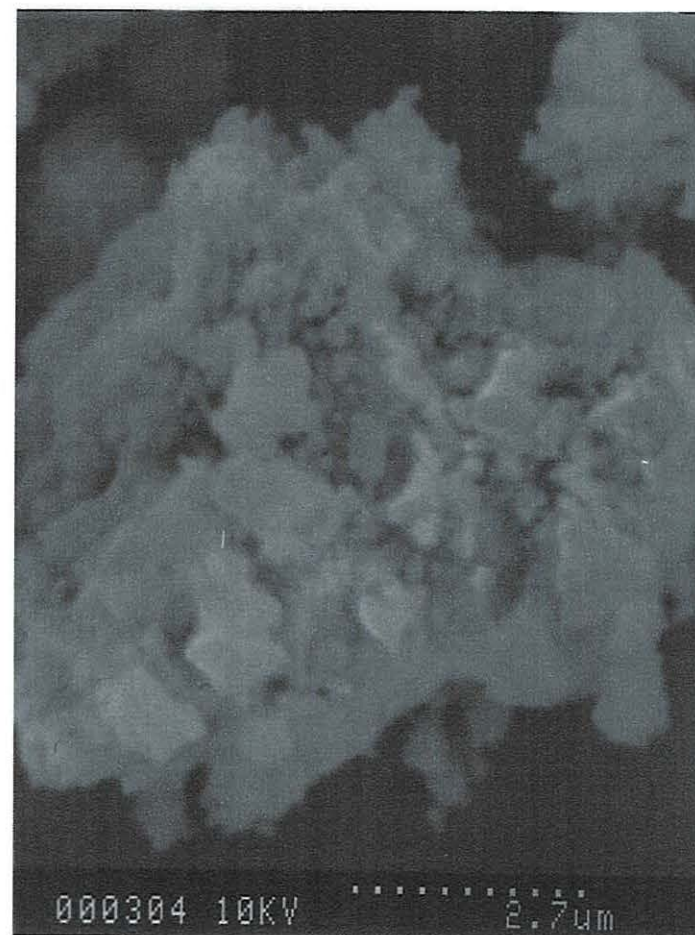
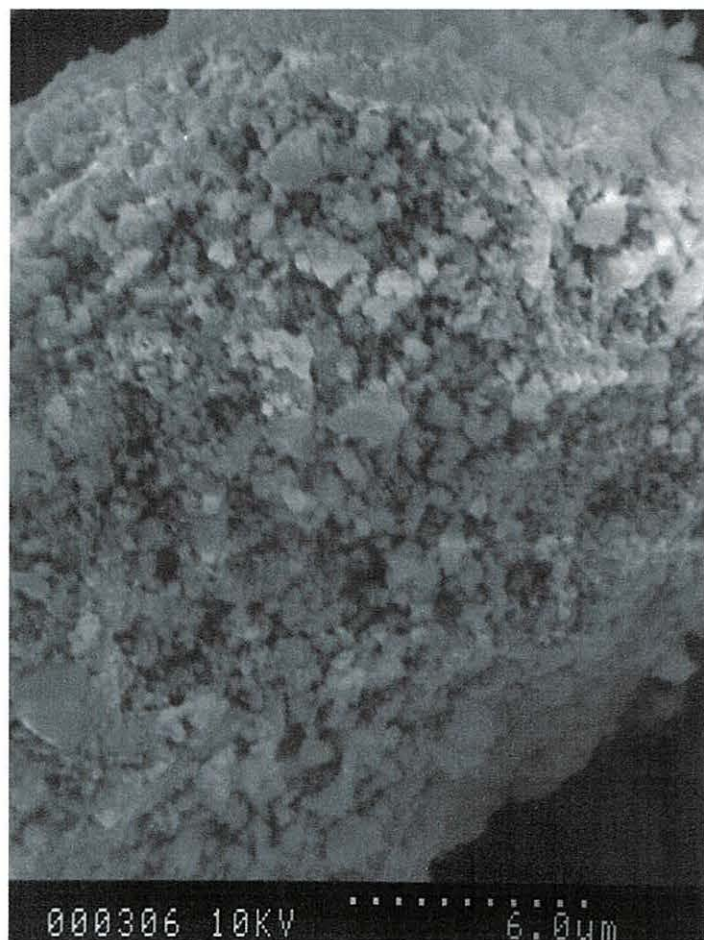
The SEM's shown in Figures 2.16 (a) & (b) for the green rust synthesised in water appear to show a mixture of two quite distinct morphologies, both of which indicate the formation of a relatively high surface area material. The first morphological type is the lath-like crystals up to *ca.* 2.5 μm in length which are similar to those described by Schwertmann and Cornell for lepidocrocite synthesised in the laboratory and found in natural systems *e.g.* soils.²⁹ The second type of crystals, agglomerated with these are only approximately one quarter of the length of the laths and do not appear to be flattened along a plane. These needle-like crystals are typical of goethite and their small size indicative of their method of formation – goethite crystals produced from the oxidation of neutral Fe^{II} solutions have been reported to be generally smaller than those obtained from alkaline Fe^{III} solutions.²⁸

The SEM's shown for the green rusts synthesised in both undried and dried methanol were remarkably similar, as shown in Figures 2.17 (a) & (b) and 2.18 (a) & (b). The agglomerated crystals were up to *ca.* 1 μm across in each sample and appeared to be quite uniform and flattened in appearance, most lying in similar planes. One of the few articles published which illustrates a micrograph of green rust shows thin plate-like hexagonal crystals, which the crystals illustrated in these figures are clearly not.⁷¹ However, they are certainly planar and not unlike some of the crystals observed in the HTc samples discussed in section 2.1.4 and may not be as crystalline as those shown in the literature.



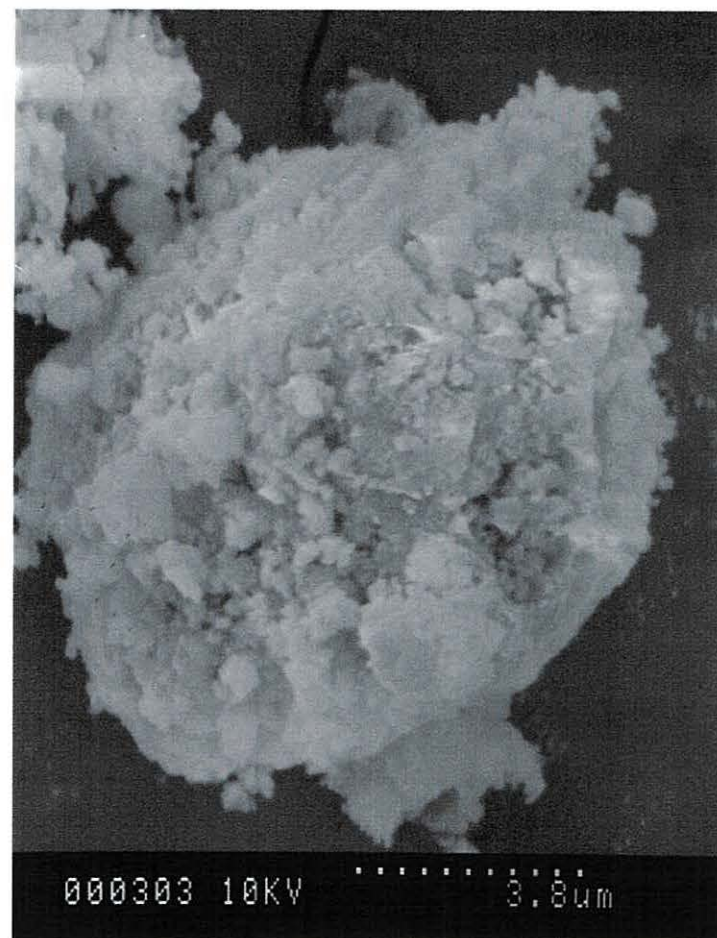
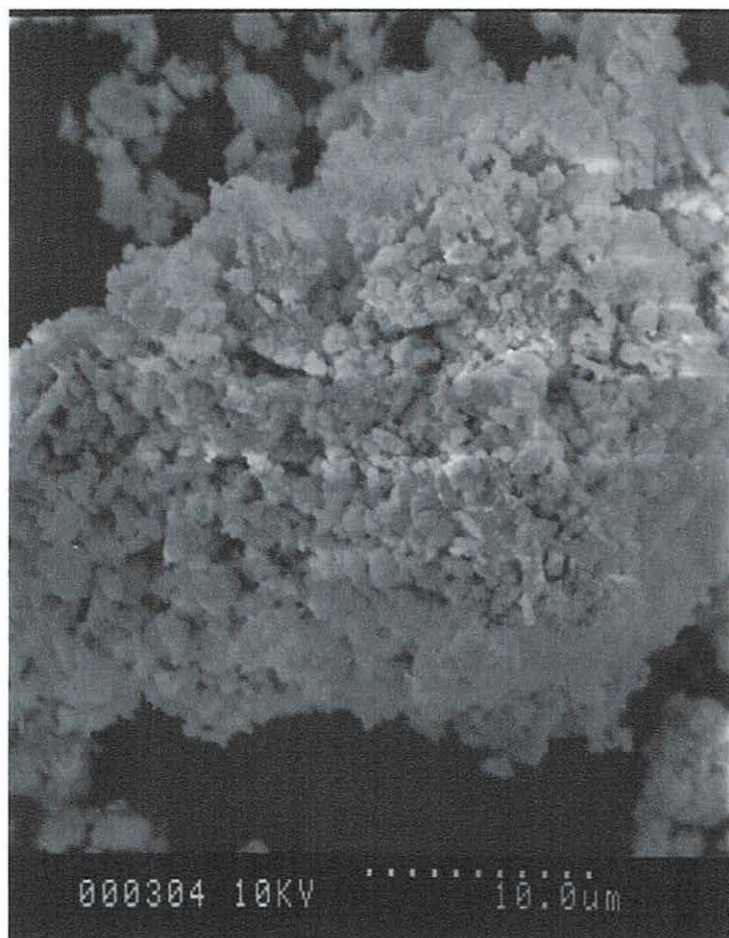
Figures 2.16 (a) & (b): SEM's of green rust product synthesised in H₂O solvent

N.B. Scale bar is represented at the bottom of each micrograph as a series of dots (approximate length $\blacklozenge \longrightarrow \blacklozenge$) with the scale below



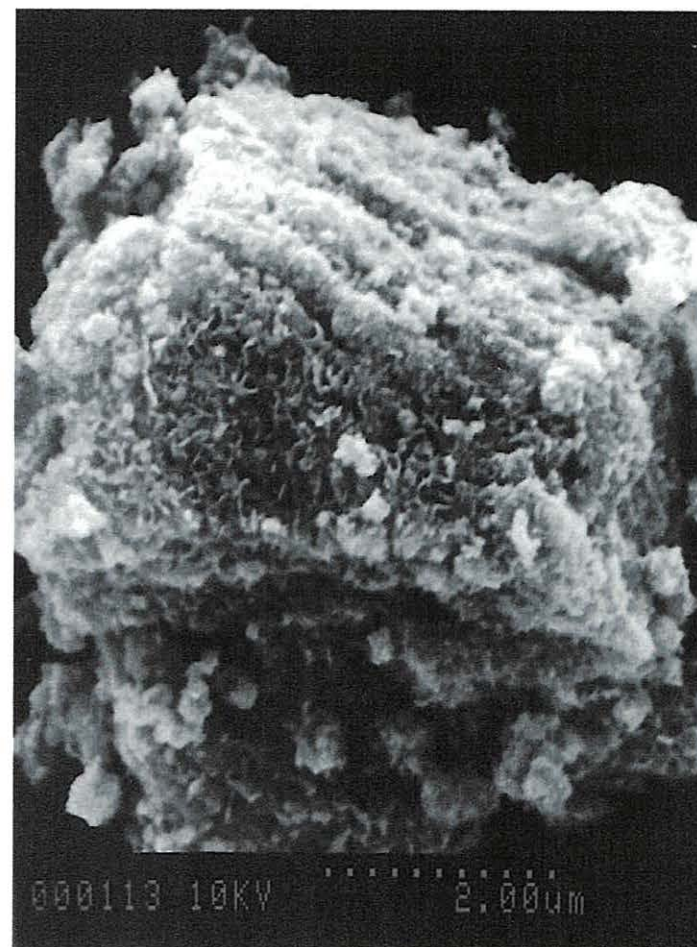
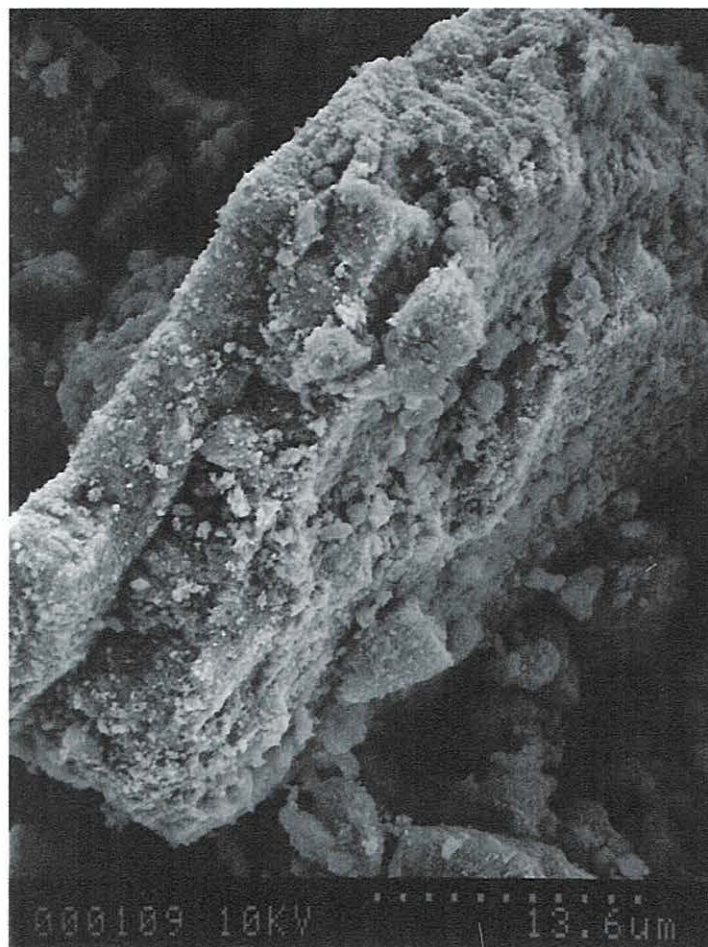
Figures 2.17 (a) & (b): SEM's of green rust product synthesised in CH_3OH solvent (undried)

N.B. Scale bar is represented at the bottom of each micrograph as a series of dots (approximate length $\blacklozenge \longrightarrow \blacklozenge$) with the scale below



Figures 2.18 (a) & (b): SEM's of green rust product synthesised in CH_3OH solvent (dried over MgSO_4)

N.B. Scale bar is represented at the bottom of each micrograph as a series of dots (approximate length $\blacklozenge \longrightarrow \blacklozenge$) with the scale below



Figures 2.19 (a) & (b): SEM's of feroxyhyte synthesised in H₂O solvent

N.B. Scale bar is represented at the bottom of each micrograph as a series of dots (approximate length $\blacklozenge \text{-----} \blacklozenge$) with the scale below

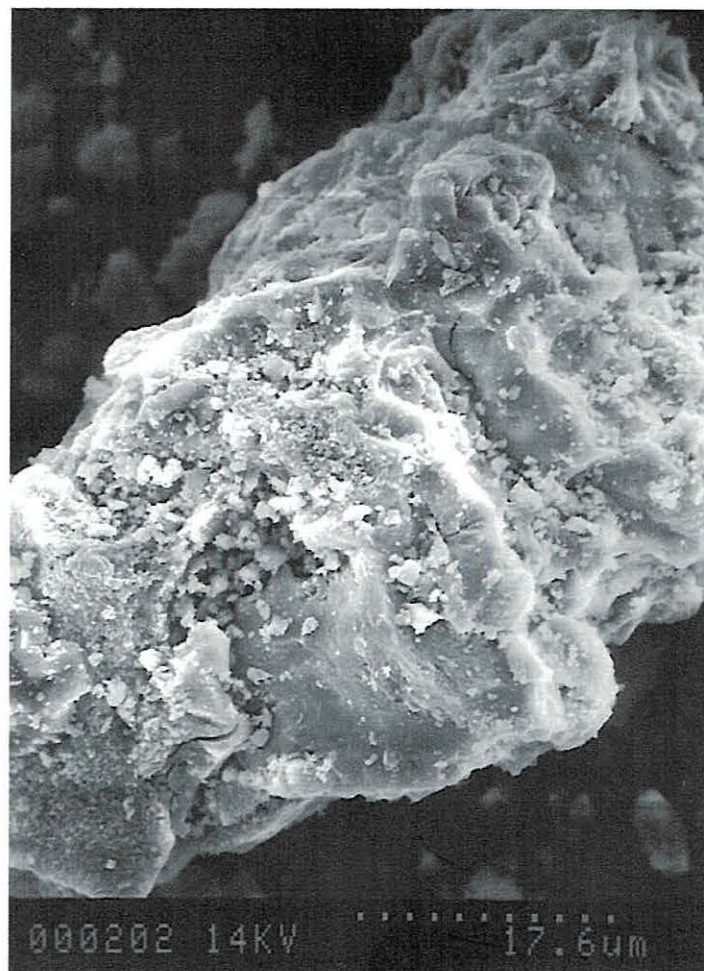


Figure 2.20: SEM of feroxyhyte synthesised in CH_3OH solvent (dried over MgSO_4)

N.B. Scale bar is represented at the bottom of each micrograph as a series of dots (approximate length $\blacklozenge \text{-----} \blacklozenge$) with the scale below

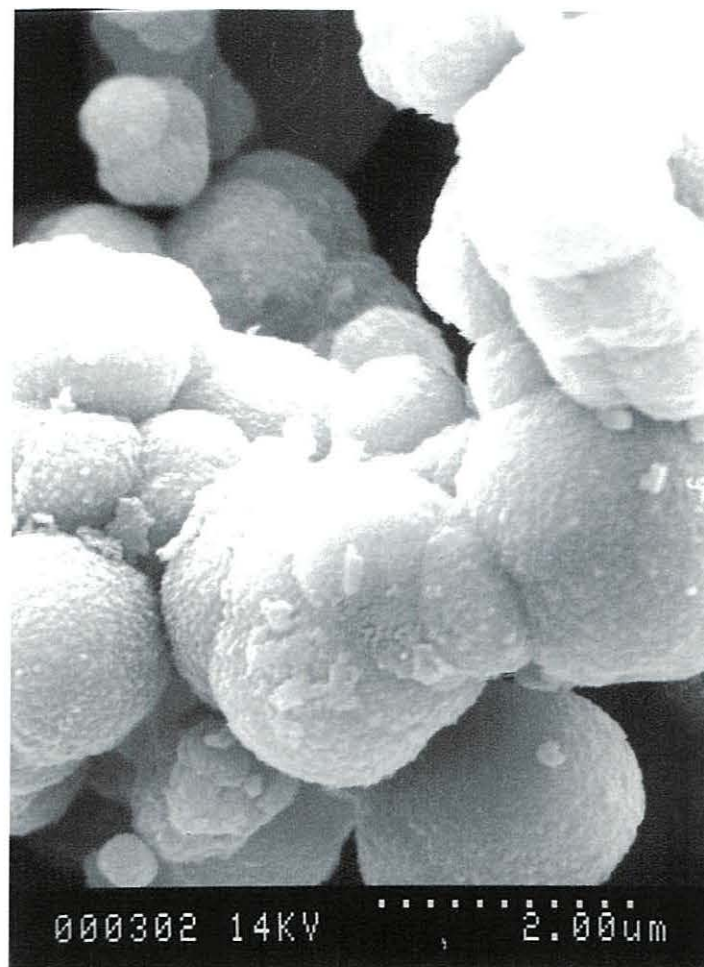


Figure 2.21: SEM of Al-feroxyhyte synthesised in H₂O solvent

N.B. Scale bar is represented at the bottom of each micrograph as a series of dots (approximate length $\blacklozenge \longrightarrow \blacklozenge$) with the scale below

By comparison with the previously described product morphology, the small, plate-like crystals observed for the feroxyhyte product synthesised in water, appeared to be distributed with the edges of a greater number clearly visible, as shown in Figure 2.19 (b). These crystals were up to only *ca.* 0.2 μm across and produced what appeared to be a high surface area material. The formation of these thin platelets has also been observed in the literature for synthetic feroxyhyte.^{28, 29, 60}

One of the few suitable SEM's recorded for the feroxyhyte synthesised in methanol is shown in Figure 2.20. The sample appeared to interact detrimentally with the electron beam, the accelerating voltage of which was reduced to reduce these effects but with little success. The sample appeared to be very smooth across the majority of the surface with only small areas appearing to exhibit areas with increased surface area due to platy crystals. However, it is not clear as to whether this smoothing of the surface may have been an electron beam induced artefact.

The SEM's of the Al-substituted feroxyhyte product exhibited the most strikingly different morphology to that expected, as can be seen in Figure 2.21. The sample consisted of spherical particles of a range of sizes, up to *ca.* 3 μm in diameter. The surface of these spheres did not appear to be completely smooth but the resolution level obtainable using the SEM was insufficient to investigate the surface microtopography further. This spherical morphology was quite unlike that observed in the literature for the known iron oxides. The morphology of the sample did not vary across the sample which eliminates the possibility of a pure aluminium phase but it is possible that this product could be isomorphous with that of an aluminium-based structure. However, the description of materials exhibiting a similar morphology could not be found in the literature.

The EDAX spectra (the results of which are summarised in Table 2.8) were generally as expected, although little information could be taken from the products containing iron solely as the metal species. The comparison of ratios of metals in the products was only applicable for the Al-substituted products which showed a homogeneous dispersal of aluminium and iron throughout the relevant samples, which further suggested that these products were single-phase materials.

Sample		Fe	Al
Green rust	(H ₂ O solvent)	N/A	-
Green rust	(CH ₃ OH solvent – not dried)	N/A	-
Green rust	(CH ₃ OH solvent – MgSO ₄ dried)	N/A	-
Green rust	(excess CO ₃ ²⁻)	N/A	-
Al-green rust	(excess CO ₃ ²⁻)	2.8-3.6	1.4-2.2
Feroxyhyte	(H ₂ O solvent)	N/A	-
Feroxyhyte	(CH ₃ OH solvent – MgSO ₄ dried)	N/A	-
Al-feroxyhyte	(H ₂ O solvent)	5.8-6.4	0.8-1.2

Table 2.8 Summarised EDAX analysis results for green rusts and feroxyhytes (expressed as relative ratios of K α peak intensities)

2.2.5 Conclusions

Whilst a similar preparative procedure was used in each of the attempted green rust syntheses, and each of the products did display the formation of a green/blue coloured air-sensitive intermediate, the characterisation data obtained for each of the products was quite different on the whole. It appears from these results that there are few general conclusions to be drawn throughout the complete range of products described. Therefore, a summary of the characterisation data for each of the products is described below, expressing obvious similarities between products when apparent.

A combination of the IR, XRPD and SEM data described for the green rust product synthesised in water suggested that the product formed following further oxidation was a mixture predominantly comprising lepidocrocite and goethite. Both of these iron oxides may be formed under similar conditions, the carbonate concentration in solution influencing the reaction product with lepidocrocite only forming preferentially under low carbonate concentrations.^{28, 29, 66} Both of these materials are formed *via* a green rust intermediate, however, which indicates that this was formed temporarily but oxidised prior to analysis.

The characterisation data recorded for each of the green rusts formed in methanol was, on the whole, quite unlike that observed previously. The IR's were similar and exhibited the bands expected for an iron oxide and methanol. The XRPD's were quite different

for the two products, particularly in the number of peaks recorded and only the pattern of the product synthesised in dried methanol showed any similarity with the green rust pattern recorded in the literature.^{56, 69} However, the morphology observed for both products in the SEM did appear to be comparable with that seen in some of the HTc's discussed in section 2.1.4. This platy morphology would be expected of a material with a layered structure which could be derived from the green rust structure. Therefore, a hydrotalcite-type structure may have been formed but further investigation would be required to ascertain the structural arrangement in these products.

The characterisation data available for the two green rust products formed in solutions with an excess of carbonate ions present exhibited great similarities. The IR spectra were very similar to those of the HTc's recorded in section 2.1.2 but the XRPD patterns, although similar to one another, were quite different from those expected. There were no similarities found with any literature patterns which suggested that, although the functional groups expected were present with similar symmetry, the final structure was not in a crystalline arrangement similar to the HTc's or goethite.

The feroxyhyte product synthesised in water exhibited much of the characteristics expected for this material. Only the XRPD pattern exhibited a deviation from that expected since the most intense, and some of the other, peaks in the JCPDS pattern were not observed. However, as explained in section 2.2.3, this has been recognised previously in the literature.^{28, 60} The SEM's confirmed the platelet morphology which was expected, given the layered structure of green rust and the relatively minor structural changes necessary to form feroxyhyte from green rust *i.e.* oxidation of Fe^{II} to Fe^{III} and the loss of interlayer carbonate and water.

The iron oxide synthesised in methanol which had been dried over MgSO_4 showed some evidence of the presence methanol in the IR spectrum, the XRPD pattern was quite unlike anything recorded previously as far as peak positions were concerned and the SEM's illustrated a material which was subject to degradation fairly readily when exposed to the electron beam. Since a rapid oxidation step was not involved in its synthesis, it is unlikely that this product is of the feroxyhyte-type but, without further studies it is difficult to draw further conclusions regarding its structural type.

The Al-substituted 'feroxyhyte' did not exhibit an IR spectrum, XRPD pattern or morphology expected for a feroxyhyte either. This was surprising since the previous studies of Al-substituted iron oxides such as goethite illustrated that the substitutions were truly isomorphous *i.e.* little or no change to the structure as a result of cation exchange. The XRPD pattern was quite unlike that of feroxyhyte and the SEM's illustrated a material which was of a completely different bulk morphology. Again, it is difficult to ascertain as to what the product formed actually was but it did appear to be homogeneous and quite different to the other recognised iron oxides.

2.3 References

- 1 S. Carlino, *Chem. Brit.*, 1997, September, 59.
- 2 A. Vaccari, *Appl. Clay Sci.*, 1999, **14**, 161.
- 3 T. Baird, K.C. Campbell, P.J. Holliman, R. Hoyle, D. Stirling and B.P. Williams, *J. Chem. Soc., Faraday Trans.*, 1995, **91**(18), 3219.
- 4 K.K. Rao, M. Gravelle, J. Sanchez-Valente and F. Figueras, *J. Catal.*, 1998, **173**, 115.
- 5 W.T. Reichle, *Solid State Ionics*, 1986, **22**, 135.
- 6 R. Allman, *Acta Cryst.*, 1968, **B24**, 972.
- 7 H.F.W. Taylor, *Min. Mag.*, 1969, **37**, 338.
- 8 H.F.W. Taylor, *Min. Mag.*, 1973, **39**, 377.
- 9 C. Frondel, *Am. Mineral.*, 1941, **26**, 295.
- 10 F. Cavani, F. Trifirò and A. Vaccari, *Catal. Today*, 1991, **11**, 173.

- 11 R.M. Taylor and R.M. McKenzie, *Clays and Clay Minerals*, 1980, **28**(3), 179.
- 12 R.M. Taylor, *Clay Minerals*, 1982, **17**, 369.
- 13 S.M. Auer, J-D. Grunwaldt, R.A. Köppel and A. Baiker, *J. Mol Cat. A: Chemical*, 1999, **139**, 305.
- 14 V.C. Farmer, in *The Infrared Spectra of Minerals*, Mineralogical Society Monograph 4, V.C. Farmer (Ed.), The Mineralogical Society, London, 1974.
- 15 D. Stirling, *The Sulfur Problem – Cleaning Up Industrial Feedstocks* (Royal Society of Chemistry Clean Technology Monographs, Series Editor J.H. Clark), The Royal Society of Chemistry, Cambridge, 2000.
- 16 P.A. Estep-Barnes, in *Physical Methods in Determinative Mineralogy* (2nd Edition), J. Zussman (Ed.), Academic Press, London, 1977.
- 17 W.B. White, in *The Infrared Spectra of Minerals*, Mineralogical Society Monograph 4, V.C. Farmer (Ed.), The Mineralogical Society, London, 1974.
- 18 A.K. Brisdon, *Inorganic Spectroscopic Methods*, Oxford University Press, Oxford, 1998.
- 19 C.L. Peterson, D.L. Perry, H. Masood, H. Lin, J.L. White, S.L. Hem, C. Fritsch and F. Haeusler, *Pharm. Res.*, 1993, **10**, 998.
- 20 S. Miyata, *Clays and Clay Minerals*, 1975, **23**, 369.
- 21 J.T. Klopogge and R.L. Frost, *J. Solid State Chem.*, 1999, **146**, 506.
- 22 M.J. Hernandez-Moreno, M.A. Ulibarri, J.L. Rendon and C.J. Serna, *Phys. Chem. Minerals*, 1985, **12**, 34.

- 23 K. Nakamoto, *Infrared and Raman Spectra of Inorganic and Coordination Compounds* (4th Edition), John Wiley & Sons, Chichester, 1986.
- 24 F. Millange, R.I. Walton and D. O'Hare, *J. Mater. Chem.*, 2000, **10**, 1713.
- 25 D.L. Bish and G.W. Brindley, *Am. Mineral.*, 1977, **62**, 458.
- 26 C.J. Serna, J.L. White and S.L. Hem, *J. Pharm. Sci.*, 1978, **67**, 324.
- 27 V.C. Farmer and A.N. Lazarev, in *The Infrared Spectra of Minerals*, Mineralogical Society Monograph 4, V.C. Farmer (Ed.), The Mineralogical Society, London, 1974.
- 28 R.M. Cornell and U. Schwertmann, *The Iron Oxides – Structure, Properties, Reactions, Occurrence and Uses*, VCH, Weinheim, 1996.
- 29 U. Schwertmann and R.M. Cornell, *Iron Oxides in the Laboratory*, VCH, Weinheim, 1991.
- 30 D.M. Moore and R.C. Reynolds Jr., *X-Ray Diffraction and the Identification and Analysis of Clay Minerals*, Oxford University Press, Oxford, 1989.
- 31 JCPDS Card N^o. 14-0191
- 32 S.K. Yun and T.J. Pinnavaia, *Inorg. Chem.*, 1996, **35**, 6853.
- 33 V.R.L. Constantino and T.J. Pinnavaia, *Inorg. Chem.*, 1995, **34**, 883.
- 34 V. Rives, *Inorg. Chem.*, 1999, **38**, 406.
- 35 M.A. Drezdon, *Inorg. Chem.*, 1988, **27**, 4628.
- 36 JCPDS Card N^o. 25-0513

- 37 JCPDS Card N^o. 12-0531
- 38 JCPDS Card N^o. 08-0133
- 39 JCPDS Card N^o. 01-1114
- 40 JCPDS Card N^o. 11-0614
- 41 JCPDS Card N^o. 03-0249
- 42 JCPDS Card N^o. 22-0353
- 43 S. Miyata, *Clays and Clay Minerals*, 1983, **31**(4), 305.
- 44 M. Köckerling, G. Geismer, G. Henkel and H-F. Nolting, *J. Chem. Soc., Faraday Trans.*, 1997, **93**(3), 481.
- 45 M.C. Gastuche, G. Brown and M.M. Mortland, *Clay Minerals*, 1967, **7**, 177.
- 46 G. Brown and M.C. Gastuche, *Clay Minerals*, 1967, **7**, 193.
- 47 N.N. Greenwood and A. Earnshaw, *Chemistry of the Elements*, Pergamon Press, Oxford, 1993.
- 48 C. Misra and A.J. Perrotta, *Clays and Clay Minerals*, 1992, **40**(2), 145.
- 49 A. Béres, I. Pálanko, I. Kiricsi, J.B. Nagy, Y. Kiyozumi and F. Mizukami, *App. Catal. A: General*, 1999, **182**, 237.
- 50 J.E. Welton, *SEM Petrology Atlas*, The American Association of Petroleum Geologists, Tulsa, 1984.
- 51 C.W. Beck, *Am. Mineral.*, 1950, **35**, 985.

- 52 W. Smykatz-Kloss, *Differential Thermal Analysis – Application and Results in Mineralogy*, Springer-Verlag, New York, 1974.
- 53 S. Miyata, *Clays and Clay Minerals*, 1980, **28**(1), 50.
- 54 D.G. Schulze and U. Schwertmann, *Clay Minerals*, 1984, **19**, 521.
- 55 R.C. Mackenzie and, in part, G. Berggren, *in* *Differential Thermal Analysis, Volume 1 – Fundamental Aspects*, R.C. Mackenzie (Ed.), Academic Press, London, 1970.
- 56 R.M. Taylor, *Clay Minerals*, 1980, **15**, 369.
- 57 R.M. Taylor and U. Schwertmann, *Clay Minerals*, 1974, **10**, 299.
- 58 V.A. Drits, B.A. Sakharov and A. Manceau, *Clay Minerals*, 1993, **28**, 209.
- 59 U. Schwertmann and R.M. Taylor, *in* *SSA Book Series: 1 – Minerals in Soil Environments* (2nd Edition), J.B. Dixon and S.B. Weed (Eds.), Soil Science Society of America, Madison, 1989.
- 60 T. Baird, K.C. Campbell, P.J. Holliman, R. Hoyle, D. Stirling and B.P. Williams, *J. Chem. Soc. Faraday Trans.*, 1996, **92**(3), 445.
- 61 D.G. Schulze and U. Schwertmann, *Clay Minerals*, 1987, **22**, 83.
- 62 S. Mann, R.M. Cornell and U. Schwertmann, *Clay Minerals*, 1985, **20**, 255.
- 63 U. Schwertmann and H. Stanjek, *Clays and Clay Minerals*, 1998, **46**(3), 317.
- 64 H.C.B. Hansen, *Clay Minerals*, 1989, **24**, 663.
- 65 R.M. Silverstein, G.C. Bassler and T.C. Morrill, *Spectrometric Identification of Organic Compounds* (5th Edition), John Wiley & Sons Inc., New York, 1991.

- 66 L. Carlson and U. Schwertmann, *Clay Minerals*, 1990, **25**, 65.
- 67 JCPDS Card N°. 08-0098
- 68 R.M. Taylor, U. Schwertmann and H. Fechter, *Clay Minerals*, 1985, **20**, 147.
- 69 G.W. Brindley and G. Brown, in *Crystal Structures of Clay Minerals and their X-ray Identification*, Mineralogical Society Monograph No. 5, G.W. Brindley and G. Brown (Eds.), Mineralogical Society, London, 1984.
- 70 R.G. Ford, P.M. Bertsch and J.C. Seaman, *Clays and Clay Minerals*, 1997, **45**(5), 769.
- 71 I.R. McGill, B. McEnany and D.C. Smith, *Nature*, 1976, **259**, 200.

Chapter 3

Precursor Activation

3.1 Calcination Studies

3.1.1 Methodology

There is a considerable quantity of information available in the literature which relates to the study of the changes which occur upon heating materials with a hydrotalcite-type structure. The majority of these studies have been conducted with the eventual aim of utilising the calcined materials as heterogeneous catalysts.¹ As outlined in Chapter 1, the use of HTc's enables the imposition of the strict control of the concentration of each metal within the material, leading to well-dispersed and stable mixed metal oxides with increased surface areas following calcination. A relatively low calcination temperature has been shown to be necessary to produce such a material from the HTc precursor and a range of mixed metal oxides may be produced as a result of the allowance of the HTc structure to accommodate a range of metal cations.² The range of combinations of these cations is wide and the possible synergistic effects hold great potential. This has resulted in the generation of much interest and research in the area with the aim of producing catalysts capable of catalysing a wide range of reactions.¹ However, the majority of research into the characterisation of the calcined materials has been focussed upon the $\text{Mg}_6\text{Al}_2\text{HTc}$ system. This has probably been because the chemical and physical properties of this precursor material are so well understood and the resulting product of calcination has been shown to possess interesting basic properties.³ There has, however, been some research investigating the characterisation of calcined MgFeHTc 's (Al^{3+} replaced by Fe^{3+} rather than Mg^{2+} by Fe^{2+} as in this study) which has been of interest since these materials have been shown to form the spinel phase at a much lower temperature than has been observed for the MgAlHTc 's.^{4, 5} As described in Chapter 1, the $\text{Mg}_6\text{Al}_2\text{HTc}$ has generally been regarded to form spinel (MgAl_2O_4) at *ca.* 1273 K.^{1, 2} It has been observed in XRPD patterns as low as 1073 K^{6, 7} but magnesioferrite

(MgFe_2O_4), which has an inverse spinel structure,^{8, 9} has been reported as a MgFeHTc calcination product as low as 673 K.^{4, 5} Spinel-type products are generally undesirable in the production of potential catalysts due to their decreased surface area and subsequent loss in activity when contrasted with that of the HTc calcined at *ca.* 723 K.¹⁰ Calcination at 723 K is generally regarded to be an optimum temperature for the calcination of $\text{Mg}_6\text{Al}_2\text{HTc}$'s since the general HTc morphology is maintained but with an increased surface area due to the formation of pores as carbon dioxide and steam burst through the layers upon heating.^{2, 6, 10, 11} Therefore, the calcination of the MgAlHTc and MgFeAlHTc precursors described in the previous Chapter of this thesis is investigated here and comparisons made with the MgAlHTc 's and MgFeHTc 's reported in the literature. The majority of results described below relate to the calcination of the range of Fe-substituted HTc materials described in the previous Chapter, at 723 K. Some data was recorded at other temperatures and is mentioned where relevant but this calcination temperature was selected as a result of the DTA results detailed in the previous Chapter combined with the observations noted in the literature relating to the increased surface area *etc.*, as described above.

The apparatus used during the calcination studies was purpose-built for this study and is described in Chapter 7, section 7.2. Gas hourly space velocity values were used throughout each set of experiments for consistency since they allowed the volume of gas passing through the calcination tube to remain constant with respect to the volume of material being calcined. This is in contrast with the majority of research described in the literature which quotes a set gas flow rate versus mass of material to be calcined.

3.1.2 IR Spectroscopy

The IR spectra recorded for each of the HTc's following calcination at 723 K were very similar in appearance. Because of this, they are explained collectively below and comparisons made with the spectra previously described for the HTc's prior to calcination and also with those of HTc calcination products described in the literature. The absorption bands are summarised for each product in Table 3.1 for comparison and some representative spectra are illustrated in Figure 3.1 (a-c).

Table 3.1 Infrared absorption bands (cm^{-1}) recorded between 4000 and 400 cm^{-1} for HTc's calcined at 723 K

Mg₆Al₂HTc Exptl. method 1	Mg₆Al₂HTc Exptl. method 2	Mg₅FeAl₂HTc	Mg₄Fe₂Al₂HTc	Mg₃Fe₃Al₂HTc	Mg₂Fe₄Al₂HTc	MgFe₅Al₂HTc	Fe₆Al₂HTc
3448 m	3448 m	3448 m	3448 s	3448 s	3446 m	3448 m/s	3448 m
1654 w, br	1654 w, br	1654 w, br	1654 w, br	1650 w, br	1636 w, br	1637 w, br	1624 w, br
		1508 w, br	1508 w, br	1508 w, br	1508 w, br		
1400 w, br	1400 w, br	1400 w, br	1410 w, br	1400 w, br	1400 w, br	1400 w, br	1400 w, br
1000 w, br	1000 w, br	1000 br, shldr	1000 br, shldr	1000 br, shldr	1000 br, shldr	1000 br, shldr	1000 vw, br
800 m, br	800 m, br	800 m, br	800 m, br	800 br, shldr			
670 m	670 m	670 m, br	670 m	670 s	670 m, shldr	670 m, shldr	
						530 s, br	550 s
477 s	472 s	472 s	470 s	472 s	492 s		470 m/s

N.B. HTc formulae correspond to uncalcined materials

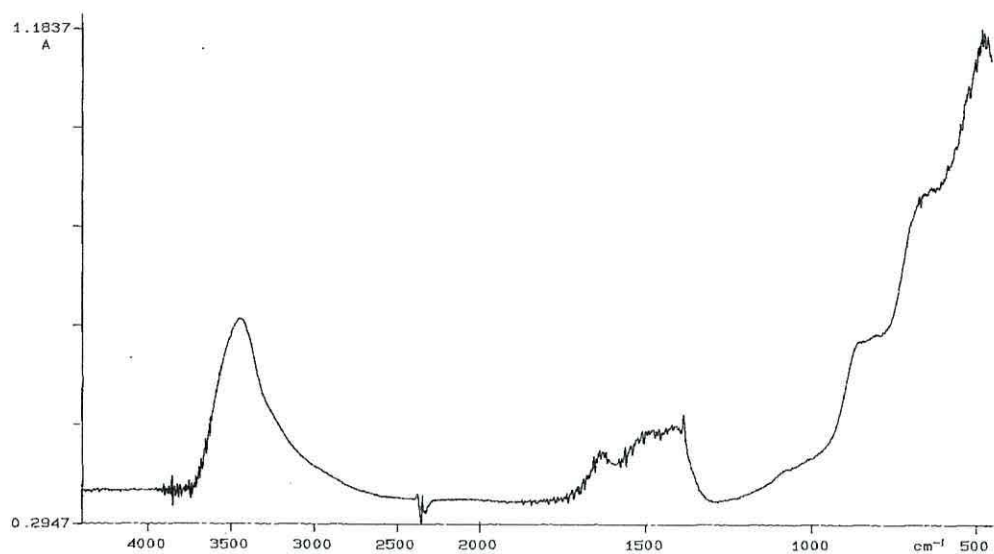


Figure 3.1 (a) IR spectrum of $\text{Mg}_6\text{Al}_2\text{HTc}$ product (Exptl. Method 1) calcined at 723 K

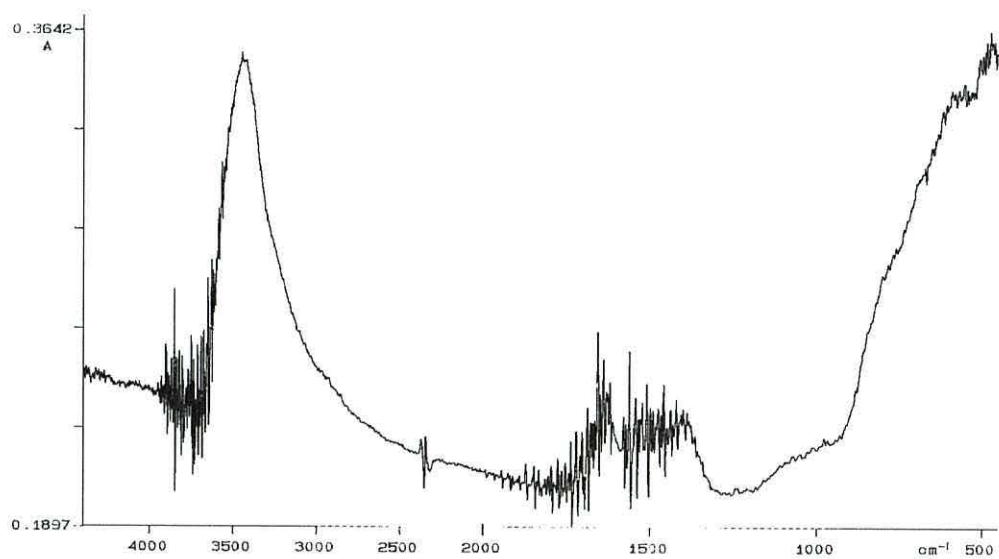


Figure 3.1 (b) IR spectrum of $\text{Mg}_3\text{Fe}_3\text{Al}_2\text{HTc}$ product calcined at 723 K

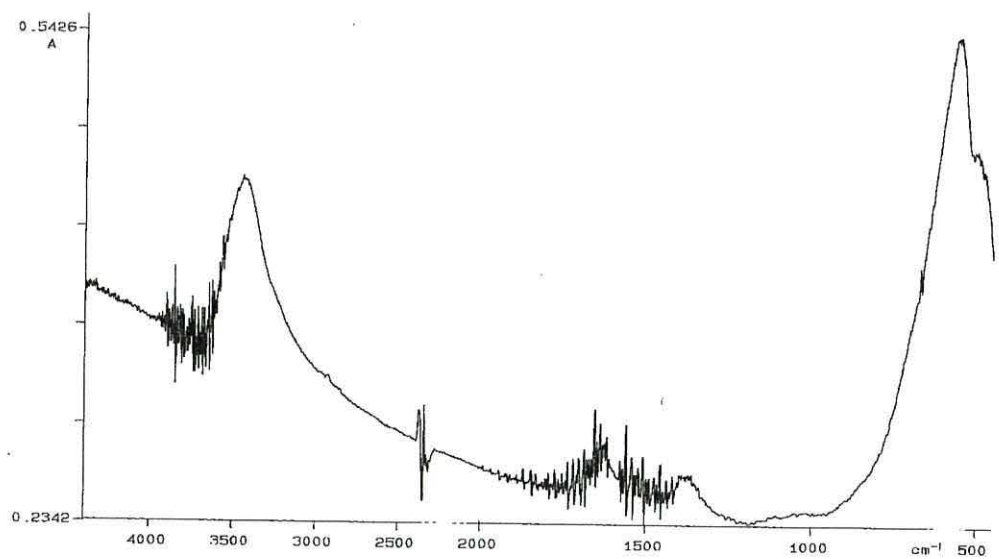


Figure 3.1 (c) IR spectrum of $\text{Fe}_6\text{Al}_2\text{HTc}$ product calcined at 723 K

Each of the spectra exhibited an absorption band which was centred consistently at *ca.* 3448 cm^{-1} . This was present at the characteristic OH stretching frequency but it was expected that the structure would have undergone dehydroxylation at this stage. However, here this absorption band was notably weaker in each case than that recorded for the uncalcined materials described in the previous Chapter and the peak maxima, although fairly broad, appeared to be more consistent in position with respect to frequency. These properties indicated that this absorption band was a result of fewer OH groups but present in a similar environment for each sample. Therefore, this absorption was assigned to surface water and possibly some reconstituted hydroxyl groups within the samples. The samples were analysed as quickly as was practicable following calcination but, without specialist apparatus, some re-adsorption of moisture from the air was unavoidable. Rey and co-workers utilised *in-situ* calcination in an FTIR spectrometer equipped with a quartz vacuum cell with CaF_2 windows to obtain IR spectra of calcined MgAlHTc 's.¹² The spectra they recorded at 673-973 K did not exhibit any peaks in the 2000-4000 cm^{-1} region which indicates that the structural hydroxyl groups had decomposed at this temperature and that a peak occurring in this region could justifiably be assigned to adsorbed water. In addition, none of the spectra recorded for the calcined HTc's described in Table 3.1 exhibited as obvious a shoulder as was previously seen at *ca.* 3000 cm^{-1} for the HTc precursors. This band had previously been assigned to hydrogen bonding within the interlayer region. Therefore, it has been assumed that there was no significant absorption of water and subsequent reconstruction of the interlayer region. A weak absorption band was also recorded at *ca.* 1650 cm^{-1} in each of the spectra which was assigned to the O-H bending mode of surface OH and/or water.

Arguably the most significant difference in the spectra recorded for the calcined materials with the HTc precursors was the absence of any strong absorption bands in the 1360-1500 cm^{-1} region. Peaks in this area of the spectra were previously assigned to the presence of interlayer carbonate ions in the HTc's. Instead, very weak bands were recorded at *ca.* 1400 and 1500 cm^{-1} for the calcined HTc's. This reduction in intensity of the carbonate absorption bands confirmed the loss of the majority of interlayer carbonate from the samples.¹³ The presence of weak bands in this region was attributed to the re-adsorption of some CO_2 from the atmosphere and possibly due to the retention of a minimal amount of carbonate within the structure. This retention of a minor

proportion of the interlayer carbonate had previously been observed by both Hibino *et al.* and Rey and co-workers and was accompanied by a splitting of the ν_3 carbonate band into two bands centred at *ca.* 1380 and 1520 cm^{-1} .^{12, 14} A band had previously been observed in the HTc precursors discussed in the previous Chapter at *ca.* 1370 cm^{-1} which was then assigned to the ν_3 vibration of CO_3^{2-} . This band was absent from the spectra of the calcined HTc's and, instead, two weak bands were observed at *ca.* 1400 and 1500 cm^{-1} for most of the calcined products indicating similar phenomena to those observed by Hibino *et al.* and Rey and co-workers, as described above. A weak, broad band at *ca.* 1000 cm^{-1} was observed for each of the calcined HTc's. This was not previously evident in the spectra of the HTc precursors and was attributed to the previously inactive ν_1 carbonate vibration.¹⁵ This splitting of the ν_3 band and the appearance of the band at *ca.* 1000 cm^{-1} can be attributed to lowering of the carbonate symmetry from D_{3h} to C_{2v} as it becomes coordinated to the (now) mixed metal oxide layers rather than being in the relatively unperturbed state adopted in the interlayers of the HTc precursor materials.

Assignment of the remaining bands observed for the calcined HTc's below 1000 cm^{-1} was more difficult and a difference in the spectra was noted in this region between the products which were obtained from the HTc's with idealised formulae of $\text{Mg}_6\text{Al}_2\text{HTc}$ to $\text{Mg}_3\text{Fe}_3\text{Al}_2\text{HTc}$ and those with higher Fe-for-Mg substitution. These latter materials exhibited bands in this region which were indicative of iron oxides.¹⁶ The more intense bands in this region are indicative of the Fe-O stretches in a number of iron oxides but the spectrum produced from the product of the calcined $\text{Fe}_6\text{Al}_2\text{HTc}$ was most similar to that of haematite (Fe_2O_3) in this region.^{16, 17} The bands observed for the calcined $\text{Mg}_6\text{Al}_2\text{HTc}$ to $\text{Mg}_3\text{Fe}_3\text{Al}_2\text{HTc}$ products below 1000 cm^{-1} were consistent in both their positions and intensities throughout the range but accurate assignment was difficult. The band at *ca.* 670 cm^{-1} may be assigned to the residual carbonate ν_4 vibration and the bands at *ca.* 800 and 470 cm^{-1} due to M-O stretches within the calcined material.⁷

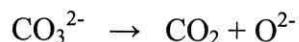
3.1.3 X-ray Powder Diffraction

The data recorded for the XRPD patterns of the HTc's calcined at 723 K is reported in Table 3.2a, together with the JCPDS pattern for hydrotalcite. A number of patterns for relevant materials are also provided in Table 3.2b for comparison.

A clear difference was observable between the patterns recorded for the calcined HTc's obtained from the precursors with idealised formulae in the range $\text{Mg}_6\text{Al}_2\text{HTc}$ to $\text{Mg}_3\text{Fe}_3\text{Al}_2\text{HTc}$ when compared with those obtained from the high Fe-for-Mg substituted calcined materials. The former exhibited just three peaks at *ca.* 6.0-6.5 Å, *ca.* 2.53 Å and *ca.* 2.10 Å; the first tended to be extremely broad and its position, therefore, difficult to accurately ascertain. In contrast, the patterns recorded for the high Fe content materials exhibited a much larger number of peaks which were considerably sharper and easier to resolve.

The peak at *ca.* 6.0-6.5 Å appeared to originate from the peak representative of the HTc basal spacing, particularly when contrasted with the peak recorded in this region for the uncalcined HTc and the HTc calcined at 523 K, as shown in Table 3.3 which highlights this shift.

This decrease in basal spacing has been reported on numerous occasions in the literature^{7, 10, 12, 14, 18-23} but a satisfactory theory for its value does not appear to have been reached as yet. Brindley and Kikkawa were amongst the first to note this phenomenon when a sample of hydrotalcite was calcined at *ca.* 533 K,²² postulating that it was a consequence of the decomposition of the interlayer CO_3^{2-} ions;



They proposed that the oxygen anions resulting from this decomposition remained in the interlayer spacing and suggested that they could pack more closely than the bulkier CO_3^{2-} ions, resulting in the reduction in the basal spacing which was noted. However, decarbonation studies by Hibino *et al.* have shown that the majority of CO_2 is evolved as a result of the decomposition of interlayer carbonate ions at *ca.* 673 K and above.^{14, 33}

Table 3.2a X-ray powder diffraction d-spacing results (Å) for HTc's calcined at 723 K (relative intensities in parentheses)

Hydrotalcite ²⁴ (Mg ₆ Al ₂ HTc)	Mg ₆ Al ₂ HTc (method 1)	Mg ₆ Al ₂ HTc (method 2)	Mg ₅ FeAl ₂ HTc	Mg ₄ Fe ₂ Al ₂ HTc	Mg ₃ Fe ₃ Al ₂ HTc	Mg ₂ Fe ₄ Al ₂ HTc	MgFe ₅ Al ₂ HTc	Fe ₆ Al ₂ HTc	Haematite ²⁵ (Fe ₂ O ₃)
7.69 (100)								7.70 (4)	
	6.03 (26) broad	6.26 (23) broad	6.40 (17) broad	6.33 (27) broad	6.48 (37) broad				
								6.07 (2)	
3.88 (70)									
								3.66 (24)	3.66 (25)
						2.95 (29)			
								2.83 (17)	
						2.76 (46)			
						2.69 (51)	2.68 (87)	2.69 (81)	2.69 (100)
2.58 (20)									
	2.53 (11) broad		2.54 (25)	2.53 (53)	2.51 (100)	2.52 (100)	2.52 (100)	2.50 (100)	2.51 (50)
						2.35 (17)			
2.30 (20)									2.29 (2)
						2.24 (37)	2.23 (84)	2.23 (22)	
								2.19 (51)	2.20 (30)
	2.10 (100)	2.10 (100)	2.10 (100)	2.11 (100)	2.10 (50)	2.09 (26)			
						2.06 (25)	2.05 (11)		2.07 (2)
						2.03 (19)	2.03 (10)	2.03 (4)	
						2.00 (15)			
1.96 (20)						1.97 (10)	1.97 (22)	1.97 (6)	
						1.84 (4)	1.84 (3)	1.83 (22)	1.84 (40)
							1.79 (12)		
1.75 (10)						1.71 (8)	1.72 (20)		
							1.69 (18)	1.68 (50)	1.69 (60)
1.65 (10)									1.63 (4)
						1.60 (11)		1.59 (4)	1.60 (16)
							1.57 (3)		
1.53 (20)						1.55 (12)		1.55 (1)	
1.50 (20)						1.50 (30)	1.51 (22)	1.51 (2)	1.48 (35)

Table 3.2b Literature values of X-ray powder diffraction d-spacings (Å) (relative intensities in parentheses) for reference materials

Hydrotalcite ²⁴ (Mg ₆ Al ₂ HTc)	Periclase ²⁶ (MgO)	Spinel ^{27, 28} (MgAl ₂ O ₄)	Magnesioferrite ²⁹ (MgFe ₂ O ₄)	Boehmite ³⁰ (AlOOH)	γ-Alumina ³¹ (γ-Al ₂ O ₃)	Magnetite ³² (Fe ₃ O ₄)	Haematite ²⁵ (Fe ₂ O ₃)
7.69 (100)							
				6.11 (100)			
			4.83 (5)			4.85 (40)	
		4.68 (50)/4.67 (4)			4.55 (10)		
3.88 (70)							
		3.35 (10)					3.66 (25)
				3.16 (65)			
			2.97 (50)			2.97 (70)	
		2.83 (50)/2.86 (40)					
					2.78 (15)		
		2.71 (10)					2.69 (100)
2.58 (20)							
			2.53 (100)			2.53 (100)	2.51 (50)
	2.42 (10)	2.43 (100)/2.44 (100)			2.39 (35)	2.42 (10)	
2.30 (20)		2.34 (10)/2.33 (3)		2.34 (55)			2.29 (2)
		2.25 (10)			2.28 (20)		
	2.10 (100)		2.09 (50)			2.10 (70)	2.20 (30)
		2.02 (80)/2.02 (58)					
				1.98 (6)	1.98 (100)		2.07 (2)
1.96 (20)							
				1.86 (30)/1.85 (25)			1.84 (40)
		1.82 (3)					
				1.77 (6)			
1.75 (10)		1.73 (10)					
			1.71 (30)			1.71 (60)	1.69 (60)
1.65 (10)		1.65 (30)/1.65 (10)		1.66 (14)			1.63 (4)
		1.59 (5)	1.61 (70)			1.61 (85)	1.60 (16)
		1.55 (80)/1.56 (45)					
1.53 (20)				1.53 (6)	1.52 (10)		
1.50 (20)							1.48 (35)

Mg ₆ Al ₂ HTc			Mg ₅ FeAl ₂ HTc			Mg ₄ Fe ₂ Al ₂ HTc			Mg ₃ Fe ₃ Al ₂ HTc		
298 K	523 K	723 K	298 K	523 K	723 K	298 K	523 K	723 K	298 K	523 K	723 K
7.71	6.88	6.03	7.63	6.75	6.40	7.60	6.75	6.33	7.53	6.71	6.48

Table 3.3 Variation in basal spacing (Å) for HTc's at 298 K, 523 K and 723 K

By comparison, the initial reduction in interlayer spacing has been reported as occurring at *ca.* 433-473 K in studies utilising high temperature XRPD.^{7, 19, 21} In one of these studies, Kanazaki proposed that hydroxyl ions produced from the reaction of interlayer carbonate ions and water molecules occupied the interlayer region and, since they were less bulky than the carbonate ions, the basal spacing was reduced as a result.¹⁹ However, as noted by Rives in a comment on Kanazaki's theory, since the ionic radius of the hydroxide ion is similar to that of the carbonate ion, there should be no marked change in basal spacing.²⁰ Indeed, meixnerite [Mg₆Al₂(OH)₁₆(OH)₂·4H₂O], a HTc which has hydroxide ions as the charge neutralising interlayer ions has a basal spacing of 7.64 Å.³⁴ The decomposition pattern of the HTc's was confirmed by Rives using mass spectrometry to analyse the gases evolved from a sample of hydrotalcite during calcination.²⁰ This confirmed that gases are evolved in two distinct stages. In the first, at *ca.* 423 K, water and a small amount of carbon dioxide was evolved which was ascribed to the loss of the interlayer water and a small amount of adsorbed carbon dioxide. In the second, at *ca.* 623 K, a large amount of carbon dioxide and water were evolved which was assigned to the simultaneous decomposition of the interlayer carbonate ions and the structural hydroxyl groups. In this and other studies, the loss of the interlayer water has been shown to occur at a temperature corresponding to that at which the basal spacing decreases which has led to a number of authors explaining this reduced 'anhydrous gallery' spacing as simply being caused by a partial collapse of the layers as a result of the elimination of the interlayer water.^{7, 18, 21} However, since the carbonate ions are still present within the layers, the extent of the reduction should not be this large. Consequently, the exact mechanism of this decrease in basal spacing remains unclear. It may be that, without the presence of the interlayer water molecules, the carbonate ions may distribute themselves in a manner which allows the layers to collapse to some degree.

As can be seen in Table 3.2a, the most obvious peak in the XRPD patterns of the low Fe HTc's was that at *ca.* 2.10 Å which is coincident with the most intense peak in the MgO pattern. This is in keeping with the high temperature XRPD patterns reported in the literature for MgAlHTc's which illustrate three main phases during calcination.^{7, 19} During the first, from room temperature to *ca.* 453 K, a gradual decrease in intensity of the hydrotalcite pattern was recorded but no other peaks were observed. During the second stage, from *ca.* 453-653 K, the reduction in basal spacing was initiated, as described above. The intensity of some of the other peaks observed for HTc's decreased considerably and it was assumed that, although a layered structure was present in this temperature range, there was increasing disorder within the structure. In the third phase, at *ca.* 653-1273 K, a pattern indicative of periclase (MgO) became apparent as the pattern indicative of a layered structure became unidentifiable. The temperature at which the MgO pattern appeared corresponded with that previously described for decarbonation and dehydroxylation of the structure and it is generally believed that a mixed metal oxide forms as a result. This has been variously described as a solid solution of MgO containing the Al ions,^{14, 35, 36} a Mg-Al double oxide^{37, 38} and a mixed metal oxide.^{18, 39-41} This phase persists up to *ca.* 1273 K, at which temperature the XRPD pattern of spinel (MgAl₂O₄) has been recorded.^{2, 6, 7, 19, 37}

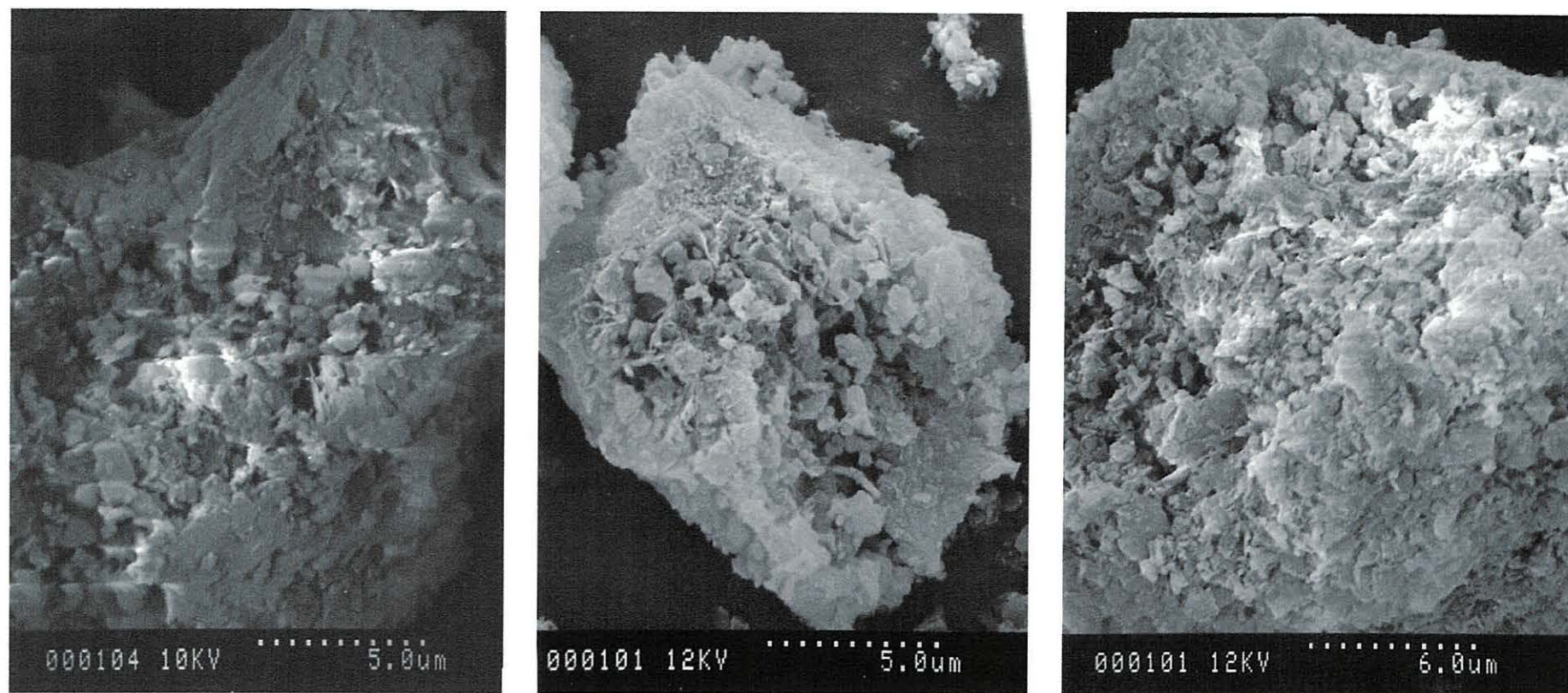
Therefore, at 723 K, an MgO pattern should be expected and was observed as the strongest pattern for the calcination products of the precursors with formulae Mg₆Al₂HTc, Mg₅FeAl₂HTc and Mg₄FeAl₂HTc. However, as can be seen in Table 3.2a, the relative intensity of the peak at *ca.* 2.53 Å became greater for the calcined HTc's with greater levels of Fe-for-Mg substitution. This was indicative of the formation of an inverse spinel phase such as magnesioferrite (MgFe₂O₄) or magnetite (Fe₃O₄). The formation of spinel-type phases had been reported in the literature for MgFeHTc's previously at similarly low temperatures when compared with formation of spinel from MgAlHTc's.^{4, 5} As in Table 3.2a, these studies illustrated that spinel-type phases did not tend to form from the lower Fe-content HTc's and Hibino and Tsunashima proposed that the mechanism of spinel-phase formation was quite different in the MgFeHTc's than in the MgAlHTc's.⁵ They suggested that the MgFe₂O₄ phase was formed deeper below the surface or inside the crystallites since its formation was not inhibited by grinding the sample which was expected to break down the spinel nuclei forming between the edges of crystallites mechanochemically. The mechanism of formation

does appear to be unclear and is beyond the scope of this research but the formation of the MgFe_2O_4 product may be a result of the low temperature at which Fe_2O_3 is formed. Since this may form as a separate phase at a lower temperature than Al_2O_3 (upon calcination of HTc's the Al^{3+} ions appear to form a solid solution in MgO), the stoichiometry of the calcination of $\text{MgO}/\text{Fe}_2\text{O}_3$ favours the formation of MgFe_2O_4 .

The material formed from the $\text{Fe}_6\text{Al}_2\text{HTc}$ precursor also exhibited some similarities with the XRPD pattern of haematite (Fe_2O_3), as shown in Table 3.2a. This was expected since the precursor was expected, from the analysis summarised in the previous Chapter, to contain iron oxide phases such as goethite which are known to form haematite upon heating to *ca.* 473-673 K due to its relative thermodynamic stability.¹⁷ Any aluminium substitution within the haematite structure would be expected to result in only relatively minor changes in the XRPD pattern with respect to peak shifts due to the similarity in ionic radii of Al^{3+} and Fe^{3+} . Peak broadening has been observed by Schwertmann as a result of increased Al-substitution but, without a haematite standard for comparison, this could not be positively identified.

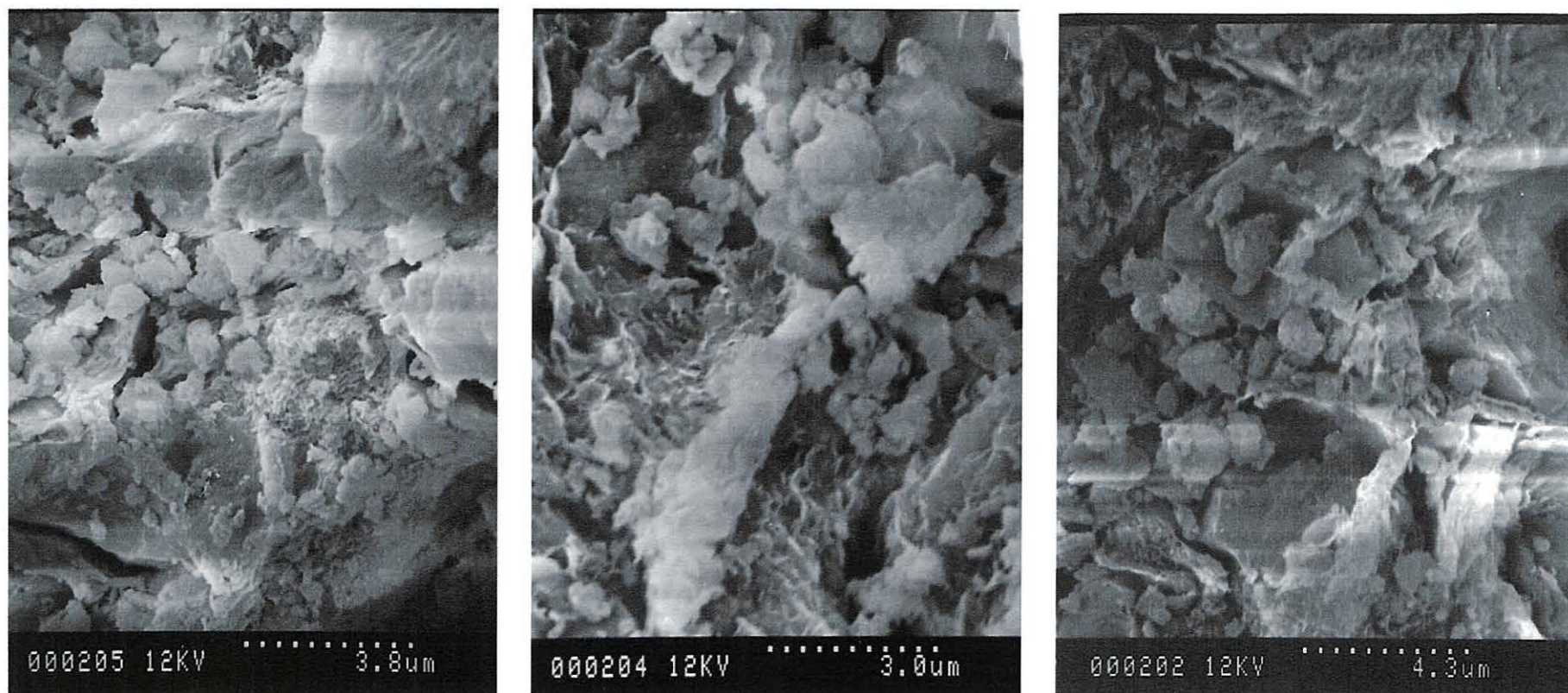
3.1.4 Scanning Electron Microscopy

Selected electron micrographs of the calcination products obtained from the precursors with idealised formulae of $\text{Mg}_6\text{Al}_2\text{HTc}$, $\text{Mg}_5\text{FeAl}_2\text{HTc}$ and $\text{Mg}_4\text{Fe}_2\text{Al}_2\text{HTc}$ are illustrated in Figures 3.2-3.4. These micrographs have been selected to represent the typical morphologies of these samples which were most similar to that of the HTc precursors discussed in the previous Chapter, section 2.1.4. It was evident during the SEM analysis that the lower Fe ratio products maintained the plate-like morphology to a greater degree than the higher Fe-for-Mg substituted samples on heating. The latter appeared to break down into smaller crystallites during calcination and some amalgamation of these was evident for the $\text{Mg}_2\text{Fe}_4\text{Al}_2\text{HTc}$, $\text{MgFe}_5\text{Al}_2\text{HTc}$ and $\text{Fe}_6\text{Al}_2\text{HTc}$ products calcined at 723 K to form what appeared to be lower surface area materials. The high porosity of the materials was evident, particularly for those samples calcined at 723 K but the fine pores which were expected as a result of the evolution of carbon dioxide and steam could not be observed at the available resolution.



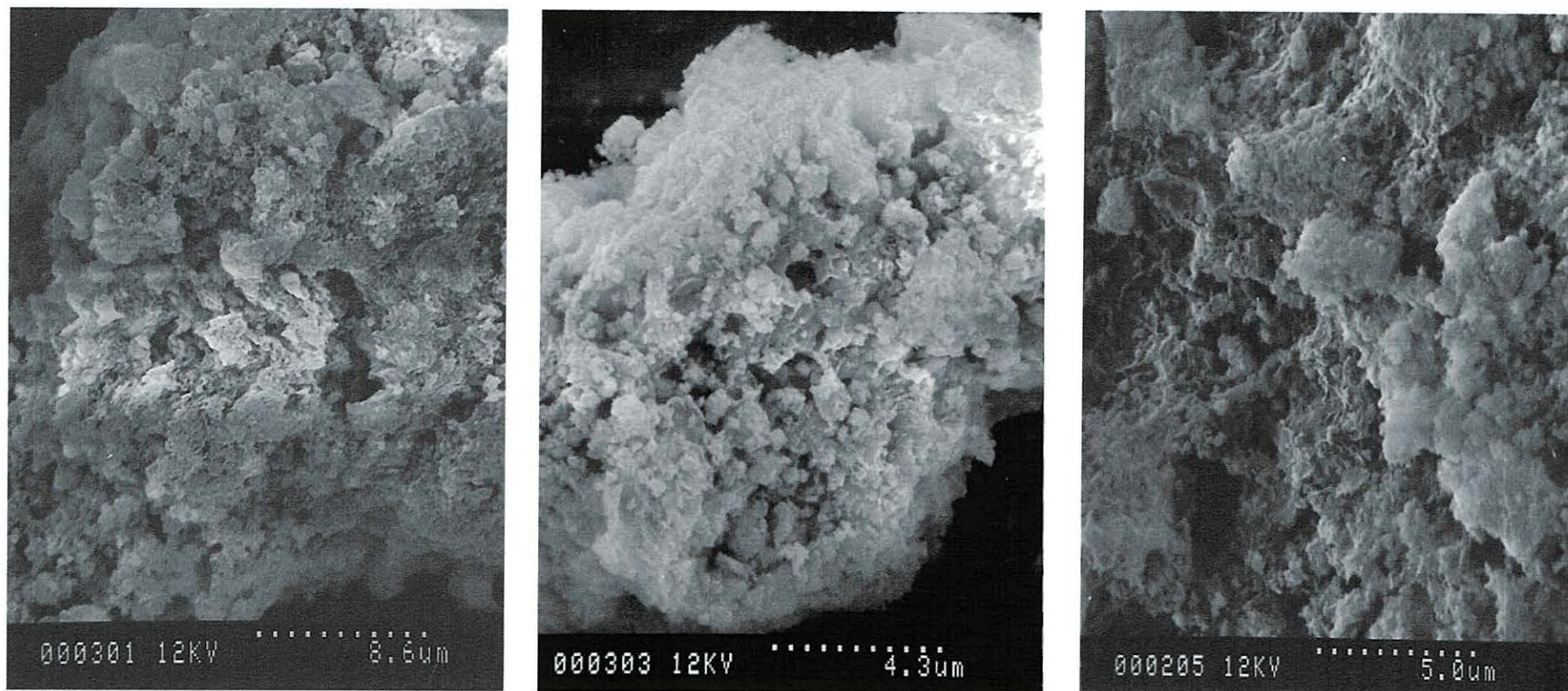
Figures 3.2 (a), (b) & (c): SEM's of $\text{Mg}_6\text{Al}_2\text{HTc}$ product formed using preparative method 1 following calcination at 383, 523 & 723 K (viewed left to right)

N.B. Scale bar is represented at the bottom of each micrograph as a series of dots (approximate length $\blacklozenge \longrightarrow \blacklozenge$) with the scale below



Figures 3.3 (a), (b) & (c): SEM's of $\text{Mg}_5\text{FeAl}_2\text{HTc}$ product following calcination at 383, 523 & 723 K
(viewed left to right)

N.B. Scale bar is represented at the bottom of each micrograph as a series of dots (approximate length $\blacklozenge \text{-----} \blacklozenge$) with the scale below



Figures 3.4 (a), (b) & (c): SEM's of $\text{Mg}_4\text{Fe}_2\text{Al}_2\text{HTc}$ product following calcination at 383, 523 & 723 K

(viewed left to right)

N.B. Scale bar is represented at the bottom of each micrograph as a series of dots (approximate length $\blacklozenge \longrightarrow \blacklozenge$) with the scale below

3.1.5 Conclusions

The IR spectra of the HTc's calcined at 723 K indicated that metal oxide formation appeared to be close to completion for each material. The spectra of the products obtained from the $\text{MgFe}_5\text{Al}_2\text{HTc}$ and $\text{Fe}_6\text{Al}_2\text{HTc}$ precursors did appear to indicate a transition towards iron oxide formation. The iron oxide product(s) could be expected to have some degree of substitution of Mg and Al into the structure as appropriate since separate phases containing these cations were not readily identifiable.

The XRPD patterns recorded for the calcination products exhibited a general trend for the formation of a spinel-type pattern with increasing Fe-for-Mg substitution. An MgO-type phase was detected as the strongest pattern for the products derived from $\text{Mg}_6\text{Al}_2\text{HTc}$, $\text{Mg}_5\text{FeAl}_2\text{HTc}$ and $\text{Mg}_4\text{Fe}_2\text{Al}_2\text{HTc}$ but the peak at 2.51 Å, which is the strongest peak of both magnetite (Fe_3O_4) and magnesioferrite (MgFe_2O_4), became the greatest intensity peak for the higher Fe-substituted products. This indicated that there was a preference for these high-Fe materials to adopt a spinel-type structure at a much lower temperature than the low-Fe HTc's upon calcination. This study which investigated the calcination of a range of materials with Fe-for-Mg substitution advanced upon previous studies in the literature for MgFeHTc 's (Fe-for Al substitution) which had exhibited similar properties.^{4, 5, 42}

The retention of the plate-like morphology has previously been observed for a range of calcined HTc's^{1, 43, 44} but not for the full range of calcined MgFeAlHTc 's studied here. For these materials, the lower Fe-substituted products did appear to have a morphology similar to that of the precursors with a porosity which may have been increased, in-keeping with the cratering mechanism of decomposition of the HTc structure.^{1, 6, 11, 12} However, the higher Fe-for-Mg substituted products appeared to have lost the lamellar structure at 723 K to a large degree; instead very small crystallites were observed which formed agglomerates towards producing a solid mass.

Overall, this study indicated that only the low Fe-for-Mg Htc's would satisfy the initial objectives *viz.* to produce a material derived from a HTc which exhibited the desired criteria for a catalytically active material at relatively low temperatures, as detailed

earlier. Retention of the HTc morphology was considered necessary for this and this was not observed to a significant degree with the high-Fe materials.

3.2 Cyanoethylation Catalyst Activation

3.2.1 Methodology

It has been previously reported that calcined HTc's have the capacity to reconstitute their original layered structure upon readsorption of interlayer anions and water.² This has been termed the 'memory effect' and its exploitation has been discussed in Chapter 1, particularly in sections 1.4.2 and 1.5.3. This effect is of significance here because it has been shown that the materials formed from MgAlHTc precursors, following calcination and subsequent rehydration with the exclusion of carbonate ions, have shown great potential for use as basic catalysts.^{21, 39, 40, 45} Although the HTc's calcined at *ca.* 723 K have also exhibited this potential, the nature of the basic sites has been shown to predominantly be the O²⁻ sites which have a Lewis-type basicity.^{36, 40, 46} In contrast, after rehydration in a carbonate-free atmosphere, the basic sites formed are believed to be predominantly of the Brønsted-type *viz.* hydroxide ions.^{45, 46} This will be discussed in more detail in the next Chapter.

It has been shown that MgAlHTc's calcined at 723 K and rehydrated in the manner described above are highly active catalysts for the cyanoethylation of alcohols, amongst other reactions.⁴⁵ Therefore, in addition to an academic investigation of the rehydration effects on the Fe-substituted HTc's, this reaction provided an opportunity to test the comparative catalytic activity of these materials. The remainder of this Chapter is focussed upon the characterisation of the rehydrated materials and the next Chapter dedicated to their testing as catalysts for the aforementioned reaction. The experimental procedure for the rehydration experiments is provided in Chapter 7, section 7.5.1.

3.2.2 IR Spectroscopy

The absorption bands observed in the IR spectra for each of the rehydration products are recorded in Table 3.4 and some representative spectra are illustrated in Figure 3.5 (a-c). The spectra were, again, similar to one another in overall appearance, with the greatest differences occurring at frequencies below 1000 cm^{-1} , although these were only slight. There is very little data available in the literature relating to HTc's which have undergone this rehydration process but the band assignments were similar to those assigned in previous sections of this thesis relating to IR spectroscopy. Therefore, this section seeks mainly to offer a comparison of these spectra with those of the HTc precursors and the calcination products, the spectra of which were described in sections 2.1.2 and 3.1.2.

In all of the spectra of the rehydration products, the OH stretching band at *ca.* $3450\text{--}3480\text{ cm}^{-1}$ exhibited a relative intensity much greater than that recorded for the calcined HTc's and more like that observed for the precursors. This seemed to indicate that the metal hydroxyl layers had been reconstructed during the rehydration process. There was, however, no shoulder evident at *ca.* 3100 cm^{-1} , as for the precursor HTc's, which suggested that there was significantly less hydrogen bonding between interlayer species or that this peak occurs as a result of hydrogen bonding between interlayer water and carbonate ions (which were expected to have been eliminated from the rehydrated material due to an absence of carbon dioxide in the rehydration process). There was a weak to medium intensity band observed at *ca.* 1380 cm^{-1} for each of the rehydration products. This suggested that there may have been some readsorption of carbonate ions to the interlayer region since these bands were marginally more intense than those in the calcination products but not nearly as intense as the bands observed in this position for the uncalcined HTc's. It could, therefore, be assumed that the interlayer ions were not predominantly carbonate as previously but would most likely be hydroxide ions instead. The other carbonate vibrations previously observed for the precursors at *ca.* 850 and 670 cm^{-1} were not clearly evident either across the range of rehydration products. The mid-range Fe-for-Mg substituted products did display a band at *ca.* 670 cm^{-1} but a number of M-O stretches could potentially overlap in this region. The bands recorded in

Table 3.4 Infrared absorption bands (cm^{-1}) recorded between 4000 and 400 cm^{-1} for activated cyanoethylation catalysts

Mg₆Al₂HTc Exptl. method 1	Mg₆Al₂HTc Exptl. method 2	Mg₅FeAl₂HTc	Mg₄Fe₂Al₂HTc	Mg₃Fe₃Al₂HTc	Mg₂Fe₄Al₂HTc	MgFe₅Al₂HTc	Fe₆Al₂HTc
3483 s	3463 s	3460 s	3448 s	3447 s	3447 s	3448 s	3449 s
1636 w/m, br	1636 w, br	1628 w, br	1610 w, br	1624 w, br	1636 w, br	1628 w, br	1628 w
		1466 br, shldr	1465 br, shldr	1490 w, br	1474 w, br		
1374 m	1382 m	1364 m	1364 m	1375 w/m	1387 w	1388 w	1400 vw, br
800 m, br	800 m, br	782 m	782 m	780 m, shldr			
642 m/s	634 m, br	658 m	662 m	670 m	670 m, shp		
				615 m			
					576 s	588 s	570 s
		558 m	562 m	564 m			
					503 m	500 m	503 m

N.B. HTc formulae correspond to uncalcined materials

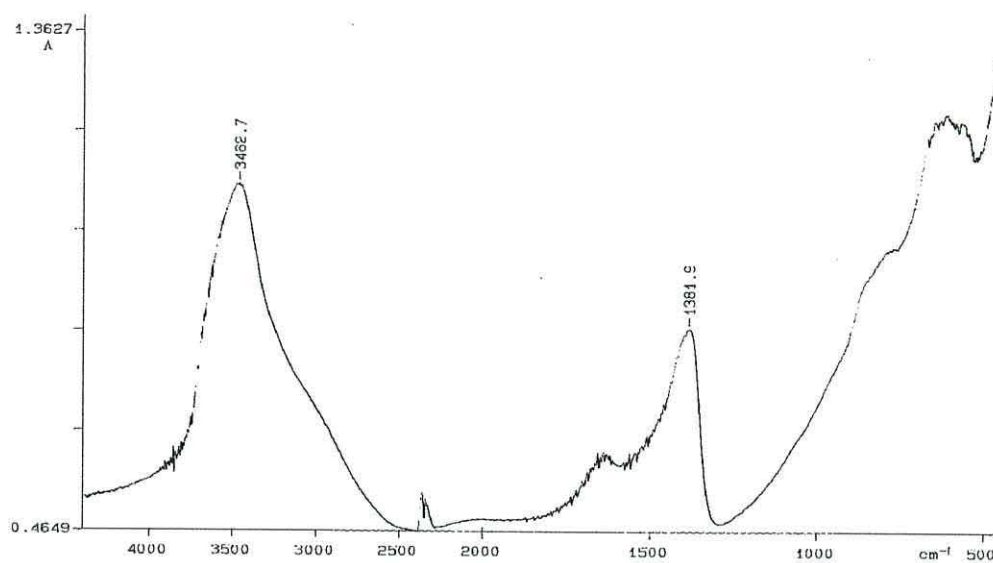


Figure 3.5a IR spectrum of $\text{Mg}_6\text{Al}_2\text{HTc}$ (Exptl. Method 2) cyanoethylation catalyst

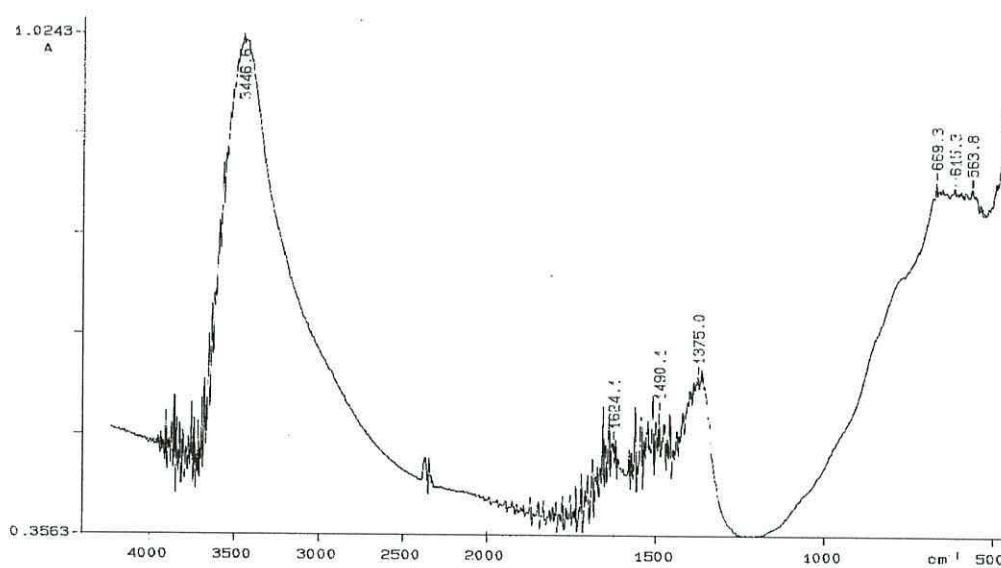


Figure 3.5b IR spectrum of $\text{Mg}_3\text{Fe}_3\text{Al}_2\text{HTc}$ cyanoethylation catalyst

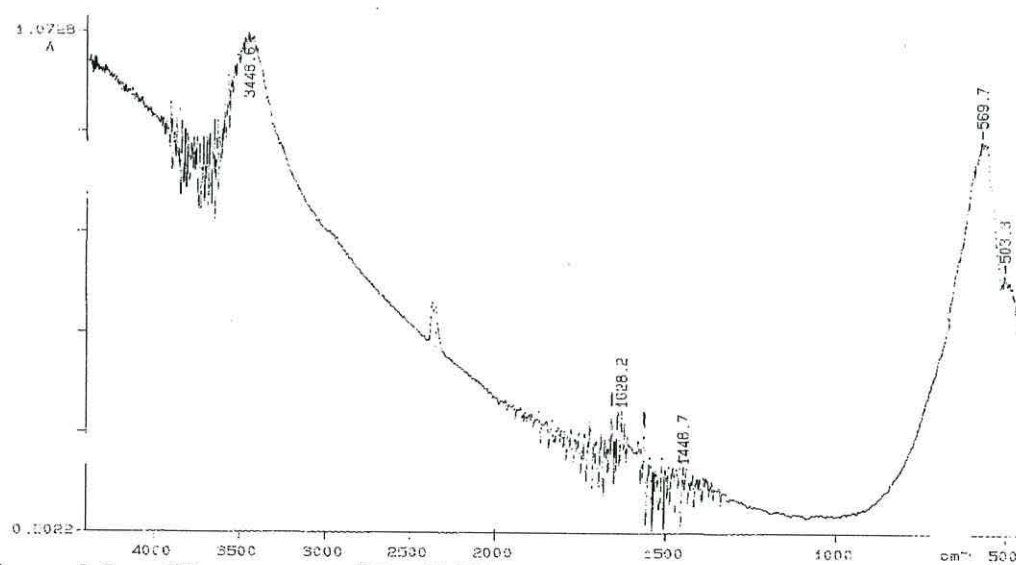


Figure 3.5c IR spectrum of $\text{Fe}_6\text{Al}_2\text{HTc}$ cyanoethylation catalyst

the area below 1000 cm^{-1} displayed a shift from the low-Fe products to the high-Fe products suggesting that the nature of the skeletal M-O bonding exhibited a transition across the range. This shift in bands appeared to cover three fairly distinct groups. The first was of higher frequency bands in this region for the MgAlHTc 's (at $600\text{-}800\text{ cm}^{-1}$), whilst the second group comprised the same bands plus an additional one at lower frequency (*ca.* 560 cm^{-1}) and the third group, evident for the high-Fe HTc's, comprised bands at lower rather than higher frequency. The precise origin of these bands is unclear but it appears that the higher frequency bands occurred in the presence of high Mg ratio products whilst the lower frequency bands occurred in high Fe ratio products.

3.2.3 X-ray Powder Diffraction

The data recorded for the XRPD patterns of the HTc rehydration products is reported in Table 3.5, together with the JCPDS pattern of hydrotalcite for comparison. The patterns themselves are illustrated in Figure 3.6 in order to allow comparison of each and with those of the HTc precursors recorded earlier in Figure 2.3. The pattern for the $\text{Mg}_6\text{Al}_2\text{HTc}$ produced using experimental method 1 is situated at the bottom of the illustration and the rehydration product of the $\text{Fe}_6\text{Al}_2\text{HTc}$ at the top with the remainder in between (increasing Fe-for-Mg substitution from bottom to top). The pattern recorded for the $\text{Mg}_6\text{Al}_2\text{HTc}$ produced using experimental method 2 has been omitted for clarity since a high background level obscured some peaks of other patterns.

The XRPD patterns recorded for the rehydration products did initially appear very similar to those of the HTc precursors. There were, however, a number of differences. For instance, the actual intensity of the peaks (in terms of counts per second) was considerably lower for the rehydration products and some peak broadening was evident. This had been previously observed in the literature for MgAlHTc 's and has been reported to be a consequence of reduced crystallite size following the calcination stage and/or increased disorder within the samples.^{21, 40, 43, 47} The patterns recorded for the products $\text{Mg}_6\text{Al}_2\text{HTc}$ to $\text{Mg}_3\text{Fe}_3\text{Al}_2\text{HTc}$ were indicative of a predominantly single phase hydrotalcite-type material which suggested that the HTc structure had been reconstructed successfully. The $\text{Mg}_3\text{Fe}_3\text{Al}_2\text{HTc}$ rehydration product did exhibit a peak

Table 3.5 X-ray powder diffraction d-spacing results (Å) for activated cyanoethylation catalysts (relative intensities in parentheses)

Hydrotalcite ²⁴ Mg ₆ Al ₂ HTc	Mg ₆ Al ₂ HTc (method 1)	Mg ₆ Al ₂ HTc (method 2)	Mg ₅ FeAl ₂ HTc	Mg ₄ Fe ₂ Al ₂ HTc	Mg ₃ Fe ₃ Al ₂ HTc	Mg ₂ Fe ₄ Al ₂ HTc	MgFe ₅ Al ₂ HTc	Fe ₆ Al ₂ HTc
7.69 (100)	7.79 (100)	7.75 (100)	7.67 (100)	7.65 (79)	7.60 (46)	7.50 (10)	7.77 (7)	7.47 (3)
							6.07 (10)	
							4.83 (10)	4.85 (6)
							4.31 (12)	
3.88 (70)	3.88 (43)	3.87 (46)	3.84 (55)	3.83 (58)	3.87 (31)			
								3.68 (15)
						2.95 (20)	2.96 (24)	2.96 (27)
								2.76 (11)
								2.68 (45)
2.58 (20)	2.58 (33)	2.58 (36)	2.58 (58)	2.58 (100)	2.56 (100)			
						2.51 (100)	2.53 (100)	2.53 (100)
2.30 (20)	2.31 (15)	2.30 (18)	2.30 (24)	2.28 (41)	2.27 (30)			
								2.19 (22)
					2.09 (29)	2.09 (42)	2.09 (27)	2.10 (21)
1.96 (20)	1.96 (9)	1.98 (12)	1.97 (14)	1.97 (19)	2.03 (24)			
								1.83 (12)
1.75 (10)				1.74 (5)			1.71 (5)	
								1.68 (25)
1.65 (10)			1.64 (2)					
							1.61 (15)	1.61 (15)
								1.60 (18)
1.53 (20)	1.53 (19)	1.53 (23)	1.53 (31)	1.53 (53)				
					1.52 (35)	1.52 (4)	1.52 (36)	1.52 (34)
1.50 (20)	1.50 (16)	1.50 (19)	1.50 (26)	1.49 (49)				

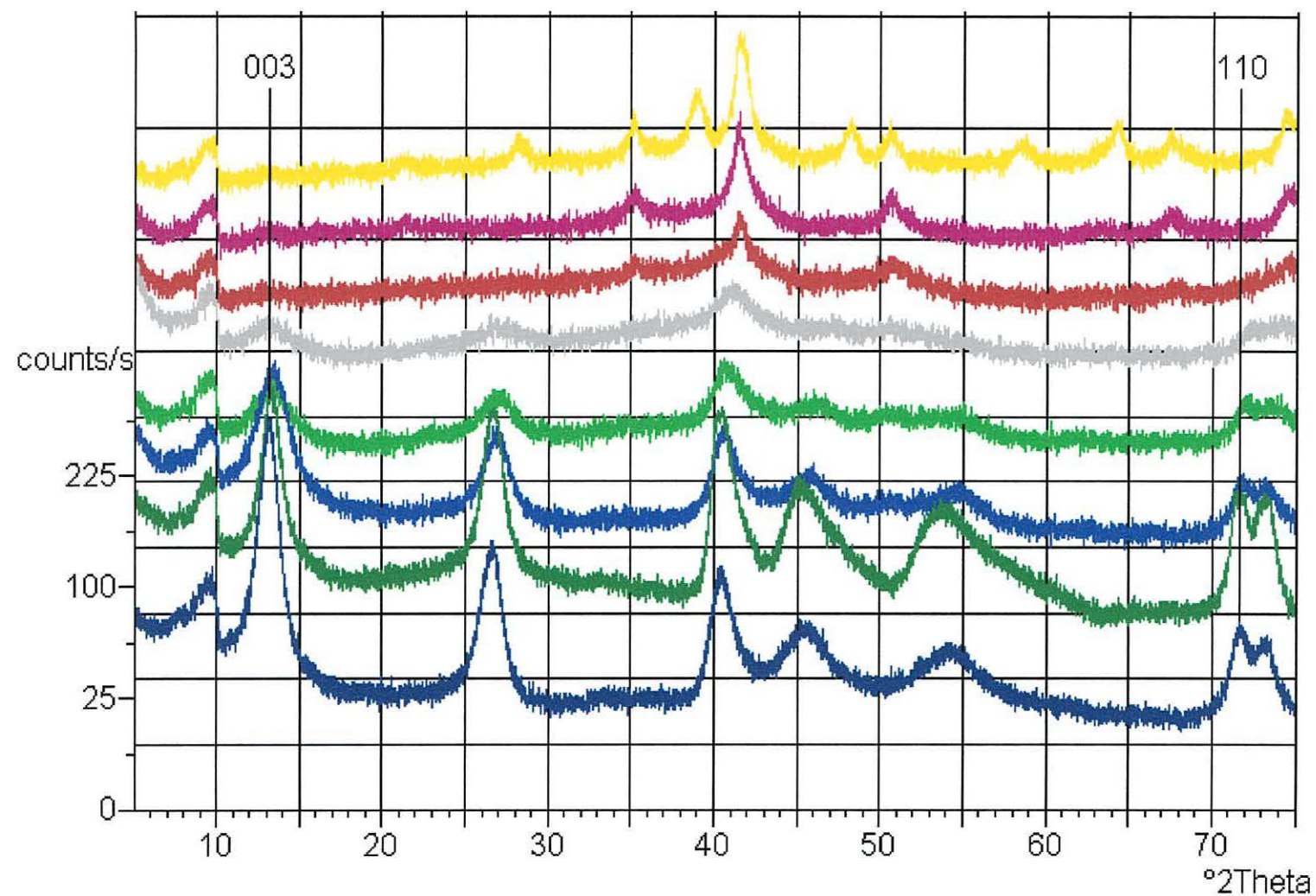


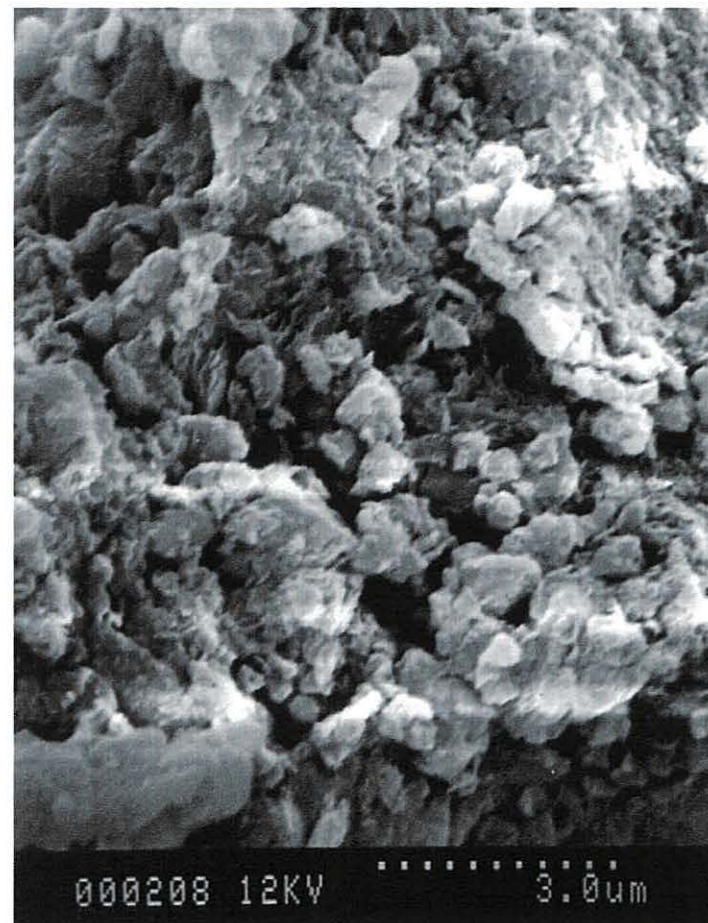
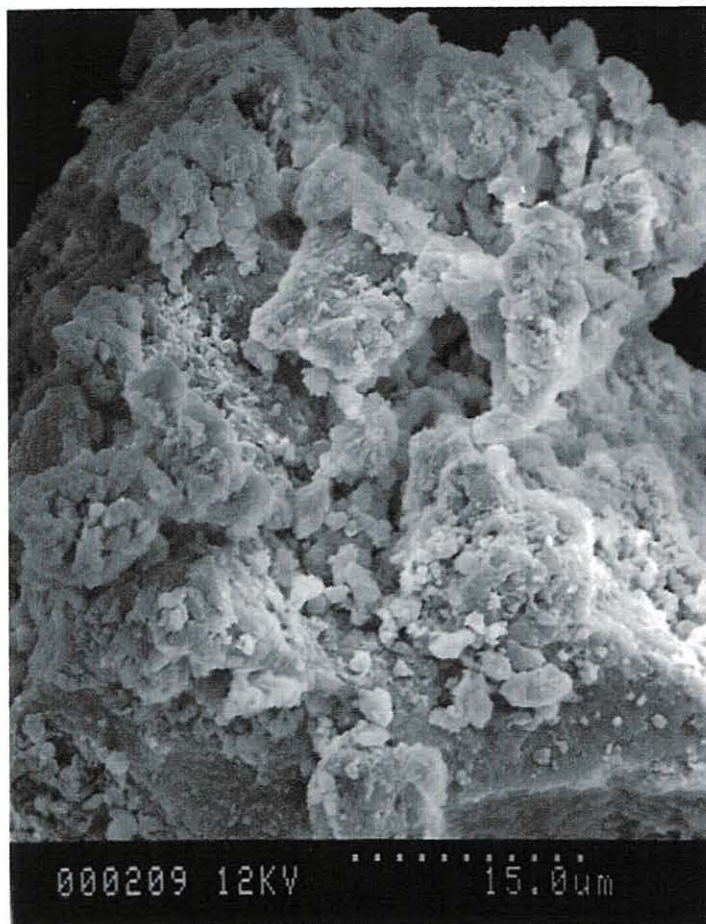
Figure 3.6 A comparison of the recorded XRPD patterns across the range of $\text{Mg}_6\text{Al}_2\text{HTc}$ to $\text{Fe}_6\text{Al}_2\text{HTc}$ after activation for use as cyanoethylation catalysts

at 2.09 Å which may have been another phase and the other high-Fe rehydration products exhibited an increasing number of additional peaks. These mainly appeared to indicate the presence of the spinel-type material which was present in the XRPD patterns of the calcined materials and would be expected to persist following rehydration due to its high stability once formed. In addition, the $\text{Fe}_6\text{Al}_2\text{HTc}$ product also exhibited a number of peaks which were assigned to the presence of haematite which was, again, present for the calcined product of this material, as previously discussed.

3.2.4 Scanning Electron Microscopy

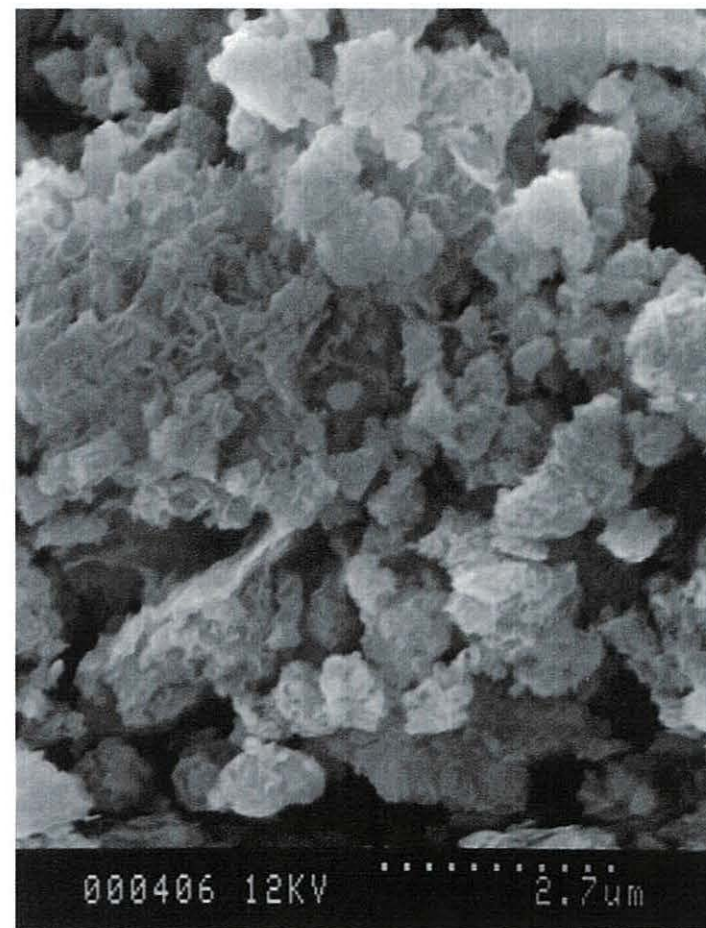
Selected electron micrographs which are considered representative of each HTc material after calcination and rehydration are shown in Figures 3.7-3.12. Suitable micrographs were not recorded for the $\text{Fe}_6\text{Al}_2\text{HTc}$ product but detailed observations were made.

A platelet morphology was observed for each of the rehydration products, except perhaps that of the $\text{Fe}_6\text{Al}_2\text{HTc}$ which exhibited some agglomeration of crystallites into a material which appeared to be of a lower surface area than that observed for the other products. The size of the platelets was quite variable across the range of products with increasing Fe-substitution; an initial decrease in this dimension saw the formation of distinct crystallites with a HTc morphology but the platelet size then appeared to increase and the crystallites became less obvious. The platelet size appeared greatest for the $\text{Mg}_3\text{Fe}_3\text{Al}_2\text{HTc}$ product but then decreased dramatically to form very small crystallites for the Fe-rich products which showed little evidence of large plates. The overall crystallite size appeared to have been reduced to the extent that the an average was extremely difficult to assess, particularly for the high-Fe products. This reduction in crystallite size was assumed to be a result of the calcination stage which, as discussed previously, would have been expected to increase the porosity. The surface area and porosity of each material did appear to be extremely high from these results but quantification using this technique was not possible. What is less clear is why the platelets should appear so large for the mid-Fe-range products although there appeared to be little evidence of the smaller crystallites.



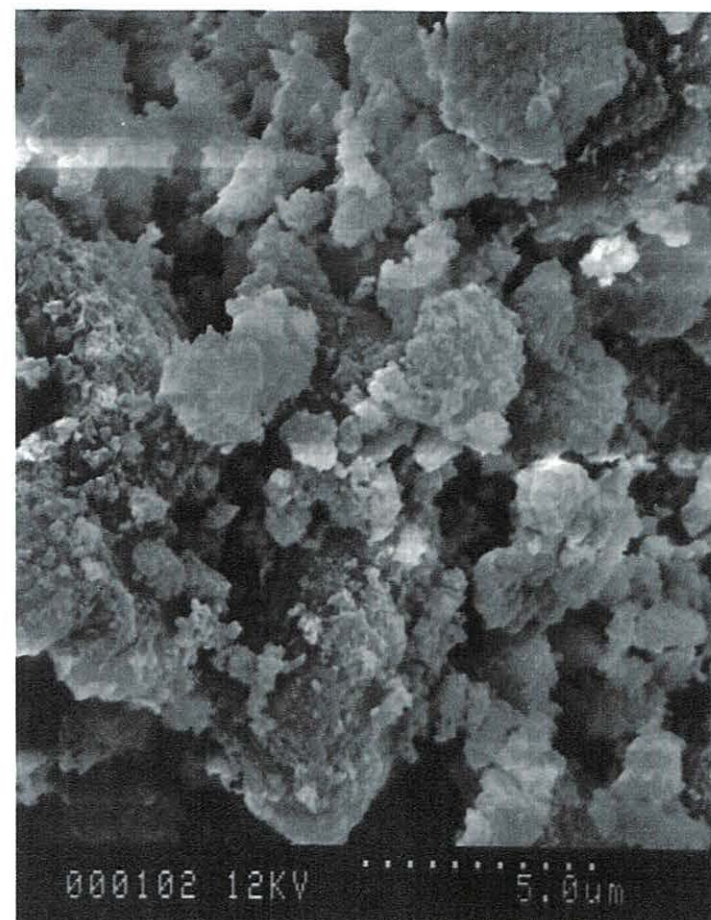
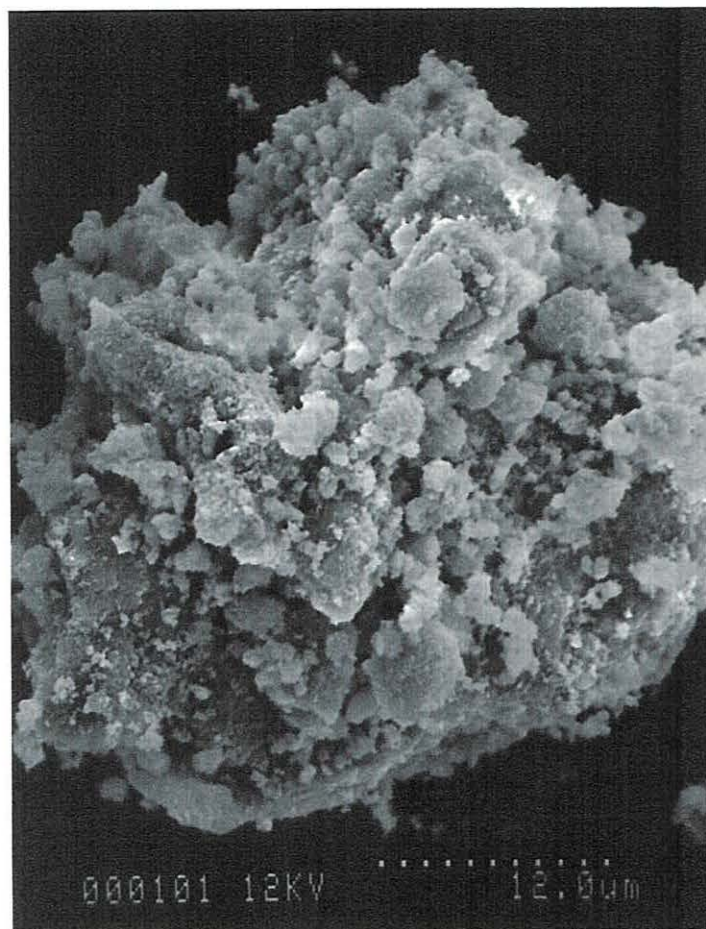
Figures 3.7 (a) & (b): SEM's of $\text{Mg}_6\text{Al}_2\text{HTc}$ product formed using preparative method 1 following activation for cyanoethylations

N.B. Scale bar is represented at the bottom of each micrograph as a series of dots (approximate length $\blacklozenge \text{-----} \blacklozenge$) with the scale below



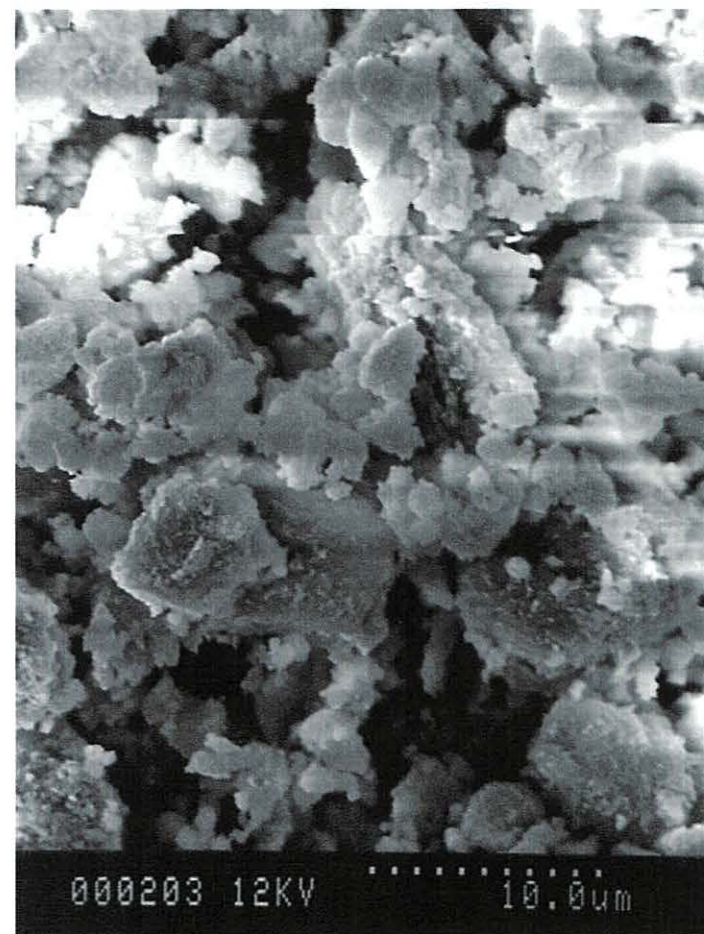
Figures 3.8 (a) & (b): SEM's of $\text{Mg}_5\text{FeAl}_2\text{HTc}$ product following activation for cyanoethylations

N.B. Scale bar is represented at the bottom of each micrograph as a series of dots (approximate length $\blacklozenge \text{-----} \blacklozenge$) with the scale below



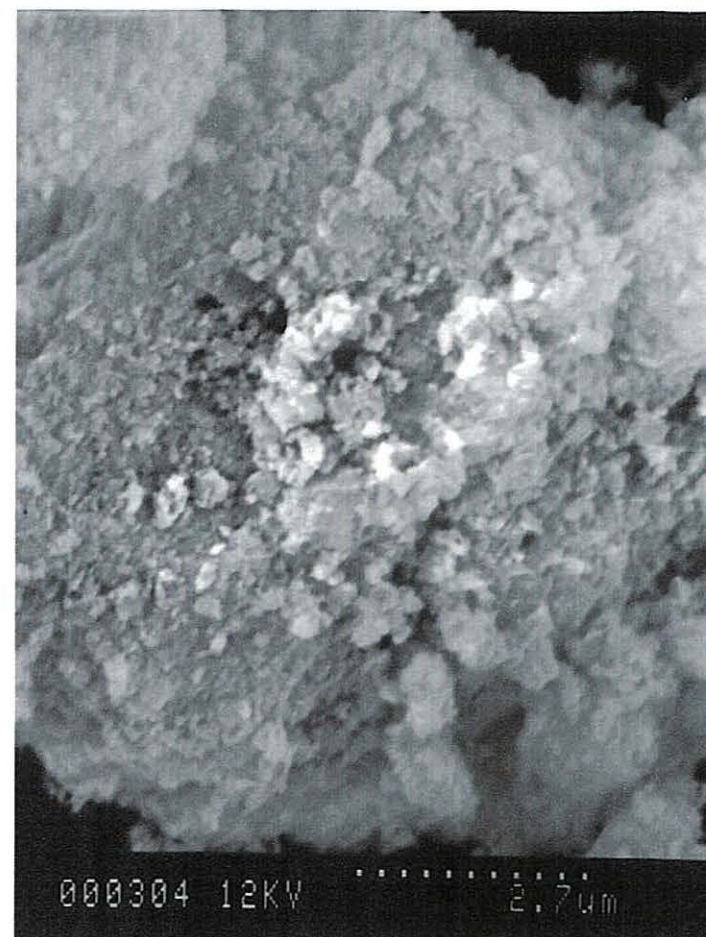
Figures 3.9 (a) & (b): SEM's of $\text{Mg}_4\text{Fe}_2\text{Al}_2\text{HTc}$ product following activation for cyanoethylations

N.B. Scale bar is represented at the bottom of each micrograph as a series of dots (approximate length $\blacklozenge \text{-----} \blacklozenge$) with the scale below



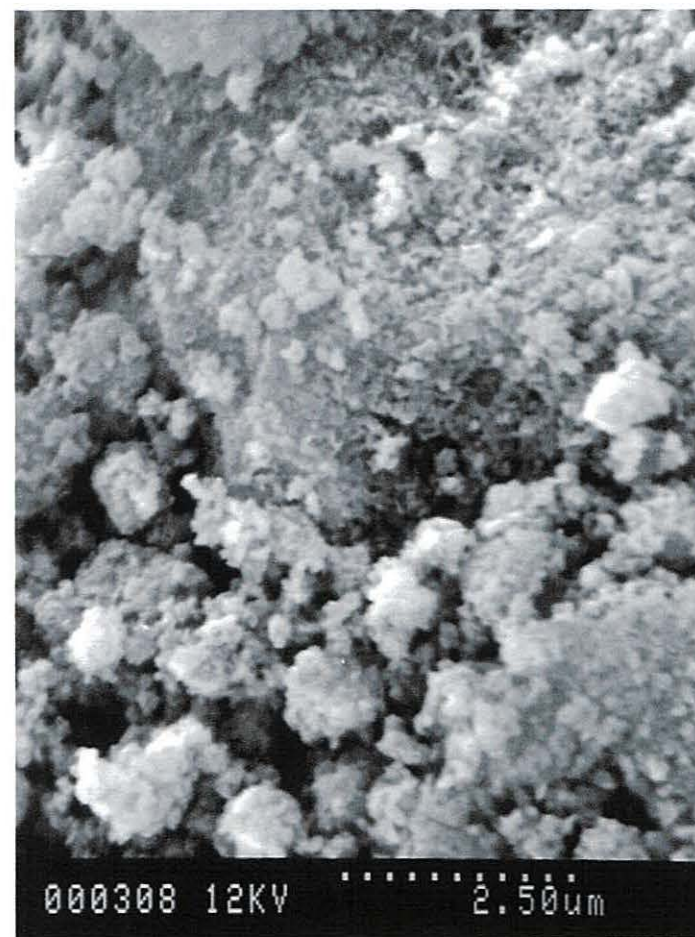
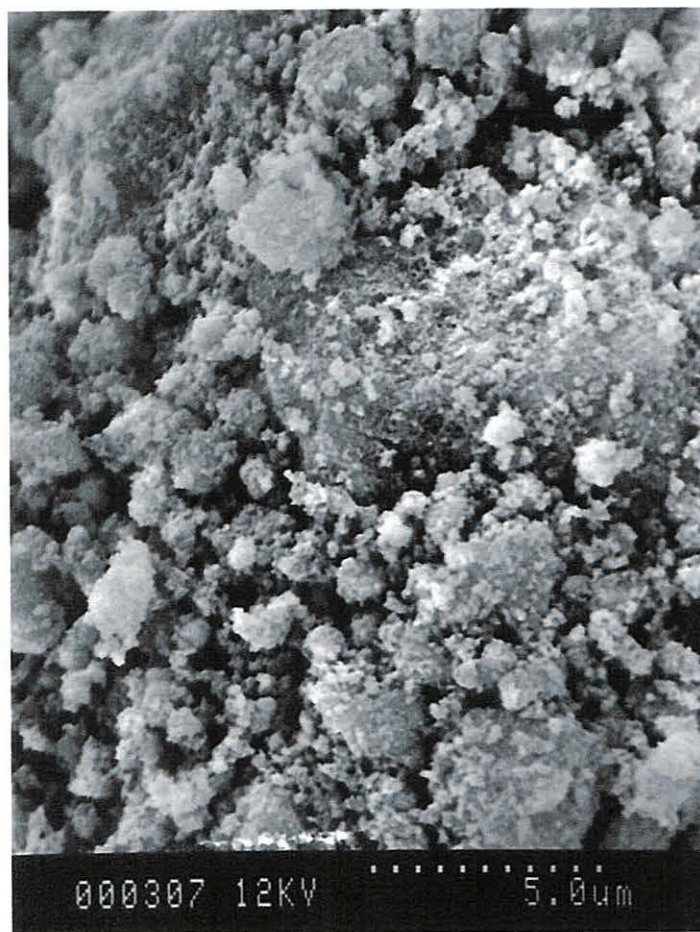
Figures 3.10 (a) & (b): SEM's of $\text{Mg}_3\text{Fe}_3\text{Al}_2\text{HTc}$ product following activation for cyanoethylations

N.B. Scale bar is represented at the bottom of each micrograph as a series of dots (approximate length $\blacklozenge \text{-----} \blacklozenge$) with the scale below



Figures 3.11 (a) & (b): SEM's of $\text{Mg}_2\text{Fe}_4\text{Al}_2\text{HTc}$ product following activation for cyanoethylations

N.B. Scale bar is represented at the bottom of each micrograph as a series of dots (approximate length $\blacklozenge \longrightarrow \blacklozenge$) with the scale below



Figures 3.12 (a) & (b): SEM's of MgFe₅Al₂HTc product following activation for cyanoethylations

N.B. Scale bar is represented at the bottom of each micrograph as a series of dots (approximate length $\blacklozenge \text{-----} \blacklozenge$) with the scale below

3.2.5 Conclusions

Very little data regarding the characterisation of this type of rehydrated calcined HTc's has been reported in the literature. Thus far, when information has appeared in the literature relating to these type of materials, the emphasis has been on their activity as catalysts rather than their characterisation. In addition, much of this work has related to the MgAlHTc's rather than Fe-containing HTc's.

These results indicate that the reconstruction of the hydrotalcite-type morphology has been successful to some degree for most, if not all, of the calcined HTc's. The IR results indicated that the interlayer carbonate ions had been replaced, probably by hydroxide ions for the materials which had undergone reconstruction. The XRPD results showed that the HTc pattern was present to some degree in all rehydrated products but, where a spinel-type phase or another stable phase such as haematite had been formed following calcination, this material persisted following rehydration. The SEM results clearly showed that the HTc morphology had been maintained for a number of the products on a micro and/or macro scale and that the rehydrated materials appeared to possess a high surface area/porosity which would be particularly suitable for use as catalysts.

3.3 References

- 1 A. Vaccari, *Appl. Clay Sci.*, 1999, **14**, 161.
- 2 F. Cavani, F. Trifirò and A. Vaccari, *Catal. Today*, 1991, **11**, 173.
- 3 Y. Ono, T. Baba, E.J. Doscocil, S. Bordawekar and R.J. Davis, in *Catalysis – Royal Society of Chemistry Specialist Periodical Report Volume 15*, J.J. Spivey (Senior Reporter), The Royal Society of Chemistry, Cambridge, 2000.
- 4 M. Tu, J. Shen and Y. Chen, *J. Solid State Chem.*, 1997, **128**, 73.
- 5 T. Hibino and A. Tsunashima, *J. Mater. Sci. Letters*, 2000, **19**, 1403.

- 6 D. Tichit, M.H. Lhouty, A. Guida, B.H. Chiche, F. Figueras, A. Auroux, D. Bartalini and E. Garrone, *J. Catal.*, 1995, **151**, 50.
- 7 F. Millange, R.I. Walton and D. O'Hare, *J. Mater. Chem.*, 2000, **10**, 1713.
- 8 D.F. Shriver, P.W. Atkins and C.H. Langford, *Inorganic Chemistry*, Oxford University Press, Oxford, 1990.
- 9 L. Smart and E. Moore, *Solid State Chemistry – An Introduction*, Chapman & Hall, London, 1992.
- 10 S. Narayanan and K. Krishna, *Chem. Commun.*, 1997, 1991.
- 11 S. Carlino, *Chem. Brit.*, 1997, September, 59.
- 12 F. Rey, V. Fornés and J.M. Rojo, *J. Chem. Soc., Faraday Trans.*, 1992, **88**(15), 2233.
- 13 T. Baird, K.C. Campbell, P.J. Holliman, R. Hoyle, D. Stirling and B.P. Williams, *J. Chem. Soc., Faraday Trans.*, 1995, **91**(18), 3219.
- 14 T. Hibino, Y. Yamashita, K. Kosuge and A. Tsunashima, *Clays and Clay Minerals*, 1995, **43**(4), 427.
- 15 K. Nakamoto, *Infrared and Raman Spectra of Inorganic and Coordination Compounds* (4th Edition), John Wiley & Sons, Chichester, 1986.
- 16 R.M. Cornell and U. Schwertmann, *The Iron Oxides – Structure, Properties, Reactions, Occurrence and Uses*, VCH, Weinheim, 1996.
- 17 U. Schwertmann and R.M. Cornell, *Iron Oxides in the Laboratory*, VCH, Weinheim, 1991.

- 18 V.R.L. Constantino and T.J. Pinnavaia, *Inorg. Chem.*, 1995, **34**, 883.
- 19 E. Kanezaki, *Inorg. Chem.*, 1998, **37**, 2588.
- 20 V. Rives, *Inorg. Chem.*, 1999, **38**, 406.
- 21 J.C.A.A. Roelofs, A.J. van Dillen, M. Versluijs-Helder, J.T.B.T. Jastrzebski and K.P. de Jong, Europa-Cat IV, 4th European Congress on Catalysis, Rimini, 1999.
- 22 G.W. Brindley and S. Kikkawa, *Clays and Clay Minerals*, 1980, **28**(2), 87.
- 23 T. Moroz, L. Razvorotneva, T. Grigorieva, M. Mazurov, D. Arkhipenko and V. Prugov, *Applied Clay Science*, 2001, **18**, 29.
- 24 JCPDS Card N^o. 14-0191.
- 25 JCPDS Card N^o. 13-0534.
- 26 JCPDS Card N^o. 03-0998.
- 27 JCPDS Card N^o. 03-0901.
- 28 JCPDS Card N^o. 05-0672.
- 29 JCPDS Card N^o. 01-1114.
- 30 JCPDS Card N^o. 21-1307.
- 31 G. Brown, in *Crystal Structures of Clay Minerals and their X-ray Identification*, Mineralogical Society Monograph No. 5, G.W. Brindley and G. Brown (Eds.), Mineralogical Society, London, 1980.
- 32 JCPDS Card N^o. 11-0614.

- 33 T. Hibino, K. Kosuge and A. Tsunashima, *Clays and Clay Minerals*, 1996, **44**(1), 151.
- 34 JCPDS Card N^o. 38-0478.
- 35 J. Santhanalakshmi and T. Raja, *Bull. Chem. Soc. Jpn.*, 1997, **70**, 2829.
- 36 P.S. Kumbhar, J. Sanchez-Valente, J. Lopez and F. Figueras, *Chem. Commun.*, 1998, 535.
- 37 T. Hibino and A. Tsunashima, *Clays and Clay Minerals*, 1997, **45**(6), 842.
- 38 J.P. Dunn, H.G. Stenger Jr. and I.E. Wachs, *J. Catal.*, 1999, **181**, 233.
- 39 M.L. Kantam, B.M. Choudary, Ch.V. Reddy, K.K. Rao and F. Figueras, *Chem. Commun.*, 1998, 1033.
- 40 K.K. Rao, M. Gravelle, J. Sanchez-Valente and F. Figueras, *J. Catal.*, 1998, **173**, 115.
- 41 P.S. Kumbhar, J. Sanchez-Valente, J.M.M. Millet and F. Figueras, *J. Catal.*, 2000, **191**, 467.
- 42 W. Kagunya, Z. Hassan and W. Jones, *Inorg. Chem.*, 1996, **35**, 5970.
- 43 A. Béres, I. Pálíko, I. Kiricsi, J.B. Nagy, Y. Kiyozumi and F. Mizukami, *App. Catal. A: General*, 1999, **182**, 237.
- 44 F. Trifirò, A. Vaccari and G. Del Piero, in “Characterisation of Porous Solids”, K.K. Unger *et. al.* (Eds.), Elsevier Science Publishers B.V., Amsterdam, 1988, 571.
- 45 P.S. Kumbhar, J. Sanchez-Valente and F. Figueras, *Chem. Commun.*, 1998, 1091.

- 46 F. Prinetto, G. Ghiotti, R. Durand and D. Tichit, *J. Phys. Chem. B*, 2000, **104**, 11117.
- 47 K. Chibwe and W. Jones, *J. Chem. Soc., Chem. Commun.*, 1989, 926.

Chapter 4

Base Catalysis

4.1 Cyanoethylation of Alcohols

4.1.1 Methodology

Because base-catalysed reactions are often carried out in the liquid phase, the diffusion of the reactants and products is relatively slow. Therefore, catalysts with a high surface area and porosity are desirable.¹ As previously discussed, mixed metal oxides produced from the calcination of HTc's possess such characteristics and have an advantage over the common single metal oxides such as MgO in that the additional metal cations may offer further catalytic potential *via* their additional chemical properties *e.g.* the Lewis acid sites of Al^{3+} .¹⁻⁵ Consequently, a number of investigations into the catalytic activity of these materials for a range reactions have been reported in the literature.^{2-4, 6-10} Calcined HTc's have been reported to display an acceptable level of activity for a number of these reactions. However, the majority of the basic sites in these materials have been shown to be of the Lewis base type.^{5, 11} Therefore, their activity towards some of the more commonly investigated reactions such as aldol and Knoevenagel condensations have been reported to be limited.^{3, 9, 10, 12} Because the rates of such reactions are known to be increased considerably by Brønsted base catalysts this initiated a number of investigations into the suitability of the materials which are formed as a result of rehydration of the calcined HTc's for these reactions.^{5, 9, 10, 12} These studies showed that rehydrated materials were highly active catalysts.

The cyanoethylation of alcohols is an important industrial reaction for the synthesis of a range of organic compounds and drug intermediates.^{13, 14} For instance; the cyanoethylation of a number of alcohols with acrylonitrile is a base catalysed reaction which is an important step in the production of industrially important amines. However, the bases most commonly used are tetraalkyl ammonium hydroxide and various alkali

hydroxides and alkoxides. These are homogeneous catalysts which have a number of associated problems, as outlined in Chapter 1. The cyanoethylation reaction is an example of a 1,4 (Michael-type) addition reaction whereby the substrate (acrylonitrile) is a conjugated nitrile. The CN group is an electron-withdrawing substituent in this conjugated system and the β -carbon of acrylonitrile is susceptible to attack from nucleophiles. The overall result of this reaction is the addition of the nucleophile and a hydrogen atom across the double bond which was conjugated with the CN group. The role of the base in this reaction is to convert the alcohol into the alkoxide ion which acts as a more powerful nucleophile towards acrylonitrile, allowing cyanoethylation of the alcohol. The mechanism for this reaction is as shown in Figure 4.1.

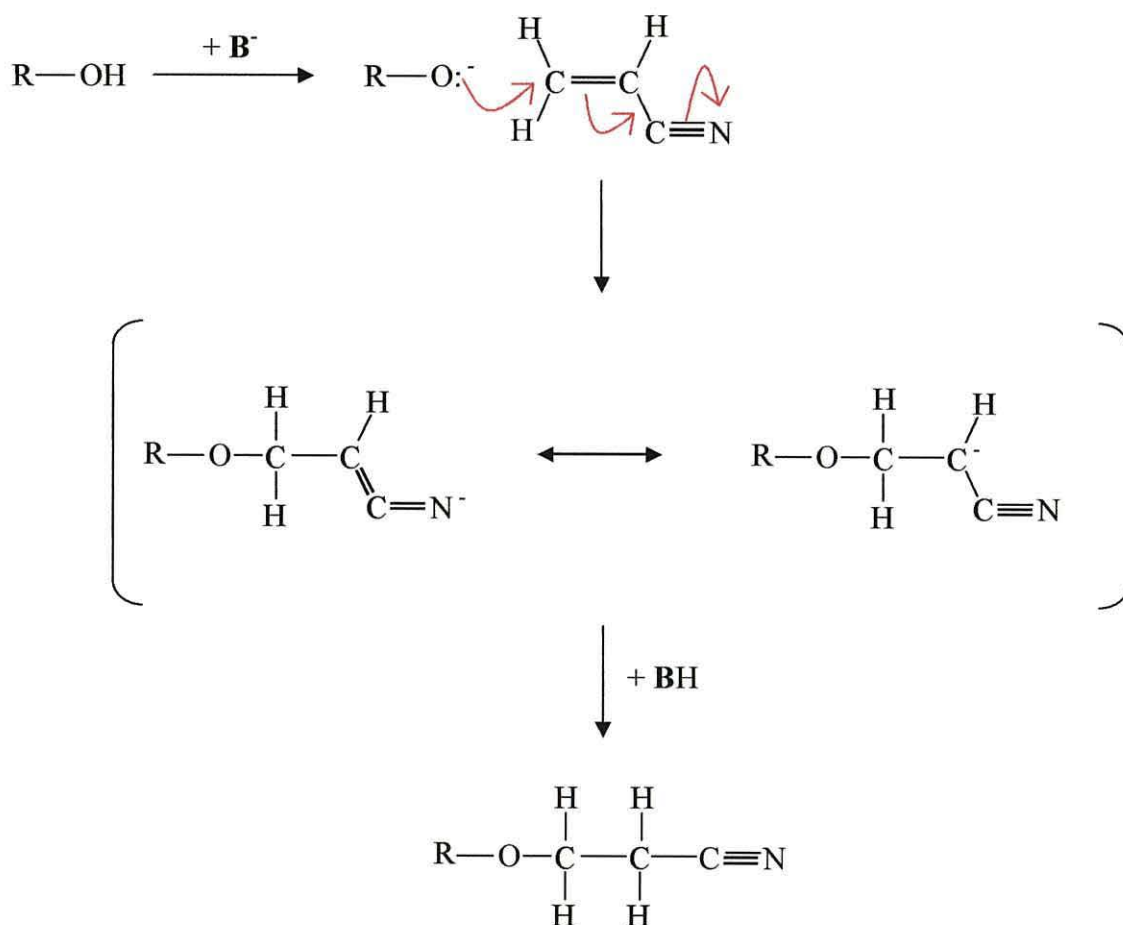


Figure 4.1 Reaction mechanism for the cyanoethylation of alcohols using a base catalyst (B).

MgAlHTc's calcined at 723 K and rehydrated in a nitrogen atmosphere have been shown to be highly active, reusable and relatively air stable heterogeneous catalysts in the cyanoethylation of a range of monohydric alcohols, exhibiting greatly increased activity over both the unmodified precursor HTc and the HTc calcined at 723 K.¹³ Because of the potential simplicity of the cyanoethylation reactions combined with the fact that the area was not as thoroughly represented in the literature as, for example, the effects of base catalysts on the rate of aldol condensation reactions, these reactions were selected for further investigation. In order to advance the current level of knowledge, the catalytic activity of the full range of Fe-substituted HTc's has been investigated and compared with that of Mg₆Al₂HTc. The cyanoethylations of methanol, ethanol and propan-2-ol have been studied since the relative rates of reaction had been shown by Kabashima and Hattori to vary for each depending on the type of catalyst used.¹⁴ In contrast with the work of Kabashima and Hattori, which had assessed reaction rate by the disappearance of acrylonitrile starting material, the activity here has been calculated from the appearance of the desired product. In order to do this, a combination of external gas chromatography standards and gas chromatography-mass spectrometry were used for product identification. These methods were also used to confirm the level of selectivity of the catalysts for each reaction. The catalyst activation procedure is detailed in Chapter 7, section 7.5.1 and the characterisation of these materials is reported in the previous Chapter. In addition, using the sampling procedure developed for these reactions (detailed in Chapter 7, section 7.5.2), further information was recorded regarding the progression of each of the reactions over time. Detailed characterisation of the used cyanoethylation catalysts was not carried out here due to the hazardous nature of the reactants and products containing the cyano-group.

4.1.2 Cyanoethylation Reactions

Graphs illustrating the percentage of acrylonitrile converted to the desired product for each cyanoethylation reaction are shown in Figures 4.2-4.4.

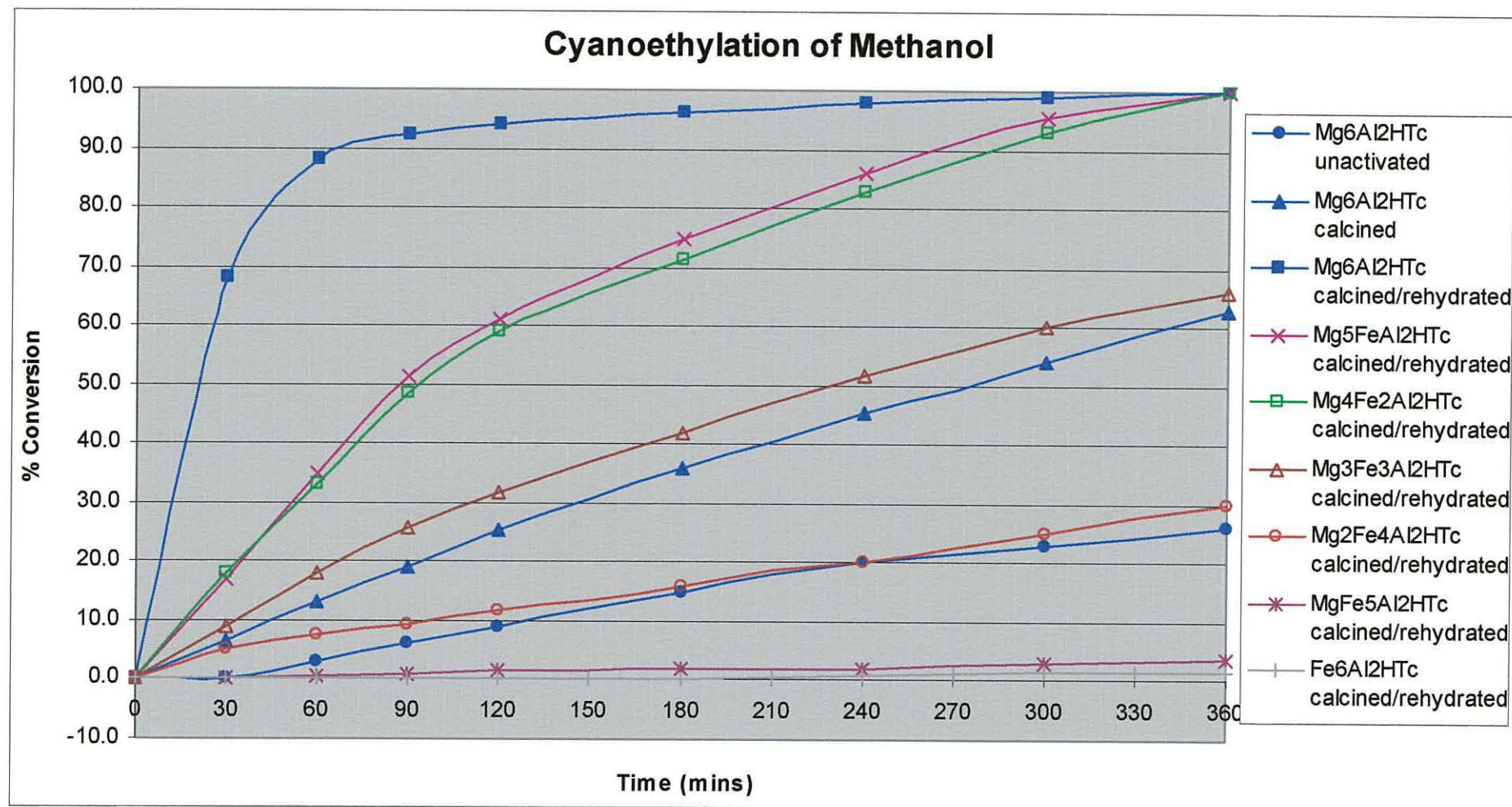


Figure 4.2 Illustration of the change in percentage conversion of acrylonitrile to 3-methoxypropionitrile over time using a range of catalysts

N.B. The results illustrated are smoothed curves produced from raw data, using an estimated error of *ca.* $\pm 2.5\%$

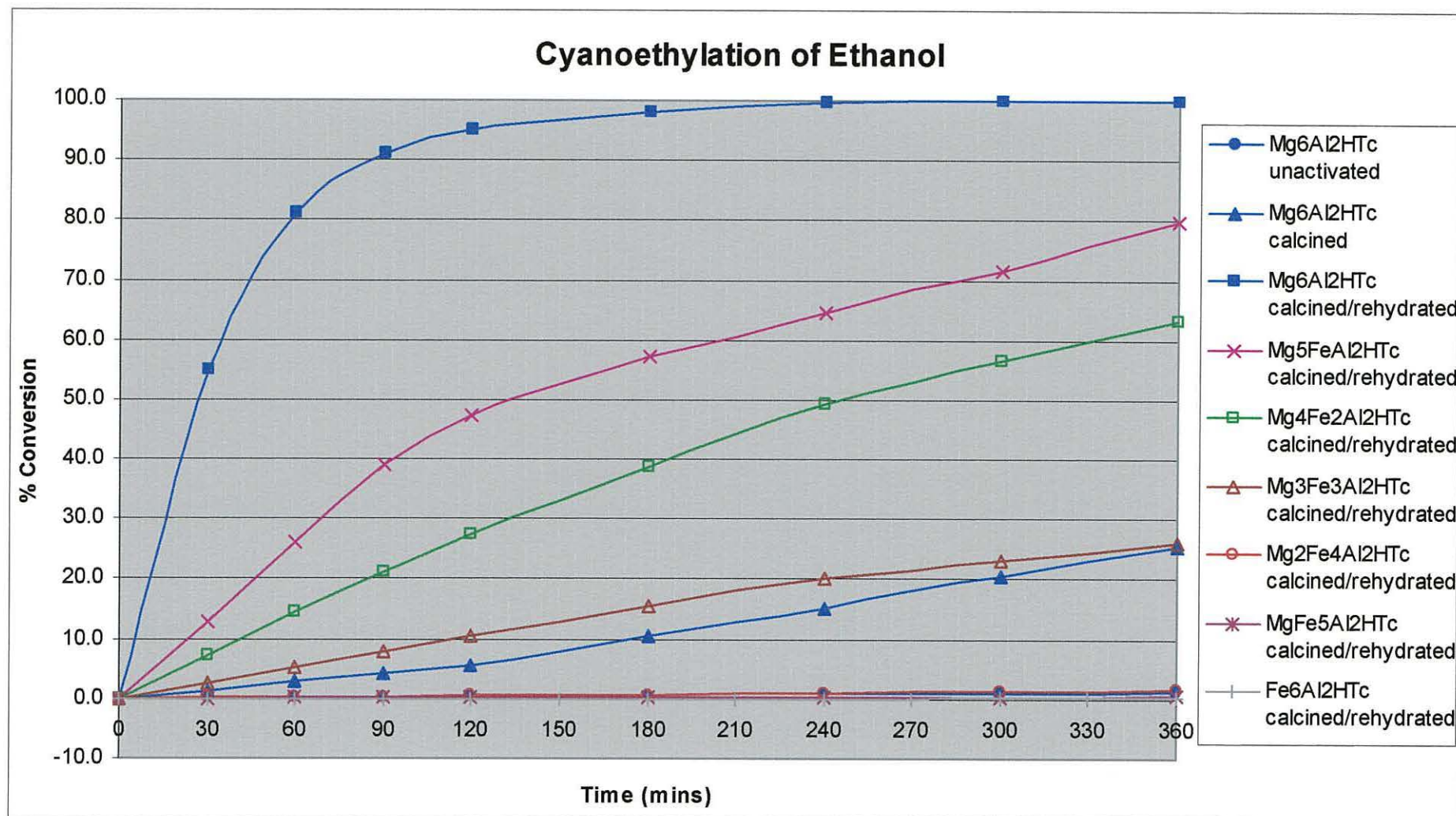


Figure 4.3 Illustration of the change in percentage conversion of acrylonitrile to 3-ethoxypropionitrile over time using a range of catalysts

N.B. The results illustrated are smoothed curves produced from raw data, using an estimated error of *ca.* $\pm 2.5\%$

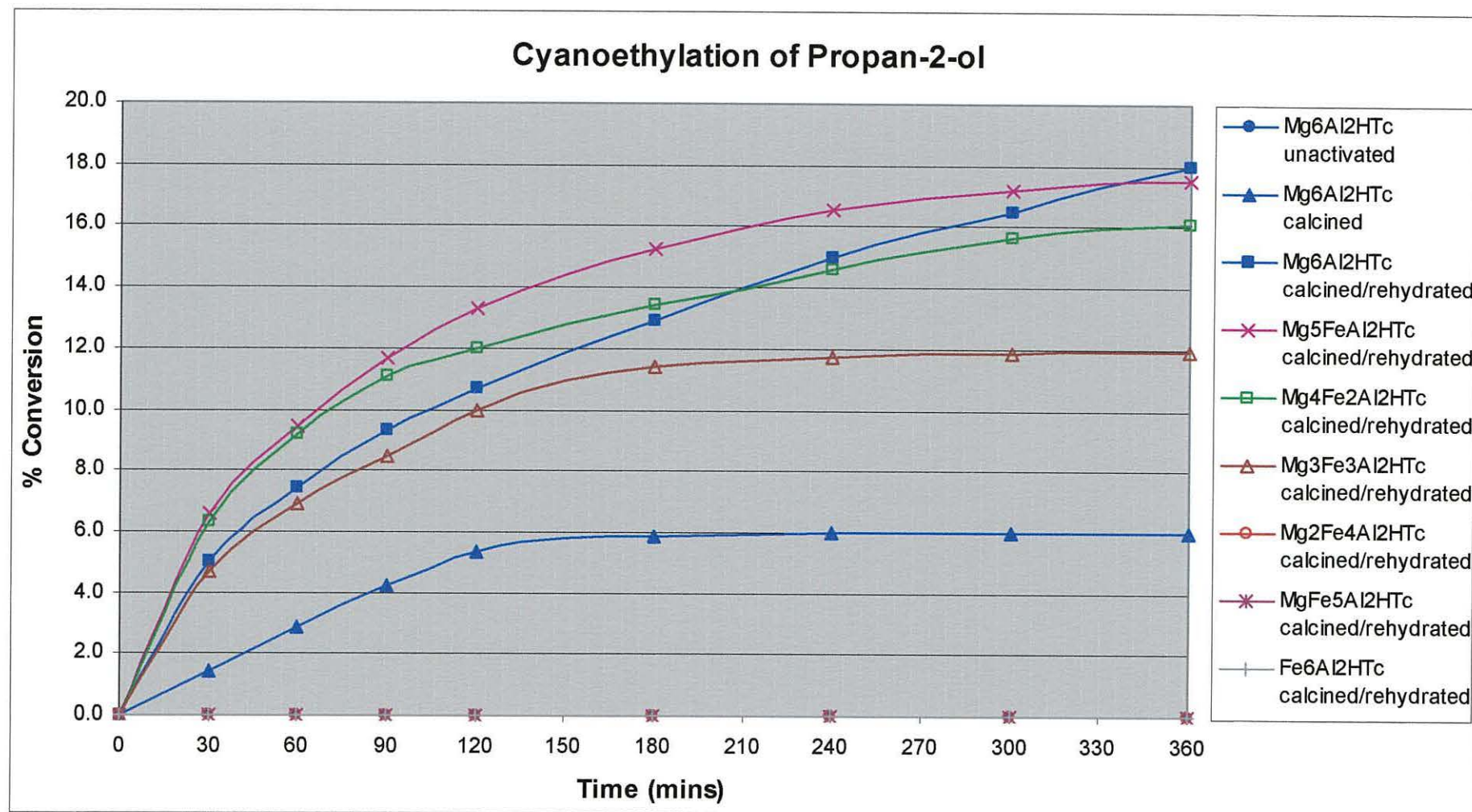


Figure 4.4 Illustration of the change in percentage conversion of acrylonitrile to 3-isopropoxypropionitrile over time using a range of catalysts (note y-axis scale is 0-20 % conversion)

N.B. The results illustrated are smoothed curves produced from raw data, using an estimated error of *ca.* ± 2.5 %

Each of the graphs illustrates the activity of the $\text{Mg}_6\text{Al}_2\text{HTc}$ and the full range of Fe-substituted HTc's following calcination at 723 K and subsequent rehydration, as previously described. In addition, the activities of the $\text{Mg}_6\text{Al}_2\text{HTc}$, as prepared and after calcination at 723 K are shown for comparison. Examining the results for cyanoethylation of methanol first; over the six hour period for which samples were taken, all of the materials selected for testing as catalysts exhibited some activity for the reaction. However, there was considerable variation in the activities across the range of catalysts. The catalyst produced following calcination and subsequent rehydration of the $\text{Mg}_6\text{Al}_2\text{HTc}$ exhibited the greatest activity, reaching *ca.* 94 % completion at 2 hours as can be seen in Table 4.1 below (conversions taken from raw data).

Catalyst	Methanol (% conversion)		Ethanol (% conversion)		Propan-2-ol (% conversion)	
	2 hrs	6 hrs	2 hrs	6 hrs	2 hrs	6 hrs
$\text{Mg}_6\text{Al}_2\text{HTc}$ unactivated	9.0	26.0	0.5	1.1	0.0	0.0
$\text{Mg}_6\text{Al}_2\text{HTc}$ calcined @ 723 K	25.5	63.0	5.7	25.6	5.7	5.1
$\text{Mg}_6\text{Al}_2\text{HTc}$ calcined & rehydrated	94.0	100.0	95.0	100.0	11.0	18.0
$\text{Mg}_5\text{FeAl}_2\text{HTc}$ calcined & rehydrated	61.0	100.0	45.8	79.9	14.0	17.5
$\text{Mg}_4\text{Fe}_2\text{Al}_2\text{HTc}$ calcined & rehydrated	59.0	100.0	26.7	63.2	10.8	18.1
$\text{Mg}_3\text{Fe}_3\text{Al}_2\text{HTc}$ calcined & rehydrated	34.0	66.0	10.4	26.1	12.2	9.6
$\text{Mg}_2\text{Fe}_4\text{Al}_2\text{HTc}$ calcined & rehydrated	10.0	30.0	0.5	1.5	0.0	0.0
$\text{MgFe}_5\text{Al}_2\text{HTc}$ calcined & rehydrated	1.5	3.5	0.3	0.5	0.0	0.0
$\text{Fe}_6\text{Al}_2\text{HTc}$ calcined & rehydrated	0.0	1.5	0.0	0.3	0.0	0.0

Table 4.1 Percentage conversion of acrylonitrile to the relevant 3-alkoxypropionitrile at 2 and 6 hours for the range of catalysts tested.

The 100 % conversion stage was achieved for the $\text{Mg}_6\text{Al}_2\text{HTc}$ -derived catalyst at the 6 hour reaction monitoring stage; the increased period of time for 100 % conversion following the high initial rate of reaction was assumed to be a result of the decreasing percentage of acrylonitrile available for the reaction. Although the calcined and rehydrated $\text{Mg}_5\text{FeAl}_2\text{HTc}$ and $\text{Mg}_4\text{Fe}_2\text{Al}_2\text{HTc}$ also took the reaction to 100 % completion at 6 hours, their conversion at 2 hours was markedly less than that for the $\text{Mg}_6\text{Al}_2\text{HTc}$ activated in the same manner. The reaction rate for these Fe-containing catalysts was more linear than that exhibited by the calcined and rehydrated $\text{Mg}_6\text{Al}_2\text{HTc}$ which indicated that may have been a different rate-limiting factor for these catalysts. The general trend through increasing Fe-for Mg substitution in the calcined and rehydrated HTc's was for a decrease in activity of the catalysts, the fully substituted $\text{Fe}_6\text{Al}_2\text{HTc}$ exhibiting no conversion at 2 hours and just 1.5 % at 6 hours. The $\text{Mg}_6\text{Al}_2\text{HTc}$ which was calcined but not rehydrated in a carbon dioxide free atmosphere showed a level of activity slightly below that of the calcined and rehydrated $\text{Mg}_3\text{Fe}_3\text{Al}_2\text{HTc}$ whilst the unactivated $\text{Mg}_6\text{Al}_2\text{HTc}$ showed a similar activity to the calcined and rehydrated $\text{Mg}_2\text{Fe}_4\text{Al}_2\text{HTc}$. The increase in Fe-substitution of the HTc's resulted in an overall decrease in activity of the calcined and rehydrated catalysts which suggested that the main basic sites of concern were linked to the presence of Mg within the structure. This was logical given the generally high activity of magnesium oxides and hydroxides for base catalysed reactions.^{1, 14}

The same general trend in activity was observed in the cyanoethylation of ethanol for the same range of materials. However, other than the calcined and rehydrated $\text{Mg}_6\text{Al}_2\text{HTc}$ which exhibited a nearly identical level of activity, the measured level of activity for each material in this reaction decreased by comparison with the cyanoethylation of methanol. The decrease in activity was such that, although all of the materials tested exhibited some activity over the 6 hour period, the level of conversion was minimal at 2 hours for the high-Fe ratio HTc's and for the unactivated $\text{Mg}_6\text{Al}_2\text{HTc}$.

The activities shown for all the materials tested in the cyanoethylation of propan-2-ol were substantially lower than those recorded in the previous two sets of reactions. Due to the low levels of conversion, the results fluctuated to some extent for some of the samples as the error in the measurement became apparent. However, a similar trend in

activities was observed as was noted in the cyanoethylations of methanol and ethanol for those materials which exhibited any recordable activity. The activities of the calcined and rehydrated $\text{Mg}_6\text{Al}_2\text{HTc}$, $\text{Mg}_5\text{FeAl}_2\text{HTc}$ and $\text{Mg}_4\text{Fe}_2\text{Al}_2\text{HTc}$ were more similar to one another than previously observed. Nonetheless, the maximum conversion recorded for any of the catalysts at 6 hours was just *ca.* 18 %.

The results recorded for the cyanoethylation of methanol were very similar to those observed by Kumbhar and co-workers for the $\text{Mg}_6\text{Al}_2\text{HTc}$'s, activated and unactivated.¹³ The activity of the calcined and rehydrated $\text{Mg}_6\text{Al}_2\text{HTc}$ for the cyanoethylation of ethanol did appear to be lower than that recorded in the literature at 25 minutes (the only time at which a conversion was provided) but the conversion rate was high at this point, as can be seen in Figure 4.3 and may have been comparable overall. However, the conversion of *ca.* 96 % at 90 minutes given in the literature for the cyanoethylation of propan-2-ol using the calcined and rehydrated $\text{Mg}_6\text{Al}_2\text{HTc}$ was substantially higher than that recorded here. The reason for this discrepancy appears to be unclear since the other results appear comparable and similar procedures were used.

Kabashima and Hattori tested a range of metal oxide-type solid base catalysts for the cyanoethylation of alcohols and recorded a range of conversions for these materials.¹⁴ Few showed a level of activity approaching that of the calcined and rehydrated $\text{Mg}_6\text{Al}_2\text{HTc}$'s and even the low-Fe HTc's tested here. Only the oxides of magnesium, calcium and strontium exhibited conversions greater than 90 % within 2 hours in the cyanoethylation of methanol. However, the activation temperatures used for these materials were substantially higher than were used in the activation of the HTc's. The hydroxides of magnesium, calcium, strontium and barium exhibited similar activities to the low-Fe HTc's but the carbonates of these metals exhibited no activity whatsoever. Kabashima and Hattori noted that the variation in conversions recorded for the hydroxides was of the order methanol > ethanol > propan-2-ol, as was noted here for the hydrotalcites. However, they also noted that this order was reversed for the oxides *i.e.* propan-2-ol > ethanol > methanol. As suggested in the literature, the reason for this order of reactivity is a result of the reaction mechanism. In homogeneous systems, the cyanoethylation of alcohols is believed to proceed *via* 3 steps. The first is the abstraction of a proton from the hydroxyl group of the alcohol to form an alkoxide ion. This then reacts with acrylonitrile in step 2 and the resulting 3-alkoxypropionitrile anion

removes a proton from what was initially the base in step 3 to form the 3-alkoxypropionitrile molecule. If a similar mechanism is assumed in heterogeneous systems, since the acidity of the alcohols is of the order methanol (pKa 15.5) > ethanol (pKa 15.9) > propan-2-ol (pKa 18.0),¹⁵ if step 1 were the rate-limiting step then this would also be the expected reaction order *i.e.* methanol would exhibit greater conversions since it is more likely to undergo proton dissociation than ethanol *etc.* This reaction order was observed for the HTc's and is consistent with the action of catalysts with relatively weak basic sites. For the calcined and rehydrated HTc's to possess the level of catalytic activity exhibited, the second and third steps must also be facilitated greatly. The exact mechanism for this reaction on the catalyst surface is unclear but does appear to be reliant to some degree upon the rehydration of the HTc's when using these catalysts. It is proposed here that the rehydration process results in hydrolysis of the water entering the calcined HTc system. The resulting protons may then reform the hydroxyl groups with the O²⁻ sites of the calcined material and the resulting hydroxide ions remain within the interlayer as the charge compensating anions thereby reconstructing the hydrotalcite-type structure to some degree, as was observed in the previous Chapter. If this was the case, this system would be more similar to that of meixnerite, Mg₆Al₂(OH)₁₆(OH)₂·4H₂O.

4.1.3 Conclusions

Overall, this work has illustrated how the substitution of cations within the HTc structure may affect the basicity of the resulting catalyst following appropriate activation. The Fe-containing HTc's may have shown decreased levels of activity, probably due to the relative decrease in magnesium within the structure since magnesium oxides and hydroxides are recognised base catalysts.^{1, 14} The results recorded in this section illustrate that the substitution of Fe-for-Mg within the structure allows the basicity of the activated HTc to be tuned to the desired level which may be useful if moderation of the level of activity shown by the activated Mg₆Al₂HTc's should be desired. In comparison with many of the alternative oxide catalysts, such as MgO, the activation temperature used for the calcined and rehydrated HTc's has been shown to be significantly lower. In addition, Kumbhar and co-workers have already shown the

calcined and rehydrated HTc's to be relatively air stable and re-usable which indicates the possible commercial viability of the use of these catalysts.

4.2 References

- 1 Y. Ono and T. Baba, *in* Catalysis – Royal Society of Chemistry Specialist Periodical Report Volume 15, J.J. Spivey (Senior Reporter), The Royal Society of Chemistry, Cambridge, 2000.
- 2 D. Tichit, M.H. Lhouty, A. Guida, B.H. Chiche, F. Figueras, A. Auroux, D. Bartalini and E. Garrone, *J. Catal.*, 1995, **151**, 50.
- 3 P.S. Kumbhar, J. Sanchez-Valente, J. Lopez and F. Figueras, *Chem. Commun.*, 1998, 535.
- 4 J.I. Di Cosimo, V.K. Diez, M. Xu, E. Iglesia and C.R. Apesteguia, *J. Catal.*, 1998, **178**, 499.
- 5 F. Prinetto, G. Ghiotti, R. Durand and D. Tichit, *J. Phys. Chem. B*, 2000, **104**, 11117.
- 6 A. Vaccari, *Appl. Clay Sci.*, 1999, **14**, 161.
- 7 J. Santhanalakshmi and T. Raja, *Bull. Chem. Soc. Jpn.*, 1997, **70**, 2829.
- 8 W. Kagunya, Z. Hassan and W. Jones, *Inorg. Chem.*, 1996, **35**, 5970.
- 9 K.K. Rao, M. Gravelle, J. Sanchez-Valente and F. Figueras, *J. Catal.*, 1998, **173**, 115.
- 10 J.C.A.A. Roelofs, A.J. van Dillen, M. Versluijs-Helder, J.T.B.T. Jastrzebski and K.P. de Jong, Europa-Cat IV, 4th European Congress on Catalysis, Rimini, 1999.

- 11 J. Shen, M. Tu and C. Hu, *J. Solid State Chem.*, 1998, **137**, 295.
- 12 M.L. Kantam, B.M. Choudary, Ch.V. Reddy, K.K. Rao and F. Figueras, *Chem. Commun.*, 1998, 1033.
- 13 P.S. Kumbhar, J. Sanchez-Valente and F. Figueras, *Chem. Commun.*, 1998, 1091.
- 14 H. Kabashima and H. Hattori, *Catalysis Today*, 1998, **44**, 277.
- 15 A. Streitwieser, C.H. Heathcock and E.M. Kosower, *Introduction to Organic Chemistry* (4th Edition), Macmillan Publishing Company, New York, 1992.

Chapter 5

Oxidation Catalysis

5.1 Sulfur Dioxide Oxidation

5.1.1 Methodology

As discussed earlier in Chapter 1, section 1.3, a catalyst capable of the conversion of sulfur dioxide to sulfur trioxide which exhibits higher activities at lower temperatures would offer a desirable improvement over the main commercial catalyst currently in use, which is based on vanadium pentoxide. The background to oxidation of sulfur dioxide and the subsequent development of the catalysts used in this reaction was provided in Chapter 1 and is not, therefore, discussed in any detail here. Instead, the focus of this section is upon the development of the equipment used for testing the activity of the materials trialled as catalysts for this reaction. The remainder of this Chapter then details the activity results recorded for the materials tested and their subsequent characterisation after the reaction. The materials tested were those derived from HTc's since the product which was obtained from substitution of aluminium into the iron oxide structure did not appear to have a favourable morphology for this reaction, as previously described in Chapter 2.

The catalyst test-rig used for the study of this reaction was purpose-built for the research detailed in this thesis and was based upon a fixed bed microreactor system, details of which are provided in Chapter 7, section 7.6.2. The volume of catalyst packed into the catalyst bed remained constant through the testing, as did flow rate of reactant gases passing through the bed. The reactor system was dynamic in that the reactants were continuously introduced and the products extracted for analysis utilising in-line gas chromatography. The use of a blank microreactor enabled the pressure drop across the reactor to be monitored which was viewed as important due to the repercussions of particle failure, as mentioned in Chapter 1. Heated sample lines were also used since the

expected product, SO_3 gas, might be expected to condense at lower temperatures. This would have resulted in lower conversions than expected. In order to activate the HTc's tested in the reactions, they were pre-calcined at 723 K in order to eliminate water from the structure which may have resulted in the formation of sulfuric acid in the sample lines should it have been produced during the reactions. The characterisation of these activated materials was detailed in Chapter 3, section 3.1.

There is relatively little information available in the literature regarding the development of SO_2 oxidation catalysts other than that previously detailed in Chapter 1, section 1.3 which mainly described the development of the V_2O_5 based catalysts used commercially. Consequently, none of this research appears to relate to catalysts derived from HTc's. With regard to the SO_2 oxidation reaction, it is known that temperatures of *ca.* 670 K can result in satisfactory equilibrium conversions.¹ This reaction temperature was selected by Dunn and co-workers in their study of SO_2 oxidation over a range of mixed metal oxide systems.² They achieved satisfactory conversions (*ca.* 15 %) in an $\text{Fe}_2\text{O}_3/\text{TiO}_2$ system and maximum conversion of *ca.* 23 % in a $\text{V}_2\text{O}_5/\text{Fe}_2\text{O}_3/\text{TiO}_2$ system. Here, the metal oxides were varied on the titania support material and the loading rates were 5 % Fe_2O_3 on TiO_2 and 1 % V_2O_5 / 5 % Fe_2O_3 on TiO_2 . This is one of the few studies to utilise iron oxide phases within a SO_2 oxidation catalyst.

5.1.2 Gas Chromatography

In the experiments for which the results are detailed below, the change in the amount of SO_2 in the gas stream was recorded at regular intervals, generally commencing from a reactor temperature of *ca.* 723 K. This was carried out using a gas chromatograph (GC) equipped with a thermal conductivity detector (TCD) to measure the change in area of the peak assigned to SO_2 in the GC trace. The reactor temperature was then decreased gradually and the change in area of this peak recorded in order to assess the activity change with temperature. Additional experiments were also carried out at a constant temperature of 723 K and over a full cycle of heating/isothermal at 723 K/decrease in temperature. The results of these experiments are illustrated in Figures 5.1-5.10.

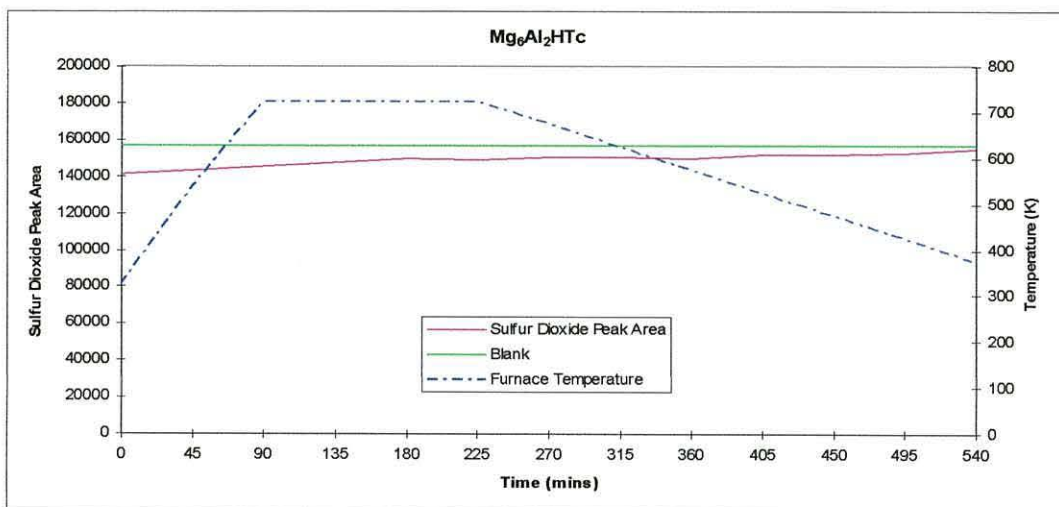


Figure 5.1 Change in SO₂ peak area versus time for Mg₆Al₂HTc calcined at 723 K

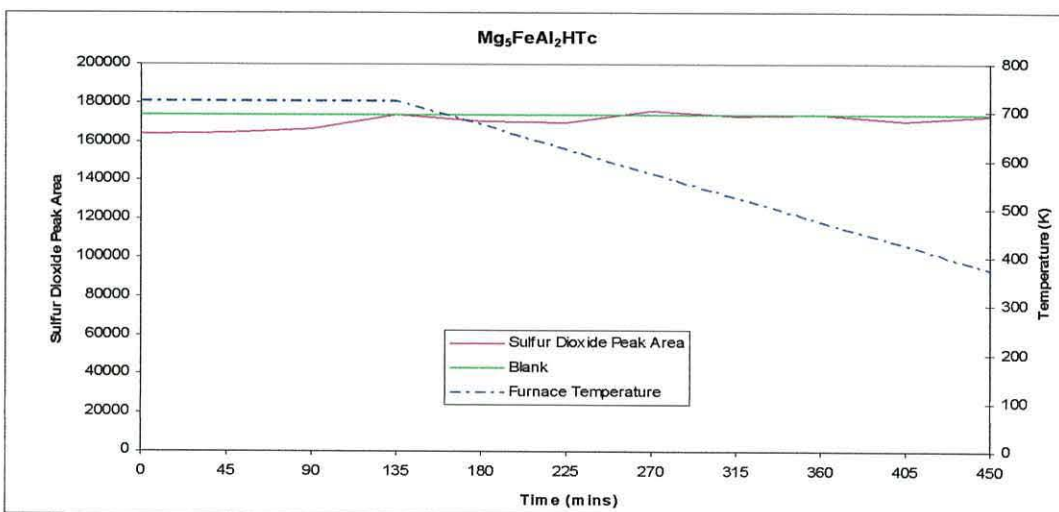


Figure 5.2 Change in SO₂ peak area versus time for Mg₅FeAl₂HTc calcined at 723 K

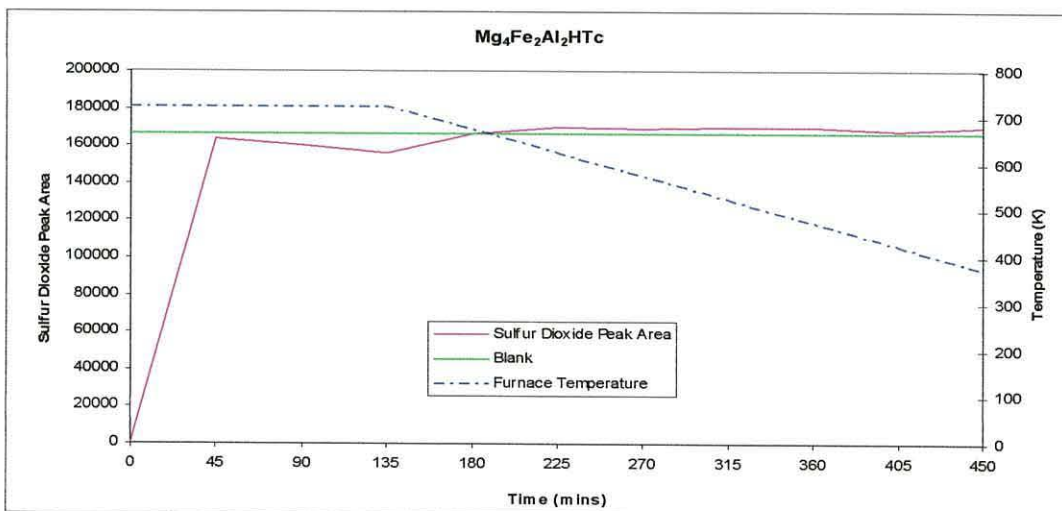


Figure 5.3 Change in SO₂ peak area versus time for Mg₄Fe₂Al₂HTc calcined at 723 K

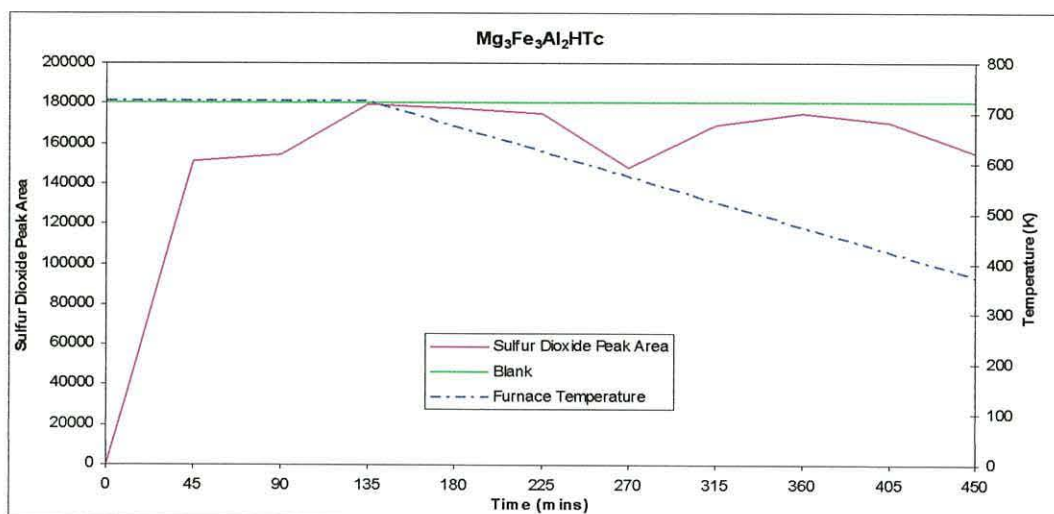


Figure 5.4 Change in SO₂ peak area versus time for Mg₃Fe₃Al₂HTc calcined at 723 K

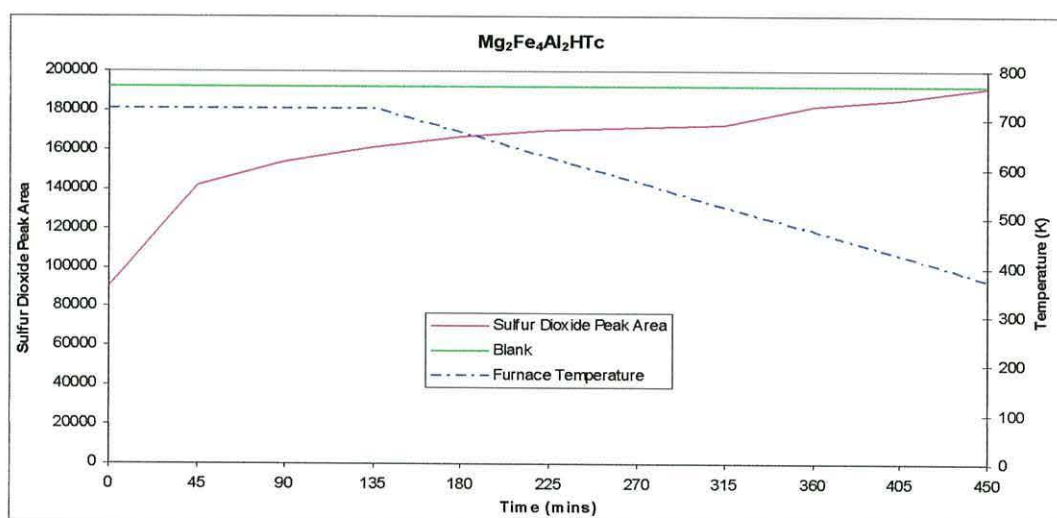


Figure 5.5 Change in SO₂ peak area versus time for Mg₂Fe₄Al₂HTc calcined at 723 K

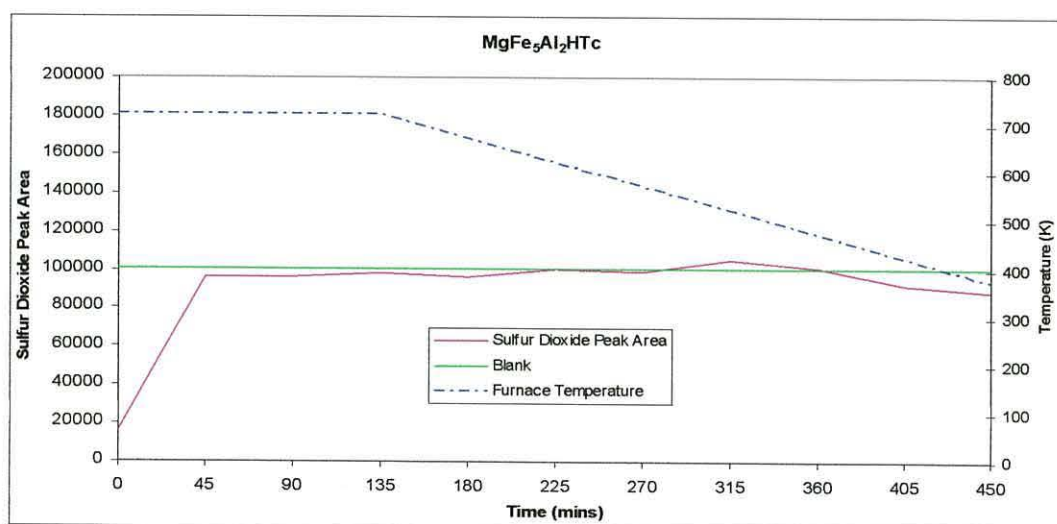


Figure 5.6 Change in SO₂ peak area versus time for MgFe₅Al₂HTc calcined at 723 K

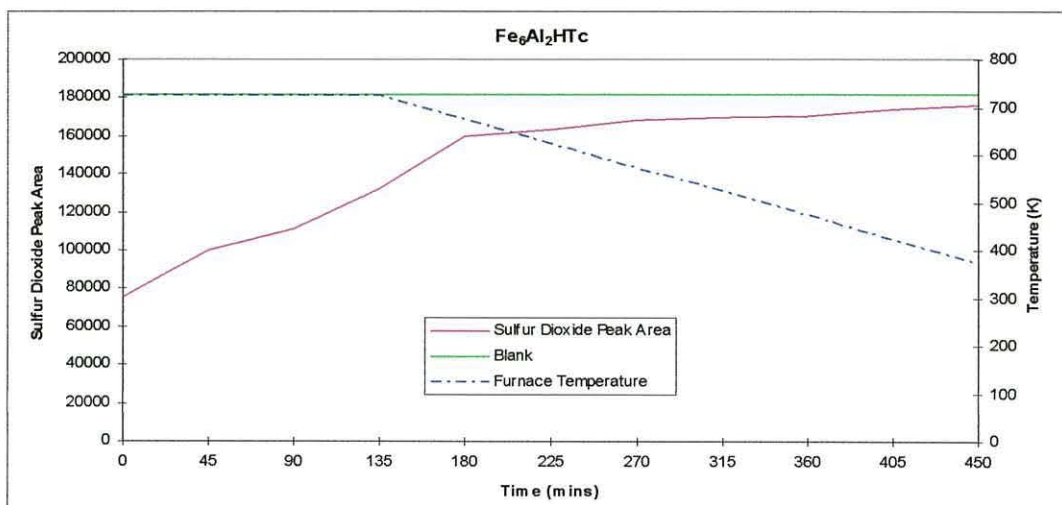


Figure 5.7 Change in SO₂ peak area versus time for Fe₆Al₂HTc calcined at 723 K

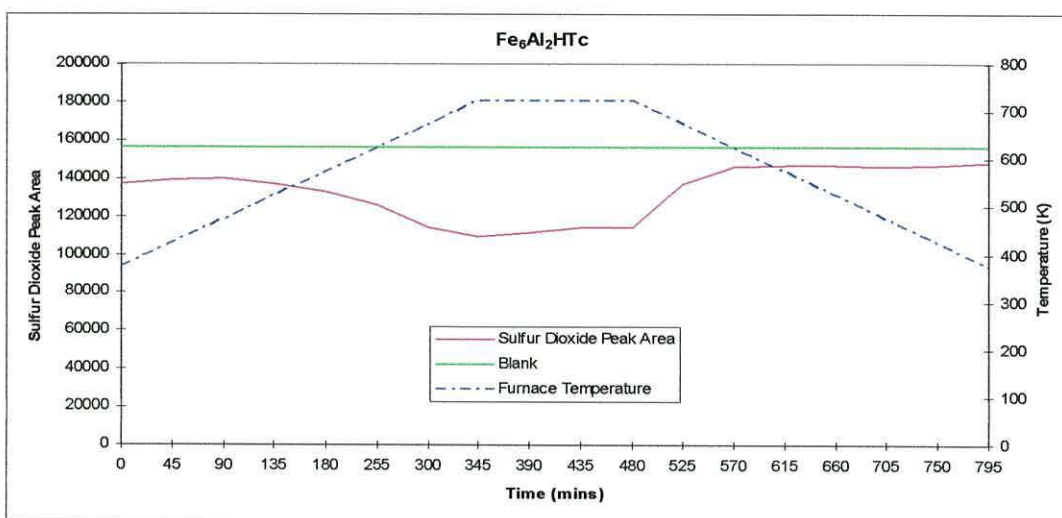


Figure 5.8 Change in SO₂ peak area versus time for Fe₆Al₂HTc calcined at 723 K

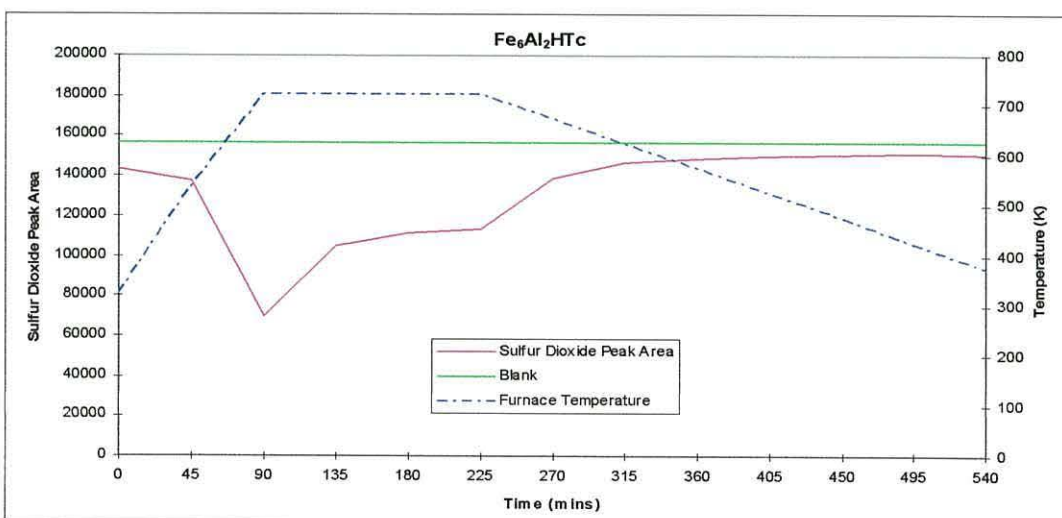


Figure 5.9 Change in SO₂ peak area versus time for Fe₆Al₂HTc calcined at 723 K

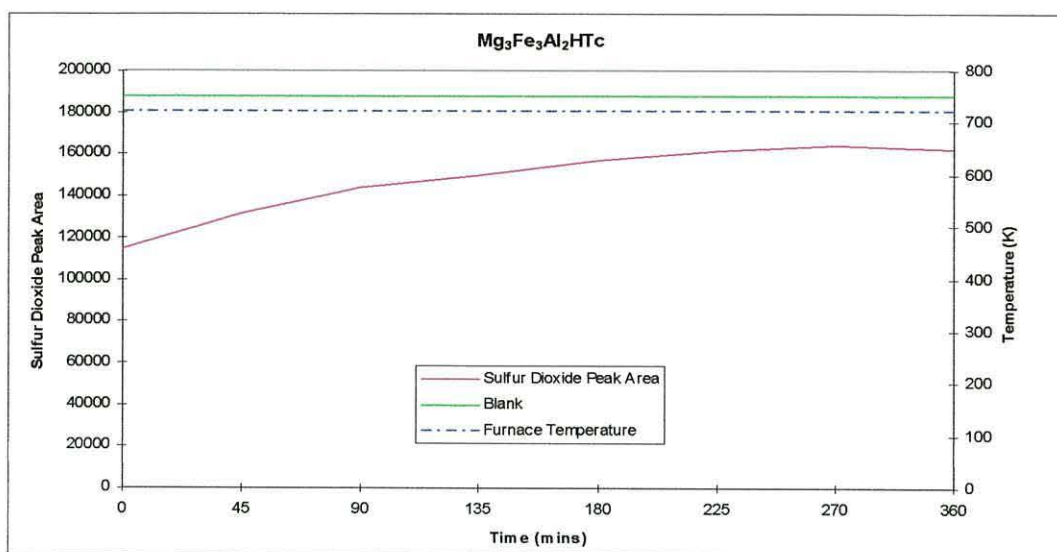


Figure 5.10 Change in SO₂ peak area versus time for Mg₃Fe₃Al₂HTc calcined at 723 K

For each of the graphs illustrated above, the first injection of gas from the GC sample loop was taken *ca.* 15 mins after SO₂/air mixture had been introduced into the system. This time period equates to 0 mins on the x-axis of the graphs and was selected since the gases were assumed to have completely filled the system and a representative sample was expected. A peak was not observed on the GC traces for any of the experiments at a retention time expected for SO₃ but variations in peak area of the peak representative of SO₂ did indicate that SO₂ was being either converted to another product or, perhaps more likely, being absorbed over time/change in reaction temperature. Consequently, a decrease in the SO₂ peak area is described here as uptake rather than conversion. Samples of gas from the by-pass 'blank' microreactor were taken after each of the reactions rather than during because the interruption in flow caused by taking 'blank' values during the experiments tended to cause channelling of the reaction gases through the catalyst beds upon the re-introduction of the gases through the beds. This introduced inconsistencies in the GC traces. In addition, there was a reasonable variability between experiments which meant that direct comparison of the absolute SO₂ peak area values (shown on the y-axis) between different samples was not possible. This variability was assigned, at least in part, to the gradual physical deterioration of the GC sample loop injection valve rotor as the experiments progressed. The deterioration was relatively slow, however, which does allow a general comparison in the trends for each graph.

Figures 5.1 to 5.7 best illustrate the comparison of SO₂ uptake between the products with increasing Fe-substitution from Mg₆Al₂HTc to Fe₆Al₂HTc. There did not appear to be a clear trend in SO₂ uptake corresponding with increased Fe-substitution - the uptake of SO₂ was variable and ranged between 100-0 %, the former at the start of many experiments and the latter approaching the end of some of the experiments. The maximum uptake of SO₂ for each of the catalysts tested is shown in Table 5.1 (this occurred at 0 mins, as shown in Figures 5.1-5.7, for each catalyst).

Mg ₆ Al ₂ HTc	Mg ₅ FeAl ₂ HTc	Mg ₄ Fe ₂ Al ₂ HTc	Mg ₃ Fe ₃ Al ₂ HTc	Mg ₂ Fe ₄ Al ₂ HTc	MgFe ₅ Al ₂ HTc	Fe ₆ Al ₂ HTc
9.7 %	5.9 %	100.0 %	100.0 %	54.8 %	80.2 %	58.8 %

Table 5.1 Maximum SO₂ uptake for each catalyst (at 0 mins)

The data presented in Table 5.1 indicates that the catalysts derived from Mg₄Fe₂Al₂HTc and Mg₃Fe₃Al₂HTc were the most active, those derived from Mg₂Fe₄Al₂HTc, MgFe₅Al₂HTc and Fe₆Al₂HTc moderately active and those derived from Mg₆Al₂HTc and Mg₅FeAl₂HTc the least active. However, the graphs recorded in Figures 5.1-5.7 indicate that, after the often high initial uptake of SO₂ by some of the catalysts, the rate of uptake is often reduced thereafter.

Overall, two main trends in the uptake of SO₂ did appear to be present across the range of catalysts. The first was that there was an initial uptake of SO₂ which was greater than at any other time of measurement. This uptake was so great for some of the Fe-containing catalysts that there was no peak present on the GC trace at a retention time corresponding to SO₂. The time-dependency of uptake can clearly be seen in Figure 5.10 which was an isothermal experiment, at 723 K. The second trend was for temperature-dependence of SO₂ uptake. There was a greater uptake at higher temperatures; the maximum occurring for each sample at 723 K which is quite obvious in a number of graphs, particularly that in Figure 5.8 which illustrates the change in SO₂ uptake over a cycle of reaction temperature change. The decreased SO₂ uptake with a reduction in temperature is clear in each of the graphs in Figures 5.1-5.10. An additional observation was that the SO₂ uptake may also have been dependent upon the furnace heating rate, being greater as the heating rate was increased. This is evident upon comparison of Figures 5.8 and 5.9.

In summary, it appears that the materials derived from the HTc's with partial but not complete Fe-substitution offered the optimum initial uptake of SO₂. In addition, increasing the temperature of the catalyst bed (to *ca.* 723 K) also appeared to increase SO₂ uptake. Therefore, it is proposed that the maintenance of the HTc morphology at this elevated temperature results in the formation of a high surface area mixed metal oxide which possesses the necessary chemical and physical characteristics to act as a SO₂ sorbent. Whether the SO₂ is subsequently oxidised is not clear at this stage.

On a number of occasions during the experiments, it was noted that an excessive pressure drop developed across the catalyst bed. The frequency of this occurrence appeared to increase with the catalysts derived from the high-Fe HTc's which suggested that particle failure was occurring more regularly in these catalyst beds. This may have been due to the change in morphology from that expected of HTc's and their calcination products to that of the iron oxides and spinel-type materials, as shown in Chapter 3. An additional experimental observation was that droplets of an highly acidic liquid (*ca.* pH 1) were formed on the exit side of the catalyst beds following the experiments. This suggested that some of the SO₂ may have been converted to SO₃/H₂SO₄ during the reactions but may have condensed within the sample lines despite them being heated.

5.1.3 Infrared Spectroscopy

The data produced from the infrared spectroscopy of the used catalysts is provided in Table 5.2 and some representative spectra are illustrated in Figure 5.11 (a-c). The IR spectra were recorded following a 'cleaning' cycle of the catalyst which was achieved by passing clean air through the catalyst bed following the reaction with SO₂. This procedure was carried out in order to remove any adsorbed material from the catalyst which may have resulted in misleading data. Each of the IR spectra exhibited peaks at *ca.* 3000-3500 cm⁻¹ and *ca.* 1600 cm⁻¹ which were assigned to OH stretches and bends, respectively. Other than the presence of these maxima, the spectra were unlike those recorded previously for the calcined HTc's in the positions of many of the remaining bands. The most obvious of these was the group at *ca.* 1020-1180 cm⁻¹ which formed a

Table 5.2 Infrared absorption bands (cm^{-1}) recorded between 4000 and 400 cm^{-1} for used SO_2 oxidation catalysts

Mg₆Al₂HTc Exptl. method 1	Mg₅FeAl₂HTc	Mg₄Fe₂Al₂HTc	Mg₃Fe₃Al₂HTc	Mg₂Fe₄Al₂HTc	MgFe₅Al₂HTc	Fe₆Al₂HTc
	3448 s	3447 s, br	3448 m, br	3422 m, br	3448 m, br	3182 m, br
2794 m, br						
1615 m, br	1637 w, br	1637 w, br	1628 w, br	1636 w, br	1636 w, br	1635 w, br
1540 m, br						
	1420 vw, br				1420 vw, br	
1180 m	1157 s	1174 s	1177 s	1174 s	1175 s	1178 s, shldr
			1150 s, shldr	1150 s	1150 s, shldr	
		1100 m, shldr	1113 s	1115 s	1124 s	1126 s
			1078 s	1080 s		
		1026 w, shp	1020 m	1024 m		1025 m, shldr
1000 w, shldr	998 w					
856 w	850 m, shldr	850 w, shldr		850 w, shldr	850 vw	
		706 w	704 w, shp	705 w		
672 w			670 w	670 m, shp	670 w, shp	670 vw, shp
						663 m, shp
					625 w, shp	625 w, shp
611 w	612 m	612 m, shp	611 m, shp	610 m	596 w, shp	598 w, shp
		500 w	496 w, shp	496 m	488 w	
473 w	475 s					474 w

N.B. HTc formulae correspond to uncalcined materials

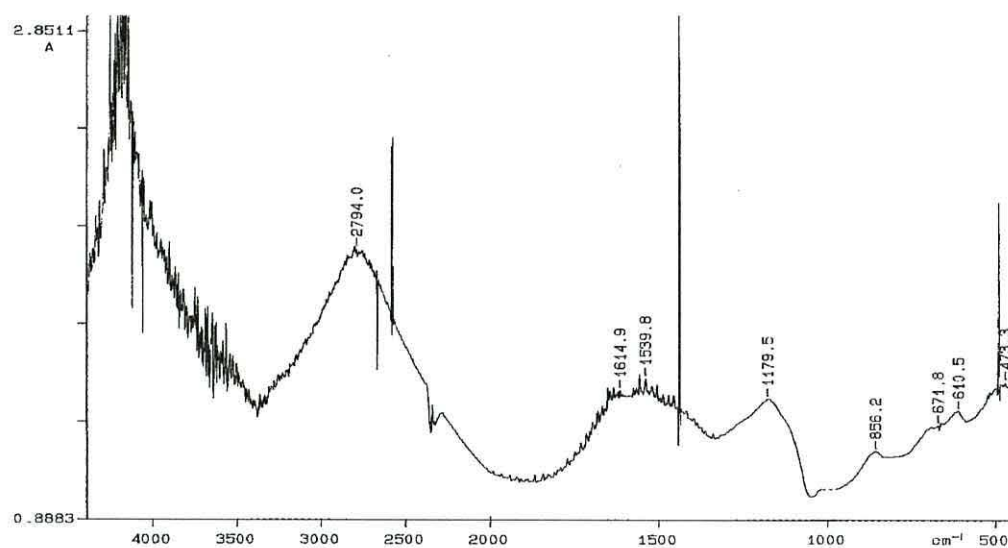


Figure 5.11 (a) IR spectrum of $\text{Mg}_6\text{Al}_2\text{HTc}$ (Exptl Method 1) used SO_2 oxidation catalyst

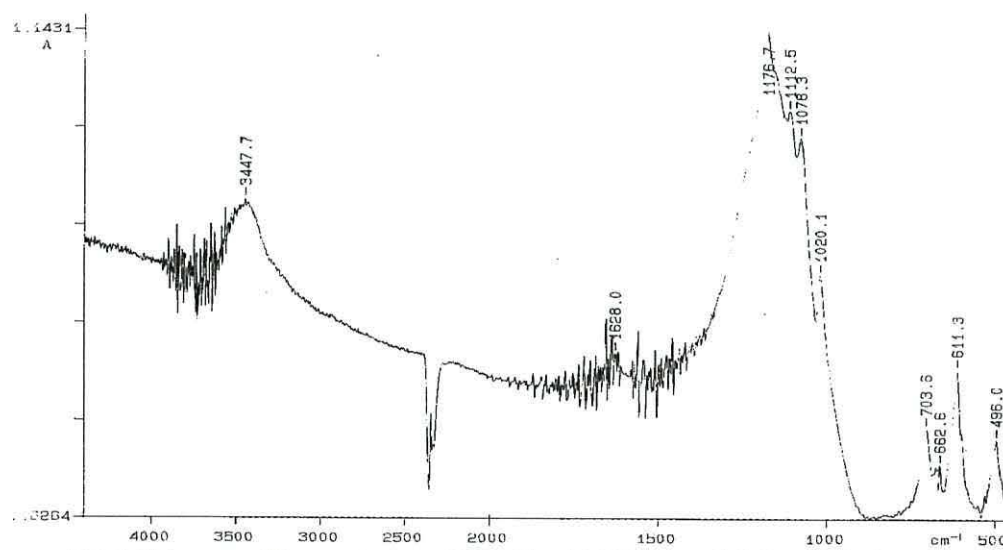


Figure 5.11 (b) IR spectrum of $\text{Mg}_3\text{Fe}_3\text{Al}_2\text{HTc}$ used SO_2 oxidation catalyst

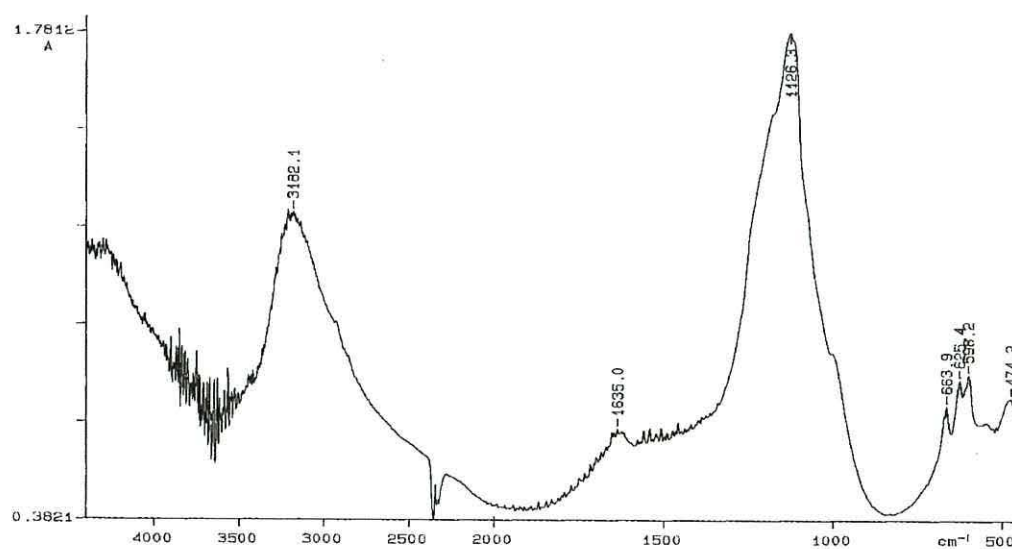


Figure 5.11 (c) IR spectrum of $\text{Fe}_6\text{Al}_2\text{HTc}$ used SO_2 oxidation catalyst

series of bands of strong absorption intensity with multiple maxima and shoulders which were difficult to resolve. There were also a number of sharp bands below 1000 cm^{-1} which had not previously been observed following the catalyst activation stage. The group of bands at *ca.* $1020\text{--}1180\text{ cm}^{-1}$ were consistent with the splitting of the $\nu_3\text{ SO}_4^{2-}$ vibration.^{3,4} This splitting is known to be a result of the lowering of symmetry of the ‘free’ sulfate ion, which has tetrahedral symmetry (point group T_d), as it becomes co-ordinated. In addition to the splitting of the ν_3 vibration, some splitting of the ν_4 mode at *ca.* $600\text{--}700\text{ cm}^{-1}$ has also been reported to occur and the ν_1 and ν_2 bands become IR active at *ca.* 1000 cm^{-1} and 480 cm^{-1} , respectively. Bands consistent with the presence of sulfate in a low symmetry environment were, therefore, evident in each of the spectra. However, the splitting of the ν_3 band was not clear for the $\text{Mg}_6\text{Al}_2\text{HTc}$ or the $\text{Mg}_5\text{FeAl}_2\text{HTc}$ reaction product where much lower SO_2 absorption was recorded. Other than the peaks assigned above, the remaining peaks were assigned to M-O skeletal vibrations; in general though, the SO_4^{2-} bands dominated the spectra.

5.1.4 X-ray Powder Diffraction

The XRPD data recorded for each of the used catalysts is shown in Table 5.3, together with reference patterns for hydrotalcite and aluminium and iron sulfates, for comparison.

Two clearly distinct phases were observed from the XRPD data of each of the used catalysts. The first was that of a hydrotalcite-type phase, as is evident upon comparison with the pattern of hydrotalcite in Table 5.3. Some reconstitution of the HTc structure was expected to a degree since air was used as a reaction/cleaning gas in post-reaction treatment at decreased temperature and the sulfate ion may have been incorporated within the interlayer region. The intensity of the peaks indicating the presence of this material decreased with increasing Fe-substitution which was in-keeping with the earlier observations recorded in Chapter 3, section 3.2.3, regarding the reconstitution of the hydrotalcite structure. The second phase was consistent with the presence of a metal sulfate. Which sulfate was not clear since the peak positions in the patterns recorded for each of the Fe-containing HTc’s were between those expected of aluminium and

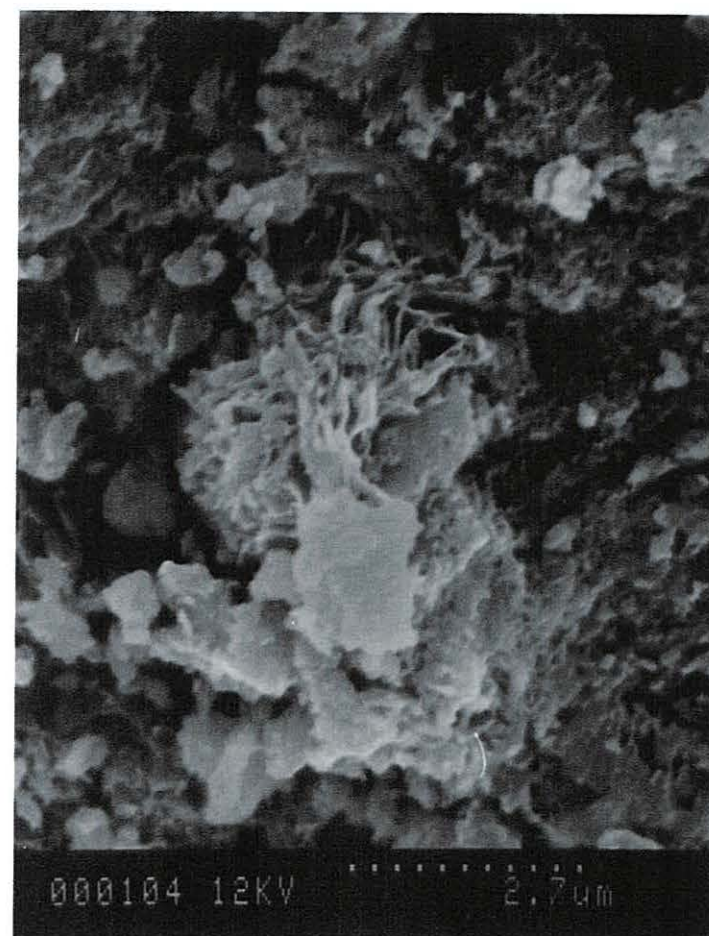
Table 5.3 X-ray powder diffraction d-spacing results (Å) for used SO₂ oxidation catalysts (relative intensities in parentheses)

Hydrotalcite ⁵ (Mg ₆ Al ₂ HTc)	Mg ₆ Al ₂ HTc (method 1)	Mg ₅ FeAl ₂ HTc	Mg ₄ Fe ₂ Al ₂ HTc	Mg ₃ Fe ₃ Al ₂ HTc	Mg ₂ Fe ₄ Al ₂ HTc	MgFe ₅ Al ₂ HTc	Fe ₆ Al ₂ HTc	Al sulphate ⁶ [Al ₂ (SO ₄) ₃]	Fe sulphate ⁷ [Fe ₂ (SO ₄) ₃]
7.69 (100)	7.71 (25) broad	7.55 (17) broad	7.85 (8) broad	7.28 (5)	7.71 (3) broad	7.68 (2) broad	7.63 (2) broad		
				5.92 (12)	5.94 (11)	5.92 (25)	5.85 (31)	5.80 (30)	6.04 (60)
			4.43 (67)	4.30 (13)	4.42 (8)				
					4.31 (14)	4.31 (18)	4.25 (24)	4.23 (13)	4.39 (40)
			4.02 (63)	4.12 (10)	4.12 (12)	4.09 (14)	4.10 (14)		4.14 (10)
3.88 (70)									
			3.61 (59)						3.71 (10)
	3.51 (20) broad		3.53 (100)	3.54 (100)	3.56 (100)	3.57 (100)	3.54 (100)	3.50 (100)	3.62 (100)
			3.16 (27)						
			2.94 (23)	2.97 (19)	2.97 (30)	2.98 (33)	2.96 (32)	2.92 (25)	
			2.83 (27)						
			2.77 (38)	2.78 (5)					2.76 (40)
				2.72 (17)	2.72 (28)	2.73 (35)	2.70 (27)		2.68 (20)
			2.63 (43)	2.64 (24)	2.65 (29)	2.66 (19)	2.65 (21)	2.65 (30)	
2.58 (20)	2.54 (5) broad	2.53 (17) broad	2.56 (37)		2.50 (25)	2.50 (18)	2.49 (15)		
			2.46 (45)	2.44 (19)	2.44 (21)	2.45 (7)			2.43 (10)
				2.37 (11)	2.38 (14)	2.38 (15)	2.38 (8)	2.35 (2)	2.38 (20)
2.30 (20)			2.28 (15)	2.29 (7)	2.30 (12)	2.26 (7)	2.28 (6)		
							2.24 (6)	2.22 (8)	2.00 (10)
						2.13 (3)	2.17 (4)		
	2.09 (100)	2.08 (100)		2.09 (7)	2.07 (7)	2.11 (3)	2.07 (3)		
			2.04 (16)	2.02 (5)		1.98 (3)		2.03 (8)	
1.96 (20)				1.97 (6)	1.97 (5)	1.96 (5)		1.95 (4)	
				1.86 (2)		1.86 (4)	1.85 (4)	1.87 (2)	1.88 (10)
			1.82 (8)					1.82 (2)	
1.75 (10)					1.78 (4)	1.79 (5)	1.78 (4)		
			1.76 (9)	1.76 (7)			1.75 (6)	1.75 (8)	1.71 (20)
			1.68 (5)	1.68 (4)	1.69 (4)	1.70 (5)	1.69 (5)	1.66 (8)	
1.65 (10)			1.62 (3)			1.60 (5)	1.59 (3)	1.63 (4)	1.61 (10)
				1.56 (6)	1.56 (6)	1.56 (6)	1.56 (5)	1.57 (2)	1.57 (10)
1.53 (20)								1.53 (10)	
1.50 (20)	1.48 (80)	1.48 (90)			1.48 (4)			1.49 (4)	1.48 (10)

iron sulfates.^{6, 7} This was to be expected for materials of this nature containing an interdispersion of Al and Fe cations. The ionic radii of Al^{3+} and Fe^{3+} are similar, being 0.54 Å and 0.65 Å respectively, and the recorded positions for many of the used SO_2 oxidation catalysts were generally between those of the Al and Fe sulfates, as shown in Table 5.3. The formation of sulfate phases illustrates two key points. Firstly, there is absorption of SO_2 and, secondly, there is subsequent oxidation to form the sulfate. There were also a number of additional, less intense, peaks present in the patterns of the high Fe-substituted HTc's but the origin of these could not be accurately assigned.

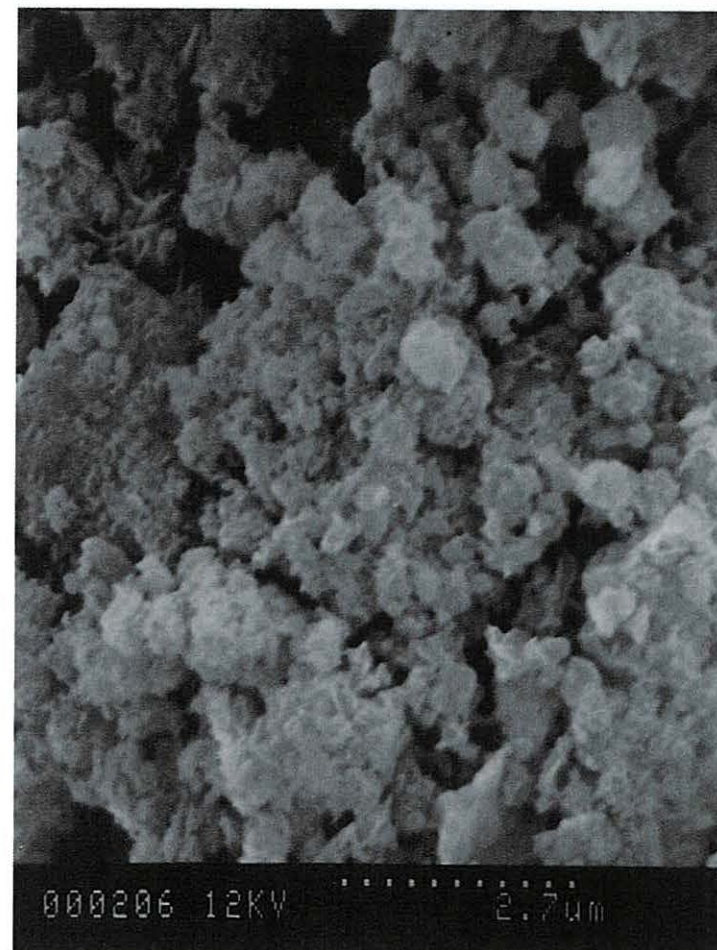
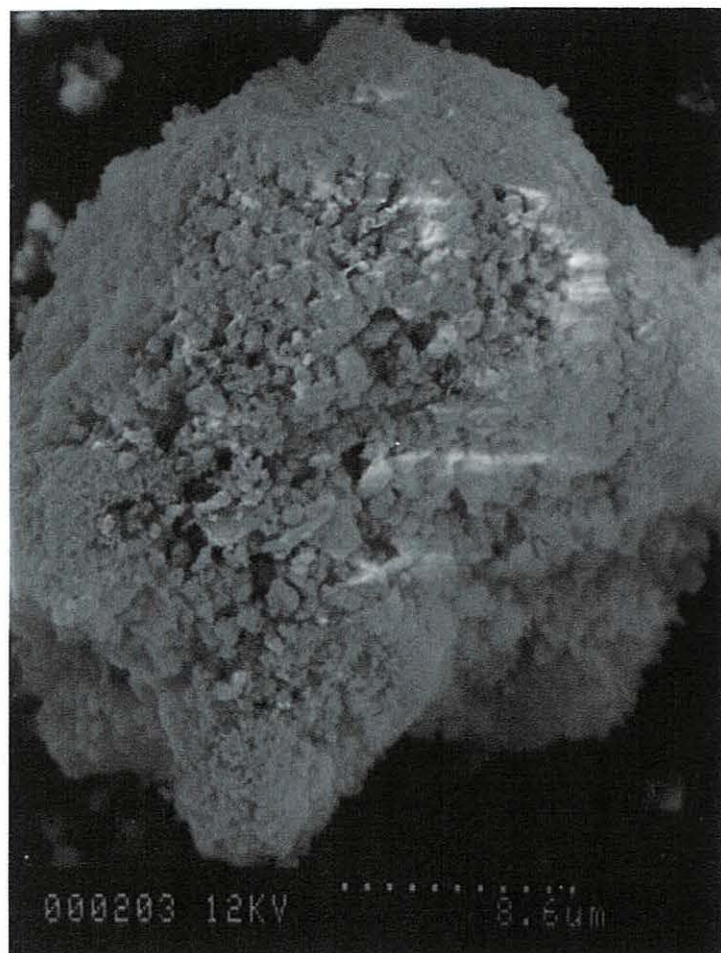
5.1.5 Scanning Electron Microscopy and Energy Dispersive Analysis of X-rays

The micrographs shown in Figures 5.12-5.17 were selected as being representative of each of the corresponding used catalysts, following careful analysis of each sample. A plate-like morphology was clearly visible for the used catalyst derived from $\text{Mg}_6\text{Al}_2\text{HTc}$ and also for the low-Fe substituted catalysts. These platelets were quite well-defined for these materials but increased Fe-substitution resulted in a decrease in the size of the crystallites. The presence of these platelets indicated that the hydrotalcite-type morphology had been maintained throughout the heating cycle of the reaction. In contrast, the high Fe-substituted materials had a morphology which was quite 'sponge-like' in nature with no evidence of larger plates. They did, however, appear to have a surface microtopography indicative of a high surface area materials. Rapid analysis of all of the used catalysts was imperative as it was observed that the used catalysts were hygroscopic in nature, adsorbing moisture from the air which resulted in a quite different morphology if they weren't stored appropriately. This characteristic was indicative of the presence of sulfate phases.



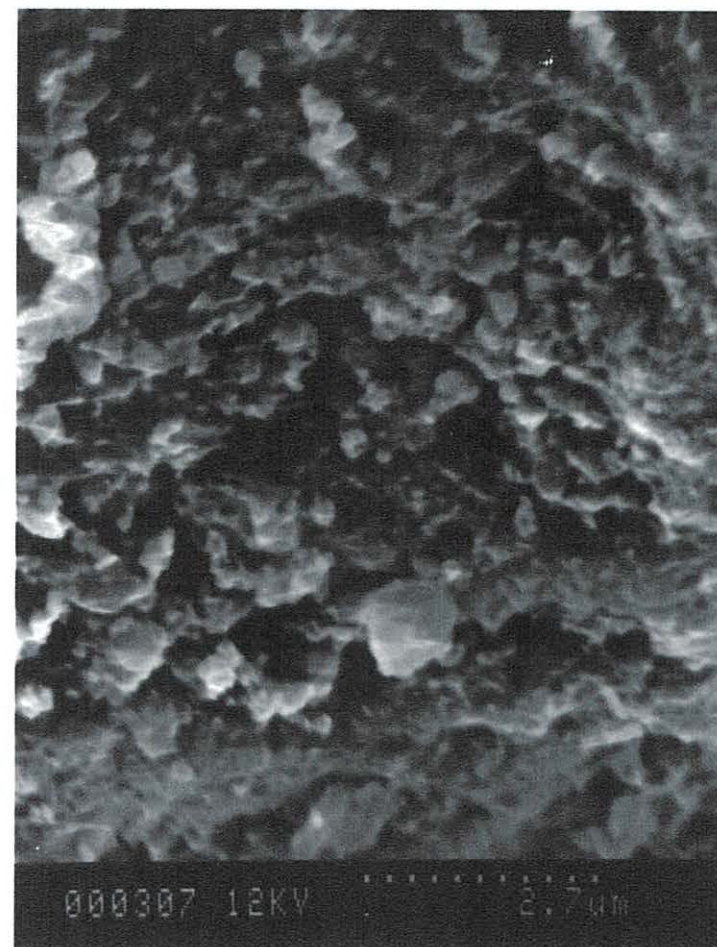
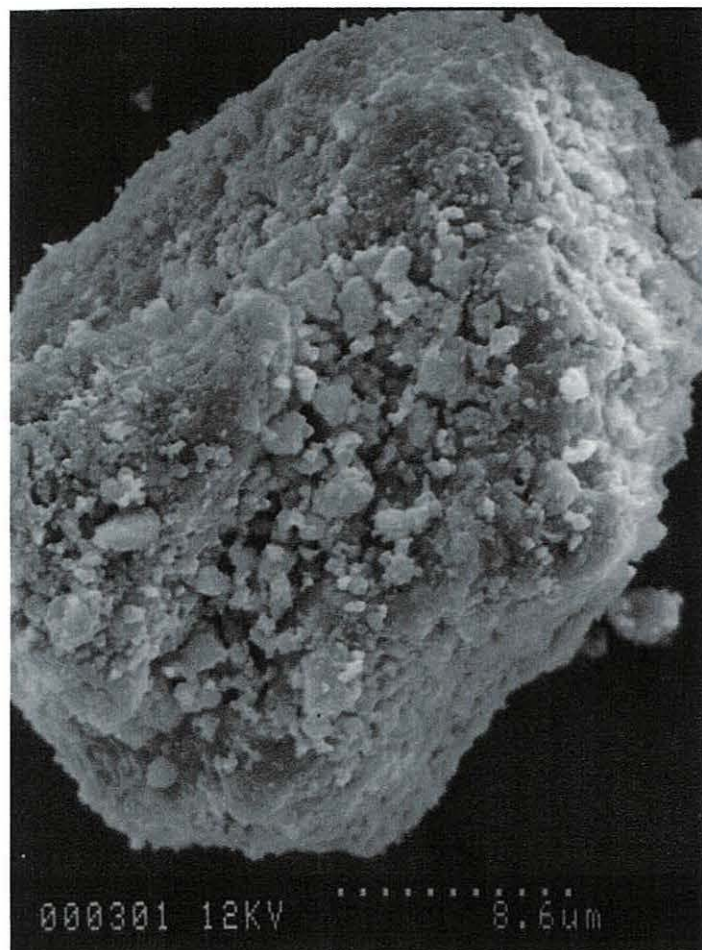
Figures 5.12 (a) & (b): SEM's of $\text{Mg}_6\text{Al}_2\text{HTc}$ product formed using preparative method 1 following sulfur dioxide oxidation reaction

N.B. Scale bar is represented at the bottom of each micrograph as a series of dots (approximate length $\blacklozenge \longrightarrow \blacklozenge$) with the scale below



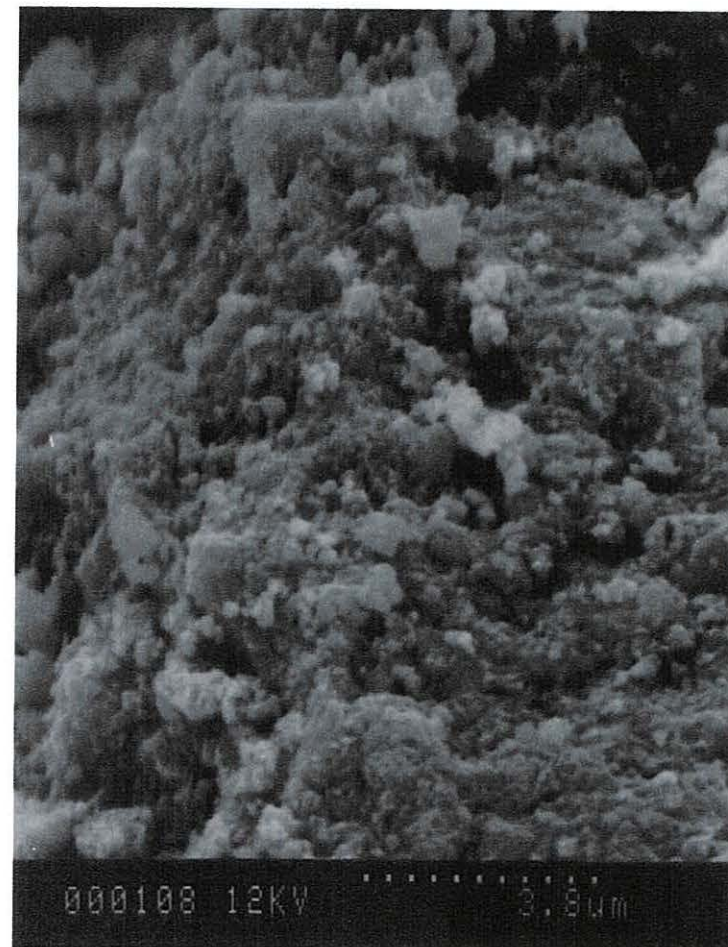
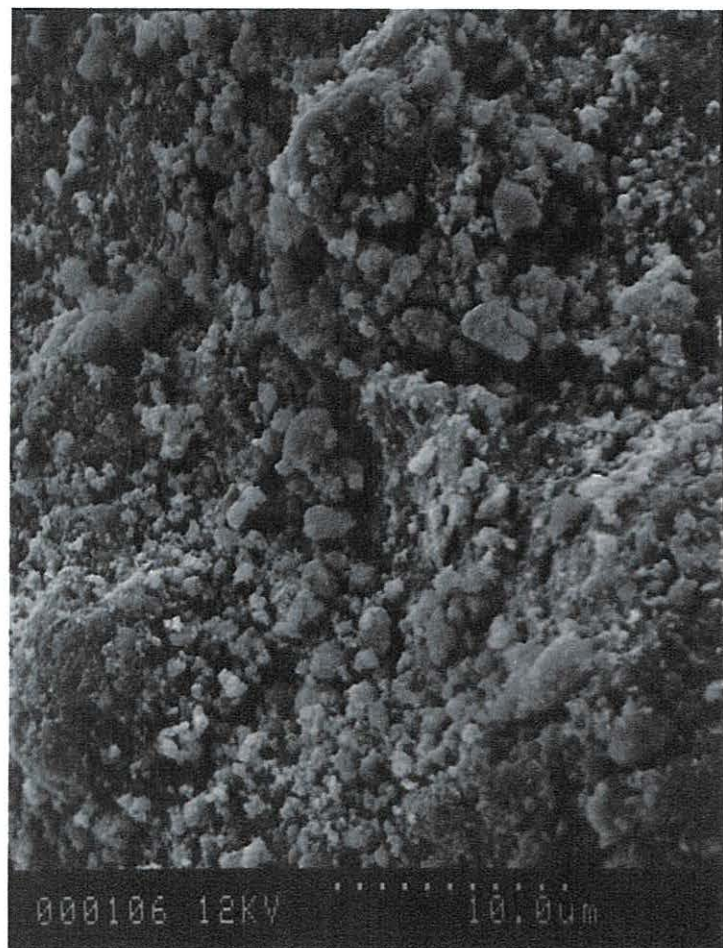
Figures 5.13 (a) & (b): SEM's of $\text{Mg}_5\text{FeAl}_2\text{HTc}$ product following sulfur dioxide oxidation reaction

N.B. Scale bar is represented at the bottom of each micrograph as a series of dots (approximate length $\blacklozenge \longrightarrow \blacklozenge$) with the scale below



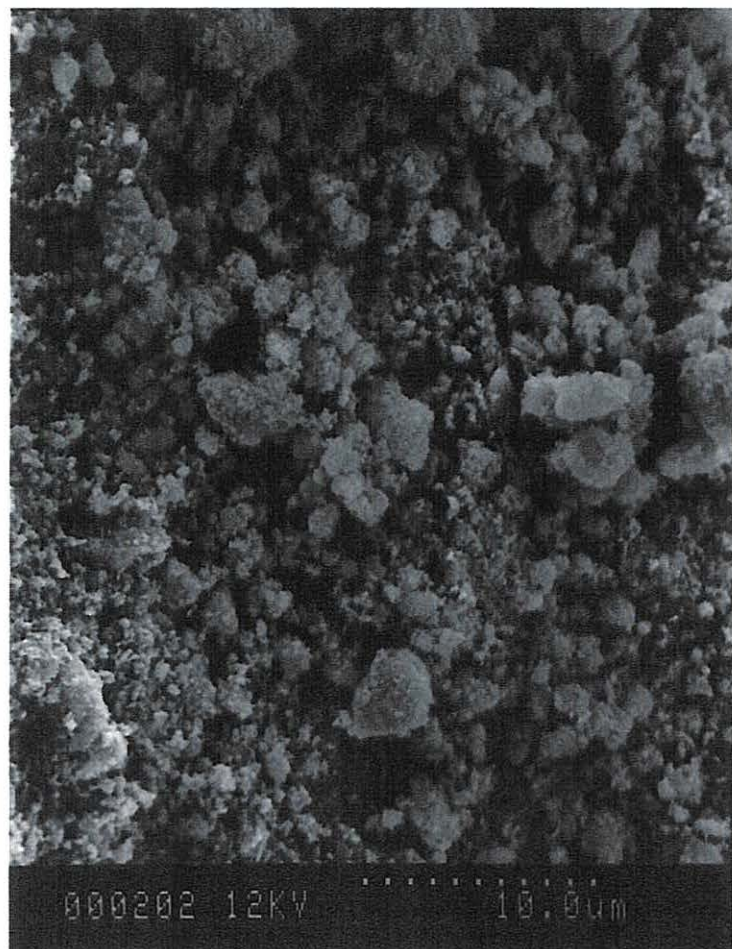
Figures 5.14 (a) & (b): SEM's of $\text{Mg}_4\text{Fe}_2\text{Al}_2\text{HTc}$ product following sulfur dioxide oxidation reaction

N.B. Scale bar is represented at the bottom of each micrograph as a series of dots (approximate length $\blacklozenge \longrightarrow \blacklozenge$) with the scale below



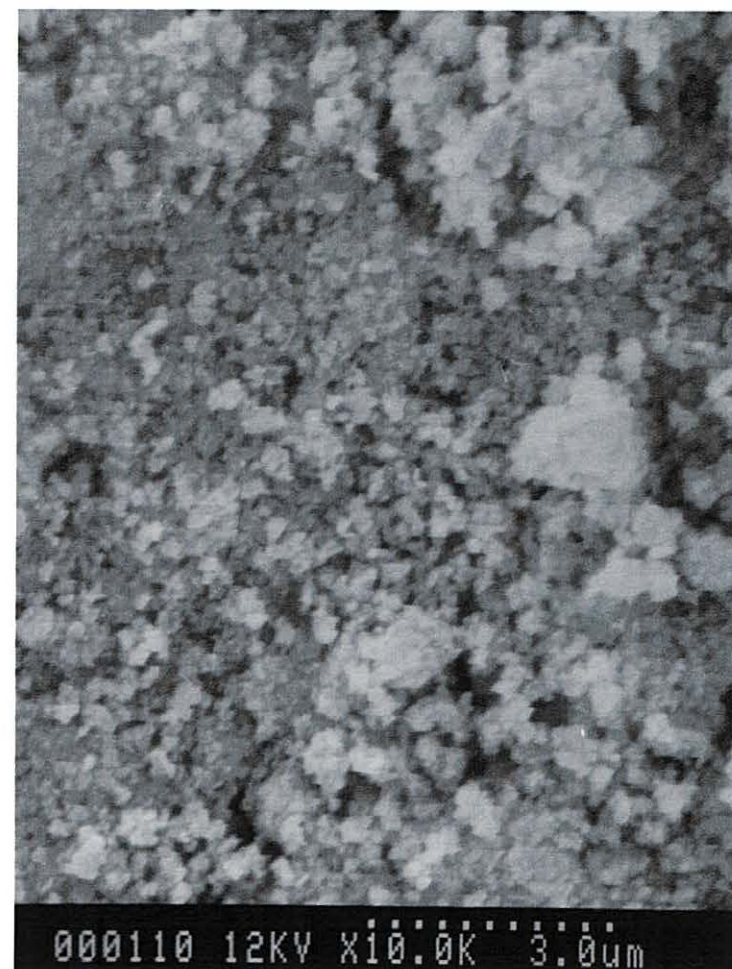
Figures 5.15 (a) & (b): SEM's of $\text{Mg}_3\text{Fe}_3\text{Al}_2\text{HTc}$ product following sulfur dioxide oxidation reaction

N.B. Scale bar is represented at the bottom of each micrograph as a series of dots (approximate length $\blacklozenge \text{-----} \blacklozenge$) with the scale below



Figures 5.16 (a) & (b): SEM's of Mg₂Fe₄Al₂HTc product following sulfur dioxide oxidation reaction

N.B. Scale bar is represented at the bottom of each micrograph as a series of dots (approximate length $\blacklozenge \longrightarrow \blacklozenge$) with the scale below



Figures 5.17 (a) & (b): SEM's of $\text{MgFe}_5\text{Al}_2\text{HTc}$ product following sulfur dioxide oxidation reaction

N.B. Scale bar is represented at the bottom of each micrograph as a series of dots (approximate length $\blacklozenge \text{-----} \blacklozenge$) with the scale below

EDAX analysis of the used catalysts (the results of which are summarised in Table 5.4) indicated that although there was a significant amount of sulfur homogeneously dispersed within all of the samples of used catalysts, the apparent intensity in the sulfur peak did change according to the proportions of metal ions within the samples. In general, the percentage of sulfur within each of the samples appeared to increase in relation to the proportion of metal ions through the materials derived from $\text{Mg}_6\text{Al}_2\text{HTc}$ to $\text{Mg}_5\text{FeAl}_2\text{HTc}$ to $\text{Mg}_4\text{Fe}_2\text{Al}_2\text{HTc}$ but then appeared to level off and remain relatively constant as the Fe-substitution continued to increase through the range of catalysts. This indicated that a saturation level had been reached at a relatively low Fe-substitution but that the Fe was probably acting as the primary absorption site, as indicated by the previously reported SO_2 uptake data.

Sample	Mg	Fe	Al	S
$\text{Mg}_6\text{Al}_2\text{HTc}$ (Exptl. Method 1)	4.8-6.0	-	2.0-3.2	2.8-3.2
$\text{Mg}_5\text{FeAl}_2\text{HTc}$	4.0-5.0	1.0-1.4	2.0-2.8	4.0-5.2
$\text{Mg}_4\text{Fe}_2\text{Al}_2\text{HTc}$	3.4-3.8	2.0-2.4	2.0-2.4	6.8-9.4
$\text{Mg}_3\text{Fe}_3\text{Al}_2\text{HTc}$	2.4-2.8	3.2-3.8	2.2-2.6	8.8-11.8
$\text{Mg}_2\text{Fe}_4\text{Al}_2\text{HTc}$	1.4-1.8	4.4-4.8	2.0-2.2	8.6-11.4
$\text{MgFe}_5\text{Al}_2\text{HTc}$	0.2-0.6	5.2-6.0	~2.0	8.8-10.6
$\text{Fe}_6\text{Al}_2\text{HTc}$	-	6.0-6.6	1.8-2.2	8.6-10.8

Table 5.4 Summarised EDAX analysis results for used SO_2 oxidation catalysts (expressed as relative ratios of $K\alpha$ peak intensities)

5.1.6 Conclusions

Overall, it appears that the materials tested here for use as SO_2 oxidation catalysts acted mainly as absorbents for SO_2 . This may not be viewed as a negative result given the demand for sorbents of such gases in pollution control. There also appeared to be some conversion to $\text{SO}_3/\text{H}_2\text{SO}_4$ upon visual inspection of the reaction vessels post-reaction but quantifying the extent of this conversion was not possible. If some SO_2 was absorbed and converted to the sulfate, as indicated by the IR and XRPD data, some desorption would be expected which would account for this acidic liquid. The combined IR, XRPD and SEM/EDAX results indicated that there was a transition in the chemical and physical nature of the used catalysts at the $\text{Mg}_5\text{FeAl}_2\text{HTc}/\text{Mg}_4\text{Fe}_2\text{Al}_2\text{HTc}$ boundary. The IR data indicated that the symmetry of the sulfate ion was lowered for the higher

Fe-substituted samples as the ν_3 band began to split at this point whilst the XRPD patterns for these samples were more similar to Al/Fe sulfates, rather than calcined HTc's. The change in morphology of the samples was less clear upon inspection of the SEM images, with more of a gradual transition from a platelet to a 'sponge-like' morphology as the Fe-substitution was increased. However, the EDAX again showed a transition point of significantly increased, though similar, S uptake for the catalysts containing higher Fe contents than $\text{Mg}_5\text{FeAl}_2\text{HTc}$. It is not clear why the transition point in SO_2 uptake should occur here but this did illustrate that mixed metal sorbents exhibited greater efficiency with respect to SO_2 uptake.

5.2 Cyclohexane Dehydrogenation

5.2.1 Methodology

Catalytic dehydrogenations are a commercially important area of oxidation catalysis, as discussed in Chapter 1, section 1.3. However, the reactions classified as dehydrogenations are many and varied and it is the dehydrogenation of cyclohexane that is investigated here. This reaction has previously been highlighted as having great significance for the future as alternative energy sources are investigated.⁸ Hydrogen is regarded as such an alternative due to its value as an energy source and 'clean' combustion product (water). However, since hydrogen exists as a gas at room temperature and pressure, and is highly combustible, there are significant associated transport and storage problems. Therefore, an ideal solution to this problem would be the use of a liquid source of hydrogen which is more convenient to store and handle and yet is cheap and plentiful enough in itself to allow the production of hydrogen *via* an economical route. Cyclohexane may provide such a source of hydrogen in its dehydrogenation to benzene and this reaction has initiated earlier investigations.⁸⁻¹⁰ As previously discussed in Chapter 1, the catalysts generally used for this reaction are not ideal due to their high initial cost and, since iron oxides are known to exhibit activity for this reaction, the activity of the full range of Fe-for-Mg substituted HTc's was intended to be investigated. However, due to insufficient time primarily as a result of equipment

failure towards the end of the experimental period of this study, only the activity of the $\text{Mg}_5\text{FeAl}_2\text{HTc}$ calcined at 723 K was investigated. This material was selected since it was expected to resist particle failure and maintain the hydrotalcite-type morphology for an extended period during the reaction when the observations noted from the previous section were considered. Time constraints did not allow detailed characterisation of the used catalysts since the preliminary experiments in this study were time consuming but experimental observations were noted. The aim of the dehydrogenation experiments in this section was to initiate an experimental investigation to achieve selective rather than total oxidation of the reactant gas.

The experimental arrangement was modified slightly from that used in the previous section since the initial physical state of the reactant was liquid rather than gas. Therefore, a bubbler unit was substituted for the reactant gas source and mixing vessel. This experimental arrangement is detailed in Chapter 7, section 7.7.2.

5.2.2 Gas Chromatography

Two different approaches were utilised for the measurement of cyclohexane conversion for the calcined $\text{Mg}_5\text{FeAl}_2\text{HTc}$ catalyst. The first method utilised the in-line GC, as previously used for the SO_2 oxidation experiments. However, due to problems with peak resolution using this particular GC, a low temperature vapour trap arrangement was used to condense the exit gases from the microreactor for consequent injection and analysis with a GC offering improved peak resolution. The results did not correlate exactly between the two analysis methods but both did indicate that the desired dehydrogenation reaction had occurred to some extent (this will be clarified below) when the reactor temperature reached 723 K. Essentially, there was no conversion recorded at 323 K or 523 K, the temperatures at which samples were taken as the reactor temperature was increased from room temperature to 723 K but, immediately upon reaching this temperature, some conversion was recorded. However, the level of conversion was not clear and the measurable quantity dependant upon the GC method used for analysis. The in-line GC recorded a *ca.* 30 % decrease in cyclohexane peak area and subsequent 30 % increase in the area of a peak with a retention time expected

for benzene. However, the GC trace recorded for the condensed sample in the capillary column GC indicated that up to *ca.* 75 % conversion had occurred. There was, however, at least one shoulder visible on the cyclohexane peak which was not fully resolvable which may have been due to the presence of other partial dehydrogenation products. The characteristic smell of cyclohexene was clearly identifiable in the reaction product and would have been expected. In addition, an asymmetric peak was also clearly observable at comparatively low retention time in the GC traces recorded using the in-line GC which suggested that some volatile gaseous material which was not condensed with the low-temperature trap was entering the GC column. Further experiments suggested that this was not CO₂ or water vapour but did not also appear to correlate with being H₂ gas due to its increased retention time relative to air on this column. The level of conversion achieved at 723 K was maintained with little change until the experiment was completed (*ca.* 24 hours).

Upon removal of the microreactor tube from the furnace following each experiment, bands of green material were frequently observed. This was indicative of the Fe in the catalyst being reduced during the reaction as the cyclohexane was oxidised. Some blackening of the catalyst was also noted following the longer experiments which suggested that there may have been some carbon deposition, or coking. Generally though, pressure drop occurred less frequently than was observed during the SO₂ oxidation experiments which suggested that there was a reduced occurrence of particle failure with this catalyst.

5.2.3 Conclusions

The possible conversions achieved appeared to be relatively high once the reactor temperature reached *ca.* 723 K which was in-keeping with the endothermic nature of the dehydrogenation reaction investigated and was coincident with the formation of the mixed metal oxide. It was not clear as to whether the reaction mechanism proceeded *via* oxidative dehydrogenation *i.e.* the formation of water rather than hydrogen, since the GC apparatus used was not suitable for the identification of such reaction products. The initial findings of these experiments indicated that the Fe-substituted HTc's hold great

potential for use as cyclohexane dehydrogenation catalysts and a more detailed study would be highly desirable but was not possible given the time constraints here. This should include experiments to investigate the activity, selectivity and lifetime attainable for the full range of Fe-for-Mg substituted HTc's and the subsequent characterisation of these materials post-reaction.

5.3 References

- 1 G.C. Bond, *Heterogeneous Catalysis – Principles and Applications* (2nd Edition), Oxford University Press, Oxford, 1990.
- 2 J.P. Dunn, H.G. Stenger Jr. and I.E. Wachs, *J. Catal.*, 1999, **181**, 233.
- 3 K. Nakamoto, *Infrared and Raman Spectra of Inorganic and Coordination Compounds* (4th Edition), John Wiley & Sons, Chichester, 1986.
- 4 P.A. Estep-Barnes, in *Physical Methods in Determinative Mineralogy* (2nd Edition), J. Zussman (Ed.), Academic Press, London, 1977.
- 5 JCPDS Card N°. 14-0191
- 6 JCPDS Card N°. 01-0566
- 7 JCPDS Card N°. 14-0253
- 8 F. Aghbalou, A. Touzani, M. Mada, M. Charia and A. Bernatchou, *Renewable Energy*, 1998, **14**, 61.
- 9 BA. Raich and H.C. Foley, *Applied Catalysis A-General*, 1995, **129**, 167.
- 10 S.B. Cheng, F.Y. Li, L.T. Luo and Z.P. Zhen, *Reaction Kinetics and Catalysis Letters*, 1995, **55**, 391.

Chapter 6

Summary of Conclusions and Further Work

6.1 Precursor Materials

The preparation of materials based on the hydrotalcite structure, with idealised formulae of $\text{Mg}_5\text{FeAl}_2\text{HTc}$, $\text{Mg}_4\text{Fe}_2\text{Al}_2\text{HTc}$, $\text{Mg}_3\text{Fe}_3\text{Al}_2\text{HTc}$, $\text{Mg}_2\text{Fe}_4\text{Al}_2\text{HTc}$, $\text{MgFe}_5\text{Al}_2\text{HTc}$ and $\text{Fe}_6\text{Al}_2\text{HTc}$ was successful in the formation of predominantly single-phase materials for the majority of those aforementioned. Only the products with idealised formulae of $\text{MgFe}_5\text{Al}_2\text{HTc}$ and $\text{Fe}_6\text{Al}_2\text{HTc}$ exhibited substantial deviations from the hydrotalcite structure, tending to form additional iron-based phases such as siderite (FeCO_3) and substituted iron oxides such as aluminium substituted goethite. Therefore, the template structure appeared to be that of the iron-containing materials rather than that of hydrotalcite as the Fe-for-Mg substitution increased.

Because of the novel nature of this study, with respect to the characterisation of a previously unreported range of Fe-for-Mg substituted HTc's, much of the characterisation data provided an advancement upon current knowledge in the area. However, there were a number of observations which were of particular interest. For example, the data presented in the IR study provided a detailed description of the type of pattern expected for the HTc's and illustrated how the formation of additional phases may cause subtle changes in the spectra, particularly in the carbonate region. The main observations noted from the study of the XRPD patterns of the Fe-substituted HTc's related to the shifts in the [003] spacing and the [110] spacing. The former illustrated the change in basal spacing and the latter the change in unit cell parameter a , as Fe-substitution was increased through the range. The SEM analysis presented was considerably more detailed than that generally observed in the literature and this study highlighted the gradual change in morphology of the samples with Fe-substitution. The DTA study was particularly notable since the use of this method of analysis is not as

frequently recorded in the literature as the aforementioned techniques but was used here as a method of assessing the temperature at which the precursors were expected to have formed mixed metal oxides. This study also provided additional information relating to the transitions within the samples during calcination and a comparison of the traces for each of the HTc's studied, building upon earlier studies – the core of which were reported in the older literature and related to $\text{Mg}_6\text{Al}_2\text{HTc}$'s in particular.^{1,2}

It is suggested that further work in this area should focus upon attempting to characterise the materials containing Fe in the unoxidised divalent state to compare some of the observations noted in this study *e.g.* the effects of charge on the metal hydroxide layers and subsequent variation in basal spacing. In addition, it would also have been interesting to compare the results of thermo-gravimetric analysis with the differential thermal analysis results recorded for the Fe-substituted HTc's since such a detailed study had not previously been reported in the literature for these materials.

The results of the green rust and iron oxide preparative studies illustrated that the continuation of novel research in this area is still possible despite the large amounts of research detailed in the literature. Perhaps the most interesting results originated from the studies of the synthesis of the green rusts and iron oxides in organic solvents since little work had previously been carried out in this area and much of the characterisation data was unlike that recorded in the literature for similar products. The substitution of aluminium into the feroxyhyte structure appeared to have been unsuccessful upon inspection of the characterisation data in the respect that the feroxyhyte structure was not produced. However, a product quite unlike any reported in the literature for a similar material was produced. Although these materials did not offer significant potential as catalysts for the reactions selected for activity testing, they were academically interesting and worthy of further investigation.

6.2 Catalyst Activation

The calcination studies carried out on the HTc's verified the observations of previously reported studies, many of which have been carried out on MgAlHTc 's, in that the

formation of metal oxides is possible from HTc precursors at relatively low temperatures. The characterisation of Fe-for-Mg substituted HTc's reported in Chapter 3 of this thesis built upon studies reported in the literature concerning similarly cation substituted HTc's^{3, 4, 5} (though not substituted across the range examined in this study) and some research which examined the calcination of the pyroaurite/sjögrenite ($\text{Mg}_6\text{Fe}_2\text{HTc}$) system.^{6, 7} The latter studies described the formation of spinel phases at considerably lower temperatures than for the unsubstituted MgAlHTc 's and, therefore, this was also investigated here. Spinel-type phases did dominate the XRPD patterns of the high Fe-for-Mg substituted HTc's, rather than the MgO pattern expected. The MgO pattern was, however, observed for the low Fe-substituted HTc's and was indicative of the formation of a mixed metal oxide; a solid solution of ions assumed to exist within the MgO structure. The SEM results illustrated that the HTc morphology was maintained for the low Fe-substituted HTc's in particular but that the higher Fe-substituted materials lost this structure to some degree, tending to form very small crystallites which were agglomerated instead. Therefore, only the lower Fe-substituted HTc's satisfied the initial objectives of the study regarding the desire to form mixed metal oxides with retention of the hydrotalcite-type morphology at low calcination temperature.

The study carried out into the activation of the HTc precursors to produce catalysts for the cyanoethylation reactions provided a significant advancement upon previous studies reporting the characterisation of similarly activated HTc's.^{8, 9, 10} The quantity of data in the literature relating to rehydrated HTc's is currently considerably less than that provided for the calcined HTc's which have been the subject of a greater number of catalysis-related studies. The data reported in section 3.2 of Chapter 3 illustrated that the hydrotalcite-type structure was reconstructed for most of the Fe-substituted HTc's prepared. IR spectroscopy illustrated that the carbonate ions had been replaced, probably by hydroxide ions, in the interlayer region which was expected to influence the catalytic activity of these materials. The XRPD patterns recorded were very similar in appearance to those of the precursors, with the exception of the high Fe-for-Mg substituted HTc's which indicated the persistence of the spinel-type phase following calcination and subsequent rehydration. The SEM micrographs suggested that high surface area/porosity materials were formed following the activation of the precursors

which inferred their suitability as catalysts for the cyanoethylation reactions studied in Chapter 4.

Further work concerning the study of Fe-for-Mg substituted HTc's, focussed upon more detailed characterisation of the calcination and calcination/rehydration products, would be highly desirable since this study highlighted gaps in the knowledge relating to this area which are still to be filled and could yet be the subject of more detailed research. For example, thorough characterisation of the products over a wider activation temperature range may offer additional information regarding the nature of the transitions within the HTc's upon calcination and a comparison in the temperatures at which they occur. To record *in-situ* high-temperature XRPD patterns of the Fe-substituted HTc's would enhance this understanding since it would bring the level of knowledge concerning phase transition temperatures nearer to that of the MgAlHTc's which have been the subject of such investigations previously in the literature. An XRPD study of this type may also offer more information relating to the peak at *ca.* 6.0-6.5 Å which was observed in the XRPD patterns of the calcined HTc's. A peak in this area had been previously reported in the literature but explanations relating to its origin appear to be unsatisfactory thus far. It is proposed here that this peak may be indicative of the separation of layers in a mixed metal MOOH-type structure [possibly similar to that of boehmite (γ -AlOOH)/ lepidocrocite (γ -FeOOH)]. The carbonate ions may then occupy specific sites in the interlayer in the absence of the interlayer water molecules but it is not clear at this stage. Since quantification of the change in surface area/porosity could not be made, this would also be desirable for the HTc's prepared here, given the influence of these physical properties on the catalytic activity of these materials.

6.3 Base Catalysis

The cyanoethylation reactions, for which the activity of the catalysts was measured, were used as an indicator of the basicity of the materials tested. It was shown that the activity of the calcined and rehydrated HTc's decreased proportionately with increased Fe-for-Mg substitution which inferred that the Mg sites strongly influenced the basicity

of the catalysts. The activity results illustrated that the basicity of the catalysts could be 'tuned' with cation substitution and that the design of a catalyst with optimum characteristics for base-catalysed reactions is possible. The work carried out in this research utilised a standard procedure for the measurement of catalyst activity in order to allow the direct comparison of activity between catalysts tested and provided significantly more detail regarding product formation over time than has previously been recorded in the literature.⁸ A mechanism for the cyanoethylation reactions which is dependent upon initial proton abstraction from the alcohol at a Brønsted basic site was also suggested. The rate of such a reaction would be dependent to some degree upon the acidity of the alcohol concerned, as appeared to be the case in the reactions tested. The relatively low temperature employed for the activation of the catalysts used was in keeping with the initial objective of the study which may facilitate the use of such catalysts on a larger scale.

Regarding further work, characterisation of the catalysts post-reaction would have been desirable and IR, XRPD and SEM data should be recorded where possible for the Fe-substituted HTc's in particular. More information regarding the re-usability of the aforementioned base catalysts for the cyanoethylation reactions would also be desirable in order to verify observations made for MgAlHTc's in the literature which reported that there was a minimal decrease in activity over 3 reaction cycles.⁸ Previous work has also reported a surprisingly high level of stability of the activated catalysts upon exposure to air and this should also be investigated for the Fe-substituted HTc's. In general, further work relating to the Fe-substituted catalysts should seek to characterise the acid/base sites of these materials and to investigate their activity for reactions which may be facilitated by the presence of Fe. The substitution of a range of other cations and their influence on basicity of the activated catalysts could also be the subject of further studies.

6.4 Oxidation Catalysis

The calcined Fe-substituted HTc's prepared did not appear to be suitable for use as SO₂ oxidation catalysts because, although the IR and XRPD studies revealed that the SO₂

was oxidised, it was absorbed and oxidised to form metal sulfate phases, rather than releasing the desired oxidation product, SO_3 . Therefore, it is assumed that the interactions between the SO_2 and the catalyst surface were too strong to allow oxidation to SO_3 and resulting desorption of this intermediate reaction product. The Fe^{3+} within the Fe-substituted catalysts is expected to have provided the main absorption sites and the main oxidation site since it may itself be relatively easily reduced to Fe^{2+} . The reduced Fe species was not, however, detected in the post reaction analysis which was probably a consequence of the catalyst 'clean-up' procedure *i.e.* purging the microreactor with air to desorb adsorbed material. The SO_2 sorption data illustrated that the SO_2 uptake was greatest upon initial interaction with the catalyst bed, was increased/decreased with a corresponding increase/decrease in reaction temperature and appeared to be greatest for the mid-range Fe-substituted catalysts. This last observation is the least definite and warrants further verification with more reliable analysis equipment. It could, however, be explained as being a result of the increased Fe ratio within the HTc whilst still maintaining the HTc morphology which may, in turn, have provided a higher surface area/porosity than the higher Fe ratio catalysts.

Further work in this area could investigate the use of the Fe-substituted HTc's as SO_2 sorbents and carry out the associated uptake and characterisation studies. The formulation of the sorbent may be further optimised but may not offer a commercially viable solution given that the metal sulfate is formed which may not be an easily reversible reaction given the practical constraints for the use of such materials. However, if a low concentration of SO_2 was expected in a gas stream, this may not pose such a problem since irreversibility may be regarded as more favourable.

Although only preliminary investigations could be made into the studying the activity of calcined Fe-substituted HTc's for the catalytic dehydrogenation of cyclohexane, the initial results were promising in terms of the levels of conversion recorded. Further research is required to verify the level of activity exhibited by the calcined $\text{Mg}_5\text{FeAl}_2\text{HTc}$ studied since the figures varied between *ca.* 30-75 %, depending upon the equipment and method used for analysis of the reactant/product mixture. However, despite the range in conversion observed, this level of activity does infer that a further study is warranted, particularly because the activity also appeared to be maintained for the duration of the studies (*ca.* 24 hours), at a reaction temperature of 723 K. This work

can, therefore, be regarded as a justifiable starting point for further studies into the investigation of the full range of calcined Fe-substituted HTc's for this reaction. The activity, selectivity and lifetime of these materials should be studied, together with detailed post-reaction catalyst characterisation to compare with the pre-reaction characterisation studies detailed in Chapter 3, section 3.1.

6.5 References

- 1 C.W. Beck, *Am. Mineral.*, 1950, **35**, 985.
- 2 W. Smykatz-Kloss, *Differential Thermal Analysis – Application and Results in Mineralogy*, Springer-Verlag, New York, 1974.
- 3 R.M. Taylor and R.M. McKenzie, *Clays and Clay Minerals*, 1980, **28**(3), 179.
- 4 R.M. Taylor, *Clay Minerals*, 1982, **17**, 369.
- 5 S.M. Auer, J-D. Grunwaldt, R.A. Köppel and A. Baiker, *J. Mol. Cat. A: Chemical*, 1999, **139**, 305.
- 6 M. Tu, J. Shen and Y. Chen, *J. Solid State Chem.*, 1997, **128**, 73.
- 7 T. Hibino and A. Tsunashima, *J. Mater. Sci. Letters*, 2000, **19**, 1403.
- 8 P.S. Kumbhar, J. Sanchez-Valente and F. Figueras, *Chem. Commun.*, 1998, 1091.
- 9 K.K. Rao, M. Gravelle, J. Sanchez-Valente and F. Figueras, *J. Catal.*, 1998, **173**, 115.
- 10 J.C.A.A. Roelofs, A.J. van Dillen, M. Versluijs-Helder, J.T.B.T. Jastrzebski and K.P. de Jong, *Europa-Cat IV, 4th European Congress on Catalysis*, Rimini, 1999.

Chapter 7

Experimental

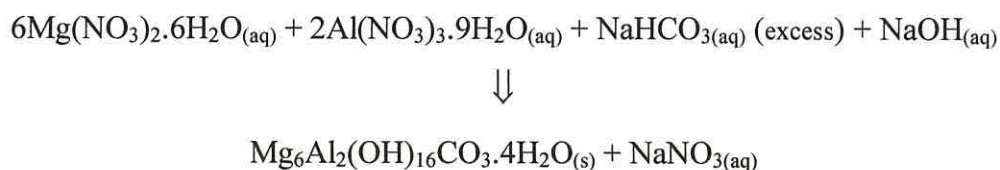
7.1 Preparation of Hydrotalcite-type Compounds

7.1.1 Preparation of Hydrotalcite, $\text{Mg}_6\text{Al}_2(\text{OH})_{16}\text{CO}_3 \cdot 4\text{H}_2\text{O}$

The primary synthesis method used for the production of hydrotalcite, $\text{Mg}_6\text{Al}_2(\text{OH})_{16}\text{CO}_3 \cdot 4\text{H}_2\text{O}$, was adapted from that of Baird and co-workers¹ in the formation of Co-Zn-Al HTc's. The preparation was carried out without the use of air-sensitive techniques since the Mg^{II} and Al^{III} ions were not at risk of oxidation and carbonate was the anion to be incorporated into the interlayer region. The overall reaction is summarised in Reaction Scheme 7.1.

In a typical preparation, a solution of metal salts containing $\text{Mg}(\text{NO}_3)_2 \cdot 6\text{H}_2\text{O}$ (33.21 g, 149.01 mmol) and $\text{Al}(\text{NO}_3)_3 \cdot 9\text{H}_2\text{O}$ (18.63 g, 49.67 mmol) was prepared in degassed, deionised water (200 ml) to form an approximately 1 M solution. A solution of NaOH (10.00 g, 250 mmol) and NaHCO_3 (42.00 g, 500 mmol) in degassed, deionised water (250 ml) was also prepared to form an approximately 2 M solution with respect to NaHCO_3 . The NaHCO_3 was present in a 10 % excess with respect to neutralisation of metal salt counterions (nitrate ions) whilst the NaOH was present in order to increase the pH to the required value. Each of the solutions were then heated to 353 K and combined, using a pair of peristaltic pumps, in a third vessel containing degassed, deionised water (200 ml) at 353 K, as depicted in Figure 7.1. The rate of flow of the solutions through the pumps was varied independently in order to maintain a pH of *ca.* 9 for the combined solution in the central vessel but was generally *ca.* 15 ml min⁻¹ through each pump.

Reaction Scheme 7.1 Preparation of hydrotalcite¹



The precipitate was aged for 1 hour, with stirring, at 353 K, filtered using quantitative filter papers and washed with deionised water (*ca.* 2 litres) to eliminate the alkali metals and nitrate ions. The precipitate was then dried for 18 hours at 333 K.

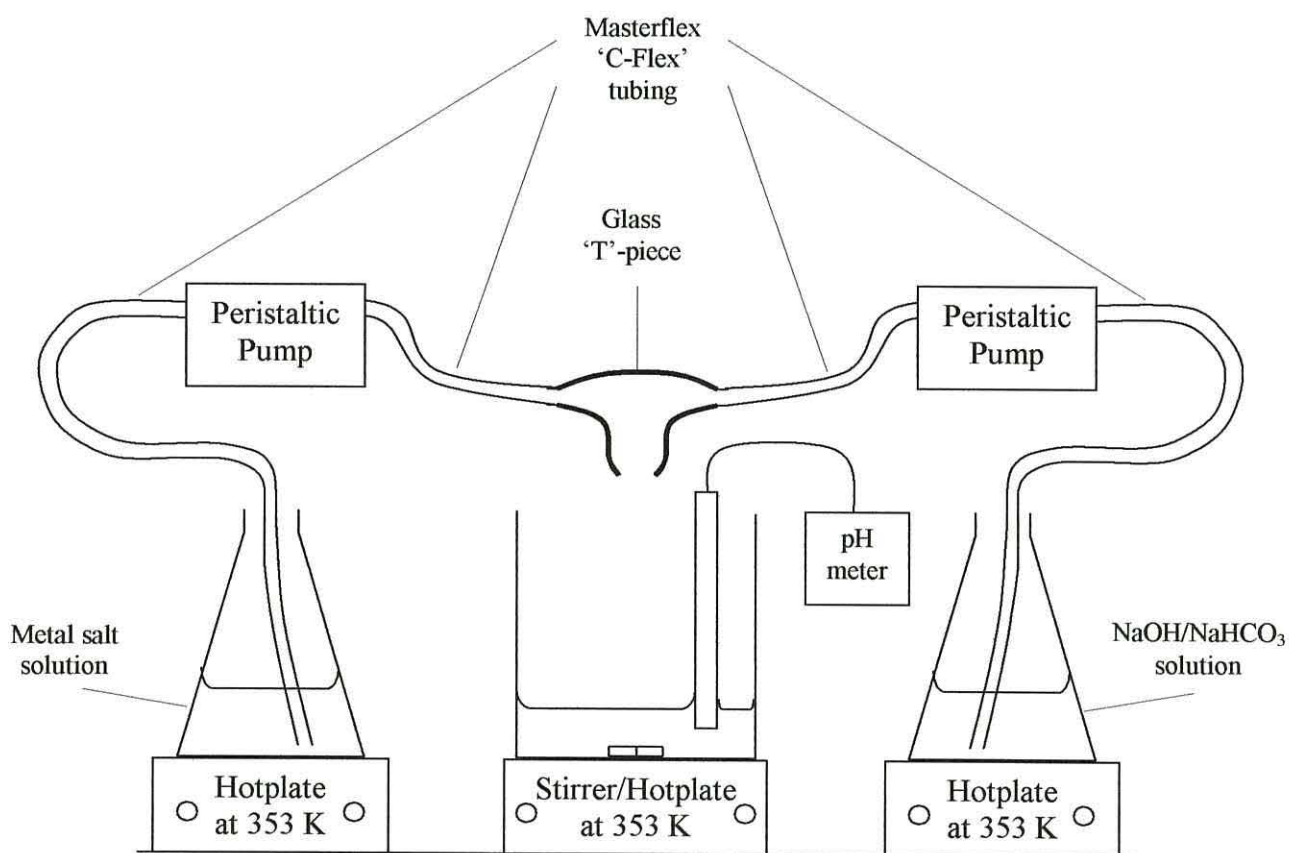
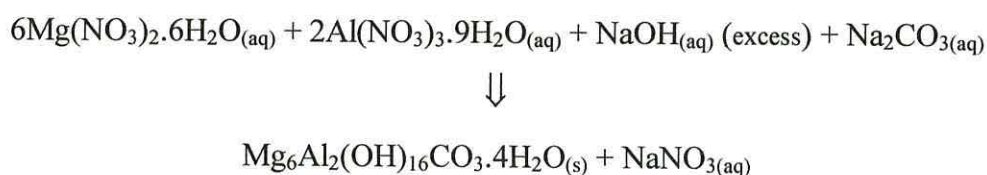


Figure 7.1 A typical coprecipitation arrangement

In addition, a second method was used for the preparation of hydrotalcite, which was adapted from that of Rao and co-workers.² Here, NaOH was used as the main constituent of the alkaline solution, rather than NaHCO₃ as in the previous synthesis method. The overall reaction is summarized in Reaction Scheme 7.2.

An aqueous solution of $\text{Mg}(\text{NO}_3)_2 \cdot 6\text{H}_2\text{O}$ (38.21 g, 149.01 mmol) and $\text{Al}(\text{NO}_3)_3 \cdot 9\text{H}_2\text{O}$ (18.63 g, 49.67 mmol) was prepared in degassed, deionised water (149 ml) *i.e.* 1 M with respect to magnesium nitrate and a $\text{Mg}^{2+}:\text{Al}^{3+}$ ratio of 1:3. A second solution of NaOH (12.00g, 300.00 mmol) and Na_2CO_3 (8.16 g, 77.00 mmol) was prepared in an equal volume of degassed, deionised water (149 ml) *i.e. ca.* 2 M with respect to NaOH. These two solutions were combined using the arrangement used previously, as shown in Figure 7.1, at a similar rate of combination *i.e.* flow rate of *ca.* 15 ml min^{-1} through each pump. The pH was regulated, by varying the flow rate through each pump independently, to maintain a pH of *ca.* 9-10 in the central vessel.

Reaction Scheme 7.2 Preparation of hydrotalcite²



The precipitate was aged for 1 hour, with stirring, at 353 K, filtered using quantitative filter papers and washed with deionised water (*ca.* 2 litres) to eliminate the alkali metals and nitrate ions. The precipitate was then dried for 18 hours at 333 K.

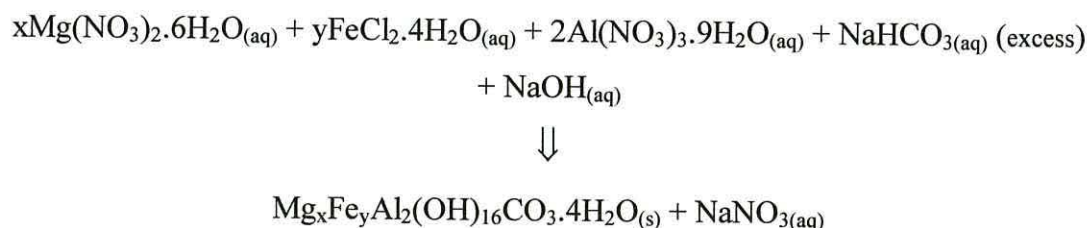
7.1.2 Air-sensitive Preparation of Iron-containing Hydrotalcite-type Compounds

A series of products were produced, having the idealised formulae of $\text{Mg}_5\text{FeAl}_2\text{HTc}$, $\text{Mg}_4\text{Fe}_2\text{Al}_2\text{HTc}$, $\text{Mg}_3\text{Fe}_3\text{Al}_2\text{HTc}$, $\text{Mg}_2\text{Fe}_4\text{Al}_2\text{HTc}$, $\text{MgFe}_5\text{Al}_2\text{HTc}$ and $\text{Fe}_6\text{Al}_2\text{HTc}$ [where $\text{HTc} = (\text{OH})_{16}\text{CO}_3 \cdot 4\text{H}_2\text{O}$]. The method described was followed for the preparation of each, varying the proportions of metal salts and NaOH/NaHCO₃ in the solutions in order to produce the required stoichiometries of metal ions in the product and neutralise metal salt counterions/increase pH, respectively. The overall reaction is summarised in Reaction Scheme 7.3.

Special care was taken during the preparations to prevent unwanted oxidation of the Fe^{II} in the reactant solution or the product due to contact with oxygen in the external atmosphere. Therefore, the metal salt solution was kept under an atmosphere of nitrogen, prior to combination with the alkali solution, and the coprecipitations were carried out in a nitrogen atmosphere. In order to facilitate the latter, a three-necked round-bottomed flask was used as the central mixing vessel. Schlenk-line techniques were used to control the atmosphere in this flask and during the subsequent filtration procedure.

In a typical preparation, a solution of metal salts containing Mg(NO₃)₂·6H₂O, Al(NO₃)₃·9H₂O and FeCl₂·4H₂O was prepared in degassed, deionised water (90 ml) to form an approximately 1 M solution. A solution of NaHCO₃ in degassed, deionised water (*ca.* 100 ml) was also prepared to form an approximately 2 M solution. The exact quantity of NaHCO₃ was adjusted for each preparation, but was always calculated to be present in sufficient quantity to neutralise the metal salt counterions (nitrate and chloride), plus a 10 % excess. Each of the solutions was then heated to 353 K, under a nitrogen atmosphere, at which point they were slowly combined using peristaltic pumps in a nitrogen filled three-necked round-bottomed flask containing degassed, deionised water (100 ml). The rate of flow of the solutions through the pumps was varied independently in order to maintain a pH of *ca.* 9 for the combined solution in the central vessel but was generally *ca.* 15 ml min⁻¹ through each pump. During the combination of the two solutions, a solution of 2 M NaOH was also added to the central mixing vessel, using a dropping funnel, in sufficient quantity to maintain the pH at the desired value.

Reaction Scheme 7.3 Preparation of iron-containing hydrotalcite-type compounds



where x:y = 5:1, 4:2, 3:3, 2:4, 1:5 and 0:6

The precipitate formed was then aged for one hour, with stirring, at 353 K and then filtered through a fine porosity glass frit under vacuum/nitrogen using the purpose-built apparatus illustrated in Figure 7.2. This filtration unit had been evacuated and refilled with nitrogen four times previously, using standard Schlenk-line techniques. The precipitates were then washed in the filtration apparatus under nitrogen/vacuum using degassed, deionised water (*ca.* 2 litres) to eliminate the alkali metals and original metal salt solution counterions (chloride and nitrate ions). Since the filtration unit was capable of accommodating *ca.* 600 ml of filtrate, the washings were drained *via* the large bore (8 mm internal diameter) tap. This procedure was carried out under a positive pressure of nitrogen, provided by the other two smaller bore (4 mm internal diameter) taps.

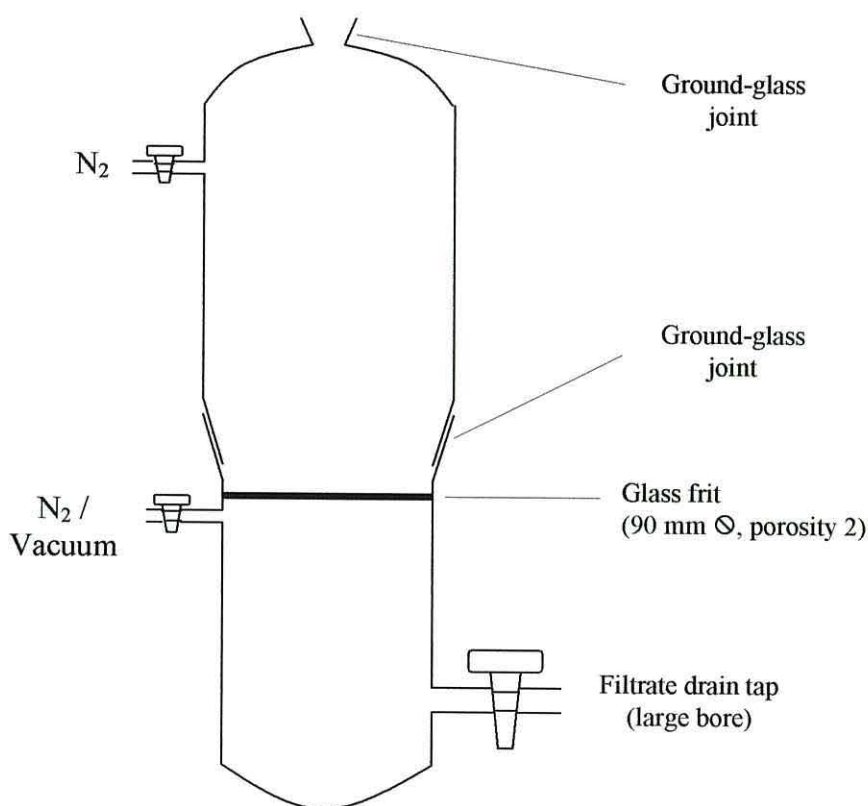


Figure 7.2 Filter apparatus for air-sensitive filtrations

The precipitates were then dried in a vacuum oven for 48 hours at 333 K.

7.2 Calcination of Hydrotalcite-type Compounds

In the initial calcination studies, *ca.* 0.5 g of the dried HTc was accurately weighed and then heated in a nickel crucible, using a muffle oven, in an air atmosphere. A sample of each compound was calcined at 393 K for 4 hours, 523 K for 4 hours and 723 K for 4 hours. The heating rate was approximately 10 K min^{-1} between holding temperatures. After calcination at each of these temperatures, the samples were allowed to cool to room temperature, accurately weighed and characterised as appropriate.

Further calcination studies, and the preparation of materials for catalytic study, were carried out using tube furnaces for which the heating zone, ramp-rate, dwell temperature and atmosphere could be controlled more accurately. Pyrex glass calcination tubes were made specifically for the calcination studies. Their dimensions were such that they fitted the tubes of the furnace with a minimum of surrounding dead-space and kept the material being calcined within the limits of the heating zone. The arrangement used is shown in Figure 7.3.

High-purity nitrogen or air was supplied from cylinders (A) equipped with two-stage regulators (B) and an additional in-line pressure regulator (C) in order to maintain a constant inlet pressure. Gas flow was monitored using an in-line flow-meter (D). The design of the calcination tube allowed the gas to pre-heat prior to contact with the material under study. Turbulent gas flow was ensured with the use of a glass sinter (E), which resulted in maximum interaction between gas and the solid material being calcined (F). The calcination tube was of sufficient diameter (35 mm) to fill the tube of the furnace as closely as possible in order to minimise heat losses. The main furnace used in the calcination/activation studies was manufactured by Carbolite, type 12/2 with a Eurotherm proportional-integral-derivative (PID) controller unit. Furnace temperatures were verified along the furnace heating zone using an independent digital thermometer equipped with a K-type thermocouple. For the initial characterisation studies of the calcined HTc's, a gas hourly space velocity of 700 hr^{-1} was used, in accordance with that used by Baird and co-workers¹ in the formation of mixed metal oxides from HTc's. Gas hourly space velocities were calculated using Formula 7.1.

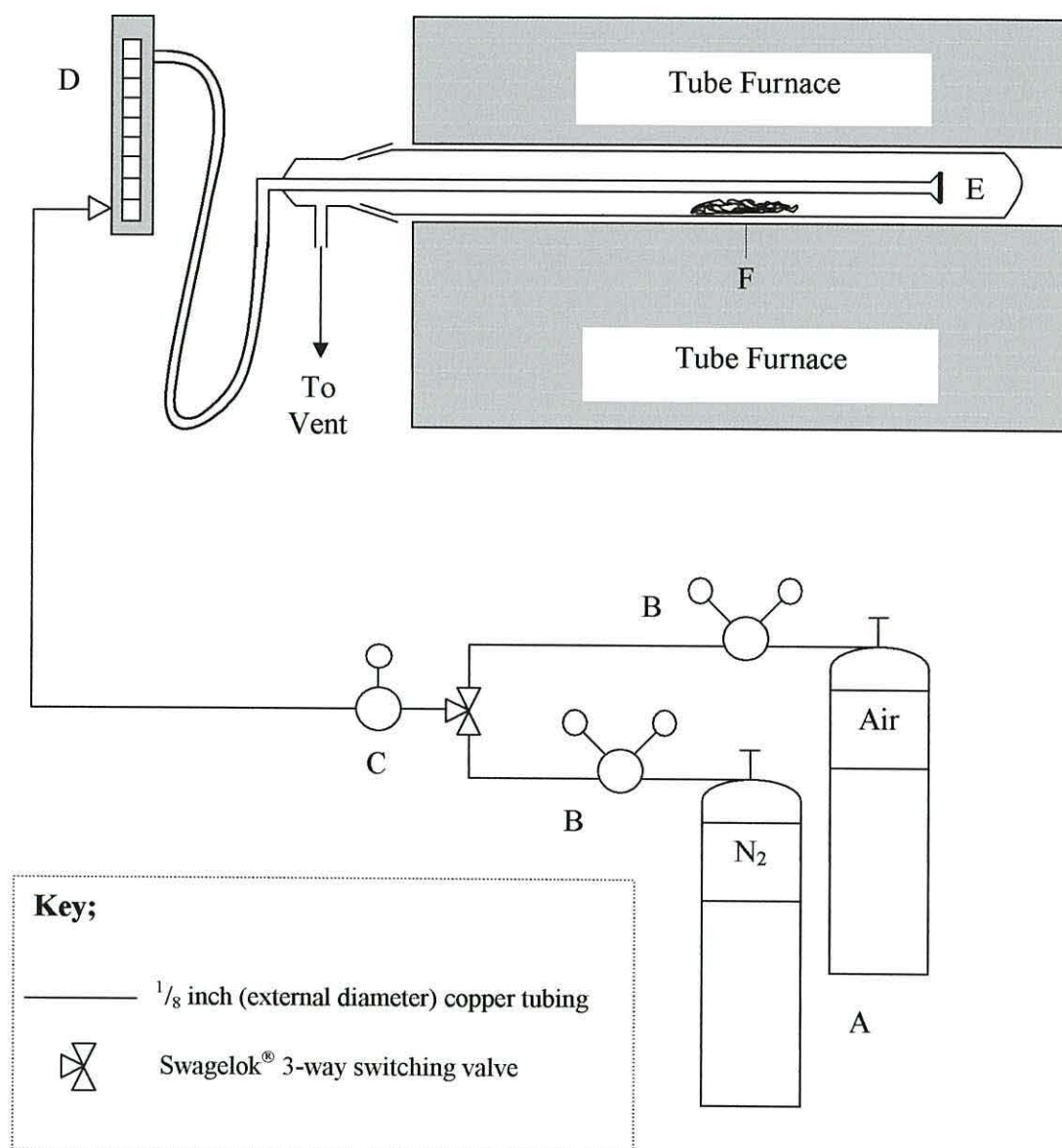


Figure 7.3 Tube furnace calcination arrangement

Formula 7.1 Calculation of gas hourly space velocity (GHSV)

$$\text{GHSV (hr}^{-1}\text{)} = \text{Gas flow rate (ml hr}^{-1}\text{)} / \text{Volume of catalyst (ml)}$$

7.3 Preparation of Green Rusts

The method of green rust formation used was adapted from a method reported by Schwertmann³ for the preparation of feroxyhyte (δ -FeOOH), where green rust was formed as an intermediate. Here, however, the method was adapted to trap the green rust as the desired product. The procedure outlined below was followed using either water (degassed/deionised) or methanol (degassed/dried over MgSO_4 or degassed/not dried) as reaction solvents. However, there was a difference in solubility of $\text{FeCl}_2 \cdot 4\text{H}_2\text{O}$ in each of the solvents; when methanol was used, the solution formed was assumed to be approaching saturation.

The preparations were carried out under a nitrogen atmosphere in a three-necked round-bottomed flask equipped with a dropping funnel and a pH electrode. An Fe^{II} solution (either 0.30 M in water or 0.06 M in methanol) was prepared in the flask from unoxidised crystals of $\text{FeCl}_2 \cdot 4\text{H}_2\text{O}$ *i.e.* crystals that had a yellow/green colouration rather than the brown iron (III) chloride oxidation product. An aqueous solution of NaOH (5 M) was then added drop wise *via* the dropping funnel to raise the pH from *ca.* 2 to 8 and a blue/green precipitate was formed. The suspension was carefully transferred, under nitrogen, to a purpose-built filtration apparatus (Figure 7.2) which had previously been evacuated and refilled with a nitrogen atmosphere. The precipitate was then filtered under vacuum/nitrogen, washed using degassed, deionised water (*ca.* 2 litres) and then dried in a vacuum oven for 48 hours at 323 K.

The method described above for the preparation of the green rust intermediate was then repeated on a similar scale. This time, however, carbonate ions were added to the reaction mixture in order to produce a reaction product more similar in chemical make-up to the HTc's. The reaction procedure was, essentially, a repeat of earlier experimental work by the author.⁴ To introduce carbonate ions, NaHCO_3 (0.50 g, 5.95 mmol) was dissolved in the aqueous solution of NaOH (28.75 ml, 2 M) used to increase the pH.

The method described above for the preparation of green rust with interlayer carbonate ions was then repeated on a similar scale. This time, however, aluminium ions were also added to the reaction mixture in an attempt to substitute Al^{3+} for Fe^{3+} ions in the green rust product. Again, a similar method to that used in earlier work by the author was followed.⁴ $\text{Al}(\text{NO}_3)_3 \cdot 9\text{H}_2\text{O}$ (2.11 g, 5.62 mmol) was dissolved in the degassed/deionised water (56.25 ml) with the $\text{FeCl}_2 \cdot 4\text{H}_2\text{O}$ (3.36 g, 16.88 mmol) to produce the metal ion solution and the reaction procedure outlined above repeated.

7.4 Preparation of Iron Oxides

A preparative method for ferrihydrite ($\delta\text{-FeOOH}$), using water as the reaction solvent, has been reported by Schwertmann.³ The procedure outlined here was developed from this method. However, methanol (degassed/dried over MgSO_4) was also used as a reaction solvent to produce a range of products as well as water (degassed/deionised) - as in Schwertmann's method. In addition, oxidation using H_2O_2 was not carried out on the material formed using methanol as the reaction solvent - air oxidation was found to be sufficient in this case.

In a typical preparation, an Fe^{II} solution (either 0.30 M in water or 0.07 M in methanol) was prepared from unoxidised crystals of $\text{FeCl}_2 \cdot 4\text{H}_2\text{O}$. A 1 litre glass beaker (large enough to contain excess effervescence later in the preparation) was placed on a magnetic stirrer and a pH electrode installed. The pH of the solution was then raised from the initial value of *ca.* 3 to 8 by addition of NaOH (5 M), dropwise, using a burette, with constant stirring. A green/blue precipitate was formed. Rapid addition of 30 % H_2O_2 (80 ml) immediately resulted in a reddish-brown precipitate which was accompanied by a drop in pH to *ca.* 2 due to proton release. The pH was once again raised to *ca.* 8 to improve flocculation by the addition of NaOH solution (*ca.* 2 ml, 5 M).

The product formed was filtered using a Büchner funnel and flask in conjunction with quantitative filter paper. The residue was washed with degassed, deionised water and a small amount of acetone. This was then dried in an oven at 333 K for 48 hours.

The above reaction was then repeated using a starting solution which also included aluminium ions in order to attempt to replace Fe^{3+} ions in the feroxyhyte structure with Al^{3+} ions. To do this, in a repeat of previous work by the author,⁴ the starting solution comprised $\text{Al}(\text{NO}_3)_3 \cdot 9\text{H}_2\text{O}$ (1.27 g, 3.38 mmol) and $\text{FeCl}_2 \cdot 4\text{H}_2\text{O}$ (6.04 g, 30.38 mmol) dissolved in degassed/deionised water (112.5 ml).

7.5 Cyanoethylation of Alcohols

7.5.1 Activation of Hydrotalcite-type Compounds

The hydrotalcite-type compounds were activated for use as base catalysts, in the cyanoethylation of alcohols, using a method developed from that reported by Kumbhar and co-workers.⁵ The HTc to be activated was evenly distributed, in powdered form, across the lower surface of a Pyrex glass calcination tube and the tube inserted into the tube furnace. The calcination apparatus arrangement was as previously described (section 7.2) and illustrated (Figure 7.3). The HTc was then heated at a rate of 10 K min^{-1} from room temperature to 723 K, under an atmosphere of high purity nitrogen. The furnace temperature of 723 K was maintained for 8 hours with the nitrogen atmosphere. The calcination tube was then removed from the furnace, without compromising the nitrogen atmosphere within and allowed to cool to room temperature. Once cool, the HTc was exposed to an atmosphere of wet high purity nitrogen which had been produced by bubbling the gas through water at room temperature for *ca.* 12 hours. A GHSV of $46,000 \text{ hr}^{-1}$ was used at all stages of activation. However, it should be noted that Kumbhar and co-workers⁵ reported activation of '*0.1 g catalyst, water saturated N_2 flow = 80 ml min^{-1}* '. In order to utilise a comparable volume of gas per volume of HTc during the activation process used here, this flow rate was converted to a value of GHSV (using Formula 7.1 supplied previously). To do this, a density value for $\text{Mg}_6\text{Al}_2\text{HTc}$ of *ca.* 0.96 g ml^{-1} was used.

7.5.2 Cyanoethylation Experiments

The reactions were carried out in a 50 ml round-bottomed flask, under an argon atmosphere using a procedure modified from that of Kumbhar and co-workers⁵ and Kabashima and Hattori.⁶ The method described by the latter appeared over-complicated whereas the exact details of the method used by Kumbhar and co-workers were not detailed. In addition, neither method followed the course of the reactions investigated but, rather, reported the conversion after a set period of time, generally 120 minutes. In the method reported in this thesis, the activated HTc catalyst (0.1 g) was initially placed in the flask and methanol (10 ml, 247 mmol) added, using a syringe and needle, through a septum. Acrylonitrile (2.6 ml, 40 mmol) was added, through the septum, using a syringe and needle and the reaction mixture refluxed at 333 K with vigorous stirring for up to 6 hours. Samples (*ca.* 0.02 ml) of the reaction mixture were taken at regular intervals using a syringe and needle equipped with a 4 mm nylon syringe filter (0.2 μ m pore size). The samples were immediately analysed using gas chromatography (methods described in section 7.8.5).

This reaction procedure was repeated using ethanol (14.0 ml, 247 mmol) and propan-2-ol (18.9 ml, 247 mmol) in place of methanol.

7.6 Sulfur Dioxide Oxidation

7.6.1 Activation of Hydrotalcite-type Compounds

The HTc's were calcined prior to the investigation of their catalytic activity in the oxidation of sulfur dioxide. The HTc to be activated was evenly distributed, in powdered form, across the lower surface of a Pyrex glass calcination tube and the tube inserted into the tube furnace. The calcination apparatus arrangement was as previously described (section 7.2) and illustrated (Figure 7.3). The HTc was then heated at a rate of 5 K min⁻¹ from room temperature to 723 K, under an air atmosphere. The furnace temperature of 723 K was maintained for 8 hours, with the air atmosphere. The calcination tube was then removed from the furnace, without compromising the air

atmosphere within and the calcined HTc allowed to cool to room temperature before catalytic investigation. A GHSV of $12,000 \text{ hr}^{-1}$ was maintained at all stages during calcination and cooling.

7.6.2 Sulfur Dioxide Oxidation Experiments

The potential catalyst was packed into a quartz glass microreactor tube ($\frac{1}{4}$ inch external diameter) to a constant bed length of 2 cm. This ensured that a constant volume of 0.25 cm^3 (since the internal diameter of the microreactor was 4 mm) was used for each material to be investigated. The packing density was important since, if the bed was too tightly packed, a large pressure drop occurred across the bed. Excessively loose packing was less of a problem since the material was powdered and could be encouraged to eliminate any trapped air with gentle tapping on the end of the tube. Quartz glass wool was used to loosely plug each end of the bed to retain the powdered material. The microreactor was then inserted into the furnace (Watlow Ceramic Fibre Heater Unit) of the catalyst test-rig illustrated in Figure 7.4 and Plate 7.1.

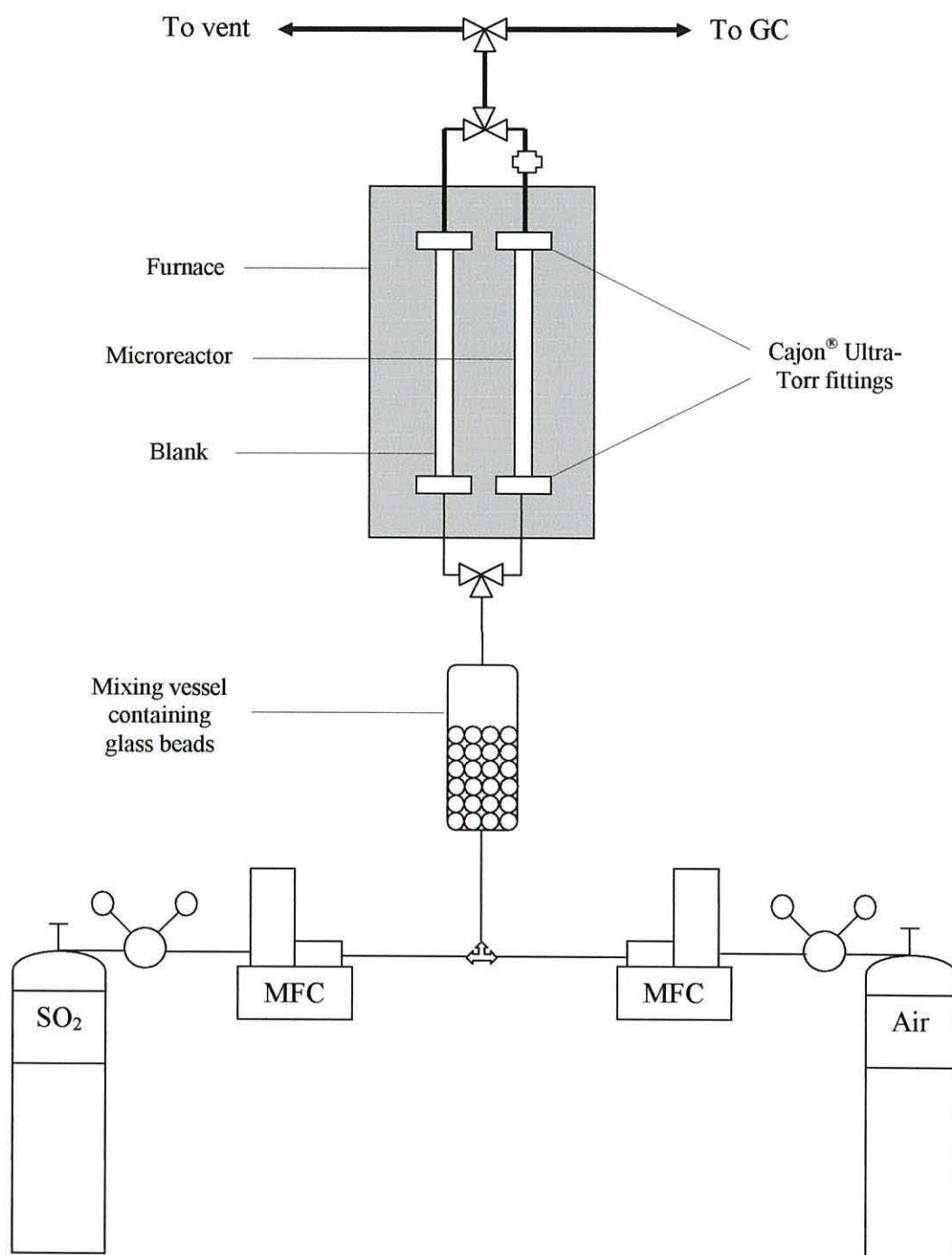
Cajon® Ultra-Torr fittings were used to provide a gas-tight seal and secure the microreactor and a blank alongside. Quartz glass wool was used as insulation between the inside of the furnace and the outside of the reactor tubes, in order to minimise temperature fluctuations. Air flow was gradually increased through the microreactor, using a Brooks 5850S mass flow controller (MFC), until a flow rate of 47.5 ml min^{-1} was achieved through the bed. Sulfur dioxide gas was then introduced into the gas flow, using a second Brooks Model 5850S mass flow controller, until the combined flow was 50 ml min^{-1} . The gases were mixed using a stainless steel (304 grade) sample cylinder with an internal volume of 75 ml (supplied by Whitey Co.), which was partially filled with glass beads (5 mm diameter) to facilitate mixing. The combined flow rate was verified using a soap bubble meter at the vent outlet of the rig, whilst pressure-drop across the bed was monitored by switching the gas to flow through the blank. A total flow of 50 ml min^{-1} resulted in a GHSV of $12,000 \text{ hr}^{-1}$ through the catalyst bed. The effect of various temperature runs on the reaction mixture were then investigated. Furnace temperature was controlled using a PID temperature control unit (CAL

Controls Ltd., Model 3300), which utilised a K-type thermocouple (RS Components) situated alongside the microreactor. The sample lines from the microreactor to the GC were kept at a constant 373 K in order to reduce the potential for condensation of reaction product in the sample lines. To do this, heating tape (supplied by Electrothermal Engineering Limited) was wrapped around the $\frac{1}{8}$ -inch stainless steel tubing. This was kept in place using expandable braided black sleeving (supplied by RS components). The temperature of the tape was adjusted, as necessary using a variable temperature regulator.

N.B.

All fittings and tubing used in the construction of the test rig selected were as chemically inert and corrosion resistant as possible. Stainless steel apparatus was 316 grade, except where stated. Stainless steel tubing was $\frac{1}{8}$ -inch external diameter.

Samples of the microreactor exit gases were taken periodically using a sample valve/loop on a dedicated gas chromatograph (GC) equipped with a thermal conductivity detector (TCD). Specific details of the GC procedure are provided in section 7.8.5.



Key;



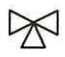
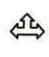

	$\frac{1}{8}$ inch 316 stainless steel tubing		heated sample lines
	Swagelok [®] 3-way switching valve		Swagelok [®] Union Tee
MFC	Mass Flow Controller		Nupro [®] 2 µm stainless steel filter

Figure 7.4 Catalyst test-rig for sulfur dioxide oxidation



Plate 7.1 Catalyst test-rig (gases exiting right *via* heated sample line to gas chromatograph)

7.7 Cyclohexane Dehydrogenation

7.7.1 Activation of Hydrotalcite-type Compounds

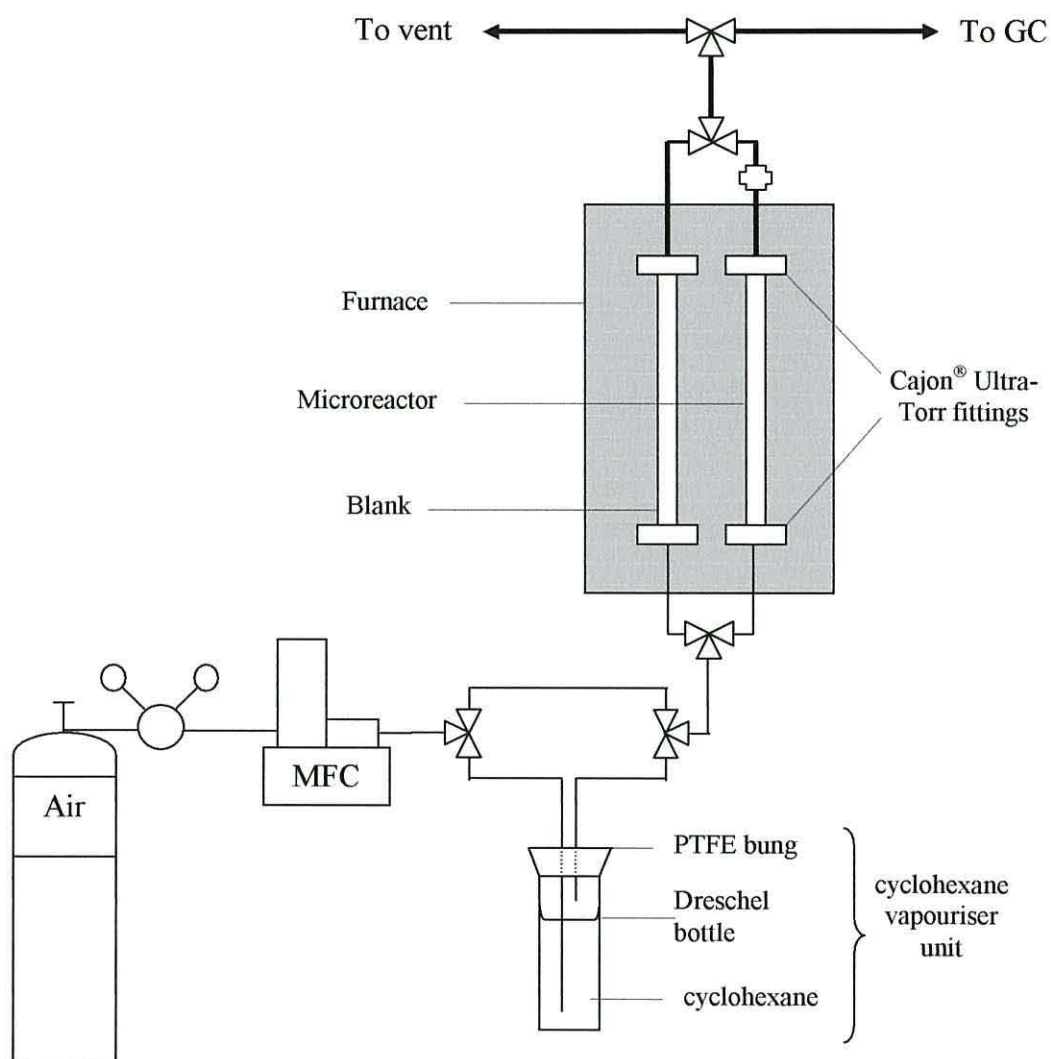
The HTc's were calcined prior to the investigation of their catalytic activity in the dehydrogenation of cyclohexane. The HTc to be activated was evenly distributed, in powdered form, across the lower surface of a Pyrex glass calcination tube and the tube inserted into the tube furnace, as previously illustrated (Figure 7.3). The HTc was then heated at a rate of 5 K min^{-1} from room temperature to 723 K, under an air atmosphere. The furnace temperature of 723 K was maintained for 4 hours with the air atmosphere. The calcination tube was then removed from the furnace, without compromising the atmosphere within and the calcined HTc allowed to cool to room temperature before catalytic investigation. A GHSV of $12,000\text{ hr}^{-1}$ was maintained at all stages during calcination and cooling.

7.7.2 Cyclohexane Dehydrogenation Experiments

The catalyst bed was arranged in the microreactor as outlined in section 7.6.2. However, since cyclohexane is liquid at room temperature and pressure, a modification of the test-rig was required. The set-up used was as illustrated in Figure 7.5 and Plate 7.1.

Air was bubbled at 50 ml min^{-1} through the cyclohexane in the vapouriser unit, which produced a *ca.* 10 % cyclohexane-in-air mixture at room temperature. This value was calculated from Formula 7.2 and assumed a constant room temperature of 293 K, which was monitored. Values specific to cyclohexane for the constants A, B and C were used.⁷

The gaseous mixture was then passed through the catalyst bed, as previously, and conversions at a series of temperatures investigated. The GHSV was, as in the sulfur dioxide oxidation studies, $12,000\text{ hr}^{-1}$.



Key;

— 1/8 inch 316 stainless steel tubing

— heated sample lines



Swagelok® 3-way switching valve



Nupro® 2 µm stainless steel filter

MFC Mass Flow Controller

Figure 7.5 Catalyst test-rig for cyclohexane dehydrogenation

Formula 7.2 The Antoine Equation⁷

$$\log_{10} P = A - B/(C + t)$$

where; P = Vapour pressure (mm Hg)

A = 6.84498, B = 1203.526, C = 222.863

t = Temperature (°C)

In-line GC was utilised initially to analyse the microreactor exit gases using a TCD but later results were analysed using another GC equipped with a flame ionisation detector (FID). In order to do this, the microreactor exit gases were condensed and collected using a vapour trap immersed in a low temperature solid carbon dioxide/acetone bath. Specific details of the GC procedure for analysis are provided in Section 7.8.5.

7.8 Analytical Techniques

7.8.1 Infrared (IR) Spectroscopy

The spectra of the powdered samples were recorded as KBr discs on a Perkin-Elmer model 1600 FT-IR spectrophotometer between the range of 4,000 and 450 cm^{-1} , at a resolution of 4 cm^{-1} . The number of scans required for a sufficient spectrum was varied to achieve a reasonable signal-to-noise ratio.

7.8.2 X-ray Powder Diffraction (XRPD)

The X-ray powder diffraction data was collected using two different diffractometers.

Early results were collected using a Philips X-ray diffractometer (Fe- $\text{K}\alpha$ radiation, $\lambda = 0.1937 \text{ nm}$) equipped with a manganese filter, operating with a continuous scan at a rate of 1.00 $^{\circ}2\theta \text{ min}^{-1}$ between the range of $2\theta = 2$ to 60° . Data obtained was manually analysed.

Later results were collected using a Philips 1050/37 X-ray diffractometer (Co $\text{K}\alpha$ radiation, $\lambda = 0.1790 \text{ nm}$) equipped with an iron filter, operating with a continuous scan between the range of $2\theta = 5$ to 75° . Philips X'Pert System software was used to collect and manipulate the data. For detailed scan results, a scan rate of 0.12 $^{\circ}2\theta \text{ min}^{-1}$ was used after a preliminary scan at 2.40 $^{\circ}2\theta \text{ min}^{-1}$. Philips X-ray diffraction pattern library software was then used to search for the pattern recorded for

each sample and compared with the X-ray powder diffraction files held in the Joint Committee on Powder Diffraction Standards (JCPDS) data-base.

Sample preparation for analysis, in each case, consisted of the formation of back-pressure mounted samples. This was achieved by loading the powder to be analysed into a standard aluminium sample holder from the back, onto a glass slide. Once the cavity was filled, sufficient pressure was then applied to lightly compact the powder, the glass slide removed and the powder analysed from the surface previously covered with the glass slide. This method was used because it was sufficiently rapid for routine analysis, yet is reported to provide a sufficiently random orientation to obtain a more complete diffraction pattern, consisting of a larger number of *hkl* reflections than would be produced with oriented specimens.^{8,9}

7.8.3 Scanning Electron Microscopy (SEM)

Ground samples were mounted (using double-sided carbon tape) on aluminium sample stubs which were then sputtered with a thin gold film in a sputter-coater for *ca.* 2-4 minutes, depending on the sample, at 1 kV. The thickness of gold film achieved using this method generally proved sufficient to disperse surface charge without masking the surface morphology of the samples. A Hitachi S-520 SEM was used for electron microscopy. Accelerating voltages used were quite low, generally in the range of 10-12 kV, in order to minimise sample degradation, the possible production of electron beam induced artefacts and transmission effects. A relatively narrow primary electron beam was used to achieve a sufficient depth of focus, whilst care was taken not to sacrifice resolution or increase charging excessively by using too narrow a beam. Whilst examination of the SEM image was carried out on a long persistence phosphor screen with relatively rapid scan speeds, micrographs were taken using a short persistence phosphor screen and relatively slow scan speeds to allow photographic recording using a stills camera. Throughout the scan (80 seconds) the shutter of the camera remained open.

Uncoated samples were also examined using α Link energy-dispersive analysis of X-rays (EDAX), whilst in the electron microscope. In order to increase the number of electrons impinging upon the specimen, which was essential for analysis using this method, the condenser lens was opened to a greater degree than during the initial sample observation.

7.8.4 Differential Thermal Analysis (DTA)

Samples of the HTc's were analysed against an alumina reference using a Stanton Redcroft DTA, heating from 273-973 K at a rate of 10 K min⁻¹ in a static air atmosphere.

7.8.5 Gas Chromatography (GC) and Gas Chromatography-Mass Spectrometry (GC-MS)

Cyanoethylation Experiments

Gas chromatography of the methanol cyanoethylation reaction products was carried out using a Perkin-Elmer 8410 GC, equipped with a flame ionisation detector (FID). High purity nitrogen was used as the carrier gas and hydrogen/air supplied the FID. Separations were carried out using a Restek Corp. Rtx-1701 capillary column with dimensions of 15 m length, 0.53 mm internal diameter, 1 μ m film thickness. The stationary phase was Crossbond® 14 % cyanopropylphenol - 86 % methylpolysiloxane. Sample volume was 0.1 μ l. Injector temperature was 473 K and detector temperature was 523 K. The temperature programme used was; 303 K isothermal for 2 minutes followed by temperature ramp at 20 K min⁻¹ to 383 K, which was held for 1 minute.

Gas chromatography of the ethanol and propan-2-ol cyanoethylation reaction products was carried out using a Chrompack CP9001 GC, equipped with a flame ionisation detector (FID). Helium was used as the carrier gas and hydrogen/air supplied the FID, nitrogen was used as make-up gas. Separations were carried out using a Restek Corp. Stabilwax® capillary column with dimensions of 15 m length, 0.53 mm internal

diameter, 0.5 μm film thickness. The stationary phase was Crossbond® Carbowax®. Sample volume was 0.1 μl . Injector temperature was 473 K and detector temperature was 523 K. The temperature programme used was; 313 K isothermal for 2 minutes followed by temperature ramp at 20 K min^{-1} to 433 K, which was held for 1 minute. Data handling software used was the 'Maestro Chromatography Data System – Version 2.4', supplied by Chrompack International.

Gas chromatography-mass spectrometry of the methanol, ethanol and propan-2-ol cyanoethylation reaction products was carried out using a Hewlett Packard HP 5790A Series GC coupled to a HP 5970A Series mass selective detector. Helium was used as the carrier gas. Chromatographic separations were carried out using a HP-5M.S. capillary column with dimensions of 30 m length, 0.25 mm internal diameter, 0.25 μm film thickness. The stationary phase was Crosslinked 5 % Ph Me Silicone. Sample volume was 0.1 μl but was split on injection. Injector temperature was 423 K. The temperature programme used was; 308 K isothermal for 1 minute followed by temperature ramp at 35 K min^{-1} to 408 K, which was held for 3 minutes. Data handling hardware, with original software, used was the Hewlett Packard HP 59970 MS ChemStation.

Sulfur Dioxide Oxidation Experiments

Gas chromatography of the sulfur dioxide reaction products was carried out using an in-line Carlo Erba Strumentazione Model 4200 GC, equipped with a thermal conductivity detector (TCD). Helium was used as the carrier/reference gas. Separations were carried out using a packed column with dimensions of *ca.* 1.8 m length and 4 mm internal diameter. The packing material was Porapak Q, supplied by Waters division of Millipore Corporation. A Valco sample valve with a 100 μl sample loop was used for sample injection. The temperature programme used was; 463 K isothermal for 2 minutes followed by temperature ramp at 5 K min^{-1} to 483 K, which was held for 9 minutes. Data handling software used was the 'JCL 6000 Gas Chromatography Data System', supplied by Jones Chromatography Limited.

Cyclohexane Dehydrogenation Experiments

Initial gas chromatographical studies of the cyclohexane reaction products were carried out using an in-line Carlo Erba Strumentazione Model 4200 GC, equipped with a

thermal conductivity detector (TCD). Helium was used as the carrier/reference gas. Separations were carried out using a packed column with dimensions of *ca.* 1.8 m length and 4 mm internal diameter. The packing material was Porapak Q, supplied by Waters division of Millipore Corporation. A Valco six-port UW series sample valve with a Valcon P rotor and a 100 μ l sample loop was used for sample injection. The temperature programme used was; 443 K isothermal for the total run-time. Data handling software used was the 'JCL 6000 Gas Chromatography Data System', supplied by Jones Chromatography Limited.

Later gas chromatographical studies of the cyclohexane reaction products, collected using a low-temperature vapour trap, were carried out using a Chrompack CP9001 GC, equipped with a flame ionisation detector (FID). Helium was used as the carrier gas and hydrogen/air supplied the FID, nitrogen was used as make-up gas. Separations were carried out using a Restek Corp. Stabilwax[®] capillary column with dimensions of 15 m length, 0.53 mm internal diameter, 0.5 μ m film thickness. The stationary phase was Crossbond[®] Carbowax[®]. Sample volume was 0.1 μ l. Injector temperature was 473 K and detector temperature was 523 K. The temperature programme used was; 318 K isothermal for 2 minutes followed by temperature ramp at 10 K min⁻¹ to 473 K, which was held for 3 minutes. Data handling software used was the 'Maestro Chromatography Data System – Version 2.4', supplied by Chrompack International.

N.B.

External standards were used to calibrate the peaks on the GC traces, which allowed subsequent peak assignments to be made, coupled with GCMS results when recorded.

7.9 Sources of Chemicals and Methods of Purification

HTc and Iron Oxide Syntheses

Mg(NO ₃) ₂ .6H ₂ O	(Aldrich, 99.0 % A.C.S. reagent)
Al(NO ₃) ₃ .9H ₂ O	(Avocado, 99.0+ %)
FeCl ₂ .4H ₂ O	(Avocado, 99.0 %)
NaHCO ₃	(BDH, 99.0+ %)

Na ₂ CO ₃	(BDH, 99.0+ %)
NaOH	(Wardle Chemicals Ltd., LR 96.0+ %)
H ₂ O ₂	(Bamford Laboratories, <i>ca.</i> 30 % w/v)
Deionised water	(general laboratory reagent)
Methanol	(Aldrich, 99.8+ % A.C.S. reagent)

Solvents were degassed by heating to *ca.* 353 K and bubbling nitrogen through them to displace gases otherwise present.

Gases (calcination and GC's)

Compressed air	(Air Products)
Nitrogen	(Air Products, high purity)
Helium	(Air Products, 5.0 grade)
Hydrogen	(Air Products, Premier grade)

Cyanoethylations

Acrylonitrile	(Aldrich, 99.0+ %)
3-Methoxypropionitrile (GC standard)	(Lancaster, 99.0 %)
3-Ethoxypropionitrile (GC standard)	(Lancaster, 99.0 %)
Methanol	(Aldrich, 99.8+ % A.C.S. reagent)
Ethanol	(Hayman Ltd., 99.86 %)
Propan-2-ol	(Aldrich, 99.5+ %)
Molecular sieves, 3A, Beads, 8-12 Mesh (Aldrich)	

Molecular sieves were activated by heating to *ca.* 573 K for 6 hours. Alcohols were dried/stored over 5 % w/v molecular sieves which also eliminated dissolved carbon dioxide.

SO₂ oxidations

Sulfur dioxide	(Aldrich, 99.9+ %)
Compressed air	(Air Products)

Cyclohexane dehydrogenations

Cyclohexane	(Aldrich, 99.9+ % HPLC grade)
-------------	-------------------------------

Cyclohexene (GC standard)	(Aldrich, 99 %)
Benzene (GC standard)	(Aldrich, 99+ % HPLC grade)
Compressed air	(Air Products)

7.10 References

- 1 T. Baird, K.C. Campbell, P.J. Holliman, R. Hoyle, D. Stirling and B.P. Williams, *J. Chem. Soc., Faraday Trans.*, 1995, **91**(18), 3219.
- 2 K.K. Rao, M. Gravelle, J. Sanchez-Valente and F. Figueras, *J. Catal.*, 1998, **173**, 115.
- 3 U. Schwertmann and R.M. Cornell, *Iron Oxides in the Laboratory*, VCH, Weinheim, 1991.
- 4 E.A. Cavanagh and P.J. Holliman, Final Year Undergraduate Project.
- 5 P.S. Kumbhar, J. Sanchez-Valente and F. Figueras, *Chem. Commun.*, 1998, 1091.
- 6 H. Kabashima and H. Hattori, *Catalysis Today*, 1998, **44**, 277.
- 7 J.A. Dean (Ed.), *Lange's Handbook of Chemistry* (11th Edition), McGraw-Hill Book Company, London, 1973.
- 8 D.M. Moore and R.C. Reynolds Jr., *X-Ray Diffraction and the Identification and Analysis of Clay Minerals*, Oxford University Press, Oxford, 1989.
- 9 G.W. Brindley and G. Brown (Eds.), *Crystal Structures of Clay Minerals and their X-ray Identification*, Mineralogical Society Monograph No. 5, Mineralogical Society, London, 1980.